

**DEFORMABLE MICROFLUIDICS: PHYSICS OF FLUID  
FLOW AND APPLICATIONS**

**By**

**Aryan Mehboudi**

**A DISSERTATION**

**Submitted to  
Michigan State University  
in partial fulfillment of the requirements  
for the degree of**

**Mechanical Engineering—Doctor of Philosophy**

**2018**

## ABSTRACT

### DEFORMABLE MICROFLUIDICS: PHYSICS OF FLUID FLOW AND APPLICATIONS

By

Aryan Mehboudi

While the rapidly-growing microfluidics technology has already permeated through many aspects of the molecular and biological sciences and enabled a wide variety of low-cost and point-of-care biomedical applications, deformable microfluidics, in which microchannel possesses at least one flexible sidewall, may offer some unique advantages. The recyclability of such platforms is improved and their lifetime is extended thanks to the minimal channel clogging. The difficulties associated with the deviation of device performance from an optimal point can also be alleviated to some extent by tuning the device. Furthermore, deformable microfluidic devices may be adjusted to have more than one optimal operating points. For example, a single deformable microfluidic filter is capable of isolating target cells with multiple sizes or deformability levels as opposed to a rigid counterpart that has only one cutoff size for filtering. In typical deformable microfluidic settings, the deformable part of microchannel is actuated via external pneumatic sources, making it difficult to fabricate and operate such devices. The main objectives of this work are 1) to develop a new class of deformable microfluidics without the need to pneumatic actuation, and 2) to develop analytical tools for studying flows of Newtonian fluids in deformable microchannels.

Pressure distribution within a deformable microchannel dictates the membrane deformation, while the membrane deformation governs the hydrodynamic resistance and consequently the pressure distribution within the channel. Deformable microfluidics, therefore, gives rise to a coupled fluid-solid interaction problem. Compressibility of the working fluid and variations of the channel's width are two other factors that can potentially make the problem even more complicated. In this work, an analytical model, with no fitting parameters, is derived simultaneously taking microchannel deformability, fluid compressibility, and microchannel's width profile into account, which makes it a universal tool for studying low-Reynolds-number flows of Newtonian liquids and gases in microscale. A new technique is also developed for fabrication of shallow (few microns in height) rigid/flexible microchannels with either small (tens of microns) or large (several millimeters) width. We show theoretically and experimentally that structural-fluid characteristics are solely dictated by dimensionless fluid compressibility and a lumped dimensionless parameter, called flexibility parameter. A master curve is obtained for fluid flow through any arbitrary shallow and long deformable microchannel presenting the dimensionless flow rate as functions of flexibility parameter and dimensionless fluid compressibility. The experimental and analytical investigations reveal various distinct fluid-structural characteristic behaviors

under different fluid compressibility and flexibility parameter regimes. We have also demonstrated that passive rectification of compressible and incompressible flows of Newtonian fluids (liquids and gases) under the Stokes flow regime ( $Re \ll 1$ ) is feasible by introducing the non-linear and direction-dependent terms to the otherwise linear equations of motion. Finally, a new class of deformable microfluidics is developed for passively-tunable particle trapping and isolation without the need to the pneumatic actuation. Filtration, isolation, and retrieval of particles are successfully demonstrated.

Copyright by  
ARYAN MEHBOUDI  
2018

This thesis is dedicated to my mother, my father, my wife,  
and my son.

## ACKNOWLEDGMENTS

I thank my advisor, professor Junghoon Yeom, very much for his supervision and everything he taught me during the past several years.

I also thank the other committee member: professor Manoochehr Koochesfahani, professor Wen Li, and professor Peter Lillehoj, very much for all their time and support.

In addition, I thank Dr. Baokang Bi and the staff of W. M. Keck Microfabrication Facility, and Karl Dersch and the staff of ECE Research Cleanroom in Michigan State University, very much for their assistance with chemistry and cleanroom fabrication.

## TABLE OF CONTENTS

<b>LIST OF TABLES</b> . . . . .	<b>x</b>
<b>LIST OF FIGURES</b> . . . . .	<b>xii</b>
<b>Chapter 1: Introduction</b> . . . . .	<b>1</b>
Separation . . . . .	2
Inertia-based separation . . . . .	2
Hydrodynamic fractionation . . . . .	5
Physical filtration . . . . .	6
Membranes . . . . .	7
Pillars . . . . .	9
Cross flow . . . . .	10
Weir-shaped . . . . .	11
Active separation . . . . .	11
Deformable microfluidic devices . . . . .	11
Objectives . . . . .	14
Outline . . . . .	15
<b>Chapter 2: A two-step sealing—and—reinforcement SU8 bonding paradigm for the fabrication of shallow microchannels</b> . . . . .	<b>17</b>
Questions . . . . .	17
Motivations . . . . .	18
Objectives . . . . .	18
Introduction . . . . .	18
Fabrication . . . . .	23
Methodology . . . . .	28
Experimental . . . . .	28
Device fabrication . . . . .	28
Hydraulic tests . . . . .	28
Experimental setup for droplet generation . . . . .	28
Modeling . . . . .	29
Results . . . . .	34
Two-step SU8 bonding paradigm’s outcome . . . . .	34
Multi-height deep–shallow microchannels . . . . .	39
Pressure-drop vs. flow rate and bonding strength tests . . . . .	40
PET film deformation and its effects on volumetric flow rate . . . . .	41
Bonding strength . . . . .	46
Droplet generation . . . . .	49
Conclusion . . . . .	49
<b>Chapter 3: Low-Reynolds-number incompressible fluid flow through straight deformable microchannels</b> . . . . .	<b>52</b>
Questions . . . . .	52
Motivations . . . . .	52
Objectives . . . . .	53
Introduction . . . . .	53
Modeling . . . . .	57
Analytical one-dimensional coupled fluid-solid mechanics model . . . . .	57
Composite membranes . . . . .	60
Linear pressure variation assumption . . . . .	60
Experiments . . . . .	61
Fabrication . . . . .	61

Volumetric flow rate measurement . . . . .	64
Low flow rate regime (below about 40 micro-litre/min) . . . . .	64
High flow rate regime (above about 40 micro-litre/min) . . . . .	64
Results and discussion . . . . .	65
Parametric study of the flexibility parameter . . . . .	65
Experimental results . . . . .	66
Linear pressure variation assumption . . . . .	74
Conclusion . . . . .	76
<b>Chapter 4: Low-Reynolds-number incompressible fluid flow through asymmetric de-</b>	
<b>formable microchannels . . . . .</b>	<b>78</b>
Questions . . . . .	78
Motivations . . . . .	78
Objectives . . . . .	79
Introduction . . . . .	79
Modeling . . . . .	80
Studying different regimes of flexibility parameter analytically . . . . .	83
Extremely small flexibility parameter . . . . .	83
Extremely large flexibility parameter . . . . .	85
Behavioral characteristics solely due to $\chi^1$ term . . . . .	86
Behavioral characteristics solely due to $\chi^2$ term . . . . .	87
Materials and methods . . . . .	89
Results and discussion . . . . .	90
Microchannel design . . . . .	90
Experimental and theoretical investigation . . . . .	90
Other liquids as working fluid: viscosity effects . . . . .	97
Effects of width profile function . . . . .	99
Conclusion . . . . .	101
<b>Chapter 5: Low-Reynolds-number compressible fluid flow through straight deformable</b>	
<b>microchannels . . . . .</b>	<b>103</b>
Questions . . . . .	103
Motivations . . . . .	103
Objectives . . . . .	104
Introduction . . . . .	104
Modeling . . . . .	106
General Compressible Fluid Flow . . . . .	106
Ideal Gas Flow . . . . .	114
Materials and methods . . . . .	115
Results and discussion . . . . .	116
Theoretical investigation . . . . .	116
Experimental investigation . . . . .	119
Conclusion . . . . .	126
<b>Chapter 6: Low-Reynolds-number compressible fluid flow through asymmetric deformable</b>	
<b>microchannels . . . . .</b>	<b>128</b>
Questions . . . . .	128
Motivations . . . . .	128
Objectives . . . . .	129
Introduction . . . . .	129
Modeling . . . . .	130
General compressible fluid flow . . . . .	130
Ideal gas flow . . . . .	132
Materials and methods . . . . .	133

Fabrication . . . . .	133
Flow rate measurement . . . . .	133
Results and discussion . . . . .	134
Conclusion and outlook . . . . .	139
<b>Chapter 7: Passive particle filtration and isolation using deformable microfluidics . . . . .</b>	<b>140</b>
Questions . . . . .	140
Motivations . . . . .	140
Objectives . . . . .	141
Introduction . . . . .	141
Design . . . . .	145
Pressure effects . . . . .	145
Height effects . . . . .	149
Width effects . . . . .	150
Fabrication . . . . .	153
Part I: Disposable platforms . . . . .	154
Rigid microfluidic filter . . . . .	155
Particle filtration using a tunable microfluidic sieve with the simple design . . . . .	157
Particle filtration using a tunable microfluidic sieve with the modified design . . . . .	163
Part II: Reusable platforms . . . . .	167
Particle trapping . . . . .	167
Particle retrieval . . . . .	170
Pressure buildup effects . . . . .	171
Summary and future works . . . . .	172
<b>Chapter 8: Conclusion and future work . . . . .</b>	<b>173</b>
Conclusion . . . . .	173
Future work . . . . .	175
<b>APPENDIX . . . . .</b>	<b>178</b>
<b>BIBLIOGRAPHY . . . . .</b>	<b>189</b>

## LIST OF TABLES

Table 1: The accessible range of the microchannel dimensions for various adhesive bonding approaches: (A) using an adhesive-coated rigid substrate to seal the microchannel sidewalls, (B) the partial exposure technique, (C) the sacrificial layer approach, and (D) the lamination method. The following definitions are used for the sake of simplicity: +: it has been reported in the literature, -: it has not been reported in the literature (to the best of the author's knowledge), -p: even though it has not been demonstrated in the literature (to the best of the author's knowledge), the author believe it is feasible, and ++: it is feasible using the proposed paradigm in this work. . . . .	20
Table 2: The fabrication considerations for various adhesive bonding approaches. The schematic presentation of the addressed techniques can be found in Fig. 17. . . . .	21
Table 3: The specifications of different SU8 films utilized in this work. The uniform SU8 films with different thicknesses have been spun by using the appropriate mixture of the SU-8 2100 and the SU-8 2000 Thinner (both from MicroChem Corp.), and utilizing the following spinning procedure: The spinner speed is ramped at a rate of 83 rpm/s up to 500 rpm and kept there for 15–20 seconds. The speed is then ramped up to the maximum speed at a rate of 83 rpm/s, remaining constant for 45 seconds, and then ramped down to zero at a rate of about 250 rpm/s. . . . .	26
Table 4: The two-step (65°C followed by 95°C) soft-bake duration times (minutes) for different SU8 layers used in the sealing step. . . . .	26
Table 5: The two-step (65°C followed by 95°C) soft-bake duration times (minutes) as well as the bonding temperature for different SU8 layers used in the reinforcement step. . . . .	27
Table 6: The maximum allowed pressure difference across the 400 $\mu m$ wide microchannels for different fabrication approaches investigated in this work. . . . .	46
Table 7: The geometry of four deformable microchannels studied in this chapter. . . . .	66
Table 8: The order of magnitude of different terms existing in Eq. 10 for the flexibility parameter, $\chi$ , with various orders of magnitude. For each flexibility scale, the most important terms with the order of magnitude equal to or greater than $10^{-1} \times O(Q^*)$ are highlighted in bold font. Note: $O(c_1) = 1$ , $O(c_2) = 10^{-1}$ , and $O(c_3) = 10^{-1}$ . . . . .	70
Table 9: The geometry of the microchannels studied experimentally in this chapter. . . . .	121
Table 10: The pressure effects investigation for a microchannel 6 mm and 2 cm in width and length, respectively. . . . .	148
Table 11: The effects of the pressure difference across the channel as well as the microchannel original height on the PET film deformation and the characteristics of the flow through a microchannel 8 mm and 4 cm in width and length, respectively. . . . .	149
Table 12: The microchannel width effects for the microchannels 4 cm long and a pressure difference of 15 kPa. . . . .	151

Table 13: The effects of microchannel width on the structural-fluid characteristics of the fluid flow through the microchannels 4 <i>cm</i> long with nearly identical opening size at the outlet section. . . . .	151
Table 14: The effects of pressure difference on the structural-fluid characteristics of the fluid flow through the simple tunable sieve consisting of a deformable microchannel 1 <i>cm</i> long and 5 <i>mm</i> wide. . . . .	161

## LIST OF FIGURES

Figure 1:	(From the work of Yeo <i>et al.</i> [1]) The approximate characteristic length scales of the microfluidic and nanofluidic systems compared with those of various biological entities.	2
Figure 2:	(From the work of Di Carlo <i>et al.</i> [2]) Differential focusing of 10- and 2- $\mu m$ mixed particles in water. The 2- $\mu m$ particles remain unfocused after transiting 3 cm of asymmetric turns, whereas 10- $\mu m$ particles are sharply focused. $R_c = 7.5$ . (Scale bar=50 $\mu m$ ).	4
Figure 3:	(From the work of Zhang <i>et al.</i> [3]) The counter-rotating vortex in the cross section of a serpentine channel with different aspect ratios, (i) AP=1/5 and (ii) AP=3/5.	4
Figure 4:	(From the work of Yoon <i>et al.</i> [4]) (left) Velocity distributions at the middle of the arc for various Dean numbers with an aspect ratio of 1.0. (middle) Size-selective separation of micro beads in the direction of the fluidic force exerted by the velocity distribution in an arc channel of aspect-ratio 1/2. (right) Comparison of the trajectories of the 40 $\mu m$ glass and 10 $\mu m$ nickel beads at the Dean number of 28.87 and aspect ratio of 1/2.	5
Figure 5:	(left) (From the work of Yamada <i>et al.</i> [5]) The schematic presentation of the pinched flow fractionation. The particles are aligned against one sidewall in the pinched segment using a sheath flow. The particles are then separated according to their size by following the different diverging streamlines. (right) (From the work of Yamada and Seki [6]) The schematic presentation of the hydrodynamic filtration. The diagram shows the particle behavior at a branch point for the case that the proportion of the flow rate through the side channels over that of the main channel is (a) low, (b) medium, and (c) high. The virtual boundaries are shown with dashed lines. (d) A schematic presentation of the particle concentration and classification in a microchannel with multiple side channels.	6
Figure 6:	(From the work of Kuiper <i>et al.</i> [7]) (left) A SEM image of the microsieve surface. (middle) A SEM image showing a free hanging perforated membrane supported by the vertical walls. (right) The theoretically calculated water flux for a microsieve with a porosity of 20% and a membrane thickness equal to the pore diameter.	7
Figure 7:	(From the work of Wickramasinghe <i>et al.</i> [8]) (top left) Experimental set up. (top right) Typical particle size distribution for influenza virus feed solution. (Bottom) Particle size distributions in the retentate (filled squares) and concentrated bulk permeate (unfilled squares) after microfiltration using (left) 0.1 $\mu m$ and (right) 0.2 $\mu m$ membranes. The particles larger than the pores size are retained more effectively by the membrane, while smaller particles tend to pass through the membrane.	8
Figure 8:	(From the work of Zheng <i>et al.</i> [9]) (left) A schematic of the filtration process. $F_L$ : force caused by fluidic pressure from top. $F_S$ : supporting force from bottom membrane. $F_T$ : tension stress force on plasma membrane. (right) Device is assembled inside a housing cassette.	9
Figure 9:	(From the work of Doh <i>et al.</i> [10]) A schematic image of the cancer cell isolation tapered slit array.	9

Figure 10: (From the work of VanDelinder <i>et al.</i> [11]) (left) (a) A camera image of the microfluidic device together with (b) a magnified image of the fragment of the filter region, marked by a rectangle in panel (a). This image is rotated 90° from the view shown in panel (a). (c) Schematic diagram showing a cross-sectional view of the device (not to scale). (middle) The plasma flow rate through the plasma outlet as a function of time at inlet pressure of 4 psi with constant zero pressure at the outlets (triangles) and with two different modes of back-pulsing: the pressure of 6 psi was applied to the outlets for 100 ms every 3 s (diamonds and circles) and also for 5 s every 2.5 min (circles). Each curve is an average of two individual tests. (right) The plasma flow rate through the plasma outlet for blood with hematocrits of 10% (circles), 20% (diamonds), and 30% (triangles) as a function of inlet pressure, $P_1$ , with outlet pressure, $P_3$ , equal to $1.5P_1$ applied for 100 ms every 3 s. For each hematocrit the data points show averages of at least five individual tests, and the error bars show the standard errors of the mean. The error bars are not shown when they are smaller than the symbols. . . . .	10
Figure 11: (From the work of Chen <i>et al.</i> [12]) (A) The design and construction of the weir-type barrier. (B) The SEM micrograph of the weir. . . . .	11
Figure 12: (From the work of Wang <i>et al.</i> [13]) (left) Pneumatic actuation of the assay chamber for solid-phase immunoassay (upper) and chemifluorescence detection (bottom). (right) The fluorescence images obtained at the concentrations of 5 ng/ml. . . . .	12
Figure 13: (From the work of Beech <i>et al.</i> [14]) (1) A modified micrometer translation stage holds the elastic-DLD device. (2) The sketch of the device. (3a) and (3b) Micrographs of posts before and after stretching showing how diameter changes. . . . .	13
Figure 14: (From the work of Huang <i>et al.</i> [15]) (left) A photograph of the micro filter chip. (right top) The relationship between the minimum applied pneumatic pressure in the filter zone and the diameters of the trapped microbeads (right bottom) The microscope images of the clogged channels with trapped microbeads. . . . .	13
Figure 15: (From the work of Liu <i>et al.</i> [16]) (left) Pneumatic microstructure presenting a height-adjustable geometry resulting reversible cell trapping (top) compared with a fixed microstructure (bottom) showing irreversible trapping. The fluorescence images show the parallel trapping of the cells under the pressure of 4 psi (middle) and 5 psi (right). . .	14
Figure 16: (From the work of Beattie <i>et al.</i> [17]) (left) Photograph of the separation device with the flow and control channels are filled with red and green food coloring respectively. (right) The probability of trapping microsphere as a function of pressure applied to the diaphragm. Smaller microspheres require smaller channel openings to be captured, and therefore require greater trapping pressure than larger microspheres. The range of trapping pressures for each particle size is shown as a colored block for each microsphere diameter, indicating the minimal overlap between sizes. . . . .	14
Figure 17: The schematic presentation of the different adhesive bonding approaches. ( $A_s$ ) The SU8 photo-lithography and bonding using a SU8-coated rigid substrate: ( $A_g$ ) The glass etching process and bonding using a rigid substrate coated with an adhesive layer such as SU8, NOA, etc: (B) The partial exposure approach. (C) The sacrificial layer approach. (D) The adhesive layer lamination approach. . . . .	22

Figure 18: Schematic presentation of the two-step sealing-and-reinforcement bonding paradigm for two different approaches that the microchannel sidewalls are made through the SU8 photo-lithography (left) or the glass wet etching (right): the microchannel sidewalls are created through SU8 photo-lithography ( $a_s$ ) or glass wet etching ( $a_g$ ). At the sealing step, a PET film coated with a thin layer of SU8 seals the microchannel sidewalls ( $S_{1,s}$  and  $S_{1,g}$ ). The chip is then undergone with UV illumination and post-exposure baking to cure the adhesive layer ( $S_{2,s}$  and  $S_{2,g}$ ). The slight SU8 reflow can result in a cross-section with round corners in this step. At the reinforcement step, a glass substrate coated with a SU8 layer is brought into contact with the bare side of the PET film ( $R_{1,s}$  and  $R_{1,g}$ ). The sample is then undergone with UV illumination and post-exposure baking to cure the adhesive layer at the bonding interface of the reinforcement glass and the PET film ( $R_{2,s}$  and  $R_{2,g}$ ). . . . . 24

Figure 19: The schematic presentation of the three-dimensional model for the structural mechanics analysis of the PET film as the ceiling of a straight microchannel. The width of the bonding interfaces is considered to be equal to that of the wet surface (PET-liquid interface). The boundary conditions are as follows: the bonding interfaces are fixed. The wet surface experiences a pressure, which linearly decreases along the channel. The lateral sides of the PET film have the free boundary condition. The back side of the PET film has also the free boundary condition if the channel is not reinforced. Otherwise, the back side of the PET film is fixed. . . . . 31

Figure 20: (top left) A camera picture of a multi-height deep-shallow microfluidic channel together with (top right) the schematic presentation of the three-dimensional model for the structural mechanics analysis of the PET film as the ceiling of the channel, as well as (bottom) the schematic presentation of the zero-dimensional model for the fluid flow analysis. The various areas of the deep-shallow microchannel are described in the following.  
**(1):** The bonding interfaces.  
**(2) and (6):** The areas connecting the inlet/outlet ports to the deep and wide portions of the channel.  
**(3) and (5):** The deep and wide portions of the channel.  
**(4):** The shallow and wide portion of the channel.  
The pressure values at different nodes ( $p_i : i = 1$  to 6), shown in the bottom schematic, together with the volumetric flow rate through different branches of the channel, as well as the structural behaviors such as the PET film's deformation, strain and stress distribution, etc., are obtained by solving the coupled equations of the zero-dimensional-fluid-mechanics—three-dimensional-structural-mechanics model using an iterative approach. . . . . 32

Figure 21: (a) An optical microscopy image showing the center of a serpentine microchannel about  $4 \mu m$  and  $15 \mu m$  in height and width, respectively, sealed by a  $2 \mu m$ -SU8-covered PET and reinforced by a  $7 \mu m$ -SU8-covered microscope slide, together with (b) a higher magnification image of the U-turns. (c) An optical microscopy image showing the cross-section of the channels, as well as (d) a higher magnification (100X) optical microscopy image, and (e) a (7.00k) SEM image of a single channel. The SU8 adhesive layer on the PET film has flown towards the sidewalls during the sealing step due to the capillary action. The dashed line has been added to the SEM image to more clearly specify the bonding interface. Scale bars:  $500 \mu m$  in (a),  $100 \mu m$  in (b) and (c),  $20 \mu m$  in (d), and  $3 \mu m$  in (e). . . . . 35

Figure 22: (a) A camera picture as well as (b) a cross-section optical microscopy image of a microfluidic channel about  $3 \mu m$  in height fabricated through the wet etching of the glass following by the sealing step using a PET film coated with a  $2 \mu m$ -thick SU8 layer without reinforcement. Scale bar =  $20 \mu m$  in (b). . . . . 37

- Figure 23: (a) A camera picture as well as (b) an optical microscopy image of a microfluidic channel  $2\ \mu\text{m}$  in height,  $2\ \text{mm}$  in width in its widest portion, and  $90\ \mu\text{m}$  in width in its narrowest portion, sealed by a  $2\ \mu\text{m}$ -SU8-coated PET film without reinforcement. Since a clear cross-section image cannot be taken for such an ultra-low aspect ratio channel, a schematic of the cross-section is shown in (a) as well. Scale bar =  $500\ \mu\text{m}$  in (b). . . . 38
- Figure 24: (a) A camera picture showing a microchannel consisting of deep (height =  $77\ \mu\text{m}$ ) and shallow (height =  $2\ \mu\text{m}$ ) regions, together with the (inset) schematic side-view of the microchannel, where  $H_d = 77\ \mu\text{m}$  and  $H_s = 2\ \mu\text{m}$ , as well as (b) a microscope image of another double-height microchannel, which is  $32\ \mu\text{m}$  and  $7\ \mu\text{m}$  high in deep and shallow regions, respectively. The channel is symmetric with respect to the horizontal dash-dotted line. The edges of the lower half of the shallow region are also shown with the dashed lines. Both of the microchannels in (a) and (b) are sealed using the  $2\ \mu\text{m}$ -thick-SU8-coated PET film without reinforcement. The scale bar =  $5\ \text{mm}$  in (b). 39
- Figure 25: (a) The DI water volumetric flow rate through a straight channel  $7.3\ \mu\text{m}$ ,  $1.55\ \text{mm}$ , and  $8\ \text{mm}$  in height, width, and length, respectively, sealed using a PET film coated with a  $7\ \mu\text{m}$ -thick SU8 layer with and without reinforcement, as a function of pressure difference across the channel in comparison with the theoretical results for a non-deformable channel with the same dimensions [18] (Eqs. 2 and 4), and the modeling for the deformable low aspect ratio channel. (b) The DI water volumetric flow rate through a straight channel  $2.2\ \mu\text{m}$ ,  $2.5\ \text{mm}$ , and  $7\ \text{mm}$  in height, width, and length, respectively, sealed using a PET film coated with a  $2\ \mu\text{m}$ -thick SU8 layer without reinforcement in comparison with the theoretical results [18] for a non-deformable channel with the same dimensions, and the modeling for the deformable low aspect ratio microchannel. . . . . 41
- Figure 26: The displacement contours of the PET film under the pressure difference of  $345\ \text{kPa}$  across two microchannels (a) A, and (b) B. (c) The displacement profile of the PET film in the middle of Microchannel B at various pressures. (d) The average PET film's displacement as a function of the pressure difference across the microchannels. Microchannel A is  $8\ \text{mm}$ ,  $1.55\ \text{mm}$ , and  $7.3\ \mu\text{m}$  in length, width, and height, respectively, while Microchannel B is  $7\ \text{mm}$ ,  $2.5\ \text{mm}$ , and  $2.2\ \mu\text{m}$  in length, width, and height, respectively. . . . . 43
- Figure 27: The contours of the PET film's (a) first principal strain, and (b) von Mises stress obtained from the fluidic-structural mechanics modeling of Microchannel A under the pressure difference of  $345\ \text{kPa}$  across the channel, together with the PET film's (c) first principal strain, and (d) von Mises stress for Microchannel B under the same pressure. Microchannel A is  $8\ \text{mm}$ ,  $1.55\ \text{mm}$ , and  $7.3\ \mu\text{m}$  in length, width, and height, respectively, while Microchannel B is  $7\ \text{mm}$ ,  $2.5\ \text{mm}$ , and  $2.2\ \mu\text{m}$  in length, width, and height, respectively. . . . . 44
- Figure 28: (left) The volumetric flow rate through the multi-height deep-shallow microchannel shown in Fig. 24, sealed using a PET film coated with a  $2\ \mu\text{m}$ -thick SU8 layer, without reinforcement, as a function of pressure difference across the channel in comparison with the modeling results for the deformable and non-deformable channels with the same dimensions. (right) The displacement contour of the PET film at the pressure difference of  $55\ \text{kPa}$  across the multi-height deep-shallow microchannel, obtained by using the coupled zero-dimensional-fluid-mechanics—three-dimensional-solid-mechanics modeling. . . . . 45
- Figure 29: The von Mises stress profiles within the PET films sealing the  $1\ \text{cm}$ -long microchannels of (a)  $400\ \mu\text{m}$  and (b)  $1.55\ \text{mm}$  in width, across the inlet (dashed lines) and outlet (continuous lines) sections. The pressure difference across the channels is  $345\ \text{kPa}$ . . . . 47

Figure 30: The oil-in-water droplets generated using a microfluidic device about (a) $6 \mu m$ and (b) $15 \mu m$ in height. The continuous phase to the dispersed phase volumetric flow rate ratio is $26 \mu l/min : 14 \mu l/min$ and $90 \mu l/min : 1 \mu l/min$ for (a) and (b), respectively. Scale bars are $50 \mu m$ and $500 \mu m$ in (a) and (b), respectively. . . . .	50
Figure 31: (a) Schematic representation of a fluid flow through a microchannel with the flexible ceiling together with the cross-section view of the channel (b) without and (c) with applying the pressure difference across the channel. . . . .	58
Figure 32: (a) Schematic diagrams of the cross section of the composite membrane consisting of the PET film with two SU8 adhesive layers together with the (b) transformed section for stress analysis. . . . .	60
Figure 33: Schematic representation of the fabrication process flow: (a) the microchannel sidewalls are created using the double-step glass wet etching. (S <sub>1</sub> ) A PET film coated with a thin layer of SU8 seals the microchannel sidewalls. (S <sub>2</sub> ) The chip is undergone with UV illumination and post-exposure baking to cure the adhesive layer. (R <sub>1</sub> ) A glass substrate with the same pattern as that of the main channel is aligned and brought in contact with the SU8 layer coated on the bare side of the PET film. (R <sub>2</sub> ) The sample is undergone with UV illumination and post-exposure baking to cure the adhesive layer at the bonding interface of the reinforcement glass and the PET film. . . . .	62
Figure 34: (a) A photograph of the fabricated device together with (b) a photograph showing the channel filled with a dye demonstrating a leakage-free bonding. The scale bar is $1 cm$ in (b). . . . .	63
Figure 35: (a) Plots of the dimensionless pressure, $p^* = p(x^*)/\Delta p$ , as a function of the dimensionless distance from the inlet $x^*$ for various flexibility parameter values. (b) The variation of the dimensionless membrane's mean deflection, $\langle \delta \rangle / H_0$ , along the microchannels for various flexibility parameter values. (c) A plot of the dimensionless flow rate $Q^* = [Q_{Deformable}/Q_{Rigid}]_{\Delta p_{Deformable}=\Delta p_{Rigid}}$ , as a function of the flexibility parameter. (d) A plot of the dimensionless pressure difference $\Delta p^* = [\Delta p_{Deformable}/\Delta p_{Rigid}]_{Q_{Deformable}=Q_{Rigid}}$ , as a function of the flexibility parameter. The insets show the logarithmic plots in (c) and (d). . . . .	65
Figure 36: (a) The volumetric flow rate through Microchannels A, B, C, and D in comparison with the analytical solutions of the one-dimensional model [19] together with (b) the magnification of the dotted box. (c) The ratio of the volumetric flow rate through the deformable microchannels to that through their theoretically rigid counterparts under the same pressure differences. (d) The master curve obtained in this work, Eq. 10, together with the experimental results. A logarithmic scale is used in (c) and (d). The error bars, obtained from three data-sets, are not shown when they are smaller than the size of markers. . . . .	67
Figure 37: (a) The flexibility parameter, $\chi$ , for Microchannels A, B, C and D under various pressure differences. The differences between the channels geometries and/or the membranes properties result in the different flexibility parameters under the same pressure difference across the channels. A sufficiently large change in the pressure difference across a specific channel can alter the flexibility parameter scale from one characteristic regime to another. (b) The fraction of the pressure difference across the rigid microchannel sufficiently large to cause the same volumetric flow rate when applied across the deformable microchannel with the same dimensions. . . . .	72

Figure 38: (a) The mean and maximum membrane deflections at the inlet section of Microchannels A and C ( $W=1.25$ mm) as well as those for Microchannels B and D ( $W=2.1$ mm) obtained using the theoretical model [19]. (b) The Reynolds number and (c) the hydrodynamic resistance for the studied microchannels under various pressure differences. . . . .	74
Figure 39: (a) The dimensionless volumetric flow obtained through the linear pressure variation assumption, Eq. 12, compared with the master curve obtained in this work, Eq. 10, as a function of the flexibility parameter. (b) The error associated with the linear pressure variation assumption: $(Q_{\text{Deformable}}^{\text{Analytical}} - Q_{\text{Deformable}}^{\text{Linear Pressure}})/Q_{\text{Deformable}}^{\text{Analytical}}$ . . . . .	75
Figure 40: Schematic diagrams showing the cross-section views of the fluid flow through a microchannel with a deformable ceiling in (a) nozzle and (b) diffuser directions together with ( $a_0$ and $b_0$ ) the top view of the channel. The dimensions in z-direction are not in scale with those in x-y plane for the sake of clarity. Note: $\hat{e}_z = \hat{e}_x \times \hat{e}_y$ , where $\hat{e}_x$ , $\hat{e}_y$ , and $\hat{e}_z$ denote the unit vector in x, y, and z directions, respectively. . . . .	81
Figure 41: Diagram showing the nomenclature of the nozzle/diffuser inlet/outlet dimensions. . . . .	84
Figure 42: Volumetric flow rates of water obtained from the 1-D coupled fluid-solid-mechanics model as a function of pressure difference across the deformable nozzle/diffuser microchannels of $2.6 \mu\text{m}$ in height with the half-angle of $\theta = 1.25^\circ$ for various small and large widths configurations: (a) $1$ mm and $2$ mm, (b) $2$ mm and $2.5$ mm, (c) $1.5$ mm and $2$ mm, and (d) $1.2$ mm and $2.1$ mm. The insets show the rectification ratio, <i>i.e.</i> $\eta = Q_{\text{Nozzle}}/Q_{\text{Diffuser}}$ , as a function of pressure difference across the channel. . . . .	91
Figure 43: Volumetric flow rates of DI water as a function of pressure difference across the deformable/rigid nozzle/diffuser microchannels for various original heights of $H_0 =$ (a) $2.6 \pm 0.1 \mu\text{m}$ , (b) $4.6 \pm 0.1 \mu\text{m}$ , (c) $8.0 \pm 0.2 \mu\text{m}$ , and (d) $10.9 \pm 0.2 \mu\text{m}$ . The dashed, dash-dotted, and dotted lines show the results obtained from the one-dimensional model for deformable nozzle, deformable diffuser, and rigid nozzle/diffuser, respectively. The insets show the rectification ratio, <i>i.e.</i> $\eta = Q_{\text{Nozzle}}/Q_{\text{Diffuser}}$ , as a function of pressure difference across the deformable nozzle/diffuser microchannels. The error bars related to the experimental results (averaged over three runs) are not visible if they are smaller than the markers size. . . . .	92
Figure 44: (a) Average of the membrane displacement at inlet over the channel original height and (b) the hydrodynamic resistance, <i>i.e.</i> $R_{\text{hyd}} = \Delta p/Q$ , as a function of pressure difference across the deformable nozzle/diffuser microchannels with the the half-angle of $\theta = 1.25^\circ$ , small and large widths of $1$ mm and $2$ mm, and various original heights, obtained from the 1-D coupled fluid-solid-mechanics model. . . . .	93
Figure 45: Volumetric flow rate of DI water as a function of pressure difference across the deformable nozzle/diffuser microchannel of $\sim 41 \mu\text{m}$ in height, small and large widths of $1$ mm and $2$ mm, and half-angle of $\theta = 1.25^\circ$ . The dashed, dash-dotted, and dotted lines show the results obtained from the one-dimensional model for deformable nozzle, deformable diffuser, and rigid nozzle/diffuser, respectively. The inset shows the rectification ratio, <i>i.e.</i> $\eta = Q_{\text{Nozzle}}/Q_{\text{Diffuser}}$ , as a function of pressure difference across the deformable nozzle/diffuser microchannel. . . . .	94
Figure 46: The rectification ratio contour obtained from the 1-D model for the nozzle/diffuser microchannels with the widths of $1$ mm and $2$ mm together with the experimental results tabulated at the corresponding $(H_0, \Delta p)$ . . . . .	94

Figure 47: (a and d) Dimensionless pressure, <i>i.e.</i> $p/\Delta p$ , along the channel, together with the (b and e) average of the membrane displacement at any x-plane over the channel original height, and (c and f) average of the membrane displacement at any x-plane for deformable nozzle/diffuser microchannels with the the half-angle of $\theta = 1.25^\circ$ , small and large widths of 1 mm and 2 mm, and various original heights under the pressure differences of (a–c) $\Delta p = 14$ kPa and (d–f) $\Delta p = 206$ kPa. Inset in (f) shows the magnified zone between $x^* = 0.5$ and $x^* = 1$ . . . . .	95
Figure 48: Reynolds number in the mid-plane ( $x^* = 0.5$ ) for water flow through the deformable nozzle/diffuser microchannels with the the half-angle of $\theta = 1.25^\circ$ , small and large widths of 1 mm and 2 mm, and various original heights, obtained from the 1-D coupled fluid-solid-mechanics model. . . . .	97
Figure 49: Volumetric flow rate as a function of pressure difference across the deformable nozzle/diffuser microchannel of $\sim 4.6 \mu\text{m}$ in height for two different working fluids: (a) Methanol ( $\mu = 5.9 \times 10^{-4}$ Pa.s) and (b) Isopropyl alcohol ( $\mu = 2.3 \times 10^{-3}$ Pa.s). The dashed and dash-dotted lines show the results obtained from the one-dimensional model for the deformable nozzle and diffuser, respectively. The insets show the rectification ratio, <i>i.e.</i> $\eta = Q_{\text{Nozzle}}/Q_{\text{Diffuser}}$ , as a function of pressure difference across the channel. . . . .	98
Figure 50: (a) Schematic presentation of the nonlinear microchannel width profiles in the nozzle direction, <i>i.e.</i> $W_N = W_o + (W_i - W_o)(1 - x^*)^\beta$ , as well as the diffuser direction, <i>i.e.</i> $W_D = W_i + (W_o - W_i)x^{*\beta}$ . (b) Volumetric flow rates of water obtained from the 1-D coupled fluid-solid-mechanics model as a function of pressure difference across the deformable nozzle/diffuser microchannels of $2.6 \mu\text{m}$ in height with the half-angle of $\theta = 1.25^\circ$ , and small and large widths of 0.3 mm and 2 mm for different with profiles. The inset shows the rectification ratio, <i>i.e.</i> $\eta = Q_{\text{Nozzle}}/Q_{\text{Diffuser}}$ , as a function of pressure difference across the channel. (c) The maximum rectification ratio for microchannels with different width profiles achievable within the pressure difference range of 14 kPa – 206 kPa. . . . .	100
Figure 51: (a) Schematic representation of a compressible fluid flow through a microchannel with a deformable ceiling together with (b) the cross-section view of the channel. . . . .	106
Figure 52: Dimensionless pressure distribution within microchannel for ideal gas flows under (a) $\Delta p/p_{\text{atm}} \ll 1$ , <i>i.e.</i> incompressible fluid flow, (b) $\Delta p = p_{\text{atm}}$ , (c) $\Delta p = 2p_{\text{atm}}$ , and (d) $\Delta p = 5p_{\text{atm}}$ for various modified flexibility parameters. Note: Solid lines, <i>i.e.</i> $\chi^* \rightarrow 0$ , show the rigid microchannel results. . . . .	117
Figure 53: Dimensionless average displacement of membrane along the microchannel for ideal gas flows with various values of $\chi^*$ and $\Delta p/p_{\text{atm}}$ . Note: Solid lines, <i>i.e.</i> $\Delta p/p_{\text{atm}} \rightarrow 0$ , show the incompressible fluid flow results. . . . .	119
Figure 54: Variations of (a) $p_i^*$ and (b) $\dot{m}/\dot{m}_{\text{Incomp., Rigid}}$ , <i>i.e.</i> $1/p_i^*$ , in ideal gas flow as functions of modified flexibility parameter under various pressure differences. Variations of (c) $p_i^*$ and (d) $\dot{m}/\dot{m}_{\text{Incomp., Rigid}}$ , <i>i.e.</i> $1/p_i^*$ , in ideal gas flow as functions of pressure difference for various modified flexibility parameters. Note: 1. Solid lines in (a) and (b), <i>i.e.</i> $\Delta p/p_{\text{atm}} \rightarrow 0$ , show the incompressible fluid flow results. 2. Solid lines in (c) and (d), <i>i.e.</i> $\chi^* \rightarrow 0$ , show the rigid microchannel results. . . . .	120

Figure 55: (a) Mass flow rate of air through Microchannel A as a function of pressure difference across the channel together with the modeling results for compressible flow through the rigid channel (Comp., Rigid) and incompressible flow through the rigid channel (Incomp., Rigid). Inset shows the proportion of mass flow rates of air through Microchannel A with and without compressibility taken into account. (b) Mass flow rates of air through Microchannels B–E as functions of pressure difference across the channels together with the modeling results for compressible flows through deformable channels (Comp., Deform.) and incompressible flows through deformable channels (Incomp., Deform.). The error bars related to the experimental results (averaged over three runs) are not visible if they are smaller than the markers' size. . . . .	121
Figure 56: Variations of (a) modified flexibility parameter and (b) $p_i^*$ as functions of pressure difference across Microchannels B–E. . . . .	123
Figure 57: Mass flow rate obtained from the modeling for compressible flows through deformable channels (Comp., Deform.), incompressible flows through deformable channels (Incomp., Deform.), compressible flows through rigid channels (Comp., Rigid), and incompressible flows through rigid channels (Incomp., Rigid). The dimensions of the microchannels are the same as those of undeformed (a) Microchannel B, (b) Microchannel C, (c) Microchannel D, and (d) Microchannel E. . . . .	124
Figure 58: Variations of (a) maximum membrane displacement at inlet and (b) Reynolds number at outlet, as functions of pressure difference across Microchannels B–E. . . . .	125
Figure 59: Mass flow rate of air as a function of pressure difference across the rigid (Rig.) nozzle/diffuser microchannels with small and large widths of 1 mm and 2 mm and a half-angle of $1.25^\circ$ for various original heights of $H_0 =$ (a) 2.6 $\mu\text{m}$ , (b) 4.6 $\mu\text{m}$ , (c) 8.0 $\mu\text{m}$ , and (d) 10.9 $\mu\text{m}$ . The modeling results with and without compressibility effects taken into account are shown by dotted and solid lines, respectively. . . . .	135
Figure 60: Mass flow rates of air as a function of pressure difference across the deformable (Def.) nozzle/diffuser microchannels with small and large widths of 1 mm and 2 mm and a half-angle of $1.25^\circ$ for various original heights of $H_0 =$ (a) 2.6 $\mu\text{m}$ , (b) 4.6 $\mu\text{m}$ , (c) 8.0 $\mu\text{m}$ , and (d) 10.9 $\mu\text{m}$ , together with modeling results for the air flow being considered as a compressible (Comp.) and incompressible (Incomp.) flow. . . . .	136
Figure 61: Experimental and theoretical values of the air flow rectification ratio, <i>i.e.</i> $\eta = \dot{m}_{\text{Nozzle}}/\dot{m}_{\text{Diffuser}}$ , as a function of pressure difference across the deformable nozzle/diffuser microchannels with small and large widths of 1 mm and 2 mm and a half-angle of $1.25^\circ$ for various original heights of $H_0 =$ (a) 2.6 $\mu\text{m}$ , (b) 4.6 $\mu\text{m}$ , (c) 8.0 $\mu\text{m}$ , and (d) 10.9 $\mu\text{m}$ . . . . .	136
Figure 62: (a) Schematic representation of different channel width profiles in the nozzle direction, <i>i.e.</i> $W_N = W_o + (W_i - W_o)(1 - x^*)^\beta$ , as well as the diffuser direction, <i>i.e.</i> $W_D = W_i + (W_o - W_i)x^{*\beta}$ . (b) Mass flow rates of air obtained from the 1-D coupled fluid-solid-mechanics model as a function of pressure difference across the deformable nozzle/diffuser microchannels of 2.6 $\mu\text{m}$ in height with the half-angle of $\theta = 1.25^\circ$ , and small and large widths of 0.1 mm and 2.4 mm for different width profiles. (c) The maximum rectification ratio, $\eta = \dot{m}_{\text{Nozzle}}/\dot{m}_{\text{Diffuser}}$ , for microchannels with different width profiles achievable within the pressure difference range of 14–206 kPa. The inset shows the rectification ratio as a function of pressure difference across the channel for three width profiles with $\beta = 0.2, 1.0, \text{ and } 2.0$ . . . . .	138

Figure 63: The schematic representation of ( $A_1 - A_3$ ) the pneumatic actuation-based strategy for particle trapping in comparison with ( $B_1 - B_4$ ) the new idea presented in this work without the the need to the pneumatic actuation. In the pneumatic actuation-based approach, the channel is sufficiently deep so that all the particles can pass through the channel ( $A_1$ ), while a sufficiently large pressure in the pneumatic channel can cause the membrane deformation and trapping the sufficiently large particles ( $A_2$ ). The trapped particles can be retrieved by lifting the pressure within the pneumatic channel and applying a particle-free fluid flow ( $A_3$ ). In the new strategy presented in this work, the duct on the weir is sufficiently shallow not to allow the large particles to enter the shallow passage under the sufficiently low pressure difference across the channel, <i>i.e.</i> filtration ( $B_1$ ), while the membrane deforms more with increasing the pressure difference enabling the target particles to be trapped on the weir under an appropriate pressure difference range, <i>i.e.</i> isolation ( $B_2$ ). Under a sufficiently large pressure difference, the particles can pass through the device without membrane obstructions ( $B_3$ ). The trapped particles can be retrieved using a particle-free fluid flow with a sufficiently large volumetric-flow rate ( $B_4$ ). . . . .	144
Figure 64: The different height levels ( $\mu m$ ) of the 200-micron-thick PET film at various pressure differences of (a) 15 kPa, (b) 30 kPa, (c) 45 kPa, (d) 60 kPa, (e) 75 kPa, and (f) 90 kPa across the microchannel 6 mm and 2 cm in width and length, respectively. . . . .	146
Figure 65: The different height levels ( $\mu m$ ) of the PET film at various pressure differences of (a) 15 kPa, (b) 30 kPa, (c) 45 kPa, and (d) 60 kPa across the microchannel 8 mm and 4 cm in width and length, respectively. . . . .	147
Figure 66: The PET film deflection profile under various pressure differences at the (a, c) inlet and (b, d) outlet sections for two microchannels of (a, b) 6 mm and 2 cm in width and length, respectively, and (c, d) 8 mm and 4 cm in width and length, respectively. . . .	147
Figure 67: The different height levels of the PET film at the pressure difference of 15 kPa across the 4 cm-long microchannels of (a) 4 mm, (b) 6 mm, (c) 8 mm, and (d) 10 mm in width. 150	150
Figure 68: The different height levels of the PET film for 4 cm-long microchannels with (a) 6 mm width and 90 kPa pressure difference, (b) 8 mm width and 20 kPa pressure difference, and (c) 10 mm width and 7 kPa pressure difference. The maximum membrane deflection at the outlet is about 4.5 $\mu m$ for all the cases. . . . .	152
Figure 69: Schematic presentation of the fabrication process flow: (A) the microchannel sidewalls are created using the double-step glass wet etching. ( $S_1$ ) A PET film coated with a thin layer of SU8 seals the microchannel sidewalls. ( $S_2$ ) The chip is undergone with UV illumination and post-exposure baking to cure the adhesive layer. ( $R_1$ ) A glass substrate with the same pattern as that of the main channel is aligned and brought in contact with the SU8 layer coated on the bare side of the PET film. ( $R_2$ ) The sample is undergone with UV illumination and post-exposure baking to cure the adhesive layer at the bonding interface of the reinforcement glass and the PET film. . . . .	154
Figure 70: (a) The microscope image of the double-height deep–shallow microfluidic sieve, together with (b) a schematic presentation of the (top) top-down-view and (bottom) side-view of the deep–shallow–deep interfaces, showing the small enough particles passing through the channel, while the large enough ones are trapped. The channel height is 32.0 $\mu m$ and 5.7 $\mu m$ in the deep and shallow regions, respectively. Scale bar = 5 mm in (a). . .	155

Figure 71: (a) The microscope image of the deep–shallow interface of the microfluidic filter, while the experiment of sieving 3-micron and 10-micron particles is running under the volumetric flow rate of $10 \mu\text{l}/\text{min}$ , showing the 3-micron particles can pass through the channel, whereas the 10-micron particles are trapped, together with a higher magnification image in (b). (c) The microscope image of the deep–shallow interface after applying the back- and lateral-flows to remove the trapped particles. Scale bar = $100 \mu\text{m}$ in (a) and (c), and $50 \mu\text{m}$ in (b). . . . .	156
Figure 72: A camera image showing the microchannel $5 \text{ mm}$ , $1 \text{ cm}$ , and $7.1 \mu\text{m}$ in width, length, and height, respectively, together with the PDMS interconnect for insertion of tubing used for the injection and collection of sample. . . . .	157
Figure 73: The particles size distribution related to the (a) injected sample, as well as that of the collected particles from the outlet under the pressure differences of (b) 2 psi (13.8 kPa), (c) 6 psi (41.4 kPa), and (d) 10 psi (69.0 kPa) across the microchannel sequentially after the microchannel is blocked at lower pressure difference. The microchannel is $5 \text{ mm}$ , $1 \text{ cm}$ , and $7.1 \mu\text{m}$ in width, length, and height, respectively. The number concentration of the glass particles in the main sample is $10^6 \text{ ml}^{-1}$ . . . . .	158
Figure 74: The PET film deflection ( $\mu\text{m}$ ) contour for the microchannel $1 \text{ cm}$ and $5 \text{ mm}$ in length and width, respectively, under the pressure differences of (left) 2 psi (13.8 kPa), (middle) 6 psi (41.4 kPa), and (right) 10 psi (69.0 kPa). . . . .	159
Figure 75: The different height levels ( $\mu\text{m}$ ) of the PET film under the pressure differences of (left) 2 psi (13.8 kPa), (middle) 6 psi (41.4 kPa), and (right) 10 psi (69.0 kPa) across the microchannel $1 \text{ cm}$ and $5 \text{ mm}$ in length and width, respectively. . . . .	159
Figure 76: The PET film deflection profile (left) along the centerline of the microchannel $1 \text{ cm}$ and $5 \text{ mm}$ in length and width, respectively, (middle) across the inlet section of the channel, and (right) across the outlet section of the channel, under the pressure differences of 2 psi, <i>i.e.</i> 13.8 kPa, (cross), 6 psi, <i>i.e.</i> 41.4 kPa, (circle), and 10 psi, <i>i.e.</i> 69.0 kPa (diamond). . . . .	159
Figure 77: A particle larger than the predicted filter opening size found in the filtrate. The particle is about $26 \mu\text{m}$ in diameter. The scale bar is 100 microns. . . . .	160
Figure 78: (left) The volumetric flow rate of DI water through the microchannel $5 \text{ mm}$ , $1 \text{ cm}$ , and $7.1 \mu\text{m}$ in width, length, and height, respectively, obtained through the experiments compared with a primitive numerical model used in this work. (right) The accumulated mass over time in a series of sequential experiments of injecting the sample containing about $10^6$ glass micro-particles per milli-litre with the pressure differences of 2 psi (13.8 kPa), 6 psi (41.4 kPa), and 10 psi (69.0 kPa) across the channel. . . . .	162
Figure 79: A microscopy image showing the trapped particles in the microchannel after the channel is blocked under the pressure difference of 10 psi (69.0 kPa). . . . .	162
Figure 80: The microscope images showing the effects of the pressure oscillation on releasing 3-micron beads trapped among the 10-micron beads next to the deep–shallow interface, enabling the 3-micron beads to pass through the filter. The pressure gradient forces particles to move toward the deep region for the images (a)–(e), while it reverses toward the shallow region for the images (f)–(l). The time duration of the shown cycle is about 5 seconds. The scale bars in the microscope images are $50 \mu\text{m}$ . . . . .	165

- Figure 81: A microscope image showing the trapped 10-micron beads under the flow rate of  $90 \mu\text{l}/\text{min}$  together with the modeling results showing the PET film deflection contour for three levels of 3, 4, and 5 microns. The deep and shallow regions are about 50 and 6 microns, respectively. The scale bar in the microscope image is  $100 \mu\text{m}$ . . . . . 166
- Figure 82: (A) A photograph of the microfluidic device consisting of a microchannel symmetric with respect to the dash-dotted line, together with the schematic presentations of the streamlines before the first deep-shallow interface and close to the lateral sidewall in (B) presence and (C) absence of the sheath flow injected from the port  $C_2$ . The  $\sim 36$ -micron deep regions are separated from the  $\sim 5$ -micron shallow region in lower half of the photograph in (A) using the dashed lines. Scale bar is  $4 \text{ mm}$  in (A). . . . . 168
- Figure 83: (A) Membrane displacement contours ranging from  $1 \mu\text{m}$  (outermost) to  $6 \mu\text{m}$  (innermost) with an increment of  $1 \mu\text{m}$ , obtained from the model, together with (B, C,  $D_1$ ,  $D_2$ , and  $D_3$ ) the microscope images showing the trapped 6- and 10-micron beads under the volumetric flow rate of  $40 \mu\text{l}/\text{min}$  in absence of the reverse sheath flows. Microchannel is about  $5 \mu\text{m}$  and  $36 \mu\text{m}$  in depth within the shallow and deep regions, respectively. Scale bars are  $100 \mu\text{m}$  in (B) and (C),  $30 \mu\text{m}$  in insets of (B) and (C), and  $200 \mu\text{m}$  in ( $D_1$ ), ( $D_2$ ), and ( $D_3$ ). . . . . 169
- Figure 84: Microscope images of ( $A_1$ – $C_1$ ) the 1<sup>st</sup> and ( $A_2$ – $C_2$ ) 2<sup>nd</sup> deep-shallow interfaces, together with ( $A_3$ – $C_3$ ) the membrane displacement contours obtained from the model, and ( $A_4$ – $C_4$ ) the size distribution of the filtrate for three net volumetric flow rates of  $Q_{\text{net}} = (A_1$ – $A_4)$   $5 \mu\text{l}/\text{min}$ , ( $B_1$ – $B_4$ )  $40 \mu\text{l}/\text{min}$ , and ( $C_1$ – $C_4$ )  $140 \mu\text{l}/\text{min}$ . The volumetric flow rate of the injected particles sample through the port A shown in Fig. 82 is the same as that of the total sheath flows through the ports  $C_1$  and  $C_2$ . The driving pressure difference obtained from the model is  $\Delta p \approx (A_1$ – $A_4)$  2 KPa, ( $B_1$ – $B_4$ ) 10 KPa, and ( $C_1$ – $C_4$ ) 18 KPa. Scale bars are  $150 \mu\text{m}$  for the main images and  $30 \mu\text{m}$  for their insets in ( $A_1$ – $C_1$ ) and ( $A_2$ – $C_2$ ). . . . . 170
- Figure 85: (A) Microscope image of the particles close to the 2<sup>nd</sup> deep-shallow interface under the net volumetric flow rate of  $Q_{\text{net}} = 40 \mu\text{l}/\text{min}$  together with the membrane displacement contours obtained from the 0DF–3DS model, and (b) the microscope image of the 2<sup>nd</sup> deep-shallow interface after the trapped particles are retrieved. Scale bars are  $200 \mu\text{m}$ . 171
- Figure 86: Microscope images showing (a) the isolated particles next to the 2<sup>nd</sup> deep-shallow interface under the net volumetric flow rate of  $Q_{\text{net}} = 40 \mu\text{l}/\text{min}$  and (b) their partial release over time due to the buildup pressure as a result of the particle trapping and open area decrease about one minute later. Scale bars are  $100 \mu\text{m}$ . . . . . 171
- Figure 87: The procedure to fabricate the sidewalls of microchannel based on:  
**SU8 photo-lithography**— ( $a_s$ ) Spin coating a thin layer of SU8 on the glass substrate, ( $b_s$ ) soft-baking and UV exposure followed by a post-exposure baking, ( $c_s$ ) patterning the side-walls of the microchannel following the standard photo-lithography process followed by a sufficiently long hard baking, and ( $d_s$ ) drilling the via-holes.  
**Wet etching of the glass**— ( $a_g$ ) spin coating a thick enough layer of photo-resists AZ4620, AZ4330, or S1813 based on the required duration time of etching, ( $b_g$ ) patterning the mask following the standard photo-lithography process followed by a sufficiently long hard baking, ( $c_g$ ) wet etching of the glass substrate in a bath of etchant, and ( $d_g$ ) drilling the via-holes. . . . . 179

Figure 88: The sealing step of the two-step SU8 bonding paradigm: (a) spin coating a thin SU8 layer on the PET film, ( $b_s$ and $b_g$ ) bringing the uncross-linked SU8 on the PET in contact with the sidewalls of microchannel, and ( $c_s$ and $c_g$ ) sufficiently long UV exposure through the PET film, followed by a post-exposure baking, for two different approaches that sidewalls are made based on SU8 photo-lithography ( $b_s$ and $c_s$ ) or wet etching of the glass ( $b_g$ and $c_g$ ). The slight SU8 reflow might result in a cross-section with round corners. . . . .	182
Figure 89: The bonding reinforcement step of the two-step SU8 bonding paradigm: (a) spin coating a thick enough layer of SU8 on the glass substrate and soft-baking, ( $b_s$ and $b_g$ ) bringing the uncross-linked SU8 on the reinforcement glass in contact with the bare side of the PET film, and ( $c_s$ and $c_g$ ) sufficiently long UV exposure through the reinforcement glass substrate, followed by a post-exposure baking, for two different approaches that sidewalls are made based on SU8 photo-lithography ( $b_s$ and $c_s$ ) or wet etching of the glass ( $b_g$ and $c_g$ ). . . . .	183
Figure 90: A microfluidic channel about $2.2 \mu m$ in height sealed by a PET film coated with a $2 \mu m$ -thick SU8 layer. The PDMS interconnect with holes corresponding to the via-holes of the glass substrate has been bonded to the glass surface after a short and gentle oxygen plasma treatment. . . . .	185
Figure 91: The optical microscopy images showing the center of a serpentine microchannel $\sim 4 \mu m$ and $\sim 15 \mu m$ in height and width, respectively, sealed by a $2 \mu m$ -SU8-covered PET and reinforced by a $7 \mu m$ -SU8-covered microscope slide. The focal plane is on the interface between the PET film and the reinforcement microscope slide in (a), and on the microchannels in (b). Some small trapped air bubbles that formed during the bonding reinforcement step are circled in (a). These bubbles do not adversely affect the microchannels, since the channels have already been cured and sealed perfectly without defects/voids, as shown in (b), before the commencement of the bonding reinforcement step. Scale bars = $500 \mu m$ . . . . .	186
Figure 92: An optical microscopy image showing the cross-section of a microchannel about $30 \mu m$ and $100 \mu m$ in height and width, respectively, sealed by an almost $7 \mu m$ -SU8-covered PET film. Scale bar = $50 \mu m$ . . . . .	187
Figure 93: The optical microscopy images showing the cross-section of a microchannel about $30 \mu m$ and $100 \mu m$ in height and width, respectively, sealed by an almost $7 \mu m$ -SU8-covered cover glass (a) with, and (b) without oxygen plasma treatment of the sidewalls before the bonding. Scale bars = $50 \mu m$ . . . . .	187
Figure 94: The camera image showing a microchannel about $7 \mu m$ , $250 \mu m$ , and $6 cm$ in height, width, and length, respectively after the sealing step using a PET film coated with a $2 \mu m$ -thick SU8 layer. The microscope slide dimensions are $25 mm \times 75 mm$ . . . . .	188

# Chapter 1: Introduction

It seems intuitively logical to design the systems handling cells, molecules and other biological entities within the same characteristic length scales as those of the biospecies [1] (Fig. 1). Microfluidics is the science of manipulating and controlling fluids, usually in networks of channels with dimensions from  $O(0.1 \mu m)$  to  $O(100 \mu m)$ . Microfluidic devices provide several important advantages over the conventional laboratory-scale techniques. The inverse characteristic length scaling of the surface-area-to-volume ratio implies that heat and mass transfer into or out of a chip can be enhanced as the dimension of the device is reduced. In addition, separation can be carried out faster and more efficiently at smaller scales [1]. Biospecies detection can also be more efficient [20] in smaller devices, since the underlying detection mechanism is based on the species interaction with the markers coated on the wall. Furthermore, the small size of the microchannels improves the cell culturing efficiency through increasing the possibility of the contact between the flexible cells and the channel walls [21]. The other advantage of the microfluidics is that it usually needs a minute amount of sample to function properly, which reduces the cost and avoid wasting chemicals, while in the case of laboratory-scale techniques, the sample volume needs to be sufficiently high. The concentration of species also needs to be sufficiently high for the laboratory-scale methods to be applicable. Otherwise, the rare target species can be easily lost during the large-scale process. Separation and analysis of the rare circulating tumor cells (CTCs) are, therefore, performed more efficiently using the microfluidics technology [22–25].

Separation and isolation of the target rare cells from a highly heterogeneous suspension such as the whole blood is vitally important for disease diagnostics, drug analysis, fundamental studies, etc. The HIV disease diagnosis and treatment are based on the efficient separation of human T-lymphocytes (CD4+) from the whole blood [26]. As another example, the diagnosis and treatment of malaria rely on the separation of parasite-infected red blood cells (RBCs) from uninfected cells [27–29]. The separation of neuronal cells is also important for the cell replacement therapy of neurodegenerative disorders such as the Parkinson’s and Alzheimer’s diseases [30, 31].

The remaining chapter will present the literature reviews and the objectives of the dissertation. Key separation mechanisms will be briefly introduced first. The applications of deformable microfluidic channels

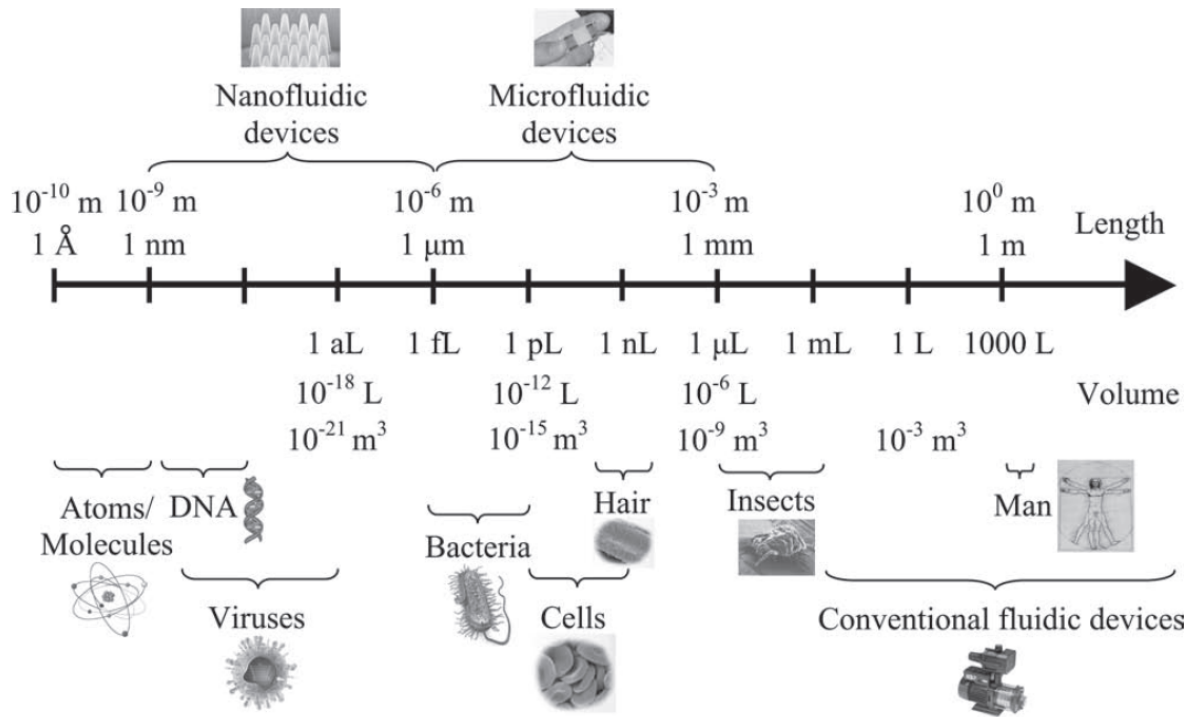


Figure 1: (From the work of Yeo *et al.* [1]) The approximate characteristic length scales of the microfluidic and nanofluidic systems compared with those of various biological entities.

will be then reviewed. The main objectives of this research will be presented afterwards. Finally, the outline of the report will be described.

## Separation

There are several extensive review papers on the separation using the microfluidic systems [32, 33]. Inertia-based separation, hydrodynamic fractionation, active fractionation, and size exclusion, which are among the most commonly used mechanisms of separation, are introduced in the following.

### Inertia-based separation

Inertial focusing refers to the migration of the particles, which flow through a channel, across the streamlines towards their equilibrium positions. This phenomenon happens due to the inertial effects of the flow field around the particles and its interaction with the channel sidewalls. A balance between the shear gradient force directed towards the channel sidewalls and a wall-induced inertial force directed away from the sidewalls dictates the equilibrium positions. One of the very first works in the context of particle inertial focusing was

published in 1961 [34]. The authors reported that the macroscopic spherical particles were collected into a thin and annular region when an initially uniform dilute suspension was passed in laminar flow through a straight tube.

Ho and Leal [35] theoretically studied the effect of inertia-induced lateral migration of a neutrally buoyant rigid sphere in a Newtonian fluid for two types of flow: simple shear flow, and two-dimensional Poiseuille flow. They showed that spheres reach a stable lateral equilibrium position independent of the initial position of release. For the simple shear flow, this position is midway between the sidewalls, whereas for the Poiseuille flow, it is 0.6 of the channel half-width from the centre-line. The numerical simulations of the inertial migration of neutrally buoyant particles in a straight square duct, conducted by Chun and Ladd [36] for various Reynolds number between 100 and 1000, also showed that particles migrate towards one of a few equilibrium positions in the cross-sectional plane, located near the duct's corners or at the center of the edges.

The inertial focusing allows the rather precise alignment of particles within the flow field, which enables a variety of different separation technologies.

Di Carlo *et al.* [2] have reported that flowing particles can migrate across streamlines even in laminar flows if the wall-induced inertial lift forces dominate the particles behavior; the condition that is met when the particle Reynolds number is of order 1. This phenomenon has been leveraged to focus randomly distributed particles continuously and at high rates to a single streamline. Later and based on this work, Di Carlo *et al.* [37] presented a microfluidic device for separating particles based on size with purities from 90 to 100% and as a high throughput as 1 mL/min.

The important advantage of inertia-based separation techniques, in general, is that they need a large enough velocity. As a result, these methods inherently deliver high throughput separations. However, they are usually limited to specific Reynolds numbers, above which the fluid flow pattern and the particles motion deviate from the desired behavior that results in the lower separation efficiency. For example, for the focusing techniques based on the Dean flow, the counter-rotating streamlines are prone to mixing particles by entraining them. It has been shown [2] that the ratio of lift to Dean drag force scales as:

$$F_z/F_D \sim \frac{1}{\delta} \left(\frac{a}{D_h}\right)^3 R_c^n : n < 0 \quad (1)$$

where  $a$ ,  $D_h$ , and  $R_c$  refer to the particle diameter, hydrodynamic diameter of the channel, and the channel Reynolds number based on the maximum channel velocity:  $R_c = \rho U_m D_h / \mu$ , in which  $U_m$  denotes the maximum channel velocity, and  $\rho$  and  $\mu$  are the fluid density and dynamic viscosity, respectively. In addition,  $\delta = D_h/2r$ , where  $r$  is the radius of curvature of the channel. It can be perceived that the Dean drag becomes

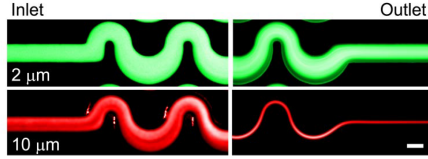


Figure 2: (From the work of Di Carlo *et al.* [2]) Differential focusing of 10- and 2- $\mu\text{m}$  mixed particles in water. The 2- $\mu\text{m}$  particles remain unfocused after transiting 3 cm of asymmetric turns, whereas 10- $\mu\text{m}$  particles are sharply focused.  $R_c = 7.5$ . (Scale bar=50  $\mu\text{m}$ ).

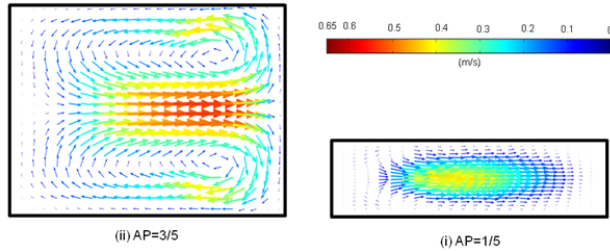


Figure 3: (From the work of Zhang *et al.* [3]) The counter-rotating vortex in the cross section of a serpentine channel with different aspect ratios, (i)  $AP=1/5$  and (ii)  $AP=3/5$ .

more significant than the inertial lift with increasing the Reynolds number, suggesting an upper limit on the Reynolds number, above which the particles of various sizes will be defocused by mixing due to the Dean flow.

Furthermore, the experimental results show that the particles need to be large enough to be focused ( $a/D_h > 0.07$ ) [2]. Otherwise, according to Eq. 1, the Dean drag force is dominant, resulting in the particles mixing. A sharply focused streak of 10  $\mu\text{m}$  particles is shown in comparison with an unfocused and broader streak of 2  $\mu\text{m}$  particles in Fig. 2.

It has been shown that the geometry can be designed in such a manner that the counter-rotating Dean vortex close to the top and down sidewalls is suppressed. For example, the velocity vector field related to the low-aspect-ratio channel (height to width) of 1/5, obtained through the numerical simulation, shows that the direction of the secondary flow velocity is towards the concave wall (outer sidewall) for the majority of the cross section, while there is just a small portion of the cross-section close to the sidewalls with the secondary flow towards the convex wall (inner sidewall) [3], see Fig. 3. The similar design has been used to achieve a single focusing streak of large particles at the channel center, while smaller particles are trapped close to the sidewalls [38].

In another work, Yoon *et al.* [4] have used curved rectangular microchannels. Their numerical simulation shows that for the aspect-ratio of 1.0, the secondary flow is towards the concave sidewalls in the middle of the cross-section between the normalized height ( $z/h$ ) of 0.27 and 0.72, while it is towards the convex sidewall out of this height window (Fig. 4 (left)). As depicted in Fig. 4 (middle), for an arc channel with an aspect

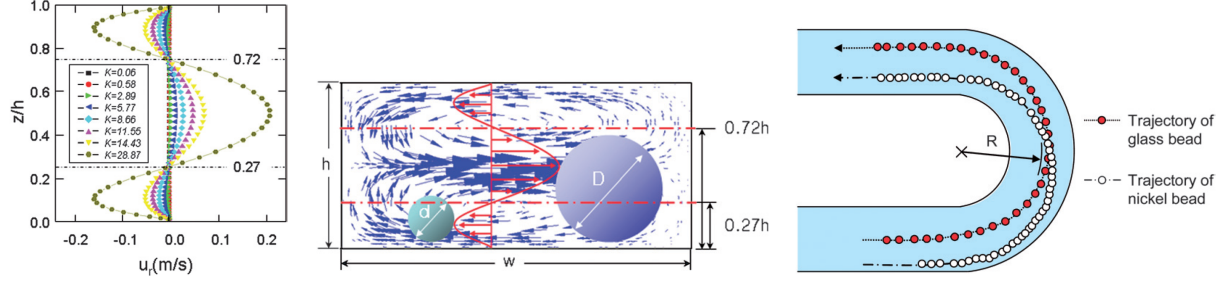


Figure 4: (From the work of Yoon *et al.* [4]) (left) Velocity distributions at the middle of the arc for various Dean numbers with an aspect ratio of 1.0. (middle) Size-selective separation of micro beads in the direction of the fluidic force exerted by the velocity distribution in an arc channel of aspect-ratio 1/2. (right) Comparison of the trajectories of the 40  $\mu\text{m}$  glass and 10  $\mu\text{m}$  nickel beads at the Dean number of 28.87 and aspect ratio of 1/2.

ratio of 1/2, the large beads mainly experience forces from the outward velocity, while the small beads are dominantly influenced by the inward velocity. As a result, the 40  $\mu\text{m}$  glass and 10  $\mu\text{m}$  nickel beads can be separated in a curved rectangular microchannel as shown in Fig. 4 (right).

Hur *et al.* [39] have introduced a label-free cell isolation and enrichment technique with cell size as the biomarker. Their approach is based on the trapping of the large enough particle/cell into microscale vortices, that are developed in expansion-contraction regions. They have empirically determined the critical diameter of the particle/cell and the volumetric flow rate above which the trapping of cells/particles is achieved. High throughput and clogging-free operations have been demonstrated using their technique.

Some of the more recent works on this topic can be found in [40–44].

## Hydrodynamic fractionation

The hydrodynamic fractionation techniques are trying to order the particles next to the channel sidewall(s). If the Reynolds number is small enough, the particles follow the streamlines without significant deviations. As a result, the ordered particles, that are now tangent to the sidewalls, can be separated according to their size, since the center of particles with different sizes is located on various streamlines. The particles, therefore, follow different streamlines, and can be collected through different outlets.

Yamada *et al.* [5] proposed the first separation technique based on the hydrodynamic fractionation, named *pinched flow fractionation*. In this method, particles suspended in liquid are continuously injected through a microchannel with a pinched segment. The particles are aligned against one sidewall in the pinched segment by the sheath flow. The particles are then separated according to their size, since the particles with different sizes follow the different diverging streamlines in the expanding portion of the microchannel. The principle underlying this technique is schematically shown in Fig. 5 (left). The separation of polymer micro-beads 15  $\mu\text{m}$  and 30  $\mu\text{m}$  in diameter has been successfully demonstrated using this technique.

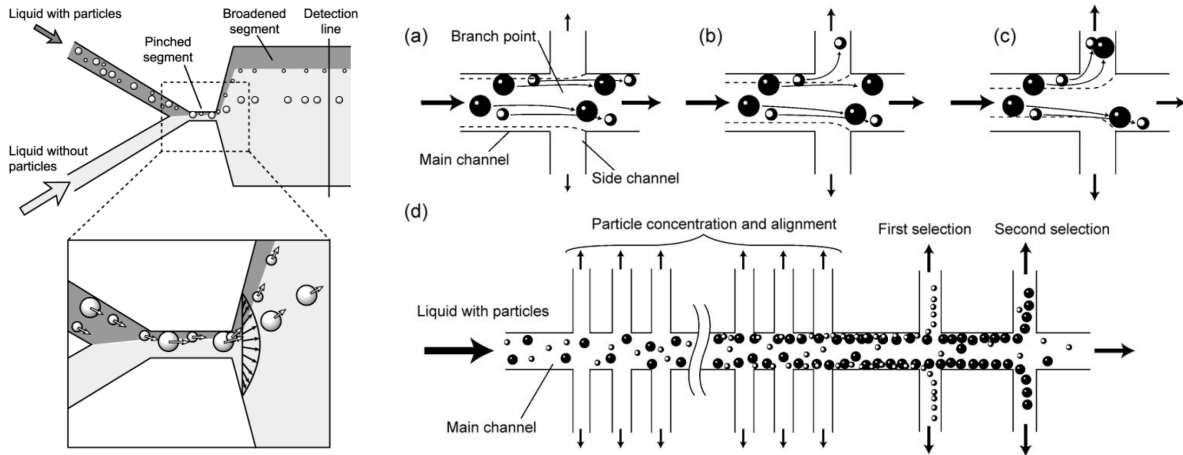


Figure 5: (left) (From the work of Yamada *et al.* [5]) The schematic presentation of the pinched flow fractionation. The particles are aligned against one sidewall in the pinched segment using a sheath flow. The particles are then separated according to their size by following the different diverging streamlines. (right) (From the work of Yamada and Seki [6]) The schematic presentation of the hydrodynamic filtration. The diagram shows the particle behavior at a branch point for the case that the proportion of the flow rate through the side channels over that of the main channel is (a) low, (b) medium, and (c) high. The virtual boundaries are shown with dashed lines. (d) A schematic presentation of the particle concentration and classification in a microchannel with multiple side channels.

Later, Yamada and Seki [6] modified the previous work by removing the sheath flow. Instead, in order to order particles next to the lateral sidewalls, they used side channels to withdraw a small amount of liquid repeatedly from the main stream. In this way, the particles are concentrated and aligned next the sidewalls. Then the concentrated and aligned particles are collected according to size through selection outlets. They named their method *hydrodynamic filtration*. The principle underlying this technique is schematically presented in Fig. 5 (right). The advantages of this method are: 1) the continuous process is feasible, 2) the channel clogging is not a concern, and 3) both the particle concentration and separation can be obtained simultaneously. The drawback, however, is that this method inherently relies on low Reynolds numbers, so that the particles can follow the streamlines. As a result, the typical throughput is limited in the order of  $1 \mu\text{l}/\text{min}$ . The authors have demonstrated the concentrations of polymer microspheres with diameters of 1-3  $\mu\text{m}$  up to 20-50-fold, and their separation according to the size. In addition, selective enrichment of leukocytes from blood has been performed. Later, Yamada and Seki [45] modified the design of the microfluidic chip to achieve a better selectivity.

## Physical filtration

The separation approaches based on the physical filtration utilize the porous structures with various opening sizes. The particles larger than the pores size are filtered, while the smaller particles can ideally (if not

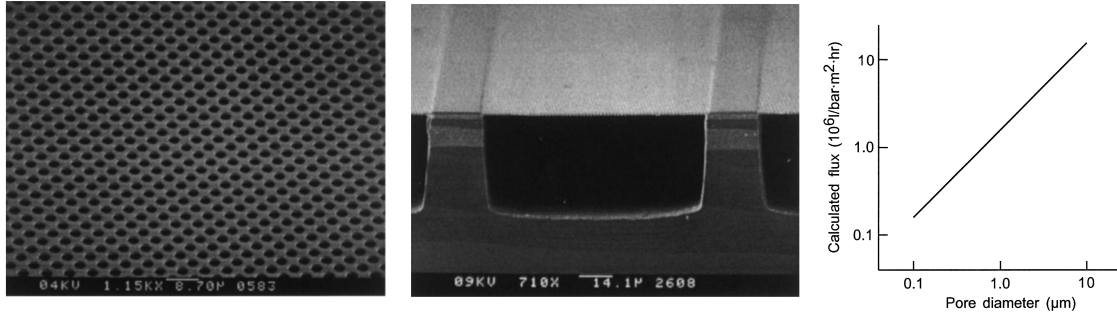


Figure 6: (From the work of Kuiper *et al.* [7]) (left) A SEM image of the microsieve surface. (middle) A SEM image showing a free hanging perforated membrane supported by the vertical walls. (right) The theoretically calculated water flux for a microsieve with a porosity of 20% and a membrane thickness equal to the pore diameter.

trapped among the filtered larger particles) pass through the pores. For a long time, the sieve has been one of the widely used utensils to filter the particles of desired sizes from the solutions. In the middle of the last century, the fine sieves were used for the isolation of cells [46–48]. Thanks to the microfluidics progress [49], the filters were also integrated into the microfluidic chips [50, 51] for handling a small amount of analytes in a more precise manner.

There are generally four types of the physical filtration technique:

- membranes,
- pillars,
- cross flow, and
- weir-shaped filters.

In the following, each category will be briefly introduced.

## Membranes

Kuiper *et al.* [7] developed inorganic micro-filtration membranes with a pore size down to 100 *nm* by using the laser interference lithography and silicon micro machining technology. The SEM images of the membrane, shown in Fig. 6, demonstrate the feasibility of fabricating pores with precise dimensions and narrow size distribution on a large area. The experiments of the yeast cell filtration of beer were successfully carried out. As shown in Fig. 6 (right), this type of membrane enables a relatively high flow rate, because of having a small thickness in the order of the pores size as well as a high porosity. However, the authors mentioned in their paper that this micro-sieve has to be made in a cleanroom environment with expensive machinery.

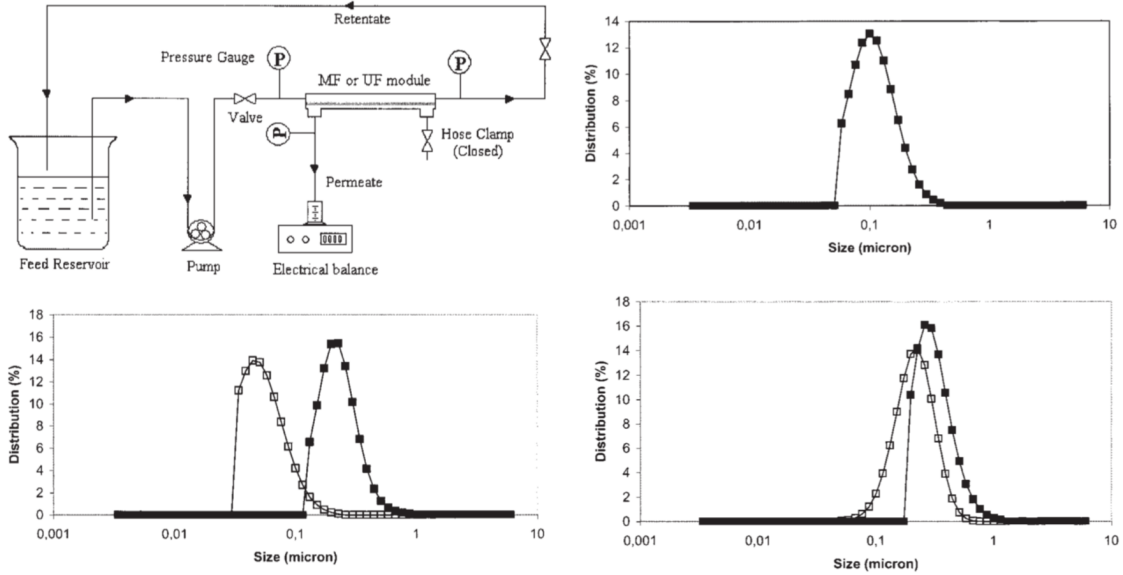


Figure 7: (From the work of Wickramasinghe *et al.* [8]) (top left) Experimental set up. (top right) Typical particle size distribution for influenza virus feed solution. (Bottom) Particle size distributions in the retentate (filled squares) and concentrated bulk permeate (unfilled squares) after microfiltration using (left)  $0.1 \mu\text{m}$  and (right)  $0.2 \mu\text{m}$  membranes. The particles larger than the pores size are retained more effectively by the membrane, while smaller particles tend to pass through the membrane.

Wickramasinghe *et al.* [8] have used a tangential flow combined with a membrane filtration to concentrate the human influenza A virus particles and remove the host cell DNA and proteins. The polyethersulphone (PES) sheet membranes with different pore sizes were used. The human influenza A virus particles are spheres about  $100 \text{ nm}$  in diameter. By using a  $0.1 \mu\text{m}$  membrane, the passage of virus particles smaller than  $100 \text{ nm}$  into the permeate and an enrichment of the larger particles in the retentate were obtained. All experiments were run at the feed flow rate of  $150 \text{ mL/min}$ , which resulted in the average transmembrane pressure of  $0.4 \text{ bar}$ . The permeate flux is also between  $20$  and  $150 \text{ lm}^{-2}\text{h}^{-1}$  based on the pores size. A schematic of the experimental set up is shown in Fig. 7. In addition, the particle size distribution related to the influenza virus feed solution, together with that of the retentate and concentrated bulk permeate are shown in Fig. 7. It can be seen that the particles larger than the pores size are retained more effectively by the membrane, while smaller particles tend to pass through the membrane.

Zheng *et al.* [9] used a three dimensional micro-filter device, consisting of two layers of the parylene membrane with pores and gap defined through photolithography, in order to enrich viable circulating tumor cells from the human blood sample. A schematic of the device and the filtration process is shown in Fig. 8. The viable CTCs enrichment with about  $86\%$  capture efficiency has been achieved in several minutes using this device. Since the captured cells were supported by the lower membrane, it did not experience a large strain. As a result, the high viability of the captured cells is still obtainable under high flow rates.

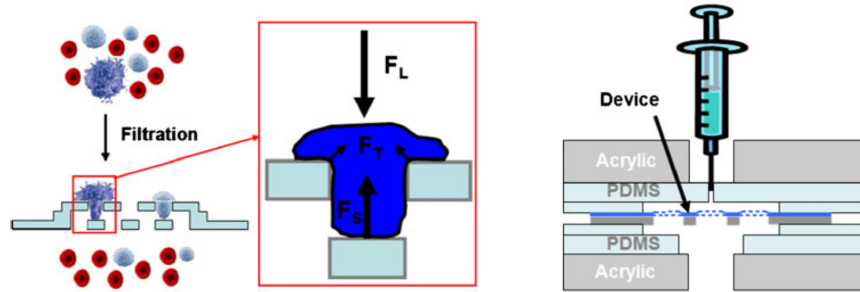


Figure 8: (From the work of Zheng *et al.* [9]) (left) A schematic of the filtration process.  $F_L$ : force caused by fluidic pressure from top.  $F_S$ : supporting force from bottom membrane.  $F_T$ : tension stress force on plasma membrane. (right) Device is assembled inside a housing cassette.

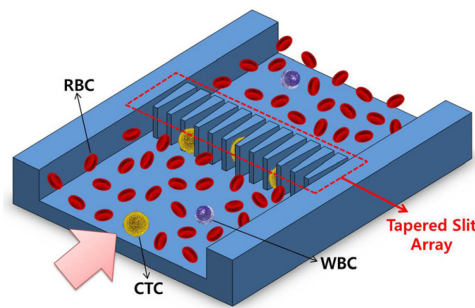


Figure 9: (From the work of Doh *et al.* [10]) A schematic image of the cancer cell isolation tapered slit array.

Lim *et al.* [52] have used a microfabricated porous silicon membrane with a densely packed pore array ( $\sim 5000$  pores per  $\text{mm}^{-2}$ ) for isolation of tumor cells from the whole blood. The low hydrodynamic resistance due to the small thickness of the membrane ( $30 \mu\text{m}$ ) enables the high throughput operations of the order of  $1 \text{ ml/min}$ .

## Pillars

Doh *et al.* [10] have used a tapered slit structure in order to isolate the cancer cells from the blood cells (Fig. 9). The trapped cells were then collected by reversed flow. The average viability of the captured cancer cells has been reported to be  $\sim 75\%$ . The collected viable cancer cells can be used for the further bio-applications such as cancer diagnosis, drug development, etc. The shortcoming of this method, however, is that some of the slits can be simply clogged by the blood cells. As a result, the velocity in the rest of the open slits increases, that reduce the viability of the cells.

Yoon *et al.* [53] have presented a microfluidic sieving technique that takes advantage of a lateral flow combined with a mechanical oscillation applied to the fluid flow by using a piezoelectric actuator to overcome the clogging challenge. The mechanical oscillation helps the aggregated small particles trapped between the

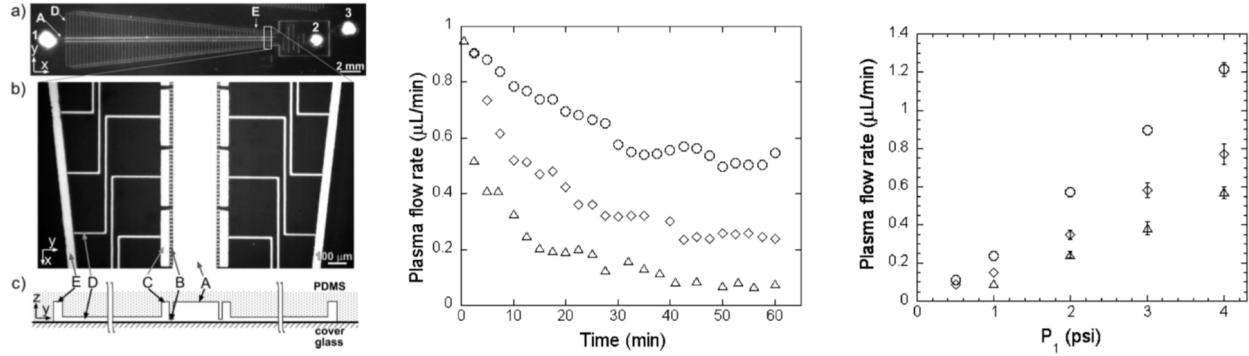


Figure 10: (From the work of VanDelinder *et al.* [11]) (left) (a) A camera image of the microfluidic device together with (b) a magnified image of the fragment of the filter region, marked by a rectangle in panel (a). This image is rotated  $90^\circ$  from the view shown in panel (a). (c) Schematic diagram showing a cross-sectional view of the device (not to scale). (middle) The plasma flow rate through the plasma outlet as a function of time at inlet pressure of 4 psi with constant zero pressure at the outlets (triangles) and with two different modes of back-pulsing: the pressure of 6 psi was applied to the outlets for 100 ms every 3 s (diamonds and circles) and also for 5 s every 2.5 min (circles). Each curve is an average of two individual tests. (right) The plasma flow rate through the plasma outlet for blood with hematocrits of 10% (circles), 20% (diamonds), and 30% (triangles) as a function of inlet pressure,  $P_1$ , with outlet pressure,  $P_3$ , equal to  $1.5P_1$  applied for 100 ms every 3 s. For each hematocrit the data points show averages of at least five individual tests, and the error bars show the standard errors of the mean. The error bars are not shown when they are smaller than the symbols.

larger target particles in the filter to be released.

### Cross flow

VanDelinder *et al.* [11] presented a microfluidic device for separation of plasma from the whole human blood by size exclusion in a cross-flow. The device was made of Polydimethylsiloxane (PDMS) sealed with a cover glass. The pulsatile pressure was used to prevent clogging of the channels with blood cells. When loaded with blood diluted to 20% hematocrit, the device was able to operate for at least one hour, extracting 8% of the blood volume as plasma at an average rate of  $0.65 \mu\text{L}/\text{min}$ . The images and schematic of the device are shown in Fig. 10 (left). In addition, the volumetric flow rate of the plasma entering the outlet is shown over time in Fig. 10 (middle) for three different modes of operation as described in the caption. As shown, the plasma flow rate rapidly decayed, since the channels were quickly clogged with RBCs and platelets. However, the performance of the device was substantially improved with pulsatile pressure (back-pulsing), which is one of the common methods of increasing efficiency in macroscale cross-flow filters [54]. Furthermore, the plasma flow rate for blood with different hematocrit concentrations is shown in Fig. 10 (right) as a function of inlet pressure. The measurements were carried out during the time interval between 2 and 10 min from injection of blood into the device.

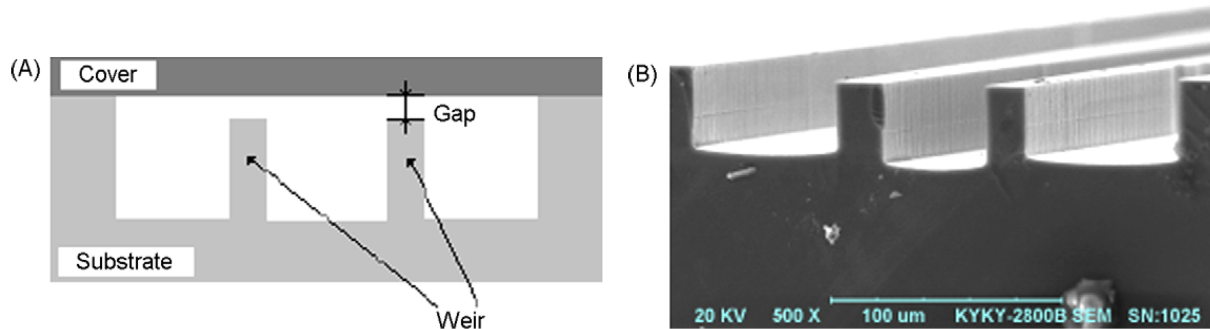


Figure 11: (From the work of Chen *et al.* [12]) (A) The design and construction of the weir-type barrier. (B) The SEM micrograph of the weir.

### Weir-shaped

Weir structures are widely used in cell sorting, which exploit the mechanical disparities between the cell samples [55, 56]. The gaps formed in between the weirs and the channel ceiling act as the filter to permit smaller cells to go through while trapping the larger ones, see Fig. 11. Chen *et al.* [12] have experimentally investigated both pillar- and weir-type filtration techniques. They have shown that the the crossflow with the pillar-type structure filtration can strongly resolve the problem of clogging, which is a more serious problem for the weir-type filtration method.

### Active separation

The mechanism introduced in the previous sections are considered *passive*, since their function is dictated by the geometry of the device and the applied pressure. The other category of the separation techniques, which is called *active*, take advantage of the external electric field [57], magnetic field [29, 58], etc., to adjust the functionality of the microfluidic device based on the needs. The long-history electrophoresis [59, 60] and dielectrophoresis [61–63] are falling under this category.

Jeon *et al.* [64] have presented a hybrid pressure-driven-electrophoresis-electroosmotic flow. The external electric field is applied in such a manner that the electrophoretic force applied to the particles opposes the hydrodynamic drag force. As a result the particles with large enough electrophoretic mobility can flow against the pressure gradient direction, and are collected in a separate outlet.

## Deformable microfluidic devices

Deformable microfluidics, in which microchannel possesses at least one flexible sidewall, is a promising emerging research area in the field of microfluidics, with a variety of potential applications such as the

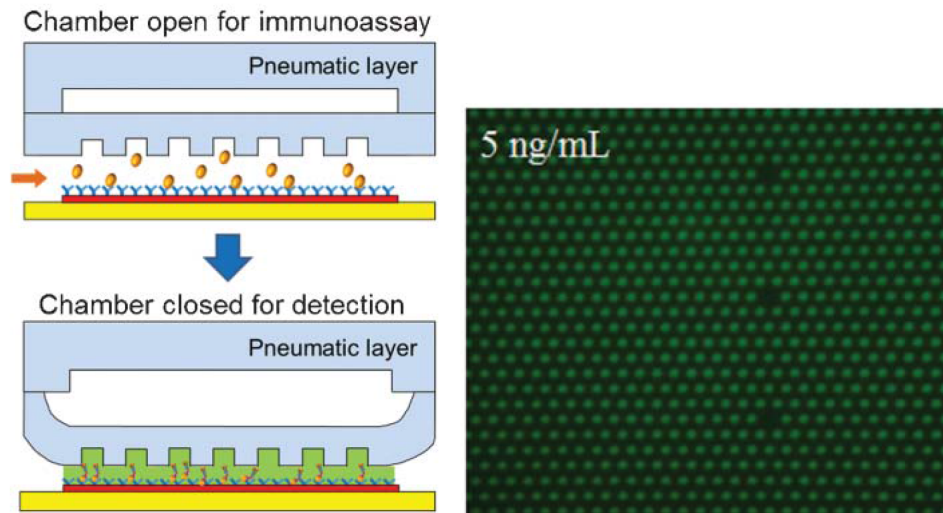


Figure 12: (From the work of Wang *et al.* [13]) (left) Pneumatic actuation of the assay chamber for solid-phase immunoassay (upper) and chemifluorescence detection (bottom). (right) The fluorescence images obtained at the concentrations of  $5 \text{ ng/ml}$ .

particle/cell separation [65, 66], controlled drug release [67], tunable optofluidic devices [68], force sensing [69], tunable droplet-size generation [70], capillary flow enhancement [71], mixing [72–74], developing fluidic circuits [75–77], etc.

Highly sensitive microfluidic enzyme-linked immunosorbent assay (ELISA) assays have been demonstrated by using the deformable channels [13]. As shown in Fig. 12 (left), the main channel is filled while no pressure is applied to the pneumatic chamber that works similar to a gate control in an electrical circuit. The channel is, therefore large enough to show the small hydrodynamic resistance and be filled quickly. On the other hand, when the pressure (30–70 kPa) is applied to the pneumatic chamber, the microwell array membrane can be quickly deformed to create an array of femtoliter detection volumes interconnected by a thin layer of liquid. Decreasing the chamber size increases the sensitivity through increasing the possibility of interactions between the antibodies and target proteins. The low concentration like  $5 \text{ ng/ml}$  has been successfully detected using this platform, Fig. 12 (right).

Externally adjusting the geometry of the flexible microfluidic devices have already been reported for tuning the functionality of the microfluidic separators [78–81]. Beech and Tegenfeldt [14] proposed a simple deterministic lateral displacement (DLD) device based on a PDMS structure, Fig. 13. They showed the critical size of the structure, and consequently the particle separation functionality, can be tuned by stretching the device.

There have been also numerous efforts to develop the tunable microfluidic filters with an adjustable cutoff pore size by using the external pneumatic actuators. Huang *et al.* [15] have used pneumatic actuation to

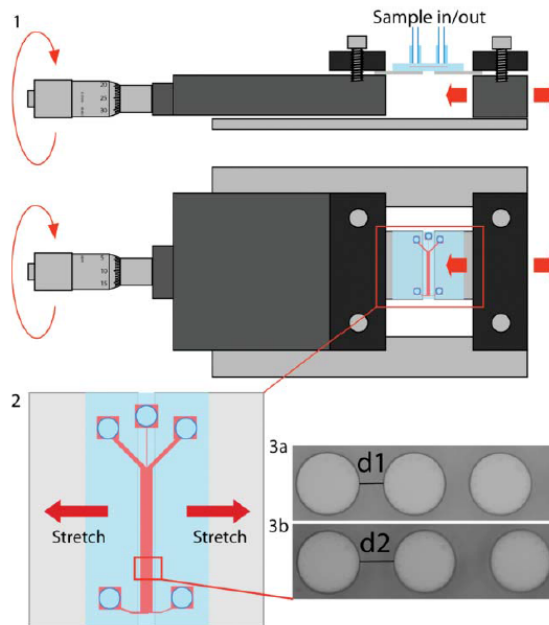


Figure 13: (From the work of Beech *et al.* [14]) (1) A modified micrometer translation stage holds the elastic-DLD device. (2) The sketch of the device. (3a) and (3b) Micrographs of posts before and after stretching showing how diameter changes.

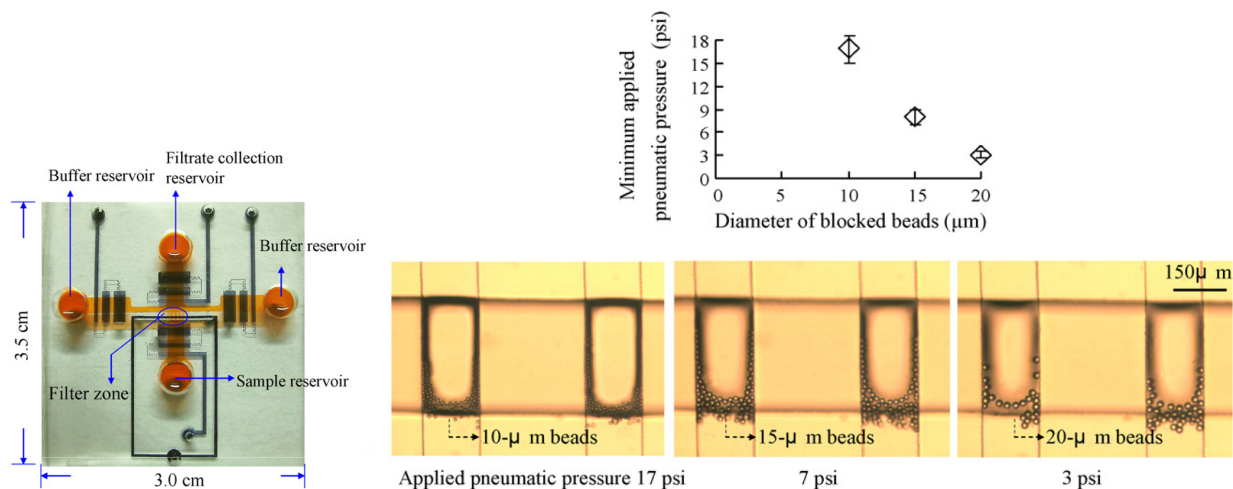


Figure 14: (From the work of Huang *et al.* [15]) (left) A photograph of the micro filter chip. (right top) The relationship between the minimum applied pneumatic pressure in the filter zone and the diameters of the trapped microbeads (right bottom) The microscope images of the clogged channels with trapped microbeads.

adjust the cutoff pore size by applying various control pressures to the membrane sealing the microfluidic filter, Fig. 14 (left). They have demonstrated the microbeads and cells with different diameters can be trapped under various pressures, Fig. 14 (right). The same idea was followed by Liu *et al.* [16] and Beattie *et al.* [17] to isolate the beads/cells with different diameters under various pressures, Figs. 15 and 16. The difficulties related to the fabrication, integration, and operation of these devices limit their applications.

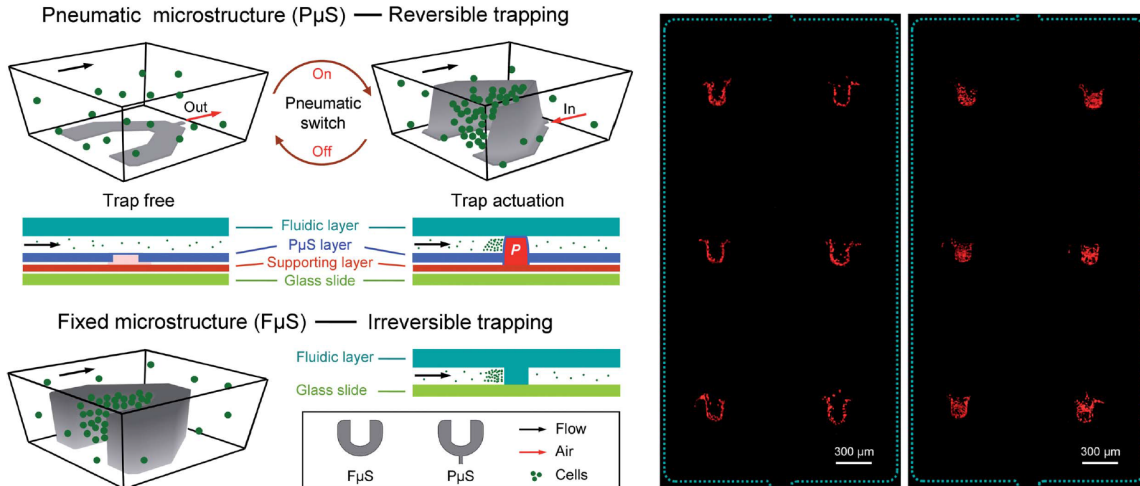


Figure 15: (From the work of Liu *et al.* [16]) (left) Pneumatic microstructure presenting a height-adjustable geometry resulting reversible cell trapping (top) compared with a fixed microstructure (bottom) showing irreversible trapping. The fluorescence images show the parallel trapping of the cells under the pressure of 4 psi (middle) and 5 psi (right).

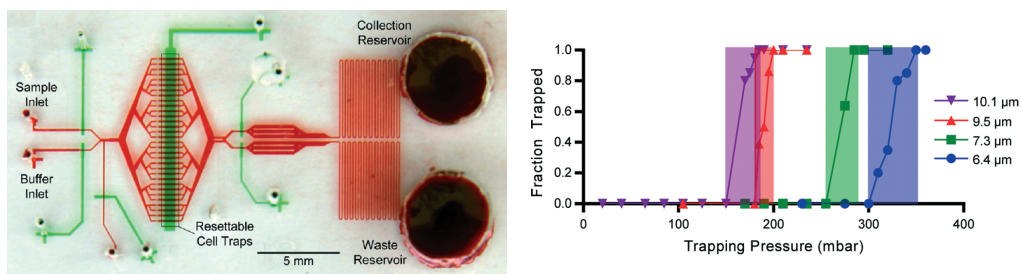


Figure 16: (From the work of Beattie *et al.* [17]) (left) Photograph of the separation device with the flow and control channels are filled with red and green food coloring respectively. (right) The probability of trapping microsphere as a function of pressure applied to the diaphragm. Smaller microspheres require smaller channel openings to be captured, and therefore require greater trapping pressure than larger microspheres. The range of trapping pressures for each particle size is shown as a colored block for each microsphere diameter, indicating the minimal overlap between sizes.

## Objectives

The main objectives of this work are enumerated in the following.

- To mathematically study the physics of low-Reynolds-number incompressible and compressible flows of Newtonian fluids (liquids and gases) through deformable microchannels.

- **To develop novel applications enabled by deformable microfluidics, including passive Stokes-flow rectifiers and passive particle sieve/separators.**

## Outline

The following shows the outline of the dissertation in the following chapters:

- **Chapter 2:** Since the target tunable microfluidic devices aimed to be developed in this work are solely tuned by the pressure difference across the channel, the minimum height of the channel needs to be sufficiently small to make the device compatible with the target particles. Therefore, a new technique is developed for the fabrication of shallow (few microns in height) rigid/flexible microchannels with the either small (tens of microns) or large (several millimeters) width.
- **Chapter 3:** Structural-fluid characteristics are solely dictated by a lumped dimensionless parameter, called flexibility parameter, introduced in this chapter. A master curve is obtained for fluid flow through any arbitrary shallow and long deformable microchannel presenting the dimensionless flow rate versus flexibility parameter. The experimental and analytical investigations reveal various distinct fluid-structural characteristic behaviors under different flexibility parameter regimes.
- **Chapter 4:** The fluid flow through asymmetrically-shaped microchannels with ultra-low aspect ratios is investigated experimentally and analytically. We have shown that passive rectification of the Stokes flow regime is possible for Newtonian liquids by introducing the non-linear terms to the otherwise linear equations of motion. The proposed nonlinearity stems from the coupled fluid-solid mechanics of the flow behavior in an asymmetrically-shaped microchannel, *i.e.* nozzle/diffuser, with deformable ceiling. The flow rectification ratio of  $\sim 1.2$ – $1.8$  is demonstrated for common Newtonian liquids like water and alcohol.
- **Chapter 5:** A theoretical coupled fluid-solid-mechanics model is developed for compressible fluid flow through deformable microchannels to predict fluid-solid character-

istics such as the mass flow rate, pressure distribution within microchannel, membrane deformation, etc. An explicit relationship is extracted for mass flow rate as a function of pressure difference across a microchannel, undeformed channel dimensions, properties of channel's ceiling such as thickness, modulus of elasticity and Poisson's ratio.

- **Chapter 6:** An analytical model is derived simultaneously taking microchannel deformability, fluid compressibility, and microchannel's width profile into account, which makes it a universal tool for studying low-Reynolds-number flows of Newtonian liquids and gases in microscale. We have mathematically and experimentally demonstrated that passive rectification of compressible and incompressible flows of Newtonian fluids (liquids and gases) under the Stokes regime is feasible by introducing the non-linear and direction-dependent terms to the otherwise linear equations of motion.
- **Chapter 7:** Based on the developed models, a new class of deformable microfluidics is proposed for passively-tunable particle trapping without the need to the pneumatic actuation. In this technique, the pore size is altered through the deformable microchannel expansion under different pressure differences across the microchannel.

# Chapter 2: A two-step sealing—and—reinforcement SU8 bonding paradigm for the fabrication of shallow microchannels<sup>1</sup>

## Questions

The main questions of this study are enumerated in the following.

- How can the risk of the channel blockage due to the SU8 reflow during the SU8 bonding be mitigated?
- Is there a microfabrication protocol for making the rigid or flexible shallow microchannels (few microns in height) with either small (tens of microns) or large (few millimeters) widths?
- What is the lowest obtainable aspect-ratio using this technique?
- What is the maximum bonding strength?

---

<sup>1</sup>Reproduced from *Aryan Mehboudi and Junghoon Yeom 2018 J. Micromech. Microeng. 28 035002 (2018); <https://doi.org/10.1088/1361-6439/aa9eb1>*, with the permission of IOP Publishing.

## Motivations

The shallow microchannels play an important role in various bio-applications such as the microfluidic ELISA assays, cell culturing, bio-sensing, etc. The deformable microchannels, on the other hand, are widely used for various applications such as particle separation, pressure sensors, fluidic capacitors, etc. The motivation of this study is to alleviate the difficulties associated with the fabrication of two important microfluidic architectures of 1) shallow microchannels with small patterns and 2) shallow microchannels with ultra-low height-to-width ratios.

## Objectives

The objective of this study is to develop a SU8 bonding protocol for sealing the shallow microchannel sidewalls with small or large widths in order to fabricate the rigid/flexible shallow microchannels. The bonding outcome such as the SU8 reflow and bonding strength are aimed to be examined for various channel dimensions and fabrication parameters.

## Introduction

As the applications of Lab-on-a-chip (LOC) devices are rapidly growing, much more attention is being devoted to sealing, fluidic/electric connections, and packaging among many serious challenges associated with these devices [82–84]. One of the most crucial steps in fabricating many LOC devices is to seal the sidewalls of the microfluidic networks properly, in such a manner that the bonding strength is sufficiently high to preserve the sealing intact without any leakage at the maximum operating pressure. One widely used strategy for sealing the microfluidic channels is the *adhesive bonding* technique based on the application of intermediate adhesive layers [84]. A wide variety of different adhesive layers such as the NOA (Norland Optical Adhesive) [85–87], parylene [88, 89], tape [90, 91], dry-film resists (DFRs) [92, 93], etc., have been successfully demonstrated. In particular, because of

its material properties such as excellent chemical resistance, transparency, and a relatively high Young modulus and its process flexibility such as high-resolution patterning capability and a wide range of achievable thickness  $O(100\text{ nm}–100\text{ }\mu\text{m})$ , the SU8 has been a choice of materials not only as an adhesive layer, but also as an important structural material in the MEMS and LOC communities [94]. The sealing of the SU-8 microfeatures are therefore truly important in many microfluidic devices [95, 96].

As one of the very first works on SU8 bonding, Jackman *et al.* [97] proposed a methodology to fabricate microfluidic devices in the SU8 epoxy. Many SU8-based techniques were quickly proposed thereafter [98–109], and many microfluidic devices were developed based on SU8 bonding [110–119]. One of the main difficulties associated with using the liquid adhesives in general, and SU8 in particular, is channel clogging due to the flow of the adhesive layer during the bonding process. As a result, the large-scale microfluidic networks with small patterns are difficult to be made. The incorporation of the auxiliary channels or moats around the main microchannel has been utilized to accommodate some of SU8 that flows during the bonding process [100, 109, 120]. Reducing the bonding temperature below the glass transition temperature of SU8 has been also effective to significantly mitigate the risk of channel clogging [98, 121].

The *partial exposure* approach is a promising technique to fabricate small SU8 channels [122–126]. In this approach, the top wall of the channel is established using a lower exposure dose, while the sidewalls are made through a larger exposure dose. The partial exposure approaches, however, become very slow for shallow and long microfluidic networks, since the uncured SU8 needs to be developed away through the channel simply by diffusion after all the sidewalls are established. Similarly, the other approaches based on the *sacrificial layers* [127–129], where the sacrificial layers are etched away through the SU8 channel after the completion of the bonding process, are also time-consuming for making shallow and long channels. *Lamination* is another popular SU8 bonding technique, which has been successfully used to fabricate three-dimensional channels with large heights ( $\geq 20\text{ }\mu\text{m}$ ) [102, 103], while the shallow channels are still prone to fill with the SU8 during the lamination. More impor-

Table 1: The accessible range of the microchannel dimensions for various adhesive bonding approaches: (A) using an adhesive-coated rigid substrate to seal the microchannel sidewalls, (B) the partial exposure technique, (C) the sacrificial layer approach, and (D) the lamination method. The following definitions are used for the sake of simplicity:

+: it has been reported in the literature, -: it has not been reported in the literature (to the best of the author’s knowledge), -p: even though it has not been demonstrated in the literature (to the best of the author’s knowledge), the author believe it is feasible, and ++: it is feasible using the proposed paradigm in this work.

Approach	Shallow microchannel $O(1 \mu m)$		Deep microchannel $O(10 \mu m)$		References
	Large width $O(1 mm)$	Small width $O(10 \mu m)$	Large width $O(1 mm)$	Small width $O(10 \mu m)$	
(A)	-	-	-p	+	[97, 98, 100, 109, 120, 131]
(B)	-p	+	-p	+	[122–126]
(C)	-p	+	-p	+	[127–129]
(D)	-	-	+	+	[102, 103, 130]
This work	++	++	++	++	This work

tantly, the maximum width-to-height ratio is limited in the lamination-based approaches by the adhesive layers sagging and the consequent channel blockage [130].

The aforementioned major adhesive bonding techniques are also schematically presented in Fig. 17. The accessible range of the microchannel dimensions and more fabrication considerations about each approach are also presented in Tables 1 and 2, respectively. Because of the rigidity of the adhesive-coated substrate, the approach (A) necessitates a thick SU8 layer (of the order of magnitude of  $10 \mu m$ ), and/or high bonding temperatures/pressures in order to obtain a conformal and leak-free sealing, which makes the microchannels highly susceptible to clogging. In addition, since they are based upon the diffusion phenomenon to establish the microchannels, the partial exposure, (B), and sacrificial layer, (C), techniques are time-consuming, particularly when it comes to shallow and long microchannels. Furthermore, the application of the lamination approach, (D), has been limited to the deep channels by the channel-clogging difficulties associated with 1) the flexible film sagging and 2) the adhesive layer reflow. One may conclude that despite these tremendous efforts in developing SU8-based adhesive bonding techniques for microchannel fabrication, creating the two important microfluidic architectures of 1) shallow microchannels with small patterns on a large area and 2) shallow microchannels with ultra-low height-to-width ratios is still a significant challenge.

Table 2: The fabrication considerations for various adhesive bonding approaches. The schematic presentation of the addressed techniques can be found in Fig. 17.

Approach	Fabrication considerations
<b>A<sub>s</sub></b>	Because of the rigidity of the sealing substrate, this approach necessitates a thick $O(10 \mu m)$ SU8 layer and/or high bonding temperatures in order to obtain a conformal and leak-free sealing. On the other hand, because of using the thick SU8 and/or high temperatures, the channels are prone to be clogged due to the SU8 reflow. Hence, the thickness of the adhesive layer should be carefully chosen to avoid the channel clogging. The creation of moats/auxiliary channels in the vicinity of the main channel has been demonstrated to mitigate the risk of channel clogging through the accommodation for some of the reflowed SU8.
<b>A<sub>g</sub></b>	The considerations mentioned for Approach A <sub>s</sub> are generally correct for Approach A <sub>g</sub> and other adhesive layers such NOA, TMMF, etc.
<b>B</b>	Since uncured SU8 is developed away purely based on the diffusion phenomenon, this approach becomes time-consuming, particularly when it comes to the fabrication of shallow and long microchannels.
<b>C</b>	Since a sacrificial layer is removed purely based on the diffusion phenomenon, this approach becomes time-consuming, particularly when it comes to the fabrication of shallow and long microchannels.
<b>D</b>	The application of this process has been limited to deep channels by the channel-clogging difficulties associated with 1) flexible film sagging and 2) adhesive layer reflow.
<b>This work</b>	As far as the pattern of the microchannel’s sidewalls is concerned, the proposed approach is consistent with both SU8 photo-lithography and glass wet etching. Regarding the accessible range of the microchannels’ dimensions, both deep and shallow microchannels with small or large widths can be fabricated.

Regarding the bonding approaches other than the aforementioned strategies based on the SU8, the shallow microchannels with an ultra-low aspect ratio are extremely challenging, if possible, to be fabricated utilizing the widely used approach of PDMS soft lithography [132–136]. The lamination-based approaches also have the risk of channel blockage due to the uniform pressure applied by the lamination device during the bonding process [103, 130]. For example, by using a lamination-based bonding technique, Wangler *et al.* [130] fabricated a microchannel 45  $\mu m$  in height, and 2 mm in width, that to the best of the author’s knowledge, shows one of the lowest height-to-width ratios ( $2.25 \times 10^{-2}$ ) in the microfluidics context, yet is still more than one order of magnitude larger than that presented in this work. De Marco *et al.* have demonstrated the shallow microchannels with an aspect ratio of 0.01 ( $200 \mu m \times 2 \mu m$ ) using a UV-based bonding process by a photocurable PFPE-urethane-methacrylate with low molecular weight [137]. Similar to the PDMS-based soft-lithography, the lowest aspect-ratio is limited by the polymer layer’s sagging and ceiling collapse.

Low-aspect-ratio shallow microchannels play an important role in various applications. For example, in the context of performing microfluidic ELISA assays, the shallow channels significantly reduce the volume of chemifluorescent reaction, markedly improving the sensi-

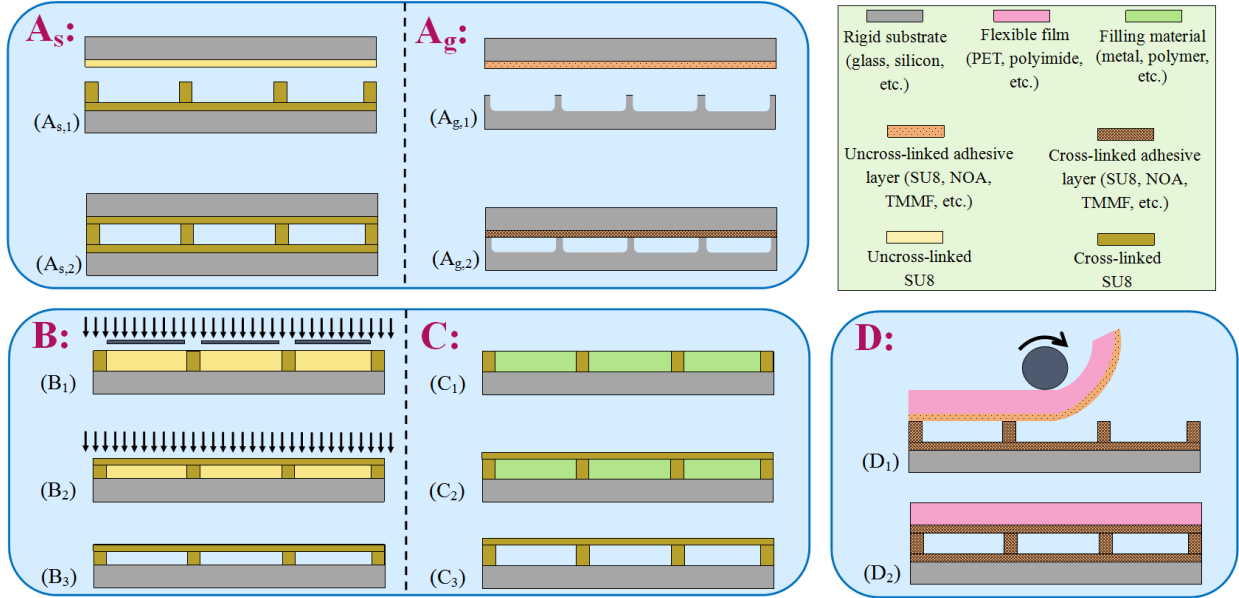


Figure 17: The schematic presentation of the different adhesive bonding approaches. ( $A_s$ ) The SU8 photo-lithography and bonding using a SU8-coated rigid substrate: ( $A_g$ ) The glass etching process and bonding using a rigid substrate coated with an adhesive layer such as SU8, NOA, etc: (B) The partial exposure approach. (C) The sacrificial layer approach. (D) The adhesive layer lamination approach.

tivity and speed of ELISA [13, 138]. Ultra-low-aspect-ratio microchannels are also important for cell culture applications, where a shallow channel with a depth slightly smaller than cell diameter is coated with cell-capturing antibodies to ensure the contact of the flexible cells with the channel walls for more efficient capturing of the cells in the target area [21]. A larger microchannel width allows a higher throughput.

As another example, the sensitivity of the biosensors involving the use of the microelectrodes in a microchannel, which are used to detect the single cells electrically (label-free format) in real time, is limited by the probability of a target cell being captured in the active area of the sensor [20]. The detection limit can be enhanced by effectively increasing the active area of the device through either or both of decreasing the channel depth and increasing the channel width. In order to detect smaller bacterial cells with a high electrical sensitivity of the device, the channel needs to be shallow enough to be compatible with the small dimensions of the target cells, and as wide as possible to provide a high probability of capturing the target species.

In this article, a new paradigm is proposed based on the low-temperature and low-pressure

SU8 bonding, which consists of two major steps, that is, sealing and bonding reinforcement. Since a thin SU8 layer spun on a flexible film (in this work, Polyethylene Terephthalate (PET)) is utilized as the adhesive layer, the capability of sealing small and long microfluidic channels fully made of SU8 is successfully demonstrated without channel clogging. On the other hand, since the PET film is sturdy enough not to sag significantly under its weight, the fabrication of microchannels with ultra-low aspect ratios is successfully demonstrated as well. Furthermore, the small microchannel sidewalls made through glass wet etching are also sealed without channel blockage, which demonstrates the compatibility of the proposed SU8 bonding paradigm with the important microchannel fabrication techniques based on the glass etching process. The effects of the microchannel size, the piranha treatment of the glass, and the oxygen plasma treatment of the microchannel sidewalls on the outcome of the developed SU8 bonding paradigm are also investigated. In addition, we demonstrate the fabrication of the multi-height deep–shallow microchannel sidewalls, and its sealing using a thin-SU8-coated PET film. Moreover, a theoretical model is developed to obtain a more profound insight into the flow characteristics such as the volumetric flow rate under various pressures, as well as the structural behavior of the microchannel including the PET film deformation, strain and von Mises stress variations, bonding strength, etc. According to the hydraulic tests combined with the fluid-structural mechanics analysis, the maximum bonding strength is predicted to be of the order of 10 MPa. Finally, small oil-in-water droplets are generated using a shallow microchannel with innermost surfaces fully made of SU8, as a proof-of-the-concept device. Two microchannels with different heights of 6  $\mu\text{m}$  and 15  $\mu\text{m}$  are used to generate 13- and 47-micron droplets.

## Fabrication

In this section, the two-step sealing–and–reinforcement SU8 bonding paradigm is described. As shown schematically in Fig. 18, the framework underlying the proposed bonding paradigm consists of two steps:

— **Sealing:** In this step, the sidewalls of the microchannel are sealed using as thin a SU8

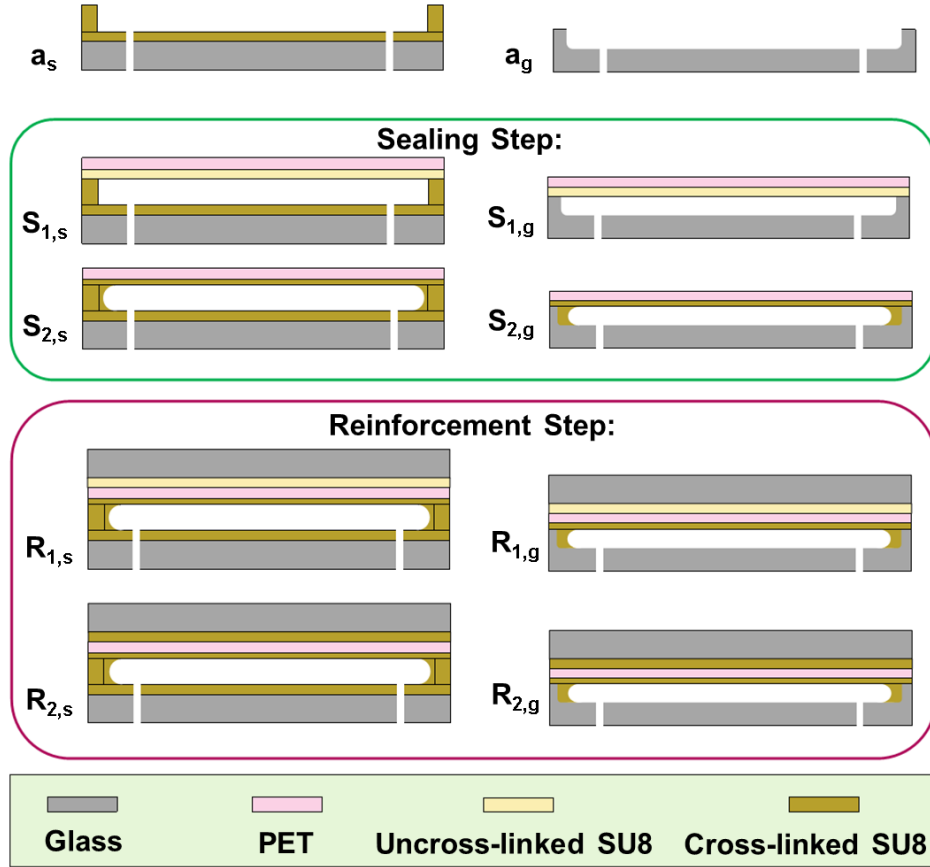


Figure 18: Schematic presentation of the two-step sealing-and-reinforcement bonding paradigm for two different approaches that the microchannel sidewalls are made through the SU8 photo-lithography (left) or the glass wet etching (right): the microchannel sidewalls are created through SU8 photo-lithography ( $a_s$ ) or glass wet etching ( $a_g$ ). At the sealing step, a PET film coated with a thin layer of SU8 seals the microchannel sidewalls ( $S_{1,s}$  and  $S_{1,g}$ ). The chip is then undergone with UV illumination and post-exposure baking to cure the adhesive layer ( $S_{2,s}$  and  $S_{2,g}$ ). The slight SU8 reflow can result in a cross-section with round corners in this step. At the reinforcement step, a glass substrate coated with a SU8 layer is brought into contact with the bare side of the PET film ( $R_{1,s}$  and  $R_{1,g}$ ). The sample is then undergone with UV illumination and post-exposure baking to cure the adhesive layer at the bonding interface of the reinforcement glass and the PET film ( $R_{2,s}$  and  $R_{2,g}$ ).

layer as possible. Using a thinner SU8 layer decreases the risk of microchannel blockage due to the SU8 reflow during the sealing process. On the other hand, the SU8 layer needs to be thick enough to accommodate the height non-uniformity that always exists (in different levels of severity) because of the nature of the spin coating process, like the presence of defects or particles at the bonding interface, edge beads, etc. Using a rigid substrate for the sealing purpose necessitates a thicker SU8 layer to create a conformal contact, which increases the risk of channel clogging due to the larger amount of SU8 reflow. The advantage of the flexible

substrates becomes particularly important when the channels are long, where the bonding of rigid substrates on such large areas necessitates a very clean bonding interface with a perfect height uniformity. In this work, a thin ( $\sim 190 \mu\text{m}$ -thick) and nonporous PET film covered by a thin layer of SU8 is used for sealing the microchannels. A 5-minute baking at a temperature above the glass transition temperature of the PET (*e.g.*  $95^\circ\text{C}$  in this work) helps it to become flat and the following spin coating process much more convenient. The PET film is then put on a spinner chuck. The SU8 layer is spun on the PET film according to Table 3.

— **Bonding reinforcement:** This step is designed to reinforce the bonding quality as well as to avoid the likely deformation of the flexible substrate under high pressures [134, 139] by using a rigid substrate (glass in this work) covered by a thick enough SU8 layer. This step becomes important for microfluidic devices with small microchannels that need to operate with highly pressurized flows.

In this work, two well-known approaches are utilized to create the microchannel sidewalls: wet etching of glass and SU8 photo-lithography. In order to create the microchannel sidewalls through glass wet etching, a buffered oxide etchant (BOE) solution mixed with hydrochloric acid ( $\text{HF}(48\%):\text{NH}_4\text{F}(40%):\text{HCl}(37\%) = 1:6:1.4 \text{ (v/v)}$ ) is used as an etchant, while photo-resists S1813 (or AZ4330) and AZ4620 are used as a mask for the fabrication of shallow and deep microchannels, respectively. Furthermore, the sidewalls pattern is established through a two-step wet etching procedure for double-height deep–shallow microchannels. First, the deep regions are etched in a glass substrate. In the next step, after the alignment between the patterned glass and the second photo-lithography mask, a new photo-resist layer is patterned in such a manner that the windows open up to the already deeply-patterned areas of the glass substrate as well as to the areas that need to be shallowly etched. The etching process is then performed to create the double-height deep–shallow microchannel sidewalls. The reversed order, *i.e.* shallow etching followed by the deep etching, has also been successfully used. More details of the fabrication technique can be found in Appendix. In addition, the specifications of the different SU8 layers used in this work are summarized in Table 3. The

Table 3: The specifications of different SU8 films utilized in this work. The uniform SU8 films with different thicknesses have been spun by using the appropriate mixture of the SU-8 2100 and the SU-8 2000 Thinner (both from MicroChem Corp.), and utilizing the following spinning procedure:

The spinner speed is ramped at a rate of 83 rpm/s up to 500 rpm and kept there for 15–20 seconds. The speed is then ramped up to the maximum speed at a rate of 83 rpm/s, remaining constant for 45 seconds, and then ramped down to zero at a rate of about 250 rpm/s.

SU-8 2100:SU-8 2000 Thinner weight ratio	maximum spin speed (rpm)	film thickness ( $\mu m$ )
1 : 3.2	1500	1
1 : 2.5	1500	2
1 : 1	1500	7
3 : 1	2500	15
16 : 1	4000	30

Table 4: The two-step ( $65^\circ C$  followed by  $95^\circ C$ ) soft-bake duration times (minutes) for different SU8 layers used in the sealing step.

SU8 thickness ( $\mu m$ )	duration ( <i>min</i> ) at $65^\circ C$	duration ( <i>min</i> ) at $95^\circ C$
2	0	1
7	1	1.5

SU8 layer thickness is measured using the Dektak profilometer. The measurements show the variations smaller than  $\pm 0.05 \mu m$  in the thickness of a thin ( $2.0 \mu m$  in average) SU8 layer all over the substrate. This variations become larger ( $\pm 0.5 \mu m$ ) for the thickest SU8 layer (about  $30.0 \mu m$  in average) used in this work. The spin coating procedure described in Table 3 resulted in uniform SU8 layers with various thicknesses.

After creating the microchannel sidewalls and drilling the via-holes (Fig. 18 ( $a_s$ ) and ( $a_g$ )), a thin layer of SU8 is spun on the PET film. The  $2 \mu m$  and  $7 \mu m$  thick SU8 layers are used in the sealing step based on the severity of the patterned sidewalls' height non-uniformity. The SU8-covered PET film is then baked according to Table 4. The prepared glass substrate with the pattern of sidewalls together with the PET film are then put on a  $69^\circ C$  hotplate. After one minute, the PET film is flipped over, and its SU8 cover is brought into contact with the microchannel sidewalls. Trapped air is then removed using tweezers and/or finger pressure (Fig. 18 ( $S_{1,s}$ ) and ( $S_{1,g}$ )). After the bubble removal step is accomplished, the chip remains on the hotplate at  $69^\circ C$  for about 30 minutes and then is cooled down to room temperature over about 20 minutes. The chip is then undergone with the UV illumination of  $1.4 J/cm^2$  through the PET film. Next, the sample is put on a hotplate, initially at  $65^\circ C$ . The temperature is then ramped up to  $95^\circ C$  over about 4 minutes, remaining constant at

Table 5: The two-step ( $65^{\circ}C$  followed by  $95^{\circ}C$ ) soft-bake duration times (minutes) as well as the bonding temperature for different SU8 layers used in the reinforcement step.

Thickness of SU8 ( $\mu m$ )	duration time ( $min$ ) at $65^{\circ}C$	duration time ( $min$ ) at $95^{\circ}C$	Bonding temperature ( $^{\circ}C$ )
7	0	1	95
15	1	1	85
22	2	1.5	75

$95^{\circ}C$  for 20 minutes, and decreases to room temperature over about 30 minutes to complete the sealing step (Fig. 18 ( $S_{2,s}$ ) and ( $S_{2,g}$ )).

In order to reinforce the bonding strength or avoid the potential deformation of the PET film in highly pressurized flows, and based on the severity of the height non-uniformity of the bare side of the PET film, a SU8 layer with a thickness of  $7 \mu m$ ,  $15 \mu m$ , or  $22 \mu m$  is spun on a glass substrate and baked according to Table 5. Next, the fabricated chip is put on a hotplate initially at  $65^{\circ}C$ . The temperature is then ramped up to the bonding temperature shown in Table 5 at a rate of about  $7^{\circ}C/min$ . The SU8-covered reinforcement glass is then put on the same hotplate. After one minute, the reinforcement glass is flipped over, and brought into contact with the PET film, and the air bubbles are removed using tweezers (Fig. 18 ( $R_{1,s}$ ) and ( $R_{1,g}$ )). It is worth mentioning here that the microchannel blockage is not a matter of concern in this step, since the SU8 layers forming the microchannel sidewalls have already been cured. The chip remains on the hotplate for 10 minutes and then cools down to room temperature at a rate of about  $3^{\circ}C/min$ . The chip is then undergone with UV illumination of  $2.1 J/cm^2$  through the reinforcement glass, followed by baking on a hotplate, initially at  $65^{\circ}C$ . The temperature is then ramped up to  $95^{\circ}C$  over about 4 minutes, remaining constant at  $95^{\circ}C$  for 10 minutes, and then decreases to room temperature at a rate of about  $3^{\circ}C/min$  to finish the bonding reinforcement step (Fig. 18 ( $R_{2,s}$ ) and ( $R_{2,g}$ )). A more detailed and step-by-step description of the two-step SU8 bonding paradigm can also be found in Appendix.

# Methodology

## Experimental

### Device fabrication

The microchannels are made through SU8 photo-lithography on or wet etching of glass substrates, and sealed by the SU8-coated PET film, with and without reinforcement. A PDMS interconnect is then bonded on the top of the glass slide after a short and gentle oxygen plasma treatment of both PDMS and glass surfaces. Since the via-holes in the glass substrate are rather big (2 mm in diameter), an acceptable alignment between the via-holes in the glass and the corresponding holes in the PDMS interconnects is achieved by eyes quickly after the oxygen plasma treatment, and before the PDMS interconnect is brought in contact with the glass substrate, as shown in Appendix.

### Hydraulic tests

In order to apply a range of pressure differences across the channel, compressed gas is injected into a large reservoir, containing DI water or other desired samples, located before the microchannel, as a result of which the liquid is being pushed out of the reservoir from its other port towards the inlet of the microchannel. A constant level of pressure can be applied to the channel in this way as opposed to a use of a syringe pump, which is known to generate a fluctuation in pressure. Furthermore, in order to measure the volumetric flow rate, the liquid discharged through the chip is collected inside a vial, and its weight is measured over time using an analytical scale. We have been able to investigate the pressure levels up to about 345 kPa (*i.e.* 50 psi), where the utilized fluidic fittings start to fail.

### Experimental setup for droplet generation

While hydrophobic materials such as PDMS and SU8 are favorable to be used as the structural materials of the microchannels for water-in-oil droplet generation, the hydrophobic nature of its surface makes the microfluidic channel fully made of SU8 inappropriate for

oil-in-water droplet generation. SU8 can be efficiently rendered a hydrophilic surface using an oxygen-plasma treatment [140]. However, after the microchannel is sealed, the oxygen plasma might not be an efficient option, particularly when it comes to shallow and long microchannels. Hence, in this work, the microfluidic chips are put on a  $55^{\circ}\text{C}$  hotplate, and the channels are rinsed with the chromium etchant (from Sigma-Aldrich) that contains 10–20 % Ceric Ammonium Nitrate (CAN). The SU8 treatment with CAN has already been demonstrated as an efficient approach to render the SU8 surface to be hydrophilic with water-SU8 contact angles as low as  $10^{\circ}$ – $40^{\circ}$  [141, 142]. One can use Ethanolamine for further decreasing the contact angle if needed [141–143]. An interesting work by Sobiesierski *et al.* [142] shows the contact angle increases up to about  $60^{\circ}$  and  $19^{\circ}$  after two weeks from the SU8 treatment with CAN and ethanolamine, respectively, and remains almost constant over more than 70 days. After the chemical treatment of the SU8 innermost surfaces of the microchannel with CAN, the channels are washed for 30 minutes with DI water being injected through the channel. The device is then ready to be used for its main mission.

In order to generate oil-in-water droplets, DI water is used as a continuous phase, while 0.01 M sodium dodecyl sulfate (SDS from Sigma-Aldrich) is added to stabilize the droplets, and 0.01 M fluorescein sodium salt (from Sigma-Aldrich) is dissolved in the solution to visualize the continuous phase. In order to uniformly mix the solution, a one-hour sonication in an ultrasonic bath is performed. A dispersed phase, on the other hand, is hexadecane (from Sigma-Aldrich). Both continuous and dispersed phases are filtered using a PTFE  $0.45\ \mu\text{m}$  filter, and are then degassed for one hour under vacuum before being used. The microchannels are also washed for 20 minutes with DI water being injected through the channel before doing the main experiments.

## Modeling

The pressure drop across a straight, non-deformable, and rectangular channel of height  $H$ , width  $W$ , and length  $L$ , entirely filled with a liquid with a dynamic viscosity of  $\mu$ , with no

bubbles present, can be obtained using the following exact solution [18]:

$$\Delta p = \frac{a\mu L}{WH^3}Q \quad (2)$$

$$a = 12 \left[ 1 - \sum_{n, \text{odd}}^{\infty} \frac{1}{n^5} \frac{192}{\pi^5} \frac{H}{W} \tanh\left(n\pi \frac{W}{2H}\right) \right]^{-1} \quad (3)$$

where  $\Delta p$ , and  $Q$  refer to the pressure difference across the channel, and the volumetric flow rate passing through the channel, respectively. The parameter  $a$  can be approximated as follows:

$$a = 12 \left[ 1 - 0.630 \frac{H}{W} \right]^{-1}, \text{ for } H \leq W \quad (4)$$

The approximated expression in Eq. 4 becomes more accurate as the aspect ratio  $H/W$  decreases. For the worst case of the square channel with  $H = W$ , the error is around 13%, while for the channel with an aspect ratio of a half,  $H = W/2$ , the error is down to 0.2% [18].

**\* Hybrid zero-dimensional-fluid-mechanics—three-dimensional-solid-mechanics modeling:**

The presented exact solution is valid for one-dimensional Poiseuille flow. For a microchannel with the PET film as its deformable ceiling (without reinforcement), the local fluid flow pattern does not change sharply across the channel if the deformed ceiling slope is small (*i.e.* PET film deformations much smaller than the channel width). In these circumstances, the streamlines are still acceptably parallel. Hence, as a primitive model for the volumetric flow rate through a microchannel with ceiling deformations much smaller than the channel width, the exact solution presented for the Poiseuille flow is still used in this work. However, the average height of the deformable channel,  $\bar{H}$ , is used in Eqs. 2 and 4. The average height is a function of the pressure difference across the channel:  $\bar{H}(\Delta p) = H_0 + \bar{\delta}(\Delta p)$ , where  $H_0$  shows the original height of the channel without any ceiling deflections, and  $\bar{\delta}(\Delta p)$  refers to the average displacement of the PET film under the pressure difference of  $\Delta p$  across the channel.

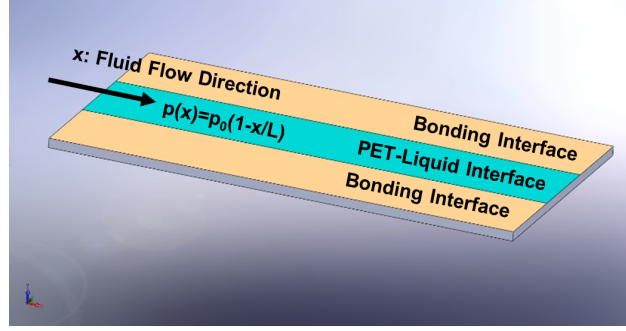


Figure 19: The schematic presentation of the three-dimensional model for the structural mechanics analysis of the PET film as the ceiling of a straight microchannel. The width of the bonding interfaces is considered to be equal to that of the wet surface (PET-liquid interface). The boundary conditions are as follows: the bonding interfaces are fixed. The wet surface experiences a pressure, which linearly decreases along the channel. The lateral sides of the PET film have the free boundary condition. The back side of the PET film has also the free boundary condition if the channel is not reinforced. Otherwise, the back side of the PET film is fixed.

By assuming a linear pressure variation along the channel, the displacement contour of the PET film is obtained through the three-dimensional structural mechanics modeling.

The three-dimensional model for the structural mechanics analysis of the PET film, as the ceiling of a straight microchannel, is shown in Fig. 19. The boundary conditions are considered as follows: (1) the bonding interfaces are fixed, (2) the wet surface (PET-liquid interface) experiences a pressure, which linearly decreases along the channel:  $p(x) = p_0 \times (1 - x/L)$ , where  $p_0$  is the applied pressure at the inlet of the microchannel,  $x$  shows the distance from the inlet, and  $L$  refers to the microchannel length, (3) the lateral sides of the PET film have the free boundary condition, and (4) the back side of the PET film is fixed if the channel is reinforced, or has the free boundary condition if the channel is not reinforced. Furthermore, the PET film's thickness is  $190 \mu m$ , and its Young modulus, Poisson's ratio, and density are  $3 \text{ GPa}$ ,  $0.4$ , and  $1350 \text{ kg/m}^3$ , respectively. The COMSOL 5.2 software is utilized to numerically solve the governing equations. After finding the displacement contour of the PET film, the average height of the channel is obtained. The volumetric flow rate is then approximated by substituting the obtained average height in Eqs. 2 and 4. For the flow analysis, the density and dynamic viscosity of water are considered to be  $10^3 \text{ kg/m}^3$  and  $10^{-3} \text{ Pa} \cdot s$ , respectively.

Figure 20 shows the schematic presentation of the three-dimensional model for the struc-

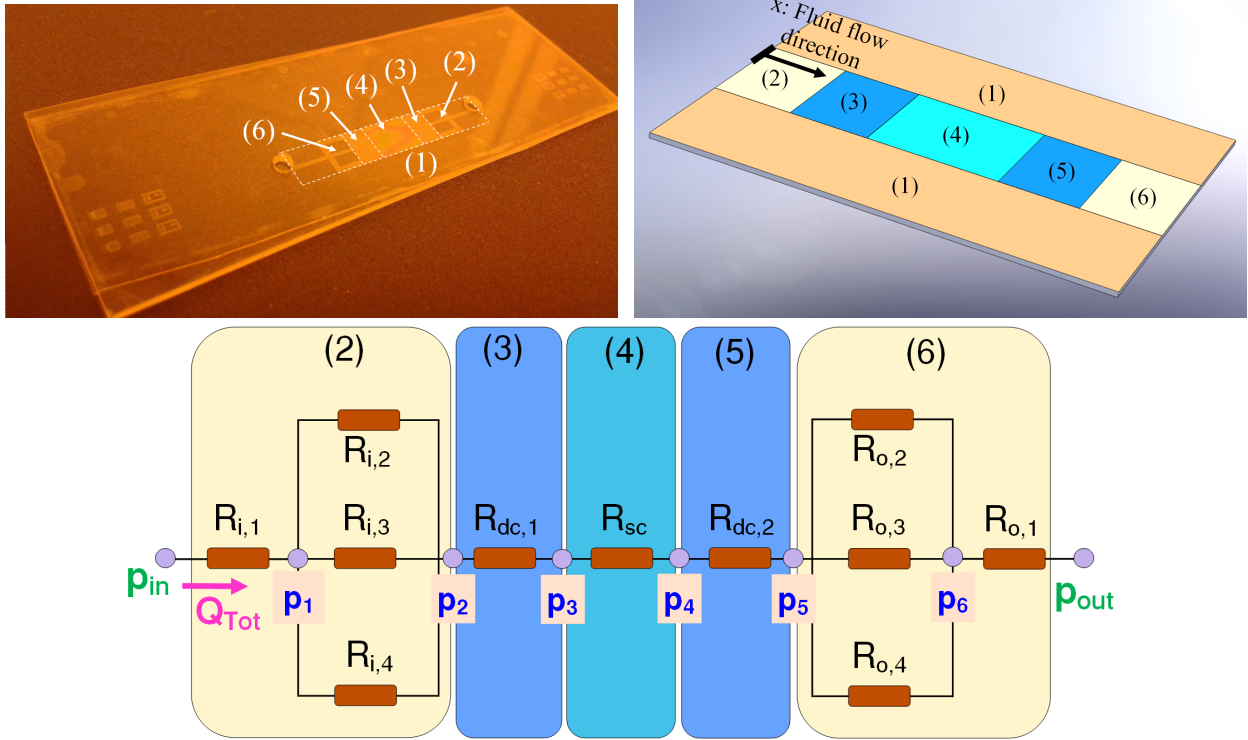


Figure 20: (top left) A camera picture of a multi-height deep-shallow microfluidic channel together with (top right) the schematic presentation of the three-dimensional model for the structural mechanics analysis of the PET film as the ceiling of the channel, as well as (bottom) the schematic presentation of the zero-dimensional model for the fluid flow analysis. The various areas of the deep-shallow microchannel are described in the following.

- (1): The bonding interfaces.
- (2) and (6): The areas connecting the inlet/outlet ports to the deep and wide portions of the channel.
- (3) and (5): The deep and wide portions of the channel.
- (4): The shallow and wide portion of the channel.

The pressure values at different nodes ( $p_i : i = 1$  to 6), shown in the bottom schematic, together with the volumetric flow rate through different branches of the channel, as well as the structural behaviors such as the PET film's deformation, strain and stress distribution, etc., are obtained by solving the coupled equations of the zero-dimensional-fluid-mechanics—three-dimensional-structural-mechanics model using an iterative approach.

tural mechanics analysis of the PET film as the ceiling of a multi-height deep-shallow microchannel together with a camera picture of a typical deep-shallow channel.

**(a) Solid mechanics aspect of the modeling** — the appropriate boundary conditions are assigned to various areas of the PET film, shown in Fig. 20 (top), as described in the following. The bonding interfaces, areas (1), are fixed. In addition, the PET film in the areas connecting the inlet/outlet ports to the deep and wide parts of the channel, areas (2) and (6), shows a negligible deflection, since the microchannel width is small enough not to

create noticeable deformations. Hence, the wet surface of the PET film in areas (2) and (6) is also assumed to be fixed. Furthermore, the pressure is assumed to linearly change through every segment of the microfluidic network shown in Fig. 20 (bottom). As a result, the areas (3), (4), and (5) have the variable pressure boundary conditions as described in Eqs. 5–7, wherein  $L_i$  refers to the length of the area ( $i$ ), and  $p_j$  shows the pressure value at the node  $j$  depicted in Fig. 20 (bottom).

$$p_{(3)}(x) = p_2 + \frac{p_3 - p_2}{L_3}(x - L_2) \quad (5)$$

$$p_{(4)}(x) = p_3 + \frac{p_4 - p_3}{L_4}(x - L_2 - L_3) \quad (6)$$

$$p_{(5)}(x) = p_4 + \frac{p_5 - p_4}{L_5}(x - L_2 - L_3 - L_4) \quad (7)$$

Moreover, the lateral sides of the PET film have the free boundary condition. The back side of the PET film also has the free boundary condition if the channel is not reinforced. Otherwise, the back side of the PET film is fixed.

**(b) Fluid mechanics aspect of the modeling** — the hydrodynamic resistance of any segment, like  $\psi$ , in the microfluidic network is defined by Eq. 8, where  $L_\psi$ ,  $W_\psi$ , and  $H_\psi$  refer to the length, width, and height of the segment  $\psi$ , respectively.

$$R_\psi = \frac{12\mu L_\psi}{W_\psi H_\psi^3 (1 - 0.63 \frac{H_\psi}{W_\psi})} \quad (8)$$

The pressure difference across the segment  $\psi$  is also related to the volumetric flow rate of this segment using  $\Delta p_\psi = R_\psi Q_\psi$ . Furthermore, the average height of the microchannel in the area ( $i$ ), where  $i$  is 3, 4, or 5, is the summation of the original height,  $H_{0,i}$ , and the average displacement of the PET film,  $\bar{\delta}(i)$ , in those areas:  $\bar{H}(i) = H_{0,i} + \bar{\delta}(i)$ . It should be noted that  $\bar{\delta}(i) = 0$ , if the bonding reinforcement is done. In that case, the channel geometry, and consequently the hydrodynamic resistances can be calculated without studying the solid-mechanics model. In other words, the solid- and fluid- mechanics models are decoupled in presence of the bonding reinforcement. However, if the bonding reinforcement is not

performed, the PET film can displace in the wide areas (3), (4), and (5). In this situation, the solid- and fluid- mechanics models are coupled. The governing equations of the coupled fluid–solid mechanics model are solved in an iterative manner: a set of initial values is considered for the pressure at different nodes,  $p_i$ . We consider  $p_2 = p_3 = p_0$ , where  $p_0$  is the pressure applied at the inlet of the channel, and  $p_4 = p_5 = 0$ . The solid-mechanics equations are then solved to obtain the PET film displacement contour and the average displacement in different areas. The average displacement is used to modify the average height of the channel in different areas. Thereafter, the fluid-mechanics equations are solved, and the pressure is obtained at different sections of the channel. The solid-mechanics model can then be studied again. This procedure is repeated until the converged results are achieved (less than 10 iterations showed enough accuracy in this work).

## Results

### Two-step SU8 bonding paradigm’s outcome

Figure 21 shows the optical microscopy and SEM images of a serpentine microchannel with the innermost surfaces fully made of SU8. In order to create the microchannel sidewalls, a  $1.5 \mu\text{m}$ -thick SU8 layer was spun on the glass substrate to form one of the sidewalls. The lateral sidewalls were patterned using a  $2.1 \mu\text{m}$ -thick SU8 layer. In order to seal the microchannel sidewalls, a  $2 \mu\text{m}$ -thick SU8 layer spun on the PET film was brought into contact with the SU8 sidewalls. In addition, a glass substrate coated with a  $7 \mu\text{m}$ -thick SU8 layer was used in the bonding reinforcement step. As shown in Fig. 21 (a) and (b), void-free bonding on a large area of microchannels with small dimensions can be obtained using the proposed SU8 bonding paradigm. The very small thickness of the SU8 sealing layer ( $2 \mu\text{m}$ ) plays a key role in achieving such small microfluidic networks on a large area, because it reduces the risk of the channel blockage due to the SU8 reflow in the sealing step. The PET film, on the other hand, makes the idea of using such a thin SU8 layer practical thanks to the high compliance of the substrate that promotes the conformal contact, while

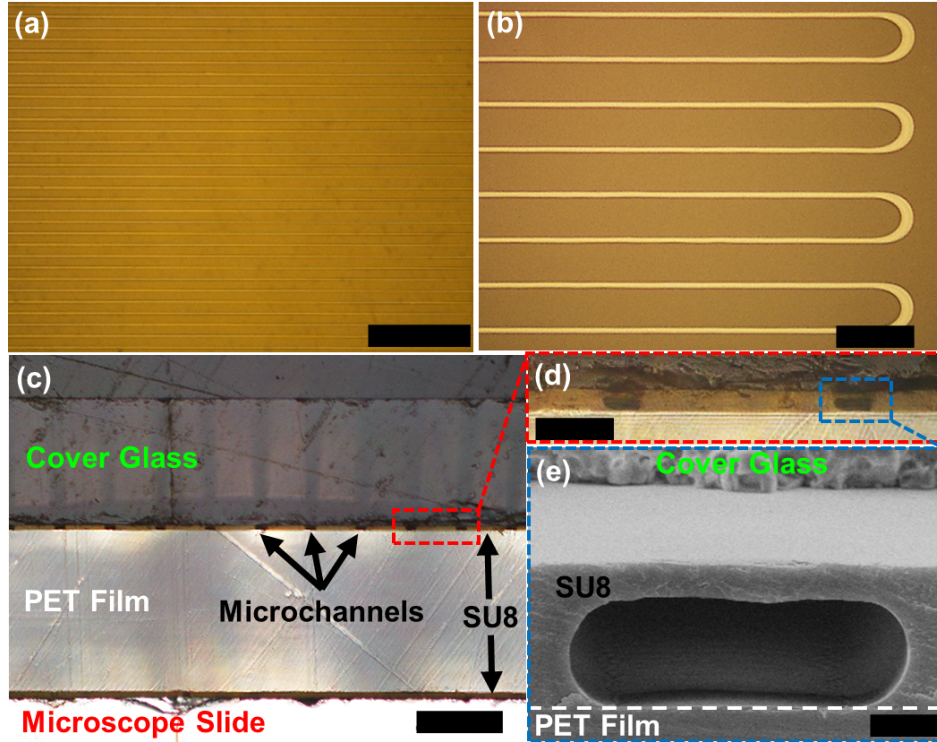


Figure 21: (a) An optical microscopy image showing the center of a serpentine microchannel about  $4\ \mu\text{m}$  and  $15\ \mu\text{m}$  in height and width, respectively, sealed by a  $2\ \mu\text{m}$ -SU8-covered PET and reinforced by a  $7\ \mu\text{m}$ -SU8-covered microscope slide, together with (b) a higher magnification image of the U-turns. (c) An optical microscopy image showing the cross-section of the channels, as well as (d) a higher magnification (100X) optical microscopy image, and (e) a (7.00k) SEM image of a single channel. The SU8 adhesive layer on the PET film has flown towards the sidewalls during the sealing step due to the capillary action. The dashed line has been added to the SEM image to more clearly specify the bonding interface. Scale bars:  $500\ \mu\text{m}$  in (a),  $100\ \mu\text{m}$  in (b) and (c),  $20\ \mu\text{m}$  in (d), and  $3\ \mu\text{m}$  in (e).

it is very difficult to obtain a conformal and leak-free sealing using a rigid substrate such as glass, silicon, etc., which is coated with such a thin adhesive layer. This fact can be clearly realized by comparing the two bonding outcomes after the sealing, and the reinforcement steps. In the sealing step, the bonding is done between a rigid substrate and a flexible film, while in the reinforcement step, neither of the substrates is flexible. As shown in Appendix, there is almost no air bubble trapped between the PET film and the glass slide with the microchannel sidewalls. However, there are some air bubbles trapped between the PET film and the glass substrate during the bonding reinforcement step. It should be noted that the bubbles, which are formed during the bonding reinforcement step, do not adversely affect the microchannels, since the channels have already been cured and sealed before the commencement of the bonding reinforcement step. More discussion can be found

in Appendix.

SU8 reflow is inevitable for any bonding technique that uses an uncured SU8 adhesive layer at a temperature above the SU8 glass transition temperature. However, the influential parameters such as the baking times and bonding temperature can be optimized to reduce the SU8 reflow [100, 102, 109]. In order to investigate the SU8 reflow during the sealing step, the chip has been diced. After polishing, the cross-section has been examined under the optical microscope as well as the SEM (Fig. 21 (c–e)). It can be perceived that the shallow microchannels with small patterns can be fabricated without the channel clogging problem.

Moreover, the cross-section SEM image, shown in Fig. 21 (e), reveals that the SU8 adhesive layer on the PET film has flown towards the hydrophobic sidewalls during the sealing step due to the capillary action. As a result, the channel height increases to about  $4\ \mu\text{m}$  in the center of channel, which is about  $2\ \mu\text{m}$  larger than that dictated by the spin coating process of the lateral sidewalls (*i.e.*  $2.1\ \mu\text{m}$ ). The SU8 reflow also causes a shrinkage in the microchannels width, that based on our experiments, can be as large as about  $5\text{--}10\ \mu\text{m}$  (*i.e.*  $2.5\text{--}5\ \mu\text{m}$  for each sidewall in average). In this work, this amount of SU8 reflow is considered to be acceptably small for the shallow microchannels.

Furthermore, as shown in Appendix, the microchannel width shrinkage becomes less noticeable for a larger channel ( $100\ \mu\text{m}$  in width and  $30\ \mu\text{m}$  in height), since the capillary action decreases for channels with larger cross-section dimensions. The small thickness of the SU8 adhesive layer in comparison with the channel dimensions makes the SU8 reflow even less important. As explained in Appendix, the oxygen plasma treatment of the SU8 sidewalls significantly impedes the SU8 reflow by providing a hydrophilic barrier against the flow of the hydrophobic SU8 adhesive layer on the PET film. It is shown that the channel dimensions remain the same as dictated by photo-lithography in case the sidewalls are treated with oxygen plasma (*i.e.* hydrophilic lateral sidewalls), since there is no reflow of the hydrophobic SU8 towards the hydrophilic sidewalls, while the SU8 reflow in absence of the oxygen plasma treatment of the sidewalls (*i.e.* hydrophobic lateral sidewalls) causes an about 50%–reduction in the thickness of the adhesive layer in the middle of channel.

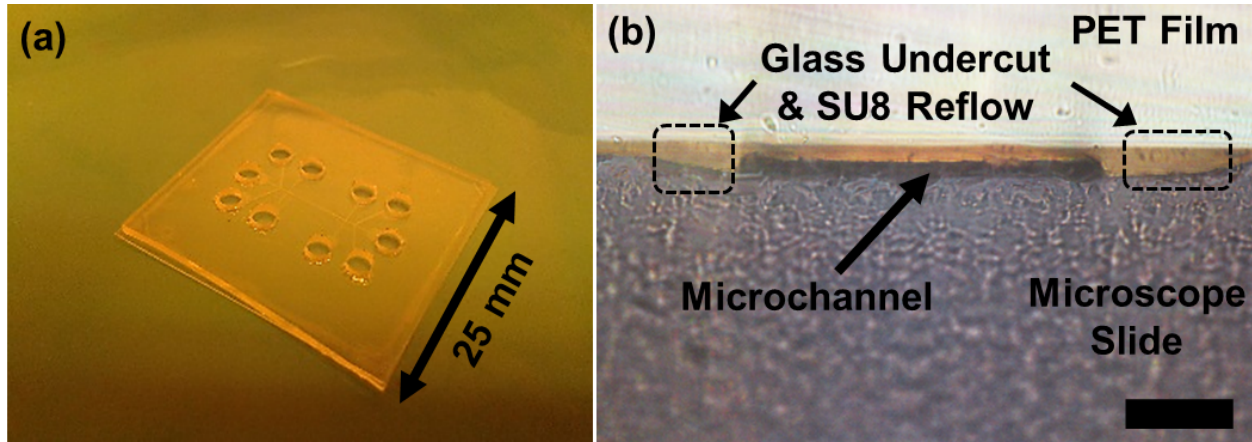


Figure 22: (a) A camera picture as well as (b) a cross-section optical microscopy image of a microfluidic channel about  $3 \mu\text{m}$  in height fabricated through the wet etching of the glass following by the sealing step using a PET film coated with a  $2 \mu\text{m}$ -thick SU8 layer without reinforcement. Scale bar =  $20 \mu\text{m}$  in (b).

In order to demonstrate the compatibility of the developed SU8 bonding paradigm with the glass-etching-based microchannel fabrication techniques, the sidewalls of a shallow microfluidic channel about  $3 \mu\text{m}$  in height, are fabricated through the glass wet etching. The microchannel sidewalls are then sealed using a PET film coated with a  $2 \mu\text{m}$ -thick SU8 layer, as shown in Fig. 22. A void-free sealing can be seen in Fig. 22 (a). In addition, the cross-section image of the channel in Fig. 22 (b) shows an undercut about  $10 \mu\text{m}$  wide due to the isotropic nature of the etching process, as well as the SU8 reflow that fills the undercut volume, which results in a rectangular cross-section with round corners.

The flexible PET film makes the bubble removal process much more efficient, enabling the fabrication of shallow and long channels (Appendix) using a thin SU8 adhesive layer. On the other hand, the fact that the PET film is sturdy enough not to sag noticeably under its weight can be utilized to fabricate shallow microchannels with ultra-low height-to-width aspect ratios by not applying pressure on the channel area of the film during the sealing step. As an example, a microchannel  $2 \mu\text{m}$  in height,  $2 \text{mm}$  in width in its widest portion, and  $90 \mu\text{m}$  in width in its narrowest portion is shown in Fig. 23. Figure 23 (a) demonstrates that because of the flexibility of the PET film a conformal contact can be achieved using a  $2 \mu\text{m}$ -thick-SU8 adhesive layer, despite the fact that minor defects might exist at the bonding interface due to the trapped air bubbles, small particles, etc. Such defects could hinder

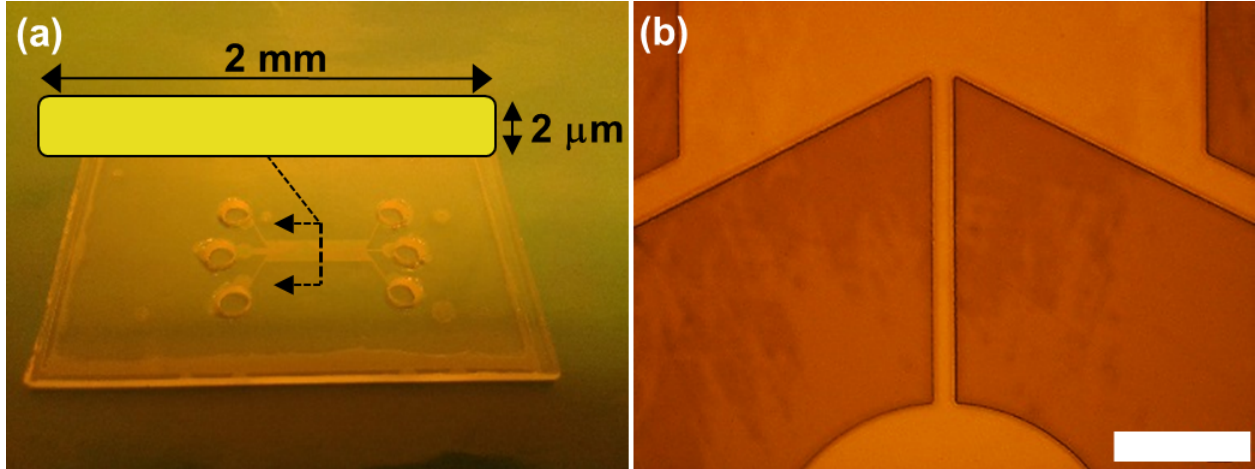


Figure 23: (a) A camera picture as well as (b) an optical microscopy image of a microfluidic channel  $2\ \mu\text{m}$  in height,  $2\ \text{mm}$  in width in its widest portion, and  $90\ \mu\text{m}$  in width in its narrowest portion, sealed by a  $2\ \mu\text{m}$ -SU8-coated PET film without reinforcement. Since a clear cross-section image cannot be taken for such an ultra-low aspect ratio channel, a schematic of the cross-section is shown in (a) as well. Scale bar =  $500\ \mu\text{m}$  in (b).

obtaining a leak-free sealing using a rigid substrate such as glass, silicon, etc., unless a thick enough adhesive layer was used, which would also make the shallow microchannel vulnerable to clogging due to the SU8 reflow during the sealing step. An optical microscopy image of the void-free and conformal sealing is also shown in Fig. 23 (b) without any channel clogging at the narrow or wide parts of the device. Such a shallow microchannel with an ultra-low aspect ratio of  $10^{-3}$  is extremely challenging, if possible, to be fabricated via PDMS-based soft lithography [132–136], or the available SU8 bonding techniques. In particular, in the bonding approaches relying on the lamination [103, 130], the uniform pressure applied by the lamination device during the bonding process causes the sagging of the cover substrate, which can easily result in the channel clogging for the wide and shallow microchannels. For example, by using a lamination-based bonding technique, Wangler *et al.* [130] fabricated a microchannel of  $45\ \mu\text{m}$  in height and  $2\ \text{mm}$  in width, that to the best of the author’s knowledge, shows the lowest height-to-width ratio ( $2.25 \times 10^{-2}$ ) in the microfluidics context, yet is still more than one order of magnitude larger than that presented in this work.

After demonstrating the sealing and reinforcement of microchannels with widths ranging from  $15\ \mu\text{m}$  to  $2\ \text{mm}$ , heights from  $2\ \mu\text{m}$  to  $30\ \mu\text{m}$ , and lengths from  $5\ \text{mm}$  to  $6\ \text{cm}$ , it

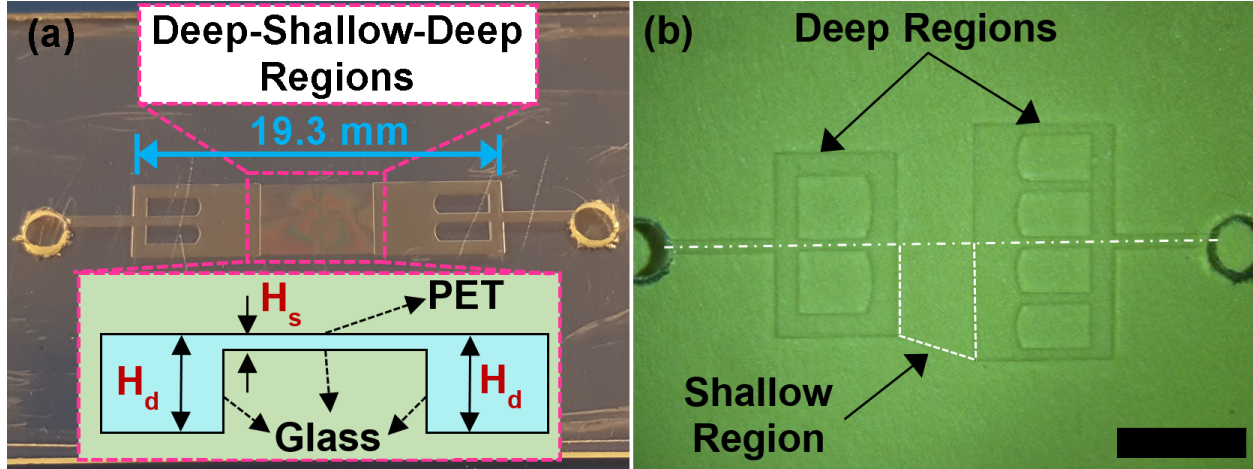


Figure 24: (a) A camera picture showing a microchannel consisting of deep (height =  $77 \mu\text{m}$ ) and shallow (height =  $2 \mu\text{m}$ ) regions, together with the (inset) schematic side-view of the microchannel, where  $H_d = 77 \mu\text{m}$  and  $H_s = 2 \mu\text{m}$ , as well as (b) a microscope image of another double-height microchannel, which is  $32 \mu\text{m}$  and  $7 \mu\text{m}$  high in deep and shallow regions, respectively. The channel is symmetric with respect to the horizontal dash-dotted line. The edges of the lower half of the shallow region are also shown with the dashed lines. Both of the microchannels in (a) and (b) are sealed using the  $2 \mu\text{m}$ -thick-SU8-coated PET film without reinforcement. The scale bar =  $5 \text{mm}$  in (b).

should be noted that the sealing—and—reinforcement paradigm is still applicable to fabricate larger channels. In particular, one might utilize the optimized recipes developed by other researchers for spin coating highly uniform and much thicker SU8 layers [99], if the microchannels fully made of SU8 with larger heights are desired to be fabricated through the sealing—and—reinforcement paradigm. On the other hand, for the case that the microchannel sidewalls are made through the glass wet etching, there is no upper limit for the accessible microchannel height as long as the mask used for protecting the glass remains intact during the wet etching process. Since the etching process does not cause height non-uniformities on the protected areas, the thin SU8 layer-coated PET film can still be used for sealing the etched microchannel sidewalls with much larger heights.

### Multi-height deep–shallow microchannels

A camera picture showing a microchannel consisting of deep and shallow areas is presented in Fig. 24 (a). By using the fabrication process, which is explained earlier and illustrated in more detail in Appendix, the sidewalls of the microchannel are created through glass

etching. The microchannel height is  $77\ \mu\text{m}$  and  $2\ \mu\text{m}$  in the deep and shallow regions, respectively. The created sidewalls are then sealed using a  $2\ \mu\text{m}$ -thick-SU8-coated PET film. The shallow zone in this microchannel is  $6\ \text{mm} \times 4\ \text{mm}$ . It can be perceived that the center of the microchannel shows a light reflection different from that of the other areas, because of having a different depth, and consequently a distinct light-sample interaction. The ultra-low height-to-width ratio ( $5 \times 10^{-4}$ ) for the shallow region ( $2\ \mu\text{m}:4\ \text{mm}$ ) is about two orders of magnitude smaller than the lowest aspect ratio ( $2.25 \times 10^{-2}$ ) that the author found for the microchannels in the literature [130]. It should be noted that we have been able to fabricate the rectangular channels with the smaller side as large as  $8\ \text{mm}$ , and with a height as small as about  $2\ \mu\text{m}$ , *i.e.* the height-to-width ratio of  $2.5 \times 10^{-4}$ , but the yield of the fabrication technique decreases noticeably for channels larger than  $6\ \text{mm} \times 6\ \text{mm}$ , due to the higher risk of the PET film sagging and the consequent channel (partial) clogging.

The three key aspects of the proposed SU8 bonding paradigm allowing us to fabricate microchannels with the ultra-low aspect ratios are (1) the PET film’s flexibility, achieving a conformal sealing even by using a thin adhesive layer, while the rigid substrates such as glass, silicon, etc., necessitate using the thicker adhesive layers to accomplish a conformal sealing, which increases the risk of channel clogging, (2) the line-by-line bubble removal process, that allows applying different levels of the pressure selectively on various areas of the channel with no pressure on the wide areas, prone to be clogged due to the PET film’s potential sagging, and (3) the PET film’s sturdiness, which helps to avoid its significant sagging under its weight. As another demonstration, the microscope image of a microfluidic device consisting of deep ( $32\ \mu\text{m}$ ) and shallow ( $7\ \mu\text{m}$ ) microchannels are shown in Fig. 24 (b).

### **Pressure-drop vs. flow rate and bonding strength tests**

In this section, the bonding strength of the proposed two-step sealing-and-reinforcement paradigm, together with the potential deformation of the flexible PET film and its effects on the volumetric flow rate passing through the microchannels with and without reinforcement

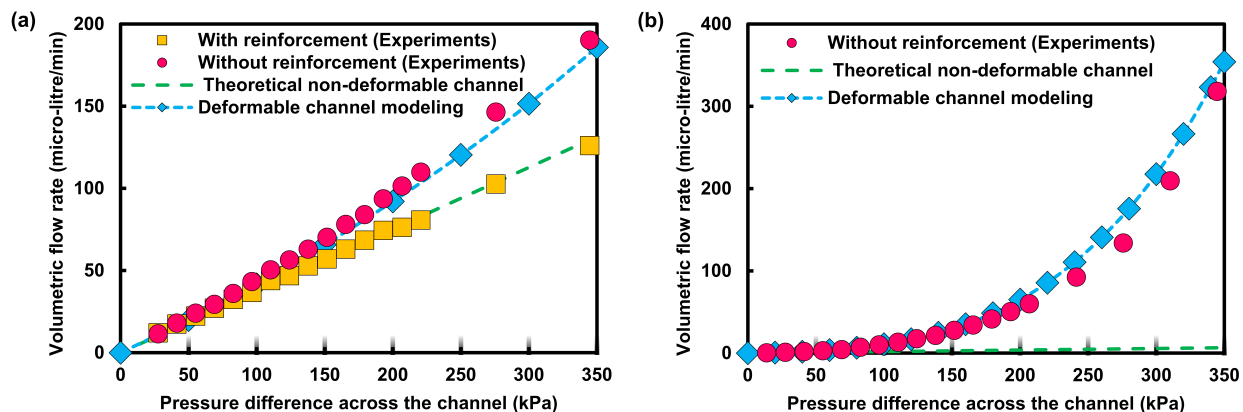


Figure 25: (a) The DI water volumetric flow rate through a straight channel  $7.3 \mu\text{m}$ ,  $1.55 \text{ mm}$ , and  $8 \text{ mm}$  in height, width, and length, respectively, sealed using a PET film coated with a  $7 \mu\text{m}$ -thick SU8 layer with and without reinforcement, as a function of pressure difference across the channel in comparison with the theoretical results for a non-deformable channel with the same dimensions [18] (Eqs. 2 and 4), and the modeling for the deformable low aspect ratio channel. (b) The DI water volumetric flow rate through a straight channel  $2.2 \mu\text{m}$ ,  $2.5 \text{ mm}$ , and  $7 \text{ mm}$  in height, width, and length, respectively, sealed using a PET film coated with a  $2 \mu\text{m}$ -thick SU8 layer without reinforcement in comparison with the theoretical results [18] for a non-deformable channel with the same dimensions, and the modeling for the deformable low aspect ratio microchannel.

is investigated by using the experimental, theoretical, and numerical simulation tools. The two approaches of SU8 photo-lithography and glass wet etching are used to establish the pattern of the microchannel sidewalls.

#### PET film deformation and its effects on volumetric flow rate

Two microchannel geometries are studied here: Microchannel A, which is  $7.3 \mu\text{m}$ ,  $1.55 \text{ mm}$ , and  $8 \text{ mm}$  in height, width, and length, respectively, and Microchannel B, which is  $2.2 \mu\text{m}$ ,  $2.5 \text{ mm}$ , and  $7 \text{ mm}$  in height, width, and length, respectively. The variation of the volumetric flow rate through Microchannel A with and without reinforcement, is shown in Fig. 25 (a) as a function of the pressure difference across the channel. The theoretical results for a non-deformable channel with the same dimensions, as well as those of the described model for the deformable microchannel are also presented. As shown, the volumetric flow rate–pressure characteristic curve related to the microchannel with reinforcement is in good agreement with the theoretical results for a non-deformable channel. On the other hand, the microchannel without reinforcement shows more deviations from the linear behavior of the non-deformable

channel as larger pressure differences are applied across the channel because of the PET film deformation. It can be seen that this behavior is acceptably predicted using the described model for the low-aspect-ratio microchannels with a deformable ceiling.

It should be noted that the term  $H^3$  in Eq. 2 intensifies the dependency of the volumetric flow rate upon the PET film deformation. Furthermore, the PET film deformation, yet small, becomes comparable with the shallow microchannel's height under high enough pressure levels, as a result of which the volumetric flow rate–pressure characteristic curve noticeably deviates from that of a non-deformable channel with the same dimensions. This fact is reflected in Fig. 25 (b), where the variation of the volumetric flow rate through Microchannel B is presented. A significantly larger volumetric flow rate through the deformable channel can be seen in comparison with that expected from the theory for a non-deformable channel with the same dimensions. At 345 kPa, the microchannel without reinforcement delivers a volumetric flow rate of 318  $\mu\text{l}/\text{min}$ , which is more than 40 times larger than that of a non-deformable microchannel with the same dimensions (6.55  $\mu\text{l}/\text{min}$ ).

Displacement contours of the PET film obtained from the structural mechanics modeling at the pressure difference of 345 kPa across the two investigated microchannels without reinforcement are shown in Figs. 26 (a) and (b). The displacement profile of the PET film in the middle of the microchannel B is also shown in Fig. 26 (c) for different pressures. The analysis shows that under the pressure difference of 345 kPa across this microchannel, the maximum displacement of the PET film is about 24.1  $\mu\text{m}$ , 10.4  $\mu\text{m}$ , and 1.6  $\mu\text{m}$  at the inlet, mid-channel, and outlet sections, respectively. The average of the PET film deformation is also about 5.99  $\mu\text{m}$ , which is almost three times as large as the original microchannel height (2.2  $\mu\text{m}$ ). This is the reason that this deformable microchannel can deliver a much larger volumetric flow rate than that of the non-deformable microchannel with the same dimensions (Fig. 25 (b)). Such an ultra-low aspect ratio microchannel with deformable ceiling might find applications in the relevant areas such as the microfluidic valves [144], micromixers [72, 73], fluidic capacitors [75], fluidic variable resistors [76], selectively control of the species transport [145], etc.

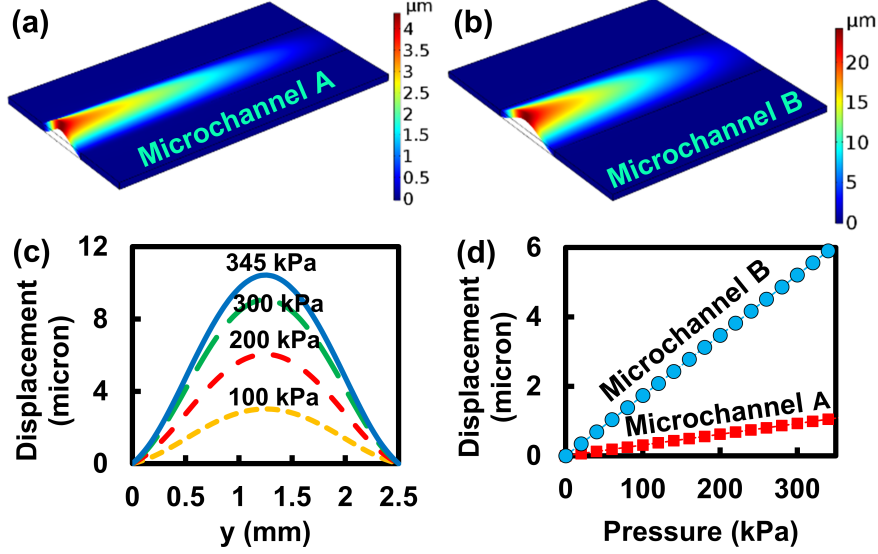


Figure 26: The displacement contours of the PET film under the pressure difference of 345 kPa across two microchannels (a) A, and (b) B. (c) The displacement profile of the PET film in the middle of Microchannel B at various pressures. (d) The average PET film’s displacement as a function of the pressure difference across the microchannels. Microchannel A is 8 mm, 1.55 mm, and 7.3  $\mu\text{m}$  in length, width, and height, respectively, while Microchannel B is 7 mm, 2.5 mm, and 2.2  $\mu\text{m}$  in length, width, and height, respectively.

Furthermore, the average displacements of the PET film under various pressure differences across the two studied microchannels are presented in Fig. 26 (d). It can be seen that the average deflection is linearly dependent upon the pressure difference across the channels due to the linear elasticity framework that has been used for the structural mechanics analysis in this work. Because of the assumption of the linear elastic behavior, this analysis is valid only for the infinitesimal strains or small deformations. It is worth mentioning that the concept of *small strains* is relative. For example, in the case of some of the traditional metals, by the time the strain falls within the range of  $10^{-4}$  to  $10^{-3}$ , the metal has already started deviating from the elastic behavior [146]. This, however, does not mean that a larger strain such as 0.01 is universally such a very large strain that the linearized theory of elasticity is inapplicable. The strain needs to be considered in comparison with the limit of the elastic range. In case of the PET film, the yield strength, *i.e.* the stress needed to induce a specified amount of permanent strain, typically 0.2%, is about 30 MPa at room temperature [147]. Since the Young’s modulus of the PET film is about 3 GPa, the strains up to about 0.01 can be still considered small enough for the linear elasticity framework to be reliably applicable.

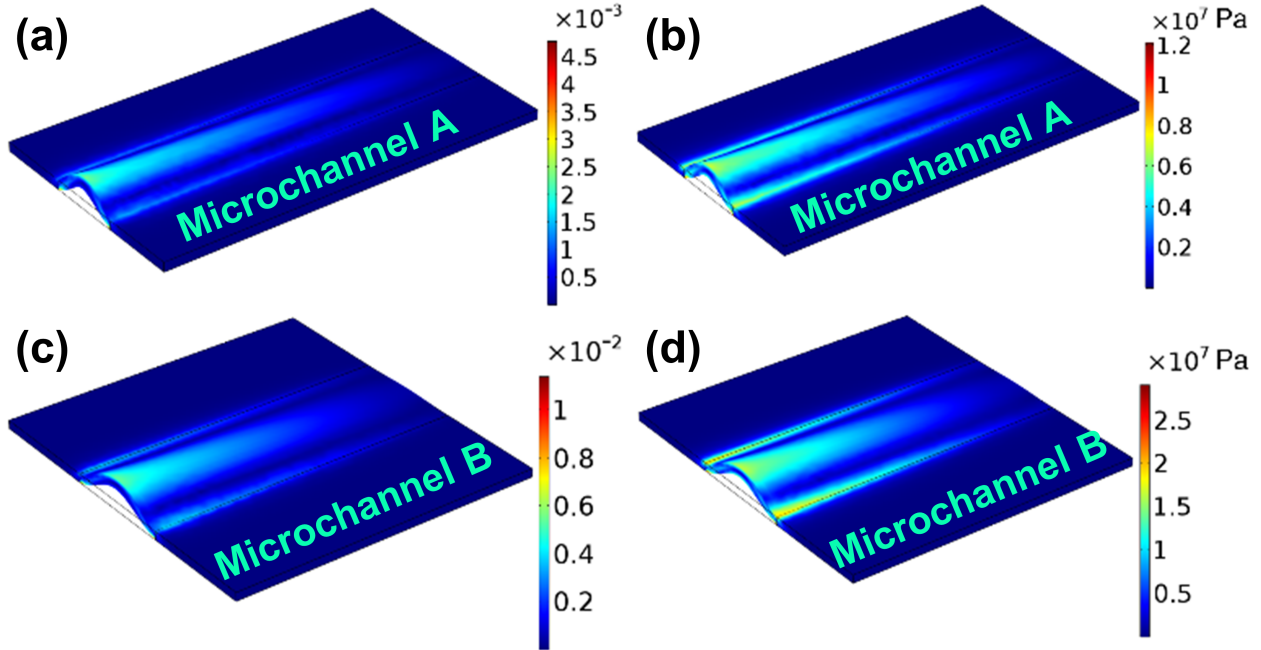


Figure 27: The contours of the PET film’s (a) first principal strain, and (b) von Mises stress obtained from the fluidic-structural mechanics modeling of Microchannel A under the pressure difference of 345 kPa across the channel, together with the PET film’s (c) first principal strain, and (d) von Mises stress for Microchannel B under the same pressure. Microchannel A is 8 mm, 1.55 mm, and 7.3  $\mu\text{m}$  in length, width, and height, respectively, while Microchannel B is 7 mm, 2.5 mm, and 2.2  $\mu\text{m}$  in length, width, and height, respectively.

The obtained first principal strain and von Mises stress contours of the PET film are presented in Fig. 27 for the two investigated microchannels A and B under the pressure difference of 345 kPa across the channels. It can be seen that the narrower microchannel (A) has smaller strains and von Mises stresses in the PET film, while the maximum von Mises stress in the wider microchannel (B) is about 28 MPa, which is close to the yield strength. Hence, the wider microchannel operates close to the limit of the elastic range under the maximum pressure difference applied to the channel in this work (345 kPa). As a result, the structural mechanics analysis of the PET film based on the linear elasticity, and consequently the extracted average displacement of the PET film for the purpose of modeling the volumetric flow rate are reliable for the two investigated microchannels under the pressure differences up to 345 kPa. However, the plastic and permanent deformations of the PET film might need to be taken into account for wider microchannels or larger pressures.

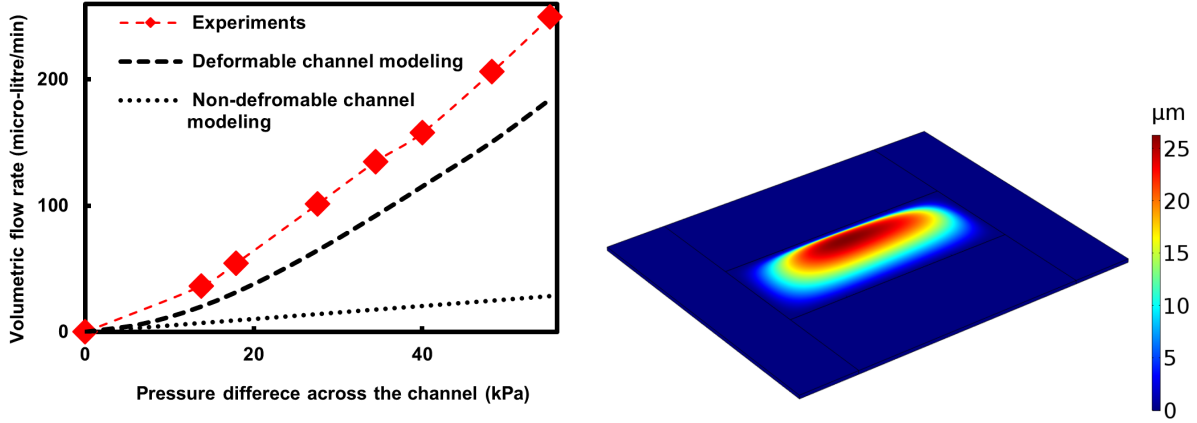


Figure 28: (left) The volumetric flow rate through the multi-height deep–shallow microchannel shown in Fig. 24, sealed using a PET film coated with a  $2\ \mu\text{m}$ -thick SU8 layer, without reinforcement, as a function of pressure difference across the channel in comparison with the modeling results for the deformable and non-deformable channels with the same dimensions. (right) The displacement contour of the PET film at the pressure difference of 55 kPa across the multi-height deep–shallow microchannel, obtained by using the coupled zero-dimensional-fluid-mechanics—three-dimensional-solid-mechanics modeling.

In the next step, the volumetric flow rate is studied at various pressure differences across the double-height deep–shallow microchannel, which is sealed using a PET film coated with a  $2\ \mu\text{m}$ -thick SU8 layer, without reinforcement. The geometry of the microchannel is similar to that shown in Fig. 24 with the difference that the deep and shallow regions for the current device are  $26\ \mu\text{m}$  and  $5\ \mu\text{m}$ , respectively. The experimental results are shown in Fig. 28 (left) in comparison with those of the modeling for the deformable and non-deformable channels with the same dimensions. It can be seen that the discrepancy between the experimental results and those of the modeling is about 25%, which is attributed to the following facts:

(1) The fluid flow deviates from the laminar regime, due to the large displacement of the PET film. The displacement contour of the PET film at the pressure difference of 55 kPa across the microchannel, obtained by using the coupled zero-dimensional-fluid-mechanics—three-dimensional-solid-mechanics modeling, is shown in Fig. 28 (right). Because of the large PET film’s deformation, the rather large Reynolds number of  $\sim 11$  is produced, while under the same pressure difference, the Reynolds number is about 0.4 and 0.04 for Microchannels A and B shown in Fig. 26, respectively. The deviation from the laminar flow makes the relationship utilized for the hydrodynamic resistance, Eq. 8, less accurate.

Table 6: The maximum allowed pressure difference across the 400  $\mu m$  wide microchannels for different fabrication approaches investigated in this work.

Approach	Without piranha treatment		With piranha treatment	
	Without reinforcement	With reinforcement	Without reinforcement	With reinforcement
SU8 photo-lithography	$\sim 80$ kPa	$> 345$ kPa	$> 345$ kPa	$> 345$ kPa
Soda lime glass wet etching	$\sim 30$ kPa	$> 345$ kPa	$> 345$ kPa	$> 345$ kPa

(2) The large inertia forces cause the formation of vortices close to the steps, *i.e.* where the deep and shallow regions of the channel meet, which necessitates more advanced theoretical relationships or empirical correlations for a more accurate approximation of the hydrodynamic resistances.

(3) The pressure variation is not necessarily linear through the ultra-low-aspect-ratio microchannels. This item will be investigated more later.

Finally, it should be noted that our experiments show a linear variation of the volumetric flow rate (*i.e.* no dependency on the PET film deformation) as a function of the pressure difference across a microchannel without reinforcement, which is 300  $\mu m$  and 2.5  $\mu m$  in width and height, respectively (results not shown here). The structural mechanics analysis also supports this observation, since the PET film’s maximum displacement under the pressure difference of 345 kPa across the channel is almost 20  $nm$ , which is two orders of magnitude smaller than the microchannel height.

### Bonding strength

In order to assess the bonding strength of the proposed SU8 bonding paradigm, the microchannels of about 400  $\mu m$  in width are fabricated through two approaches of SU8 photolithography and glass etching. The maximum permissible pressure difference across the channels are compared in Table 6 for different fabrication approaches. According to our observations, the maximum permissible pressure difference across the channels is rather low without piranha treatment of the glass substrate and reinforcement step, while adding either the piranha treatment or the bonding reinforcement step to the process flow enables

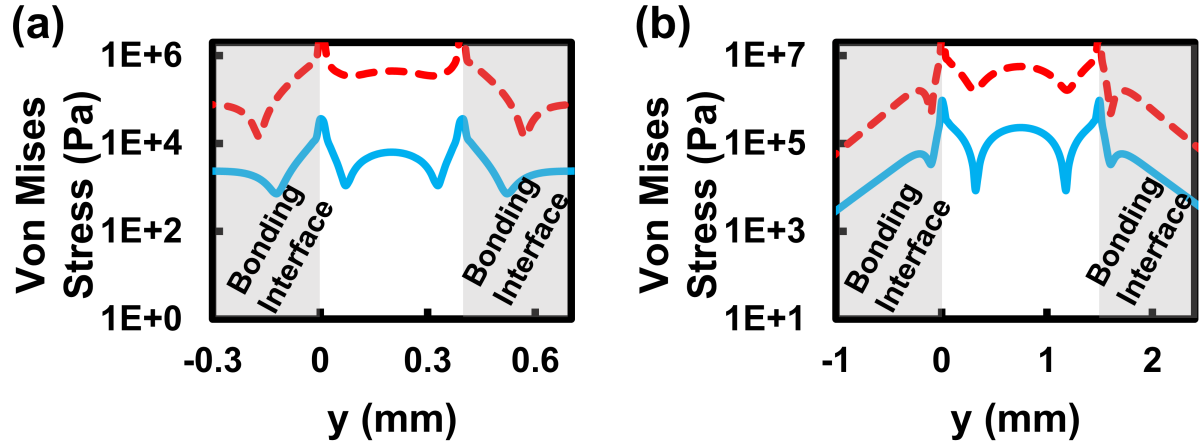


Figure 29: The von Mises stress profiles within the PET films sealing the 1 *cm*-long microchannels of (a) 400  $\mu\text{m}$  and (b) 1.55 *mm* in width, across the inlet (dashed lines) and outlet (continuous lines) sections. The pressure difference across the channels is 345 kPa.

the devices to operate safely under the pressure of 345 kPa. The reason of such significant improvement using the piranha treatment of the glass or the bonding reinforcement is that the former improves the adhesion between the glass substrate and the SU8 layer through decreasing the surface energy [101, 109], while the latter suppresses the PET film deformations and consequently decreases the maximum von Mises and shear stresses at the bonding interface. A more quantitative account on the maximum bonding strength cannot be made experimentally because of the connection failure at 345 kPa, yet a deeper insight can be obtained using the previously described fluid-structural mechanics modeling.

The von Mises stress profiles within the PET films sealing the 1 *cm*-long microchannels of 400  $\mu\text{m}$  and 1.55 *mm* in width, under the pressure difference of 345 kPa, are presented in Fig. 29. It can be perceived that the maximum von Mises stress is formed close to the edges of the bonding interfaces at the inlet section. Since the pressure decreases along the channel, the PET film experiences the lower von Mises stresses as it gets farther away from the inlet section. Furthermore, the modeling shows that the maximum von Mises stress within the PET films is one and two orders of magnitude larger than the pressure difference applied across the 400  $\mu\text{m}$  and 1.55 *mm* wide microchannels, respectively. The reason is that the PET film deformations and consequently its von Mises stress increase with the microchannel

width. This finding explains how the bonding reinforcement step significantly increases the maximum pressure difference that can be applied across the microchannels, as shown in Table 6. The bonding reinforcement step keeps the maximum stresses in the same order of magnitude as that of the pressure difference applied across the channel through quelling the PET film deformations.

Microchannels of 5 *mm* in width, with and without reinforcement, are fabricated through glass etching followed by the sealing step using a 2  $\mu\text{m}$ -thick-SU8-coated PET film after the piranha treatment of the glass substrate. The pressure drop vs. flow rate experiments show that the pressure differences as large as 345 kPa can be safely applied across the reinforced microchannel. However, in absence of the bonding reinforcement, the pressure difference across the channel can be as high as about 55 kPa, above which the SU8 bonding fails. The modeling shows that the maximum von Mises stress is about 8.4 MPa when the bonding fails. Thus, we predict that the proposed SU8 bonding paradigm is strong enough for the reinforced microchannels, made through the glass wet etching process, to safely operate under the pressure levels up to about 8.4 MPa. This prediction is in good agreement with the reported values for the SU8-glass bonding strength [99, 109]. A similar analysis leads us to the conclusion that the bonding strength is even larger (above 25 MPa) for the microchannels made through the SU8 photo-lithography approach, with a hard-baked thin SU8 layer between the piranha-treated glass substrate and the SU8 patterns of the channel sidewalls. The reasons are that (1) the adhesion of the SU8 interfaces is greater than that of the SU8-glass substrate [99, 101], and (2) a thin SU8 layer ( $O(1 \mu\text{m})$ ), which is spun on the glass substrate, cured, and hard-baked at a high enough temperature ( $\sim 170^\circ\text{C}$ ) shows a much stronger adhesion with the glass surface in comparison (a) with the adhesion between the thick SU8 layers and the glass substrate [101, 148], as well as (b) with the adhesion of the SU8 layers that are brought in contact with the glass substrate at a low temperature and pressure, similar to what happens when the microchannel sidewalls, etched in a glass substrate, are sealed using a SU8-coated PET film. The strong adhesion of the SU8/SU8 and thin-SU8/piranha-treated-glass interfaces, therefore, causes the SU8-photo-

lithography-based approach to deliver a bonding strength noticeably higher than that of the glass-etching-based technique.

### **Droplet generation**

In order to generate oil-in-water droplets, the microfluidic chips with the innermost surfaces fully made of SU8 with the same geometry as shown in Fig. 23 are utilized. After rendering the SU8 innermost sidewalls a hydrophilic property using a post-bonding chemical treatment with CAN, as described earlier, the dispersed phase is injected using a syringe pump through the central channel shown in Fig. 23 (b), which is about  $90\ \mu\text{m}$  in width, while the continuous phase is injected through both the lateral  $170\ \mu\text{m}$ -wide channels using another syringe pump. The underlying mechanism of the droplet formation is based on the instability of the oil phase at a sudden expansion in the geometry, which has already been demonstrated [149, 150]. In this work, however, the droplets are formed at the interface of the microchannel and the central outlet's large reservoir ( $2\ \text{mm}$  in diameter), which makes the fabrication process much more straightforward, since the expansion in the geometry is created simply at the interface of the microchannel and the drilled via-holes, instead of using more complex fabrication techniques to create a step-shaped expansion. The generated droplets are then collected from the outlets. The generated droplets using the microchannels  $6\ \mu\text{m}$  and  $15\ \mu\text{m}$  in height with the continuous phase to the dispersed phase volumetric flow rate ratio equal to  $26\ \mu\text{l}/\text{min} : 14\ \mu\text{l}/\text{min}$  and  $90\ \mu\text{l}/\text{min} : 1\ \mu\text{l}/\text{min}$  are shown in Fig. 30 (a) and (b), respectively. More than 90% of the generated droplets have a diameter in the range of  $13 \pm 2\ \mu\text{m}$  and  $47 \pm 3\ \mu\text{m}$  for the microchannels  $6\ \mu\text{m}$  and  $15\ \mu\text{m}$  in height, respectively.

### **Conclusion**

In this work, a two-step sealing—and—reinforcement SU8 bonding paradigm was proposed. In the first step, a conformal and leakage-free sealing is created for the microchannel sidewalls using a PET film coated with a thin SU8 layer, while in the second step, the PET film is reinforced using a SU8-coated rigid glass substrate. The key components of the proposed

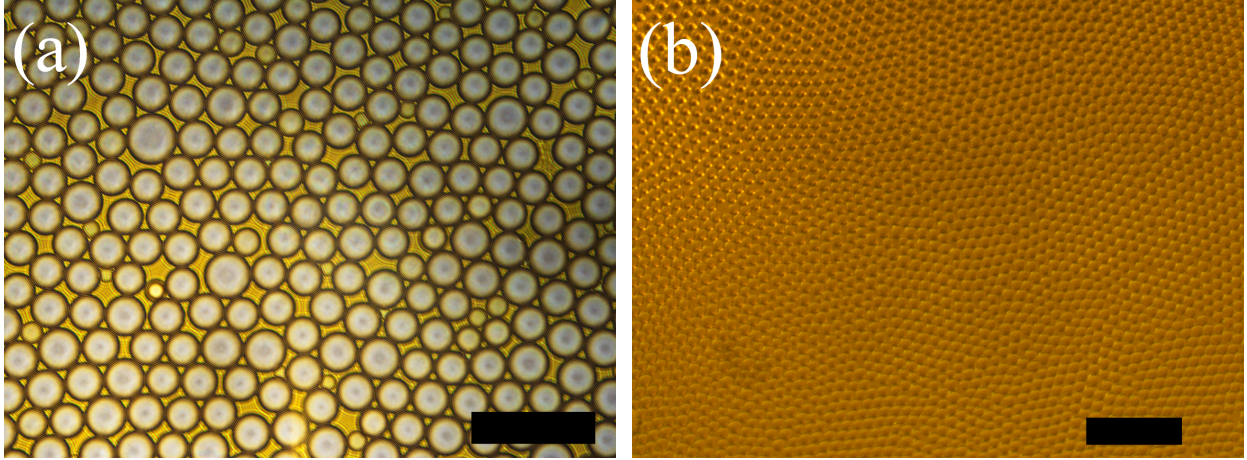


Figure 30: The oil-in-water droplets generated using a microfluidic device about (a)  $6\ \mu\text{m}$  and (b)  $15\ \mu\text{m}$  in height. The continuous phase to the dispersed phase volumetric flow rate ratio is  $26\ \mu\text{l}/\text{min} : 14\ \mu\text{l}/\text{min}$  and  $90\ \mu\text{l}/\text{min} : 1\ \mu\text{l}/\text{min}$  for (a) and (b), respectively. Scale bars are  $50\ \mu\text{m}$  and  $500\ \mu\text{m}$  in (a) and (b), respectively.

bonding paradigm can be summarized as follows: 1) a thin SU8 adhesive layer that alleviates the channel clogging difficulties due to the SU8 reflow, enabling the sealing of the small microchannels, 2) the PET film's flexibility that allows achieving a conformal sealing on a large area even by using a thin adhesive layer, 3) the PET film's sturdiness that enables the sealing of the ultra-low aspect ratio microchannels (e.g.  $2\ \mu\text{m}$  in height and  $6\ \text{mm}$  in width) without sagging and channel clogging, and 4) the reinforcement of the PET film, which suppresses the PET film deformations and strengthens the bonding quality. The developed bonding paradigm was successfully implemented to seal the microchannel sidewalls that were made through 1) the SU8 photo-lithography to fabricate microchannels with the innermost surfaces fully made of SU8, and 2) the glass wet etching. Furthermore, the fabrication of the multi-height deep-shallow microchannel sidewalls, and their sealing using a SU8-coated PET film were demonstrated. The oil-in-water droplets were generated using microfluidic devices with the innermost surfaces fully made of SU8, after rendering the SU8 sidewalls to be hydrophilic using a post-bonding treatment with Ceric Ammonium Nitrate. Two microchannels with different heights of  $6\ \mu\text{m}$  and  $15\ \mu\text{m}$  were used to generate the 13- and 47-micron droplets. The proposed SU8 bonding paradigm provides a high quality bonding, with the capability of fabricating shallow microchannels with ultra-low aspect ratios, or with

small patterns on large areas. This technique is inexpensive, since it does not need complicated instruments such as wafer bonding machine and laminate device. The aforementioned advantages together with its compatibility with different fabrication methods such as SU8 photo-lithography and glass wet etching for making the microchannel sidewalls are some of the indications that the two-step sealing-and-reinforcement SU8 bonding paradigm will provide more capabilities to the rapidly growing MEMS and LOC areas.

# Chapter 3: Low-Reynolds-number incompressible fluid flow through straight deformable microchannels

## Questions

The main questions of this research are enumerated in the following.

- Can a master curve be found for volumetric flow rate versus pressure drop of arbitrary low-Reynolds-number incompressible flows of Newtonian fluids through deformable straight channels?
- What parameters can cause the characteristics of fluid flows through flexible microchannel to differ from those of the rigid counterpart? How important is each parameter?
- The pressure variation through the channel is unknown. How erroneous would the linear-pressure-variation assumption be for various channel geometries, membrane properties, pressure differences, etc?

## Motivations

Deformable microchannels are widely used by lab-on-a-chip and MEMS communities. However, it is difficult to find experimentally all the structural-fluid characteristics such as the membrane deflection, stress distribution, pressure variation through the channel, etc. On

the other hand, the three-dimensional modeling of the deformable microchannels is time consuming. These difficulties motivate us to develop a simpler and more intuitive framework to provide a deeper insight into the structural-fluid characteristic behavior of the fluid flow through the deformable microchannels by using a one-dimensional theoretical coupled solid-fluid mechanics modeling.

## Objectives

The main objective of this research is to obtain a deeper insight into the fluid-solid interactions as well as the effects of the different parameters on the structural-fluid characteristics of the fluid flow through the deformable microchannels with low aspect-ratios. A master curve is also expected to be found for flow rate vs. pressure drop, valid for any arbitrary pressure difference, channels dimensions, and membrane properties.

## Introduction

While the rapidly-growing microfluidics technology has already permeated through many aspects of the molecular and biological sciences, the emerging field of deformable microfluidics has been attracting an increasing attention during the last decade, enabling a variety of different applications such as developing fluidic circuits [75, 76], tunable optofluidic devices [68], size-tunable droplet generation [70, 151], particle/cell separation [15, 17, 152, 153], etc. Shallow microchannels with a low height-to-width ratio, on the other hand, are important for various bio-applications such as the label-free cell detection [20], immunoassays [13, 138], cell culturing [21], etc., where the underlying detection mechanism is based on the biospecies interaction with the innermost surface of the microchannel. Under these situations, the performance or detection limit can be improved by increasing the probability of interactions of the target species and the wall surfaces through decreasing the channel height and/or increasing the channel width.

Even though there are several experimental reports on the fluid-solid mechanics of a

fluid flow within a deformable shallow microchannel [154–160], measuring the velocity and pressure throughout the channel is still a serious challenge. The two-/three-dimensional mathematical models have been, therefore, used to better understand the pertinent physics [161,162]. For the mathematical modeling with the mutual fluid-solid interactions taken into account, the pressure, as a property from the fluid mechanics domain, affects the membrane deflection, as a parameter belonging to the solid mechanics domain. On the other hand, any change in the microchannel geometry can alter the pressure and the velocity fields throughout the microchannel. Hence, the solid and fluid aspects of this problem can be potentially highly coupled, which makes it hard, if not impossible, to present an analytical solution for the two-/three-dimensional models. The governing equations are, therefore, solved numerically, which can be very time consuming [162], particularly for the shallow microchannels with the ultra-low height-to-width-ratios because the grid size needs to be sufficiently small to capture the variations of the parameters across the channel’s small height as well as its large width and length.

One-dimensional modeling is considered as a fast and convenient tool for studying and designing the deformable microchannels. Gervais et al. [134] proposed a mathematical model for the rectangular microchannels with a thick deformable ceiling by means of the scale analysis. They experimentally corroborated the proposed model with a fitting parameter that led to the acceptable agreement between the experiments and the modeling. The fitting parameter is dependent on the channel geometry as well as the physical properties of the membrane and working fluid. Therefore, the model with the fitting parameters requires experimental results and cannot be widely used [19,157]. Relying on several assumptions including the parabolic shape for the deflection profile of the thin membrane wall, Raj and Sen [163] developed a one-dimensional model expressing the relationship between the volumetric flow rate and the pressure difference across the microchannel, without the need of the fitting parameters.

Christov *et.al.* [19] have more recently developed a one-dimensional coupled fluid-solid mechanics model using the lubrication theory. The main idea behind the model is to assume

each infinitesimal slice of the membrane (normal to the flow-wise direction) independently deflects under the corresponding local pressure of the working fluid within the microchannel. From the solid-mechanics point of view, an infinitesimal slice of the membrane is replaced by a wide beam, the deflection profile of which is determined as a function of the local pressure. This assumption necessitates the microchannel length to be much larger than its width, which is also a basic assumption for the lubrication theory. From the fluid-mechanics point of view, the lubrication theory suggests the Poiseuille flow to be locally valid for the equivalent channel with the same cross sectional area dictated by the deflection profile. This approximation provides a first-order ordinary differential equation, and from its solution, a relationship is extracted between the local pressure and the volumetric flow rate. Even though this framework was initially applied to the thin-plate-bending-dominated ceiling deformation, the same strategy has been implemented to other elastic deformation regimes of thick-plate-bending and stretching [162].

Christov *et.al.* [19] demonstrated the volumetric flow rate can be written as shown in Eq. 9, where  $Q$  is the flow rate,  $\Delta p$  is the pressure drop,  $W$  is the channel width,  $H_0$  is the undeformed channel height,  $L$  is the channel length,  $\mu$  refers to the fluid dynamic viscosity, and  $D = Et^3/12(1 - \nu^2)$ , in which  $t$ ,  $E$ , and  $\nu$  refer to the membrane thickness, modulus of elasticity, and Poisson's ratio, respectively:

$$Q = \frac{\Delta p W H_0^3}{12\mu L} \left[ 1 + \frac{1}{480} \frac{W^4}{DH_0} \Delta p + \frac{1}{362,880} \left( \frac{W^4}{DH_0} \right)^2 \Delta p^2 + \frac{1}{664,215,552} \left( \frac{W^4}{DH_0} \right)^3 \Delta p^3 \right] \quad (9)$$

By keeping only the leading-order elasticity contribution in Eq. 9, Christov *et.al.* [19] have summarized the key result for the bending-dominated deformation as:

$Q \approx \frac{\Delta p W H_0^3}{12\mu L} \left[ 1 + \frac{3}{160} \left( \frac{W}{t} \right)^3 \left( \frac{W}{H_0} \right) \left( \frac{\Delta p}{E} \right) \right]$ , assuming an incompressible material, *i.e.* the Poisson ratio  $\nu = 1/2$ . However, they have also pointed out in their paper that for a sufficiently large

value of  $\Delta p W^4 / D H_0$ , the higher-order terms become important in Eq. 9. To the best of our knowledge there is no literature studying the low-Reynolds-number flows under the large regimes of  $\Delta p W^4 / D H_0$  perhaps due to the lack of the fabrication method to create the ultra-low height-to-width-ratio deformable microchannels. Most of the deformable microchannels like those investigated in [162] show the relatively high Reynolds numbers and small values of  $\Delta p W^4 / D H_0$ . The large regimes of this parameter and its effects on the fluid-solid mechanics behavioral characteristics of the low-Reynolds-number fluid flows still remain unexplored.

In this chapter, we experimentally and mathematically investigate the *volumetric flow rate—pressure difference* relationship for the shallow deformable microchannels with ultra-low height-to-width-ratios. The microchannels of few millimeters in width and few microns in height are fabricated by modifying our previously reported fabrication protocol [164] to enable the membrane to freely deform, while the bonding reinforcement allows the high pressure differences to be applied. This fabrication method enables us to uncover new fluid-solid behavioral characteristics for the low-Reynolds-number flow, *i.e.*  $Re \sim O(10^{-2}—10^{+1})$ .

Our experimental results combined with the scale analysis of the model in [19] reveal that various distinct fluid-structural characteristics emerge under different regimes of the flexibility parameter. The flexibility parameter is a lumped variable in this work, reflecting the effects of different parameters such as the microchannel dimensions, membrane properties, and pressure difference across the channel. We show that introducing the flexibility parameter along with an appropriate form of dimensionless volumetric flow rate leads to a master curve, which is valid for any arbitrary shallow and long deformable microchannel. For the sufficiently small flexibility parameter, the characteristics match with those of the fluid flow through the rigid microchannels, while the *height-independent* characteristics emerge for the sufficiently large flexibility parameter. It is observed that the differences between the microchannel geometries result in the different flexibility parameters under the same pressure difference across the channels, while a significantly large change in the pressure difference across a fabricated microchannel with given geometry and membrane properties can alter the flexibility parameter scale from one characteristic regime to another. It is shown that

the microchannel width plays an important role in the fluid-solid characteristics; a relatively small difference in the microchannels widths ( $\sim 60\%$ ) can result in a one-order-of-magnitude difference in the flexibility parameters, which can potentially cause two distinct fluid-solid behavioral characteristics. Our further analysis provides a threshold for the flexibility parameter, by which the coupled and decoupled fluid-solid mechanics regimes are separated. Below this threshold, the pressure varies linearly through the microchannel, while the assumption of linear pressure variation becomes noticeably erroneous for the large flexibility parameters, since the coupled fluid-solid interactions enforce a non-linear pressure distribution within the channel.

The rest of this chapter is organized as follows. The mathematical aspect of this investigation is described first. The fabrication and experimental setup are then illustrated. Results and discussion are presented afterwards. We conclude with a brief summary at the end.

## Modeling

### Analytical one-dimensional coupled fluid-solid mechanics model

In this section, we revisit the one-dimensional coupled fluid-solid mechanics model in [19] for the fluid flow through the shallow microchannels. The governing equations and parameters are, however, rearranged to provide a better insight into the underlying physics.

The schematic presentation of a fluid flow through a straight microchannel with a deformable ceiling is shown in Fig. 31. The model in [19] is based on the lubrication theory, *i.e.*  $H_0 \ll W \ll L$ , where  $H_0$ ,  $W$ , and  $L$  refer to the microchannel original height with no membrane deformation, width, and length, respectively. From the various types of the elastic deformation studied in [162] such as thin-membrane-bending, thick-plate-bending, stretching, etc., the *thin-plate-bending framework* is utilized in this work, since it suits the configuration of the fabricated microchannels with a deformable thin PET (polyethylene terephthalate) film. This framework requires  $\delta_{\max} \ll t \ll W$ , where  $\delta_{\max}$  is the maximum displacement of the membrane and  $t$  denotes the membrane thickness.

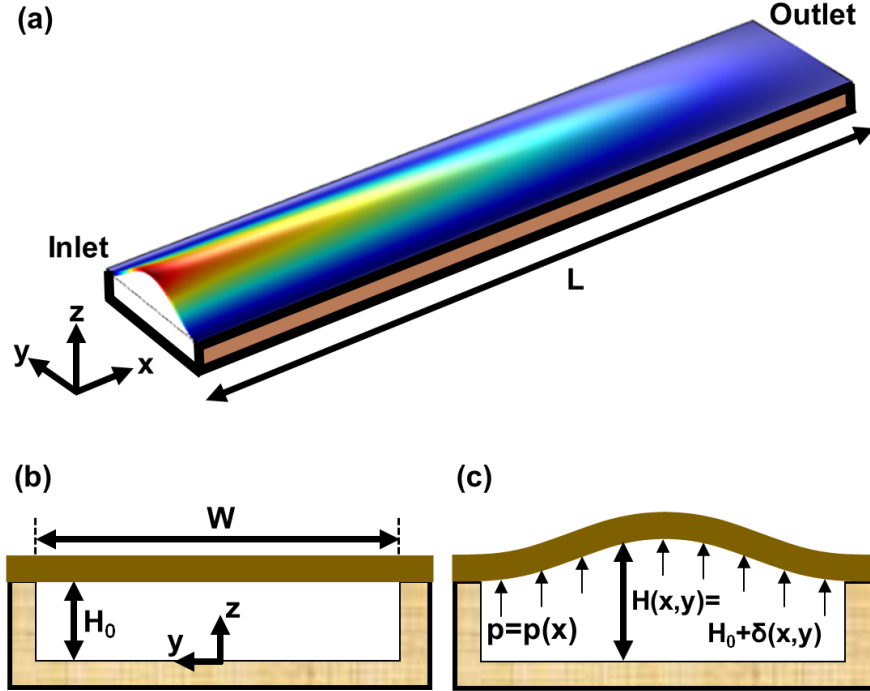


Figure 31: (a) Schematic representation of a fluid flow through a microchannel with the flexible ceiling together with the cross-section view of the channel (b) without and (c) with applying the pressure difference across the channel.

It should be noted that despite the three-dimensional nature of the membrane deformation and the velocity field in a general fluid flow through deformable channels, because of the assumptions made in [19] such as  $H_0 \ll W \ll L$ , the small components of velocity in  $y$  and  $z$  directions (Fig. 31) do not appear in the leading-order equations using the perturbation technique. The pressure and the flow-wise component of velocity are the only variables associated with the fluid-mechanics aspect of the problem appearing in the leading-order equations of the perturbation method. Regarding the solid-mechanics domain, because of the similar assumptions, the ceiling deformation's dependence on the upstream and downstream membrane slices does not appear in the leading-order equations of the perturbation method, leading to the one-dimensional Euler–Bernoulli beam theory through correlating the membrane deformation in each slice with the local pressure load. Because of the aforementioned reasons, we still refer to the model in [19] and its extension in [162] as one-dimensional models.

In this work, the volumetric flow rate–pressure difference relation obtained in [19], pre-

sented in Eq. 9, is rearranged as shown in Eq. 10, in which  $Q_{\text{Deformable}}$  and  $Q_{\text{Rigid}}$  respectively refer to the volumetric flow rate through the deformable microchannel and that through the corresponding rigid microchannel

$$\begin{aligned}
Q^* &= \frac{Q_{\text{Deformable}}}{Q_{\text{Rigid}}} = 1 + c_1\chi + c_2\chi^2 + c_3\chi^3 \\
c_1 &= \frac{4}{5} = 0.8 \\
c_2 &= \frac{128}{315} \approx 0.4063 \\
c_3 &= \frac{256}{3003} \approx 0.0852
\end{aligned} \tag{10}$$

where we define the dimensionless parameter  $\chi = \Delta p W^4 / 384 D H_0$ , namely a *flexibility parameter* hereafter. In addition,  $D = Et^3 / 12(1 - \nu^2)$ , in which  $E$ , and  $\nu$  refer to the membrane modulus of elasticity and Poisson's ratio, respectively. The volumetric flow rate through the rigid microchannel can be written as  $Q_{\text{Rigid}} = \Delta p W H_0^3 / 12 \mu L$ , where  $\mu$  is the fluid dynamic viscosity. By defining the flexibility parameter and the dimensionless volumetric flow rate in this manner, we aim at directly observing the effects of various dimensional or operational parameters on how different the flow characteristics of a deformable microchannel and those of its theoretically rigid counterpart are. Such differences between the rigid and deformable microchannels are reflected into the magnitude of  $Q^*$ . The minimum value of  $Q^*$  is 1, which corresponds to a theoretically rigid microchannel. A configuration with  $Q^* \approx 1$  shows that the channel deformability effects are negligible and flow characteristics are close to those of the flow through the rigid counterpart, while an increase in  $Q^*$  implies a more significant deviation from the rigid channel characteristics.

The mean and maximum dimensionless displacements of the membrane are expressed in Eq. 11:

$$\begin{aligned}
\frac{\langle \delta(x^*) \rangle}{H_0} &= \frac{8}{15} \chi p^*(x^*) \\
\frac{\delta_{\max}(x^*)}{H_0} &= \chi p^*(x^*)
\end{aligned} \tag{11}$$

where  $p^* = p / \Delta p$  shows the dimensionless pressure within the channel, and  $x^* = x / L$  is the dimensionless distance from the inlet. The parameters  $\langle \delta(x^*) \rangle$  and  $\delta_{\max}(x^*)$  denote the

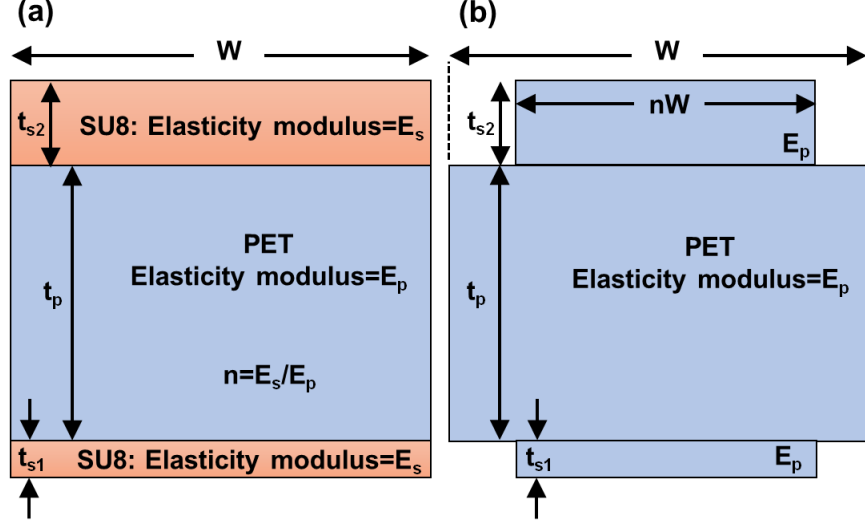


Figure 32: (a) Schematic diagrams of the cross section of the composite membrane consisting of the PET film with two SU8 adhesive layers together with the (b) transformed section for stress analysis.

mean and maximum membrane displacement at  $x^*$ , respectively.

### Composite membranes

Because of the adhesive bonding technique used in this work, the structural effects of the adhesive layers need to be taken into account. As will be described later, the microchannel ceiling consists of a PET film coated with SU8 on both sides, forming a three-layer membrane; see Fig 32 (a). By using the transformed-section method [165], the flexural rigidity  $F = EI$ , where  $I$  denotes the moment of inertia, is obtained for the transformed section; see Fig 32 (b). The equivalent membrane thickness,  $\tilde{t}$ , is calculated from  $\tilde{t} = \sqrt[3]{12F/EW}$ , and replace the membrane thickness,  $t$ , to evaluate the flexibility parameter,  $\chi$ , in Eq. 10. The composite membrane is then considered as a single-layer film with the equivalent thickness of  $\tilde{t}$ , *i.e.*  $t$  is replaced by  $\tilde{t}$ , and the elasticity modulus of PET, *i.e.*  $E$  is replaced by  $E_{\text{PET}}$ .

### Linear pressure variation assumption

The membrane displacement is dictated by the pressure variation within the microchannel. On the other hand, the membrane displacement changes the cross sectional area and in turn hydrodynamic resistance, which influences the pressure variation through the channel.

Hence, the fluid and solid aspects of this problem are potentially highly coupled. However, the fluid and solid aspects can be studied in a decoupled fashion when the membrane deformation is sufficiently small compared to the microchannel original height. This decoupled state arises with a small pressure difference, deep and/or narrow channel, or thick/stiff membrane. Under these situations, the pressure varies almost linearly within the microchannel. By substituting the linear pressure variation of  $p^*(x^*) = 1 - x^*$  in Eq. 11, we have  $\frac{\langle \delta(x^*) \rangle}{H_0} = \frac{8}{15}\chi (1 - x^*)$ . The average of the membrane displacement over the whole channel can be obtained through  $\int_{x^*=0}^{x^*=1} \langle \delta(x^*) \rangle dx^* = \frac{4}{15}\chi H_0$ . If the deformable microchannel is replaced with a rigid rectangular microchannel with the height of  $H_0 + \frac{4}{15}\chi H_0$ , the volumetric flow rate can be expressed as in Eq. 12.

$$\frac{Q_{\text{Deformable}}^{\text{Linear Pressure}}}{Q_{\text{Rigid}}} = 1 + d_1\chi + d_2\chi^2 + d_3\chi^3$$

$$d_1 = \frac{4}{5} = 0.8$$

$$d_2 = \frac{16}{75} \approx 0.2133$$

$$d_3 = \frac{64}{3375} \approx 0.0190$$
(12)

A criterion is sought later to identify the threshold value separating the two regimes of coupled and decoupled fluid-solid mechanics through examining the Eqs. 10 and 12.

## Experiments

### Fabrication

The schematic representation of the fabrication process flow is shown in Fig. 33. The procedure is similar to what we described in our previous work [164] with the difference that the flexible membrane is allowed to deform even after the reinforcement step. Briefly, the patterns of the microchannel sidewalls are created through the glass wet etching procedure. The via-holes are drilled in the glass slide using a 2-mm drill bit; see Fig. 33 (a). The 100  $\mu\text{m}$ -thick PET (Polyethylene terephthalate) film coated with a thin SU8 film ( $\sim 2 \mu\text{m}$ )

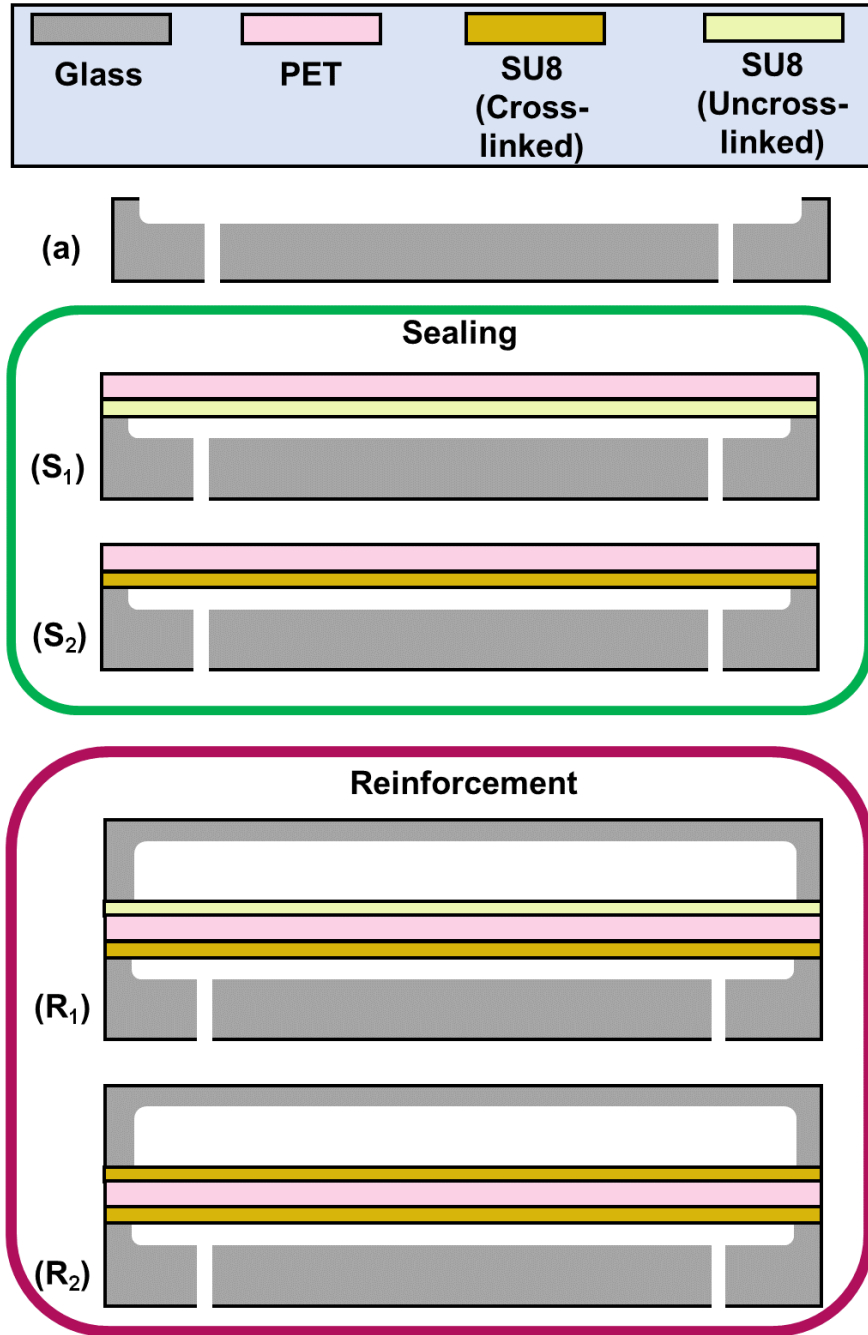


Figure 33: Schematic representation of the fabrication process flow: (a) the microchannel sidewalls are created using the double-step glass wet etching. (S<sub>1</sub>) A PET film coated with a thin layer of SU8 seals the microchannel sidewalls. (S<sub>2</sub>) The chip is undergone with UV illumination and post-exposure baking to cure the adhesive layer. (R<sub>1</sub>) A glass substrate with the same pattern as that of the main channel is aligned and brought in contact with the SU8 layer coated on the bare side of the PET film. (R<sub>2</sub>) The sample is undergone with UV illumination and post-exposure baking to cure the adhesive layer at the bonding interface of the reinforcement glass and the PET film.

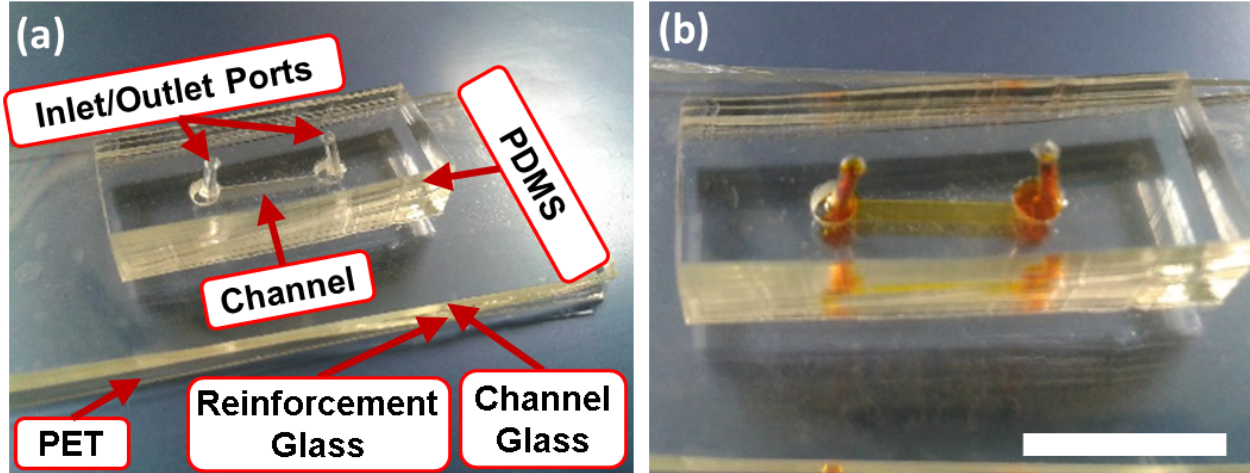


Figure 34: (a) A photograph of the fabricated device together with (b) a photograph showing the channel filled with a dye demonstrating a leakage-free bonding. The scale bar is 1 cm in (b).

then seals the channel sidewalls on the hotplate at  $69 \pm 1^\circ\text{C}$ ; see Fig. 33 (S<sub>1</sub>). After 30 minutes, the temperature decreases to the room temperature over 20 minutes. The SU8 adhesive layer is cured using the UV exposure of  $\sim 1.3 \text{ J/cm}^2$  and baking on the hotplate, initially at  $65^\circ\text{C}$  ramping up to  $95^\circ\text{C}$  over 5 minutes, remaining at this temperature for 30 minutes and cooling down to the room temperature over 30 minutes; see Fig. 33 (S<sub>2</sub>). A separate glass slide is patterned and etched to create a cavity for accommodating the deflected membrane while providing the bonding reinforcement; see Fig. 33 (R<sub>1</sub>). The etched cavity is sufficiently deep ( $\geq 45 \mu\text{m}$ ) to enable the membrane to displace freely. The reinforcement glass slide is bonded with the PET/glass microchannel stack using the partially cured SU8 as an adhesive layer. Prior to bonding, the SU8 layer of about  $14 \mu\text{m}$  in thickness is spun onto the bare side of the PET film and baked on the hotplate at  $65^\circ\text{C}$  for 4 minutes. During bonding, the stack is baked at  $69^\circ\text{C}$  for 20 minutes, followed by the UV exposure of  $2 \text{ J/cm}^2$  and postbaking at  $95^\circ\text{C}$  for 30 minutes; see Fig. 33 (R<sub>2</sub>). A PDMS interconnect with holes are bonded to the glass slides for injection and collection of the fluid. The photographs of a fabricated device are shown in Fig. 34. A dye was injected through the channel to ensure a leak-free bonding. The photograph shown in Fig. 34 (b) demonstrates a leakage-free bonding between the PET film and the glass as well as between the PDMS and the glass.

## **Volumetric flow rate measurement**

In order to create a pressure driven flow under a specific pressure difference, a reservoir is used with two ports. The compressed air, the pressure of which is adjusted using a pressure regulator (PneumaticPlus, PPR2-N02BG-4 Miniature Air Pressure Regulator), is injected through one of the ports causing the liquid to be pushed out from the other port, which is connected to the microchannel's inlet. Two approaches are used to measure the volumetric flow rate depending on its magnitude.

### **Low flow rate regime (below about 40 micro-litre/min)**

The discharged liquid is guided through a capillary tube. The meniscus displacement,  $\Delta x_m$ , and the time interval,  $\Delta t_m$ , are measured over 2–7 centimeters of the capillary tube length depending on the meniscus speed. The meniscus speed is calculated from  $u_m = \Delta x_m / \Delta t_m$ . The volumetric flow rate equals  $\frac{\pi}{4} D_c^2 u_m$ , where  $D_c$  refers to the capillary inner diameter. Two different capillary tubes with  $D_c = 530$  and  $793.75$  microns were used for the volumetric flow rates below  $\sim 2 \mu\text{l}/\text{min}$  and above that, respectively. The hydrodynamic resistance of the capillary tubes ( $< 10^{11} \text{Pa}\cdot\text{s}/\text{m}^3$ ) is at least three orders of magnitude smaller than that of the studied devices to avoid the spurious effects on the measured volumetric flow rate.

### **High flow rate regime (above about 40 micro-litre/min)**

The liquid discharging from the microchannel outlet is collected in a vial, the mass of which is monitored over time using an analytical balance (Mettler Toledo-XS105, 0.01 milligram resolution). The slope of the accumulated mass versus time is the mass flow rate,  $\dot{m}$ . The volumetric flow rate is obtained from  $Q = \dot{m} / \rho$ , where  $\rho$  denotes the fluid density.

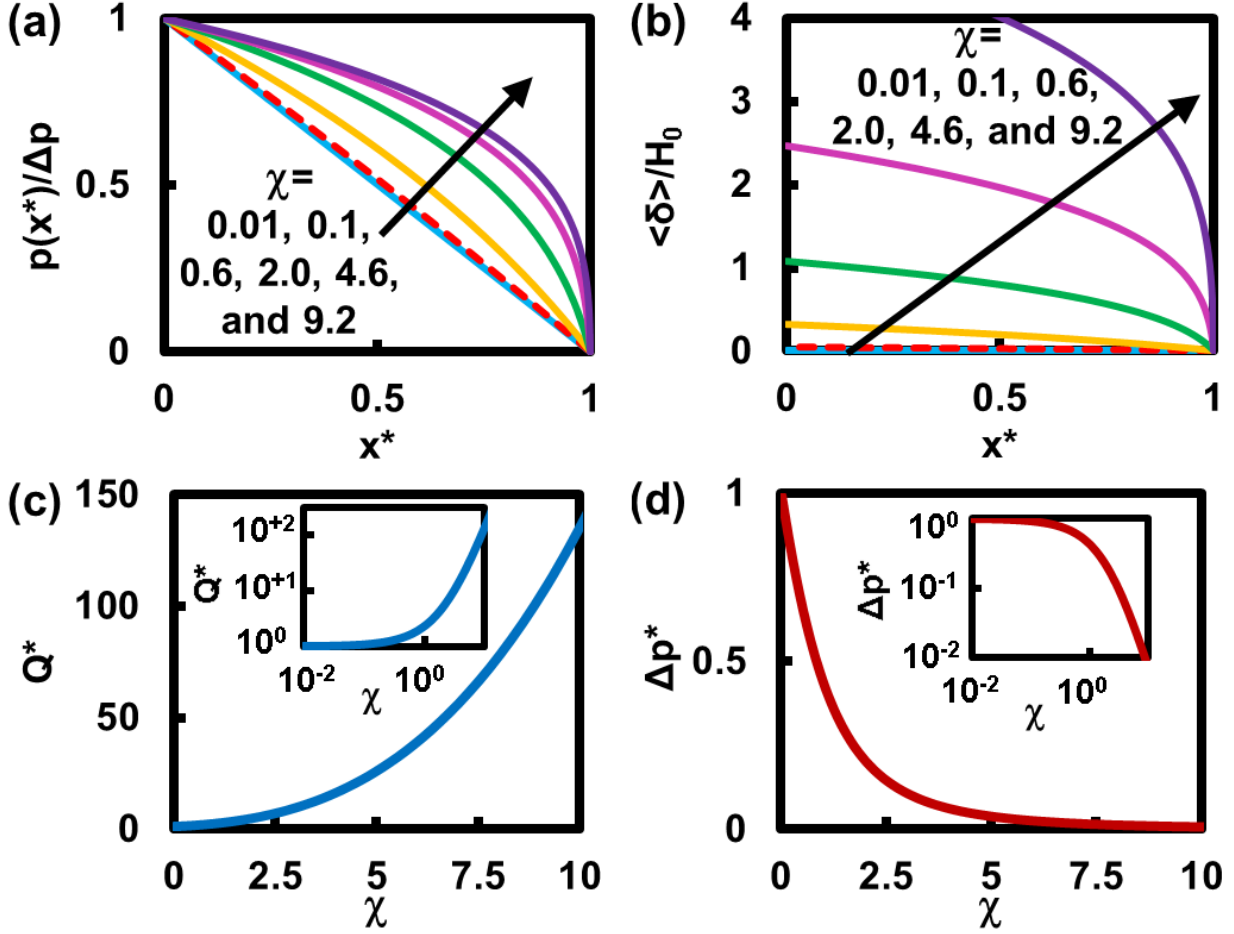


Figure 35: (a) Plots of the dimensionless pressure,  $p^* = p(x^*)/\Delta p$ , as a function of the dimensionless distance from the inlet  $x^*$  for various flexibility parameter values. (b) The variation of the dimensionless membrane's mean deflection,  $\langle \delta \rangle / H_0$ , along the microchannels for various flexibility parameter values. (c) A plot of the dimensionless flow rate  $Q^* = [Q_{\text{Deformable}}/Q_{\text{Rigid}}]_{\Delta p_{\text{Deformable}} = \Delta p_{\text{Rigid}}}$ , as a function of the flexibility parameter. (d) A plot of the dimensionless pressure difference  $\Delta p^* = [\Delta p_{\text{Deformable}}/\Delta p_{\text{Rigid}}]_{Q_{\text{Deformable}} = Q_{\text{Rigid}}}$ , as a function of the flexibility parameter. The insets show the logarithmic plots in (c) and (d).

## Results and discussion

### Parametric study of the flexibility parameter

The dimensionless pressure variation along the deformable microchannel is plotted for various flexibility parameters as shown in Fig. 35 (a). It is perceived that the pressure variation deviates more from the linear one as the flexibility parameter increases. In case of the large flexibility parameters, the slope of the curve increases in magnitude towards the exit of the channel (increasing  $x^*$ ), which can be attributed to the increasing local hydrodynamic

Table 7: The geometry of four deformable microchannels studied in this chapter.

Microchannel	Length ( $mm$ )	Width ( $mm$ )	Height ( $\mu m$ )	Height-to-Width Ratio
<b>A</b>	$9.5 \pm 0.5$	$1.25 \pm 0.1$	$2.3 \pm 0.1$	$1.84 \times 10^{-3}$
<b>B</b>	$9.5 \pm 0.5$	$2.0 \pm 0.1$	$2.3 \pm 0.1$	$1.15 \times 10^{-3}$
<b>C</b>	$9.5 \pm 0.5$	$1.25 \pm 0.1$	$7.5 \pm 0.4$	$6.00 \times 10^{-3}$
<b>D</b>	$9.5 \pm 0.5$	$2.2 \pm 0.1$	$8.2 \pm 0.4$	$3.73 \times 10^{-3}$

resistance. The larger pressure levels close to the inlet cause the larger membrane deflections, decreasing the hydrodynamic resistance through increasing the cross-sectional area; see Fig. 35 (b). From Fig. 35 (b), at any  $x^*$ , the bulging becomes larger as the flexibility parameter increases, inducing the more non-linear pressure variation within the microchannel, as shown in Fig. 35 (a).

Plots of the dimensionless flow rate ( $Q^*$ ) and dimensionless pressure drop ( $\Delta p^*$ ) are shown in Fig. 35 (c) and (d) as a function of  $\chi$  and can be directly obtained from Eq. 10. While  $Q^*$  is a cubic polynomial function of  $\chi$ ,  $\Delta p^*$  is a rational function, *i.e.*  $\Delta p^* = 1/Q^*$ . The *dynamic rescaling* of the vertical axis takes place when plotting  $Q^*$  versus  $\chi$  because of the term of  $\Delta p$  included in the definition of  $Q^*$ , allowing us to obtain the master curve shown in Fig. 35 (c). The vertical axis represents an extent of deviation between the characteristic behavior of a deformable microchannel and that of its theoretically rigid counterpart.

Figure 35 (d) shows what fraction of the pressure difference applied across its rigid counterpart is needed to be applied across a deformable microchannel to produce the same volumetric flow rate. It is perceived that for large values of  $\chi$ , small fractions of the pressure difference are needed to be applied across the deformable microchannels to deliver the same volumetric flow rates as those of their rigid counterparts.

## Experimental results

Four different shallow microchannels with ultra-low height-to-width ratios have been fabricated. The microchannels geometries are summarized in Table 7. In our mathematical modeling, the modulus of elasticity and Poisson’s ratio of the PET are 2.5 GPa and 0.4, respectively. The modulus of elasticity of the SU8 is considered to be 2 GPa (MicroChem Corp.). Poisson’s ratio of SU8 is  $\sim 0.22$ – $0.26$  [166]. Since the thicknesses of the SU8 layers

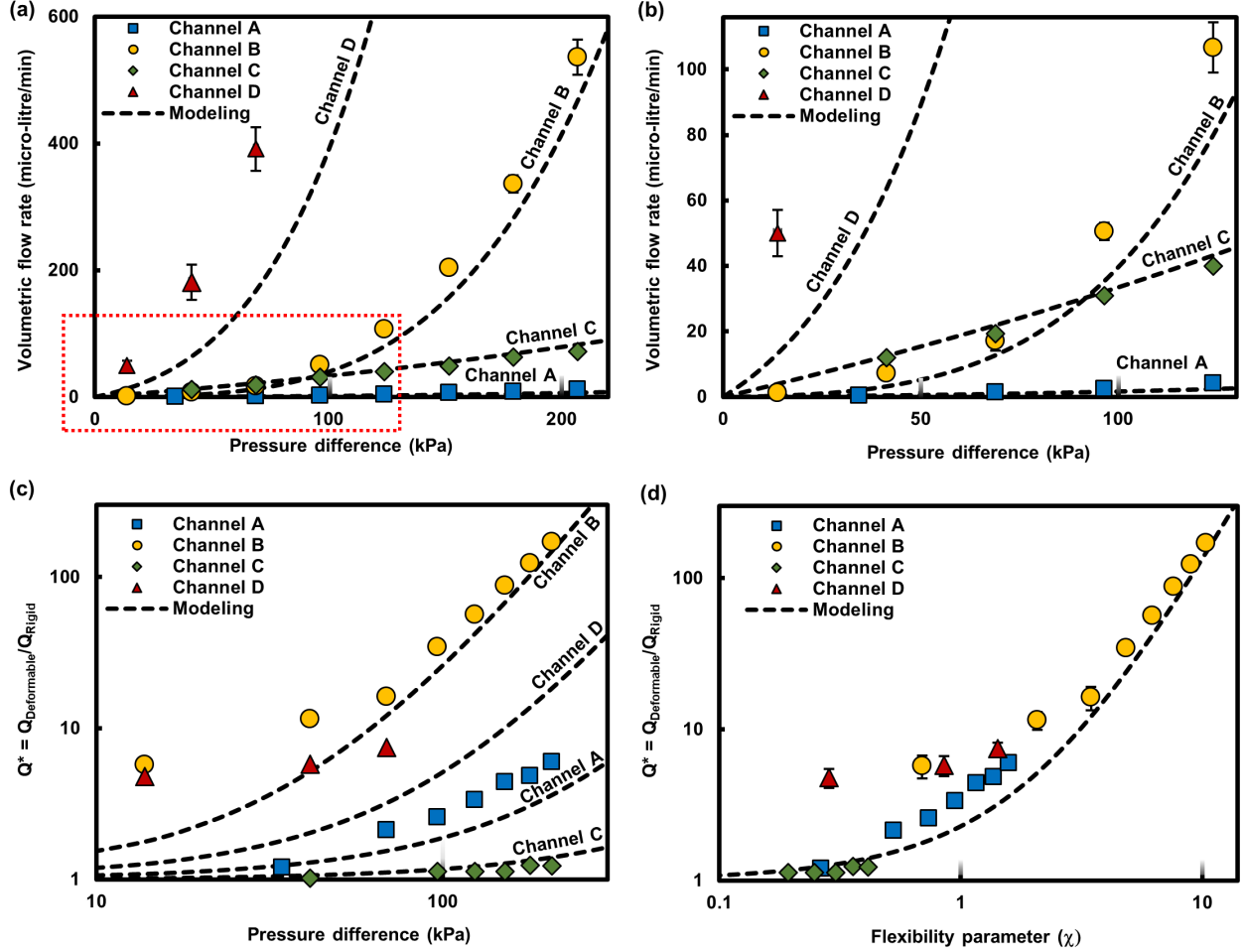


Figure 36: (a) The volumetric flow rate through Microchannels A, B, C, and D in comparison with the analytical solutions of the one-dimensional model [19] together with (b) the magnification of the dotted box. (c) The ratio of the volumetric flow rate through the deformable microchannels to that through their theoretically rigid counterparts under the same pressure differences. (d) The master curve obtained in this work, Eq. 10, together with the experimental results. A logarithmic scale is used in (c) and (d). The error bars, obtained from three data-sets, are not shown when they are smaller than the size of markers.

and the PET film are  $t_{s1} = 2 \mu m$ ,  $t_{s2} = 15 \mu m$ , and  $t_p = 100 \mu m$  (Fig. 32), the equivalent thickness of the SU8-coated PET membrane equals  $\tilde{t} \approx 113 \mu m$ . The thermophysical properties of the DI water are considered to be  $\rho = 1000 \text{ kg/m}^3$  and  $\mu = 8.9 \times 10^{-4} \text{ Pa.s}$ .

The volumetric flow rates through Microchannels A, B, C, and D are shown in Fig. 36 (a) and (b) for various pressure differences across the microchannels. The volumetric flow rates of Microchannels A–D normalized by those of the rigid counterparts, *i.e.*  $Q^* = Q_{\text{Deformable}}/Q_{\text{Rigid}}$ , are also shown in Fig. 36 (c) under various pressure drops. A good agreement is observed between the one-dimensional model in [19] and the experimental results.

The larger discrepancies between the modeling and experimental results of Microchannels B and D can be attributed to the rather large width-to-length ratio,  $W/L \approx 0.22$ , which does not perfectly satisfy the requirement of the wide-beam framework and lubrication theory, *i.e.*  $W/L \ll 1$ . If the microchannel is not sufficiently long, the membrane's infinitesimal slices normal to the flow-wise direction cannot be accurately approximated by the wide beams. Under these situations, at any  $x^*$ , the membrane deflection is not solely dependent on the corresponding local pressure  $p(x^*)$  within the channel. Instead, the local membrane deflection is influenced by the upstream pressure as well. Therefore, the membrane displacement becomes larger than predicted by the model based on the wide-beam framework and lubrication theory, causing the model to underestimate the volumetric flow rate.

In addition to the larger value of  $W/L$  for Microchannel D ( $\approx 0.232$ ) compared with that of Microchannel B ( $\approx 0.211$ ), the larger discrepancies from modeling observed in experimental mass flow rates through Microchannel D may be partially due to the inaccurate location of the inlet/outlet via-holes drilled manually in glass slides. In our fabricated devices, the center of the holes has an offset of 0.1–0.5 mm from the expected locations, causing uncertainties to rise not only in the overall length of microchannels, but also in the channels' width in proximity of the inlet/outlet ports; see Fig. 34 (b). In case of narrow microchannels, *e.g.* a few hundreds of microns in width, the interface between the main part of channel and the inlet/outlet via-holes of 2 mm in diameter can be reasonably assumed to be a straight line. Under these situations, the channel width remains intact after creating the via-holes. Whereas, for wide microchannels like Microchannels B and D, the round shape of the inlet/outlet via-holes can significantly change the microchannel width close to the inlet/outlet ports. For such situations, the channel's width is not constant in the proximity of the inlet/outlet sections. An offset from the expected locations of the via-holes causes even more deviations from the expected straight microchannel. Therefore, the fluid flows through Microchannels B and D can be quite different from each other close to the inlet/outlet sections due to the existing lateral and axial offsets in locations of the created via-holes.

Figure 36 (d) shows that, to a reasonable agreement, the experimental data points of

flow rate versus pressure drop for all four channels fall onto the master curve presented in Eq. 10 over a large range of the flexibility parameter. This master curve demonstrates that difference between the volumetric flow rate of a deformable channel and that of its rigid counterpart under the same pressure drop is solely dictated by the flexibility parameter introduced in this chapter. Because of having a relatively large width and small height, Microchannel B exhibits the largest flexibility parameter and consequently the most significant deviation from its rigid counterpart (largest  $Q^*$ ), whereas the relatively small width and large height of Microchannel C cause it to show the smallest flexibility parameter and consequently the closest resemblance to its rigid counterpart (smallest  $Q^*$ ). In the following, we are elaborating how the flexibility parameter's scale dictates the characteristic behavior of the fluid flow through deformable microchannels.

According to Fig. 36 (a), under the sufficiently large pressure differences, Microchannels B and D deliver much larger volumetric flow rates than Microchannels A and C because the larger membrane deflection and averaged cross-section area result from the larger width of Microchannel B and D. In particular, under the maximum investigated pressure, *i.e.*  $\sim 207$  kPa, the volumetric flow rate delivered by Microchannel B is about 70 times larger than that of Microchannel A. It is worth mentioning that such distinct characteristic behaviors emerge due to the rather small difference of the microchannels widths,  $(W_B - W_A)/W_A \approx 0.6$ .

According to Fig. 36 (c), the deformable microchannels behave similar to their corresponding rigid microchannels ( $Q^* \approx 1$ ) under the sufficiently low pressure differences. By increasing the pressure difference, however,  $Q^*$  increases and the difference between the deformable and rigid microchannels becomes more significant. The graphs also show that  $Q^*$  increases as the microchannel width increases and/or its height decreases. Compared to its corresponding rigid microchannel, Microchannel C shows only 40% increase in the volumetric flow rate under 207 kPa, while Microchannel B delivers the flow rate of about 148 times larger than its corresponding rigid microchannel. Despite the fact that Microchannel C's height is more than three times as large as that of Microchannel B, the volumetric flow rate delivered by Microchannel B under 207 kPa is about six times as large as that delivered by

Table 8: The order of magnitude of different terms existing in Eq. 10 for the flexibility parameter,  $\chi$ , with various orders of magnitude. For each flexibility scale, the most important terms with the order of magnitude equal to or greater than  $10^{-1} \times O(Q^*)$  are highlighted in bold font. Note:  $O(c_1) = 1$ ,  $O(c_2) = 10^{-1}$ , and  $O(c_3) = 10^{-1}$ .

$O(\chi)$	$10^{-2}$	$10^{-1}$	$10^0$	$10^{+1}$	$10^{+2}$
$O(1)$	<b><math>10^0</math></b>	<b><math>10^0</math></b>	<b><math>10^0</math></b>	$10^0$	$10^0$
$O(c_1\chi)$	$10^{-2}$	<b><math>10^{-1}</math></b>	<b><math>10^0</math></b>	<b><math>10^{+1}</math></b>	$10^{+2}$
$O(c_2\chi^2)$	$10^{-5}$	$10^{-3}$	<b><math>10^{-1}</math></b>	<b><math>10^{+1}</math></b>	$10^{+3}$
$O(c_3\chi^3)$	$10^{-7}$	$10^{-4}$	<b><math>10^{-1}</math></b>	<b><math>10^{+2}</math></b>	<b><math>10^{+5}</math></b>

Microchannel C. A rigid microchannel possessing triple a specific height would result in a 26-time larger volumetric flow rate due to the term of  $H_0^3$  in  $Q_{\text{Rigid}} = \Delta p W H_0^3 / 12 \mu L$ . It is worth mentioning that under the sufficiently low pressure differences, where the fluid flow characteristics are more similar to those of the rigid microchannel, Microchannel C delivers the larger volumetric flow rate in comparison with Microchannel B; see Fig. 36 (b). By increasing the pressure difference, the volumetric flow rate of Microchannel B surpasses that of Microchannel C at  $\Delta p \approx 92$  kPa. In order to obtain a more profound insight into the underlying physics of the observed distinct flow characteristics, the Eq. 10 is more deeply examined in the following.

The order of magnitude of different terms existing in Eq. 10 is presented in Table 8 for the flexibility parameter,  $\chi$ , with various orders of magnitude. This table shows the contribution of each term in the volumetric flow rate through the deformable microchannels. The terms with 10% contribution or more are highlighted in bold font for each order of magnitude of  $\chi$ . It is perceived that the higher orders of the flexibility parameter become more important as the flexibility parameter increases. The magnitude of the truncation error can also be extracted from this table for the expressions consisting of various terms, that can be used to approximate the Eq. 10. The important finding is that a variety of distinct characteristic behaviors can emerge under different flexibility parameter scales. For example, the dimensionless volumetric flow rate can be approximated as  $Q^* \approx 1$  and  $Q^* \approx c_3\chi^3$  for the flexibility parameter scales of  $O(\chi) \leq 10^{-2}$  and  $O(\chi) \geq 10^{+2}$ , respectively, while the truncation error is only about 1% of the exact value. For the same truncation error, Eq. 10 can be approximated as  $Q^* \approx 1 + c_1\chi$  and  $Q^* \approx c_1\chi + c_2\chi^2 + c_3\chi^3$  for the flexibility parameter

scales of  $O(\chi) = 10^{-1}$  and  $O(\chi) = 10^{+1}$ , respectively, while all the terms are needed for the flexibility scale of  $O(\chi) = 10^0$  and truncation error of 1%.

From the definition of the flexibility parameter,  $\chi = \Delta p W^4 / 384 D H_0$ , the fluid-solid behavioral characteristics rely on the following three general categories: 1) microchannel dimensions:  $W$  and  $H_0$ , 2) membrane thickness and structural properties, which are lumped into the parameter of  $D$ , and 3) pressure difference across the microchannel,  $\Delta p$ . Regardless of the microchannel geometry and the membrane properties, if the pressure difference is **sufficiently** low, the flexibility parameter becomes much smaller than unity. Under these situations, the first term in the right side of Eq. 10 is dominant:  $Q^* \approx 1$ . As long as the condition of  $\chi \ll 1$  is satisfied, any change in the dimensions of the microchannel, pressure difference, or membrane properties causes no significant influence on  $Q^*$ , and the deformable microchannel behaves similar to its corresponding rigid microchannel. On the other hand, for the **sufficiently** large pressure difference across the flexible microchannels, the last term becomes dominant:  $Q^* \approx c_3 \chi^3$ . Under these situations, a slight change in the microchannel dimensions, pressure difference, or membrane properties is significantly magnified because of the term of  $\chi^3$ . As a result, two deformable microchannels slightly different in their dimensions and/or the membrane properties might exhibit the similar or the noticeably different characteristic behaviors dependent upon the pressure difference applied across the microchannels.

A sufficiently large change in the pressure difference across a specific fabricated microchannel can activate/inactivate the different terms in the right side of Eq. 10 through changing the order of magnitude of the flexibility parameter; see Table 8. As a result, a deformable microchannel might exhibit a variety of distinct characteristic behaviors depending on the pressure difference applied across the microchannel.

The flexibility parameter is presented in Fig. 37 (a) as a function of the pressure difference across the investigated microchannels. Even though the flexibility parameter of the microchannels varies with the applied pressure difference, the ratio of the flexibility parameters related to the different microchannels of  $i$  and  $j$  remains constant under various applied

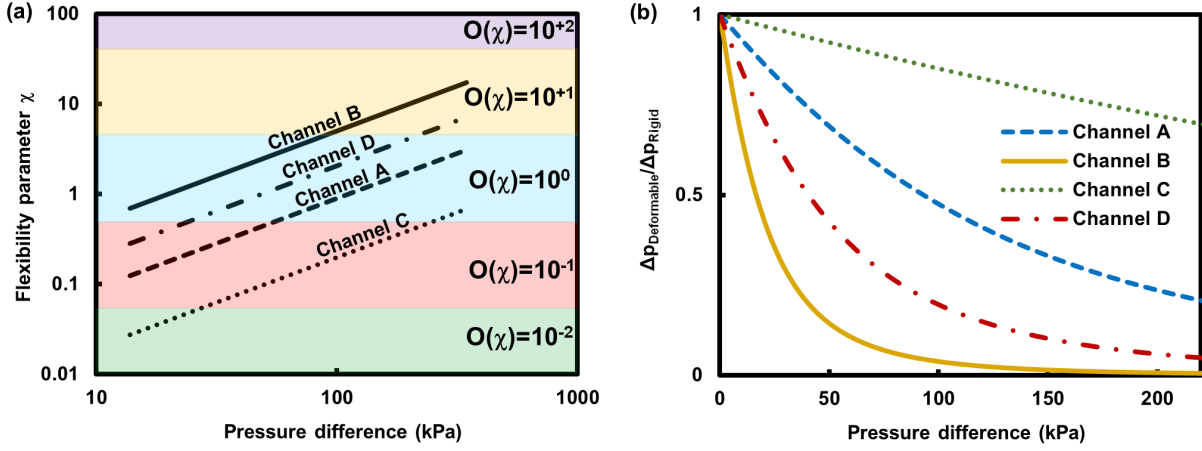


Figure 37: (a) The flexibility parameter,  $\chi$ , for Microchannels A, B, C and D under various pressure differences. The differences between the channels geometries and/or the membranes properties result in the different flexibility parameters under the same pressure difference across the channels. A sufficiently large change in the pressure difference across a specific channel can alter the flexibility parameter scale from one characteristic regime to another. (b) The fraction of the pressure difference across the rigid microchannel sufficiently large to cause the same volumetric flow rate when applied across the deformable microchannel with the same dimensions.

pressure differences:

$$\left[ \chi_i / \chi_j \right]_{\Delta p_i = \Delta p_j} = (W_i / W_j)^4 \times (H_{0,j} / H_{0,i}) \quad (13)$$

where  $W_i$  and  $W_j$  refer to the widths of the microchannels  $i$  and  $j$ , respectively. Similarly,  $H_{0,i}$  and  $H_{0,j}$  show the original heights of the microchannels  $i$  and  $j$ , respectively. Because of the term of  $W^4$ , any difference in width of the microchannels causes a noticeable difference in the flexibility parameters and potentially the fluid flow characteristics. This is the reason that a 60% larger width results in Microchannel B's flexibility to be  $1.6^4 \approx 6.6$  times as large as that of Microchannel A. This ratio is sufficiently large to cause the two microchannels to operate within the different flexibility regimes. For example, under the pressure difference of 207 kPa, where  $\chi_A \approx 1.59$  and  $\chi_B \approx 10.39$ , the order of magnitude of  $\chi$  is  $10^0$  and  $10^1$  for Microchannels A and B, respectively. As a result, the term of  $c_3\chi^3$  plays the most important role in the characteristic behavior of Microchannel B (Table 8), while the lower orders of  $\chi$  dictate the behavior of Microchannel A, which causes the volumetric flow rate through Microchannel B to be about 70 times larger than that of Microchannel A.

According to Table 8, for the sufficiently small flexibility parameter, *e.g.*  $O(\chi) \leq 10^{-1}$ , the

term of 1 is dominant in Eq. 10. The volumetric flow rate is, therefore, mainly proportional to  $WH_0^3$ , which resembles the rigid microchannel characteristics. By contrast, for the large-flexibility regime, *e.g.*  $O(\chi) \geq 10^{+1}$ , the term of  $c_3\chi^3$  plays the most important role. In these situations, the volumetric flow rate is proportional to  $W^{13}$ . One can show that

$$\chi \gg 1 : Q_{\text{Deformable}} \approx \frac{1}{7,970,586,624} \times \frac{W^{13}\Delta p^4}{\mu LD^3}. \quad (14)$$

It is perceived that the height-dependency vanishes, while the microchannel width plays a significant role in the fluid-solid characteristic behavior. Despite the fact that the height of Microchannel C is about 3.3 times as large as that of Microchannel B, such distinct characteristics cause the volumetric flow rate through Microchannel B to be about six times as large as that through Microchannel C under 207 kPa (Fig. 36 (a)), whereas the volumetric flow rate through Microchannel C is about 8 times larger than that through Microchannel B under the relatively low pressure difference of 41 kPa (Fig. 36 (b)). At the lowest extreme of the pressure range, where both microchannels behave similar to their corresponding rigid microchannels, we have  $Q_C/Q_B = W_C/W_B \times (H_{0,C}/H_{0,B})^3 \approx 21.7$ .

The fraction of the pressure difference across the rigid microchannels enough to produce the same volumetric flow rate when applied across the corresponding deformable microchannels is shown in Fig. 37 (b). Microchannel B exhibits the smallest fraction values because of having the largest flexibility parameter. Under the pressure difference of 207 kPa,  $\Delta p^*$  is about  $6.7 \times 10^{-3}$  for Microchannel B, which means a rigid microchannel with the same dimensions as those of the undeformed Microchannel B would need about 149 times as large pressure as 207 kPa, *i.e.*  $\approx 30.8$  MPa, to deliver the same volumetric flow rate ( $\sim 468$  micro-litre/min).

The mean and maximum deflections of the membrane obtained using the theoretical model are shown in Fig. 38 (a) for the inlet section. The wider microchannels have about 0.6 times larger width, which is sufficiently large to cause the noticeably larger deflections, since the membrane deflection is proportional to  $W^4$ . The maximum membrane deflection is reasonably smaller than the membrane thickness (100  $\mu m$ ), which suggests that the *thin*

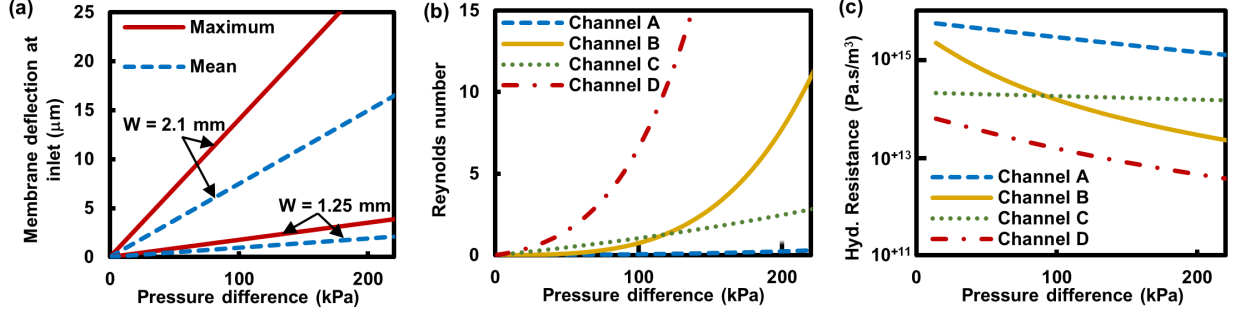


Figure 38: (a) The mean and maximum membrane deflections at the inlet section of Microchannels A and C ( $W=1.25$  mm) as well as those for Microchannels B and D ( $W=2.1$  mm) obtained using the theoretical model [19]. (b) The Reynolds number and (c) the hydrodynamic resistance for the studied microchannels under various pressure differences.

*membrane bending* assumption is valid. The Reynolds number is also calculated for the microchannels:  $Re = \rho \bar{u} D_h / \mu = 2\rho Q / \mu W$ , in which  $\bar{u}$  and  $D_h$  denote the average velocity and the hydraulic diameter of the microchannel, respectively, where  $D_h \approx 2H$ . The results are shown in Fig. 38 (b). The assumption of the laminar flow regime is clearly valid in this study. In addition, the hydrodynamic resistance,  $R_h = \Delta p / Q$ , of the microchannels is presented in Fig. 38 (c). Microchannel C shows the least variations of the hydrodynamic resistance due to the small membrane deflections compared to its original height, whereas Microchannel B exhibits a few orders-of-magnitude change in the hydrodynamic resistance over the investigated pressure difference range.

### Linear pressure variation assumption

The dimensionless volumetric flow rate related to the one-dimensional decoupled fluid-solid mechanics model based on the linear pressure variation assumption, Eq. 12, is shown in Fig. 39 (a) in comparison with the master curve obtained in this work, Eq. 10. The volumetric flow rate is underestimated by assuming the linear pressure variation through the microchannel. The associated error is shown in Fig. 39 (b). It is observed that the linear pressure assumption is acceptable for the small-flexibility regime. In particular, the error is less than 1% if  $\chi < 0.241$ . From Fig. 35 (a), one can perceive that the pressure behavior obtained through the analytical solution is close to the linear variation for such a small flexibility parameter, which explains the acceptable agreement between the coupled and decou-

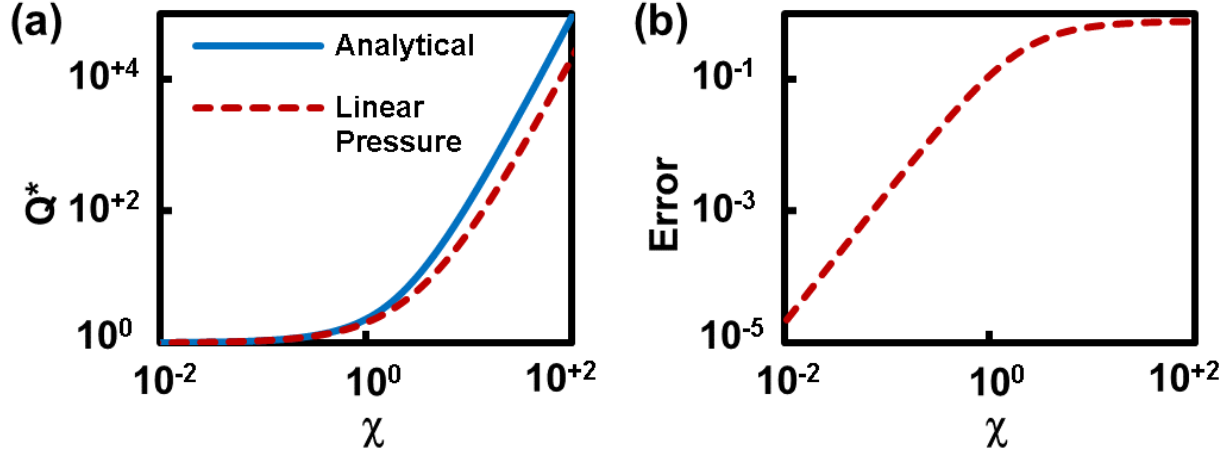


Figure 39: (a) The dimensionless volumetric flow obtained through the linear pressure variation assumption, Eq. 12, compared with the master curve obtained in this work, Eq. 10, as a function of the flexibility parameter. (b) The error associated with the linear pressure variation assumption:  $(Q_{\text{Deformable}}^{\text{Analytical}} - Q_{\text{Deformable}}^{\text{Linear Pressure}})/Q_{\text{Deformable}}^{\text{Analytical}}$ .

pled models. The flexibility parameter for many of the deformable microchannel applications is smaller than 0.241. The maximum flexibility parameter investigated in the comparative study of several benchmarks in [162] equals  $\chi \approx 0.209$ . As previously explained, our work allowed us to study the low-Reynolds-number fluid flow in the deformable microchannel with the new behavioral characteristic regimes related to the flexibility parameter much greater than 0.241.

Our rearrangement of the one-dimensional model in [19] presents the concept of the flexibility parameter, giving a deep insight into the underlying physics. It also provides a governing parameter that helps the engineers to design the deformable microchannels. One of the advantages of the one-dimensional model in [19] in comparison with the three-dimensional coupled fluid-solid mechanics model is its convenience, since the one-dimensional model does not need the (several-hour) time-consuming simulations [162], yet it predicts the main fluid-structural characteristics acceptably with no fitting parameters. On the other hand, three dimensional model is a useful tool when the detailed information of the fluid-solid characteristics are desired, particularly when the effects of elastic membrane clamping at inlet and outlet, drag at the sidewalls of a microchannel that is not sufficiently shallow, etc., are needed to be taken into account.

In case that three-dimensional model is preferred, the threshold of  $\chi \approx 0.241$  can be considered as a guideline. According to Figs. 35 (a) and 39, the linear pressure variation assumption is reasonably acceptable when  $\chi < 0.241$ , practically decoupling the fluid and solid aspects of the problem. The three-dimensional solid mechanics model, where a linear pressure variation is applied to the membrane, can then be used in order to obtain more accurate details of the structural characteristics. Similarly, the obtained deformed shape of the membrane can be used as the ceiling of a rigid microchannel for the three-dimensional fluid mechanics modeling if the details of the fluid flow field are needed.

When their requirements are met, such one-way-coupled strategies significantly reduce the computational costs, while they provide acceptably accurate details of the fluid-solid mechanics. A similar approach was used by Ozsun *et. al.* [155] in order to find the pressure distribution within deformable microchannels through two-dimensional fluid flow simulations. They replaced the ceiling with a rigid wall, but the deformed wall shape was preserved by importing the experimentally measured profile of the deformed membrane into the simulation.

## Conclusion

Volumetric flow rate—pressure difference relationship for the shallow deformable microchannels with ultra-low height-to-width-ratios was investigated in this work. Our work enabled us to study the low-Reynolds-number, *i.e.*  $Re \sim O(10^{-2}—10^{+1})$ , fluid flow in the deformable microchannel under the new regimes of the flexibility parameter ( $\chi$ ) with values a-few-orders-of-magnitude greater than those currently available in the literature. The experimental results together with the scale analysis of the one-dimensional model in [19] based on the *lubrication theory* and *thin-membrane-bending framework*, revealed the various distinct fluid-structural characteristic behaviors under the different flexibility parameter regimes. The difference between the characteristic behavior of fluid flow through a deformable microchannel and that related to its rigid counterpart was reflected into  $Q^*$ , which represents the ratio of the volumetric flow rate through the deformable channel to that through its theoretically rigid

counterpart. A master curve was obtained for the fluid flow through any arbitrary shallow and long deformable microchannel via plotting  $Q^*$  versus  $\chi$ . It was shown that depending on the flexibility parameter's magnitude, altering the pressure difference across the shallow deformable microchannel can activate/inactivate the various orders of the flexibility parameter. The shallow deformable microchannels act similar to their corresponding rigid microchannels under the sufficiently small flexibility parameter. In this regime, the volumetric flow rate is proportional to  $WH_0^3$ , where  $W$  and  $H_0$  respectively refer to the microchannel width and original height. On the other hand, sufficiently increasing the pressure difference across the microchannel can result in the transition to the higher-flexibility regimes. Under the sufficiently large pressure differences across the deformable microchannel, the effects of the microchannel original height on the fluid-solid characteristics disappear. In these situations, the volumetric flow rate becomes proportional to  $W^{13}$ . Such a significantly distinct behavior together with the fact that the flexibility parameter is proportional to  $W^4$  suggest that two nearly identical microchannels with the slightly different widths ( $\sim 60\%$ ) can have two flexibility parameters one order of magnitude different from each other, which can result in the two distinct fluid-solid characteristic behaviors under the same pressure difference across the channels. It was also found that the linear pressure assumption through the deformable microchannel is acceptable for the regimes with the flexibility parameter smaller than 0.241 with less than 1% error in the predicted volumetric flow rate, while this assumption is noticeably erroneous for the regimes with the large flexibility parameter. For the cases that the flexibility parameter is smaller than 0.241, the fluid and solid mechanics can be considered decoupled.

# Chapter 4: Low-Reynolds-number incompressible fluid flow through asymmetric deformable microchannels

## Questions

The main questions of this research are enumerated in the following.

- How does a width profile affect the fluid-solid mechanics of low-Reynolds-number incompressible flows of Newtonian fluids through deformable microchannels?
- Can a membrane deformation-induced change in hydrodynamic resistance provide a direction-dependent net hydrodynamic resistance and flow rectification under the Stokes flow regime?

## Motivations

Passive flow regulations are of importance for various applications such as integrated microfluidic circuits, micro-pumps, etc. There have been some interests in developing a valveless, passive flow rectifier in asymmetric (or tapered) microchannels for low Reynolds number flows. The fundamental challenge associated with rectifying flows of Newtonian fluids under Stokes flow regime ( $Re \ll 1$ ) is associated with the lack of non-linearity in the equation of motion, which motivates this research.

## Objectives

The objectives of this research are to investigate the width profile's effects on fluid-solid mechanics of incompressible flows of Newtonian fluids through asymmetrically-shaped deformable microchannels under the Stokes flow regime and examine the feasibility of flow rectification.

## Introduction

Directional dependence of the hydrodynamic resistance in asymmetrically-shaped microchannels results in the fluid flow rectification, which is important for different applications such as integrated microfluidic devices [75, 167–169], micropumps [170–172] and drug delivery [173–175]. In particular, the rigid nozzle/diffuser microchannels are widely used to rectify the fluid flow at sufficiently high Reynolds numbers ( $Re \gg 1$ ) [170, 171], wherein the underlying mechanism is rooted in the directional dependence of the hydrodynamic resistance due to the non-linear nature of the Navier-Stokes equations. Under the Stokes flow regime ( $Re \ll 1$ ), however, the inertial terms forming the non-linear behavior of the governing equations diminish, causing the Newtonian fluid flow through a rigid nozzle/diffuser microchannel to exhibit a direction-independent hydrodynamic resistance disallowing the fluid flow rectification.

To realize a fluidic rectifier that operates under the Stokes flow regime, the researchers have resorted to another source of nonlinearity, that is, the use of non-Newtonian working fluids with nonlinear rheological characteristics [176–179]. Among the available mechanisms to rectify the Newtonian fluid flows under the Stokes regime, one can refer to mechanically intervening in the microchannel design using the flap structure [180–182], or ball/particle-based check-valves [183–185], where the flap and balls allow the fluid to preferentially flow in one direction. In addition to the channel clogging risk due to the flap structure and ball/particle-based check-valves, a notable difficulty associated with these mechanisms is that the particles and biospecies to be transferred can get damaged or stuck after hitting

the flap and balls/particles.

In this chapter, we present a passive flow rectification mechanism for Newtonian liquids under the Stokes flow regime by introducing nonlinearity into the otherwise linear Stokes equations. Asymmetric flow resistances arise in shallow nozzle/diffuser microchannels with deformable ceiling, in which the fluid flow is governed by a non-linear coupled fluid-solid mechanics equation. A rectification ratio of  $\sim 1.2$ – $1.8$  has been achieved for low-Reynolds-number flows ( $\text{Re} \sim O(10^{-3}) - O(10^0)$ ) of common Newtonian liquids such as water and alcohol. This mechanism can pave the way for regulating the low-Reynolds-number fluid flows with potential applications in precise low-flow-rate micropumps, drug delivery systems, etc.

## Modeling

We demonstrate that a shallow nozzle/diffuser microchannel with deformable ceiling provides a non-linear governing coupled fluid-solid-mechanics equation leading to direction-dependent hydrodynamic resistances enabling flow rectification of Newtonian fluids under the Stokes flow regime. The schematic representation of the fluid flow through a nozzle/diffuser microchannel with a deformable ceiling is shown in Fig. 40. The ceiling membrane deflection depends on the fluid flow direction, *i.e.* nozzle versus diffuser, causing the overall hydrodynamic resistances of diffuser and nozzle to differ from each other. The one-dimensional model used in this work is based on the lubrication theory, *i.e.*  $H_0 \ll W \ll L$ , where  $H_0$ ,  $W$ , and  $L$  refer to the microchannel's original height, width, and length, respectively. The thin-plate-bending framework is considered for the elastic deformation, which requires  $\delta H \ll t \ll W$ , where  $\delta H$  is the membrane displacement and  $t$  denotes the membrane thickness. As mentioned in Chapter 3, under these situations, the displacement of an arbitrary membrane's infinitesimal slice across the channel can be correlated solely with the local fluid pressure within the channel. The deflection profile of the slice is then obtained from the

Euler-Bernoulli beam theory:

$$\delta H(x, \zeta) = \frac{p(x)}{384D} W^4(x) f(\zeta), \quad (15)$$

where  $\zeta \equiv 2y/W(x)$ ,  $f(\zeta) = (\zeta + 1)^2(\zeta - 1)^2$ , and  $D = \frac{Et^3}{12(1-\nu^2)}$ , in which  $E$  and  $\nu$  denote the membrane's modulus of elasticity and Poisson's ratio [186]. In addition,  $p$  refers to the pressure within the channel, which is constant at any x-plane according to the lubrication theory.

Since the membrane displacement is significantly smaller than the channel width and length, *i.e.*  $\delta H \ll W \ll L$ , the membrane slope is very small, *i.e.*  $\partial\delta H/\partial x \ll 1$  and  $\partial\delta H/\partial y \ll 1$ . Under these situations, and considering the sufficiently small nozzle/diffuser half-angle ( $\theta$ ) with an attached flow throughout the channel, the Poiseuille flow pattern can be assumed to be locally valid. In order to introduce the dimensionless variables, we consider the characteristic scales for length, volumetric flow rate, and pressure to be  $L$ ,  $Q_{\text{ref}}$ , and  $\Delta p_{\text{ref}} \equiv 12\mu L Q_{\text{ref}}/W_i H_0^3$ , where  $\mu$  is the fluid dynamic viscosity, and  $W_i$  refers to the channel width at inlet. The dimensionless volumetric flow rate through the deformable

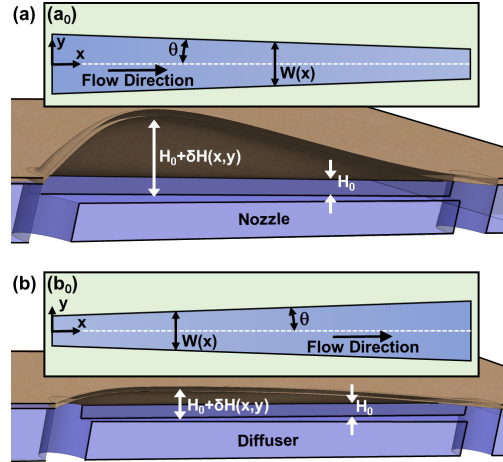


Figure 40: Schematic diagrams showing the cross-section views of the fluid flow through a microchannel with a deformable ceiling in (a) nozzle and (b) diffuser directions together with (a<sub>0</sub> and b<sub>0</sub>) the top view of the channel. The dimensions in z-direction are not in scale with those in x-y plane for the sake of clarity. Note:  $\hat{e}_z = \hat{e}_x \times \hat{e}_y$ , where  $\hat{e}_x$ ,  $\hat{e}_y$ , and  $\hat{e}_z$  denote the unit vector in x, y, and z directions, respectively.

channel, *i.e.*  $Q^* \equiv Q/Q_{\text{ref}}$ , is written as

$$Q^* = -\frac{dp^*(x^*)}{dx^*} \frac{W^*(x^*)}{W_i^*} \frac{\langle H^3 \rangle_{(x^*)}}{H_0^3}, \quad (16)$$

where  $H = H_0 + \delta H$  shows the channel's local height,  $p^* \equiv p/\Delta p_{\text{ref}}$ ,  $x^* \equiv x/L$ ,  $W^* \equiv W/L$ , and  $W_i^* \equiv W_i/L$ . The average of an arbitrary variable like  $\phi$  over a plane at  $x^*$  normal to the flow-wise direction is obtained through  $\langle \phi \rangle_{(x^*)} = \frac{1}{2} \int_{\zeta=-1}^{\zeta=+1} \phi(x^*, \zeta) d\zeta$ . By defining  $\gamma(x) \equiv p(x)W^4(x)/384DH_0$ , Eq. 15 can be rewritten as  $\delta H(x, \zeta)/H_0 = \gamma(x)f(\zeta)$ . Considering that  $\langle H^3 \rangle = H_0^3 + 3H_0^2 \langle \delta H \rangle + 3H_0 \langle (\delta H)^2 \rangle + \langle (\delta H)^3 \rangle$ , one can show that

$$\begin{aligned} \frac{\langle H^3 \rangle}{H_0^3} &= 1 + 3\gamma(x) \langle f(\zeta) \rangle \\ &+ 3\gamma^2(x) \langle f^2(\zeta) \rangle + \gamma^3(x) \langle f^3(\zeta) \rangle. \end{aligned} \quad (17)$$

We know  $\langle f(\zeta) \rangle = 8/15$ ,  $\langle f^2(\zeta) \rangle = 128/315$ , and  $\langle f^3(\zeta) \rangle = 1024/3003$ . Considering that  $p^* = 0$  at  $x^* = 1$  due to the fluid discharge into the ambient air, after defining  $\xi \equiv 1 - x^*$  and substituting Eq. 17 in Eq. 16, one can obtain an initial-value problem for an arbitrary volumetric flow rate of  $Q = Q_{\text{ref}}$ , *i.e.*  $Q^* = 1$ , as shown in the following first-order non-linear ordinary differential equation (ODE):

$$\begin{aligned} \tau(\xi) \left( 1 + \alpha_1 \tau^4(\xi) p^*(\xi) + \alpha_2 \tau^8(\xi) p^{*2}(\xi) \right. \\ \left. + \alpha_3 \tau^{12}(\xi) p^{*3}(\xi) \right) \frac{dp^*(\xi)}{d\xi} = 1, \end{aligned} \quad (18)$$

$$\text{Initial value: } \quad \xi = 0 : p^* = 0,$$

where the width profile function, *i.e.*  $\tau(\xi)$ , flexibility parameter, *i.e.*  $\chi$ , and  $\alpha_i$  coefficients

are

$$\tau(\xi) \equiv W^*(\xi)/W_i^*, \quad (19a)$$

$$\chi \equiv \frac{\Delta p_{\text{ref}} W_i^4}{384 D H_0}, \quad (19b)$$

$$\alpha_1 = \frac{8}{5}\chi, \alpha_2 = \frac{128}{105}\chi^2, \text{ and } \alpha_3 = \frac{1024}{3003}\chi^3. \quad (19c)$$

For a nozzle/diffuser microchannel with a linear variation of the width,  $\tau(\xi) = \tau_o + (1 - \tau_o)\xi$ , where  $\tau_o \equiv W_o/W_i$  and  $W_o$  refers to the channel width at outlet. It is worth mentioning that the governing equation is reduced to that of the fluid flow through a deformable shallow straight microchannel [19, 187] for the special case of  $\tau = 1$ . The ODE presented in Eq. 18 is solved numerically to find the pressure distribution within the channel, *i.e.*  $p^*(\xi)$ , and other fluid-solid characteristics.

## Studying different regimes of flexibility parameter analytically

### Extremely small flexibility parameter

For a rigid channel, the flexibility parameter equals zero, *i.e.*  $\chi = 0$ . For deformable channels under sufficiently small pressure differences, the flexibility parameter can also be very small, *i.e.*  $\chi \approx 0$ . Under these conditions, the terms with  $\alpha_i$  :  $i = 1, 2$ , and 3 multipliers vanish from the coupled fluid-solid-mechanics governing equation presented in Eq. 18, simplifying the ODE into

$$\tau(\xi) \frac{dp^*(\xi)}{d\xi} = 1, \quad (20)$$

$$\text{Initial value: } \quad \xi = 0 : p^* = 0.$$

For a nozzle/diffuser, where  $\tau(\xi) = \tau_o + (1 - \tau_o)\xi$ , one can solve Eq. 20 to obtain the following analytical expression for the pressure distribution within the channel:

$$p^*(\xi) = \frac{1}{1 - \tau_o} \ln \left( 1 + \left( \frac{1}{\tau_o} - 1 \right) \xi \right). \quad (21)$$

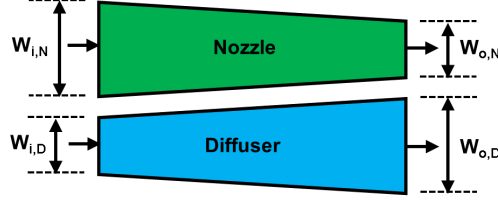


Figure 41: Diagram showing the nomenclature of the nozzle/diffuser inlet/outlet dimensions.

The dimensionless pressure at inlet can then be obtained as

$$p_i^* = \frac{\ln(\tau_o)}{\tau_o - 1}. \quad (22)$$

Since  $\Delta p = p_i^* \times \Delta p_{\text{ref}}$  and  $\Delta p_{\text{ref}} \equiv 12\mu L Q_{\text{ref}} / W_i H_0^3$ , the volumetric flow rate correlation with pressure difference across the channel can be elicited as

$$Q = \frac{\tau_o - 1}{\ln(\tau_o)} \frac{W_i H_0^3}{12\mu L} \Delta p. \quad (23)$$

It should be noted that the relationship for a straight channel, *i.e.*  $\tau_o = 1$ , can be obtained through  $\lim_{\tau_o \rightarrow 1} Q$ , that results in

$$Q = \frac{W_i H_0^3}{12\mu L} \Delta p, \quad (24)$$

which is the well-known characteristic of shallow rigid microchannels. Using Eq. 23, we can calculate the rectification ratio as follows:

$$\eta \equiv \frac{Q_{\text{Nozzle}}}{Q_{\text{Diffuser}}} = \frac{\frac{\tau_{o,N} - 1}{\ln(\tau_{o,N})} \times W_{i,N}}{\frac{\tau_{o,D} - 1}{\ln(\tau_{o,D})} \times W_{i,D}}, \quad (25)$$

where  $W_{i,N}$  and  $W_{i,D}$  refer to the width at inlet section for the fluid flow in nozzle and diffuser directions, respectively. Similarly,  $W_{o,N}$  and  $W_{o,D}$  denote the width at outlet section of for the fluid flow in nozzle and diffuser directions, respectively. We have  $\tau_{o,N} = W_{o,N} / W_{i,N}$  and  $\tau_{o,D} = W_{o,D} / W_{i,D}$ . We know that  $W_{i,N} = W_{o,D}$ ,  $W_{i,D} = W_{o,N}$ , and  $\tau_{o,N} = 1 / \tau_{o,D}$ ; see Fig. 41. Since  $\ln(\tau_{o,N}) = -\ln(\tau_{o,D})$ , after some algebraic calculations, one can obtain

$$\begin{aligned}
\eta &= \frac{\tau_{o,N} - 1}{1 - \tau_{o,D}} \frac{W_{i,N}}{W_{i,D}} \\
&= \frac{\tau_{o,N} - 1}{1 - 1/\tau_{o,N}} \frac{1}{\tau_{o,N}} \\
&= 1,
\end{aligned} \tag{26}$$

which states there is no flow rectification using a rigid nozzle/diffuser microchannel under the Stokes flow regime.

### Extremely large flexibility parameter

For deformable channels under sufficiently large pressure differences, the flexibility parameter can be extremely large, so that the term with the third order of flexibility parameter, *i.e.*  $\chi^3$ , dominates the left-side of Eq. 18 simplifying the ODE into

$$\alpha_3 \tau^{13}(\xi) p^{*3}(\xi) \frac{dp^*(\xi)}{d\xi} = 1, \tag{27}$$

$$\text{Initial value: } \quad \xi = 0 : p^* = 0.$$

For a nozzle/diffuser, where  $\tau(\xi) = \tau_o + (1 - \tau_o)\xi$ , one can solve Eq. 27 to obtain the following analytical expression for the pressure distribution within the channel:

$$p^*(\xi) = \left( \frac{\tau^{12}(\xi) - \tau_o^{12}}{3\tau_o^{12}\tau^{12}(\xi)\alpha_3(1 - \tau_o)} \right)^{\frac{1}{4}}. \tag{28}$$

The dimensionless pressure at inlet, where  $\tau(\xi = 1) = 1$ , can then be obtained as

$$p_i^* = \left( \frac{1 - \tau_o^{12}}{3\tau_o^{12}\alpha_3(1 - \tau_o)} \right)^{\frac{1}{4}}. \tag{29}$$

Since  $\alpha_3 = \frac{1024}{3003}(\Delta p_{\text{ref}} W_i^4 / 384 D H_0)^3$ ,  $\Delta p = p_i^* \times \Delta p_{\text{ref}}$ , and  $\Delta p_{\text{ref}} \equiv 12\mu L Q_{\text{ref}} / W_i H_0^3$ , the volumetric flow rate correlation with pressure difference across the channel can be elicited as

$$Q = \left( \frac{1}{664,215,552} \frac{(1 - \tau_o)\tau_o^{12}}{1 - \tau_o^{12}} \frac{W_i^{13}}{\mu L D^3} \right) \times \Delta p^4, \tag{30}$$

which shows a height-independent characteristic behavior, because the membrane deformation is significantly larger than the original height of microchannel under this regime. It should be noted that the relationship for a straight channel, *i.e.*  $\tau_o = 1$ , can be obtained through  $\lim_{\tau_o \rightarrow 1} Q$ , that results in

$$Q = \frac{1}{664, 215, 552} \times \frac{W_i^{13}}{12\mu LD^3} \times \Delta p^4, \quad (31)$$

which is in agreement with [187]. Using Eq. 30, the rectification ratio of nozzle/diffuser channel under this regime is calculated as follows:

$$\begin{aligned} \eta \equiv \frac{Q_{\text{Nozzle}}}{Q_{\text{Diffuser}}} &= \frac{\frac{(1-\tau_{0,N})\tau_{0,N}^{12}}{1-\tau_{0,N}^{12}} \times W_{i,N}^{13}}{\frac{(1-\tau_{0,D})\tau_{0,D}^{12}}{1-\tau_{0,D}^{12}} \times W_{i,D}^{13}} \\ &= \frac{\frac{(1-\tau_{0,N})\tau_{0,N}^{12}}{1-\tau_{0,N}^{12}}}{\frac{(1-\tau_{0,N}^{-1})\tau_{0,N}^{-12}}{1-\tau_{0,N}^{-12}}} \times \frac{1}{\tau_{0,N}^{13}} \\ &= 1. \end{aligned} \quad (32)$$

### Behavioral characteristics solely due to $\chi^1$ term

The potential characteristic behavior appearing when the first order of flexibility parameter, *i.e.*  $\chi$ , becomes important can be examined from solving the following ODE:

$$\alpha_1 \tau^5(\xi) p^*(\xi) \frac{dp^*(\xi)}{d\xi} = 1, \quad (33)$$

$$\text{Initial value: } \quad \xi = 0 : p^* = 0.$$

For a nozzle/diffuser, where  $\tau(\xi) = \tau_o + (1 - \tau_o)\xi$ , one can solve Eq. 33 to obtain the following analytical expression for the pressure distribution within the channel:

$$p^*(\xi) = \left( \frac{(\tau^4(\xi) - \tau_o^4)}{2\tau_o^4 \tau^4(\xi) \alpha_1 (1 - \tau_o)} \right)^{\frac{1}{2}}. \quad (34)$$

The dimensionless pressure at inlet, where  $\tau(\xi = 1) = 1$ , can then be obtained as

$$p_i^* = \left( \frac{(1 - \tau_o^4)}{2\tau_o^4 \alpha_1 (1 - \tau_o)} \right)^{\frac{1}{2}}. \quad (35)$$

Since  $\alpha_1 = \frac{8}{5}(\Delta p_{\text{ref}} W_i^4 / 384 D H_0)^2$ ,  $\Delta p = p_i^* \times \Delta p_{\text{ref}}$ , and  $\Delta p_{\text{ref}} \equiv 12\mu L Q_{\text{ref}} / W_i H_0^3$ , the volumetric flow rate correlation with pressure difference across the channel can be elicited as

$$Q = \left( \frac{1}{1,440} \frac{(1 - \tau_o) \tau_o^4}{1 - \tau_o^4} \frac{W_i^5 H_0^2}{\mu L D} \right) \times \Delta p^2. \quad (36)$$

It should be noted that the relationship for a straight channel, *i.e.*  $\tau_o = 1$ , can be obtained through  $\lim_{\tau_o \rightarrow 1} Q$ , that results in

$$Q = \frac{1}{1,440} \times \frac{W_i^5 H_0^2}{4\mu L D} \times \Delta p^2, \quad (37)$$

which is in agreement with [187]. The rectification ratio of nozzle/diffuser channel under this regime is calculated as follows:

$$\begin{aligned} \eta \equiv \frac{Q_{\text{Nozzle}}}{Q_{\text{Diffuser}}} &= \frac{\frac{(1 - \tau_{0,N}) \tau_{0,N}^4}{1 - \tau_{0,N}^4} \times W_{i,N}^5}{\frac{(1 - \tau_{0,D}) \tau_{0,D}^4}{1 - \tau_{0,D}^4} \times W_{i,D}^5} \\ &= \frac{\frac{(1 - \tau_{0,N}) \tau_{0,N}^4}{1 - \tau_{0,N}^4}}{\frac{(1 - \tau_{0,N}^{-1}) \tau_{0,N}^{-4}}{1 - \tau_{0,N}^{-4}}} \times \frac{1}{\tau_{0,N}^5} \\ &= 1. \end{aligned} \quad (38)$$

### Behavioral characteristics solely due to $\chi^2$ term

The potential characteristic behavior appearing when the second order of flexibility parameter, *i.e.*  $\chi^2$ , becomes important can be examined from solving the following ODE:

$$\alpha_2 \tau^9(\xi) p^{*2}(\xi) \frac{dp^*(\xi)}{d\xi} = 1, \quad (39)$$

Initial value:  $\xi = 0 : p^* = 0$ .

For a nozzle/diffuser, where  $\tau(\xi) = \tau_o + (1 - \tau_o)\xi$ , one can solve Eq. 39 to obtain the following analytical expression for the pressure distribution within the channel:

$$p^*(\xi) = \left( \frac{3(\tau^8(\xi) - \tau_o^8)}{8\tau_o^8\alpha_2(1 - \tau_o)} \right)^{\frac{1}{3}}. \quad (40)$$

The dimensionless pressure at inlet, where  $\tau(\xi = 1) = 1$ , can then be obtained as

$$p_i^* = \left( \frac{3(1 - \tau_o^8)}{8\tau_o^8\alpha_2(1 - \tau_o)} \right)^{\frac{1}{3}}. \quad (41)$$

Since  $\alpha_2 = \frac{128}{105}(\Delta p_{\text{ref}} W_i^4 / 384 D H_0)^2$ ,  $\Delta p = p_i^* \times \Delta p_{\text{ref}}$ , and  $\Delta p_{\text{ref}} \equiv 12\mu L Q_{\text{ref}} / W_i H_0^3$ , the volumetric flow rate correlation with pressure difference across the channel can be elicited as

$$Q = \left( \frac{1}{544,320} \frac{(1 - \tau_o)\tau_o^8}{1 - \tau_o^8} \frac{W_i^9 H_0}{\mu L D^2} \right) \times \Delta p^3. \quad (42)$$

It should be noted that the relationship for a straight channel, *i.e.*  $\tau_o = 1$ , can be obtained through  $\lim_{\tau_o \rightarrow 1} Q$ , that results in

$$Q = \frac{1}{544,320} \times \frac{W_i^9 H_0}{8\mu L D^2} \times \Delta p^3, \quad (43)$$

which is in agreement with [187]. The rectification ratio of nozzle/diffuser channel under this regime is calculated as follows:

$$\begin{aligned} \eta \equiv \frac{Q_{\text{Nozzle}}}{Q_{\text{Diffuser}}} &= \frac{\frac{(1 - \tau_{0,N})\tau_{0,N}^8}{1 - \tau_{0,N}^8} \times W_{i,N}^9}{\frac{(1 - \tau_{0,D})\tau_{0,D}^8}{1 - \tau_{0,D}^8} \times W_{i,D}^9} \\ &= \frac{\frac{(1 - \tau_{0,N})\tau_{0,N}^8}{1 - \tau_{0,N}^8}}{\frac{(1 - \tau_{0,N}^{-1})\tau_{0,N}^{-8}}{1 - \tau_{0,N}^{-8}}} \times \frac{1}{\tau_{0,N}^9} \\ &= 1. \end{aligned} \quad (44)$$

## Materials and methods

In order to validate the mathematically-described underlying coupled fluid-solid mechanics of the fluid flow through a deformable nozzle/diffuser microchannel, we fabricated microfluidic devices and performed experiments to obtain the volumetric flow rate over the applied pressure difference range of 14–206 kPa. The microchannels were created through glass wet etching process, drilling the via-holes, and adhesive bonding using a 2  $\mu\text{m}$ -SU8-coated PET (polyethylene terephthalate) film ( $t = 100 \mu\text{m}$ ,  $E = 3 \text{ GPa}$ , and  $\nu = 0.4$ ) followed by bonding reinforcement using a glass slide with the sufficiently deep ( $\sim 45 \mu\text{m}$ ) etched pattern of the microchannel allowing the membrane to deform freely under pressure. The reinforcement glass was bonded to the bare side of the membrane using a 16  $\mu\text{m}$  SU8 layer ( $E \sim 2 \text{ GPa}$ ) [187]. The blank glass slides were used for reinforcement of rigid channels to avoid membrane deformations [164]. The structural effects of the adhesive layers can be taken into account in our model by using the transformed-section method [165]. The equivalent membrane thickness is calculated from  $\tilde{t} = \sqrt[3]{12I/W}$ , where  $I$  denotes the three-layer membrane's moment of inertia. The equivalent membrane thickness, *i.e.*  $\tilde{t}$ , replaces  $t$  in the parameter  $D$  of Eq. 19 (b) to evaluate the flexibility parameter. Considering the aforementioned values for thickness and modulus of elasticity of different layers,  $\tilde{t} \approx 113 \mu\text{m}$ .

A pressure-driven flow was generated at constant pressure levels by employing a compressed air to push a working fluid out of a custom-made flask with two ports. A pressure source is connected to one end of the flask via a pressure regulator (PneumaticPlus, PPR2-N02BG-4 Miniature Air Pressure Regulator), while the other end is connected to the microchannel's inlet. The liquid discharged from the microchannel was guided through a tube with a known inner diameter, where the meniscus position was monitored over time to calculate the volumetric flow rate.

## Results and discussion

### Microchannel design

The fluid-solid characteristics rely on the following three general categories: 1) microchannel cross-sectional dimensions:  $W_i$ ,  $W_o$ , and  $H_0$ , 2) membrane thickness and structural properties, which are lumped into the parameter of  $D$ , and 3) pressure difference across the microchannel,  $\Delta p$ . Once the channels are fabricated, the first two categories become fixed and pressure difference dictates the channel characteristic behavior. Based on our available resources and our developed fabrication protocol, we have chosen a 100-micron-thick PET film for the channels' ceiling, which makes the second category fixed. In order to choose the cross-sectional dimensions of the microchannels for the experimental investigations, we have used the developed model to predict the rectification ratios of nozzle/diffuser microchannels with different geometries.

We have theoretically studied the performance of numerous fluidic rectifiers with  $2.6 \mu\text{m}$  in original height and different widths under our experimentally accessible range of applied pressure difference ( $14 \text{ kPa} < \Delta p < 206 \text{ kPa}$ ), the obtained results for several of which are shown in Fig. 42. We have chosen the nozzle/diffuser channels with the pair of widths of 1 and 2  $\text{mm}$  to be studied experimentally due to their relatively larger rectification ratios. It is worth mentioning that the half-angle is not a design parameter, since it needs to be very small ( $\theta \approx 0$ ) so that the Poiseuille flow characteristics for a straight channel and the Euler-Bernoulli beam theory are locally valid. In practice, this parameter needs to be sufficiently small ( $\theta \ll 1$ ) to meet the aforementioned requirement reasonably.

### Experimental and theoretical investigation

One of the several width profiles theoretically studied is chosen here for our experimental investigation, in which the nozzle/diffuser large and small widths equal 2  $\text{mm}$  and 1  $\text{mm}$ , respectively, and half-angle is  $\theta = 1.25^\circ$ , *i.e.*  $L \approx 22.9 \text{ mm}$ . The half-angle is chosen to be sufficiently small so that  $dW/2dx \approx 0.022$  meets the requirement of  $dW/2dx \ll 1$

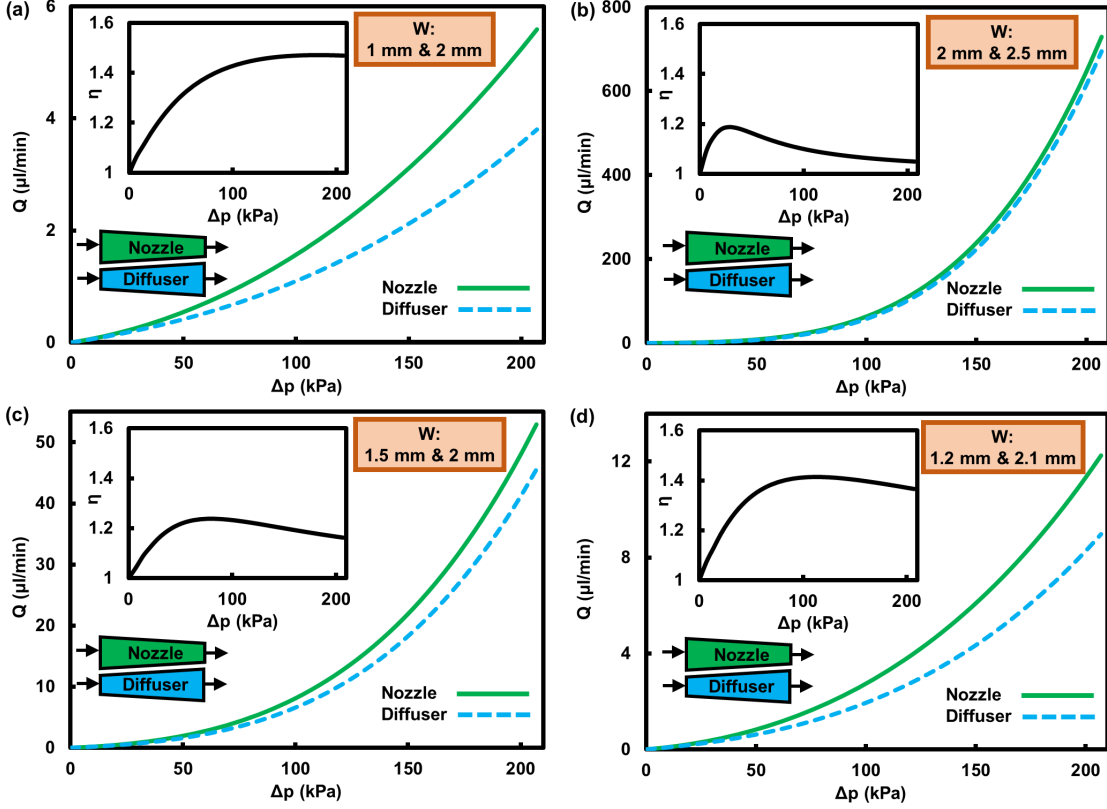


Figure 42: Volumetric flow rates of water obtained from the 1-D coupled fluid-solid-mechanics model as a function of pressure difference across the deformable nozzle/diffuser microchannels of  $2.6 \mu\text{m}$  in height with the half-angle of  $\theta = 1.25^\circ$  for various small and large widths configurations: (a)  $1 \text{ mm}$  and  $2 \text{ mm}$ , (b)  $2 \text{ mm}$  and  $2.5 \text{ mm}$ , (c)  $1.5 \text{ mm}$  and  $2 \text{ mm}$ , and (d)  $1.2 \text{ mm}$  and  $2.1 \text{ mm}$ . The insets show the rectification ratio, *i.e.*  $\eta = Q_{\text{Nozzle}}/Q_{\text{Diffuser}}$ , as a function of pressure difference across the channel.

and the Poiseuille flow characteristics for a straight channel and the Euler-Bernoulli beam theory are locally valid. The obtained experimental results are shown in Fig. 43 for DI water ( $\mu = 8.9 \times 10^{-4} \text{ Pa}\cdot\text{s}$ ) flow through deformable/rigid nozzle/diffuser microchannels with different original heights. Regarding the theoretical results for the rigid microchannels, the analytical expression obtained in Eq. 23 is used. Alternatively, one can still numerically solve Eq. 18 considering an infinitely large membrane's modulus of elasticity so that  $\chi = 0$ .

For rigid microchannels, the volumetric flow rate increases linearly with pressure difference. The rigid nozzle and diffuser exhibit the same behavior resulting in no flow rectification, *i.e.* the hydrodynamic resistance is not dependent on the flow direction. For the deformable microchannels, however, because of the membrane deformation the volumetric flow rate increases non-linearly with pressure difference, causing the hydrodynamic resistance to be

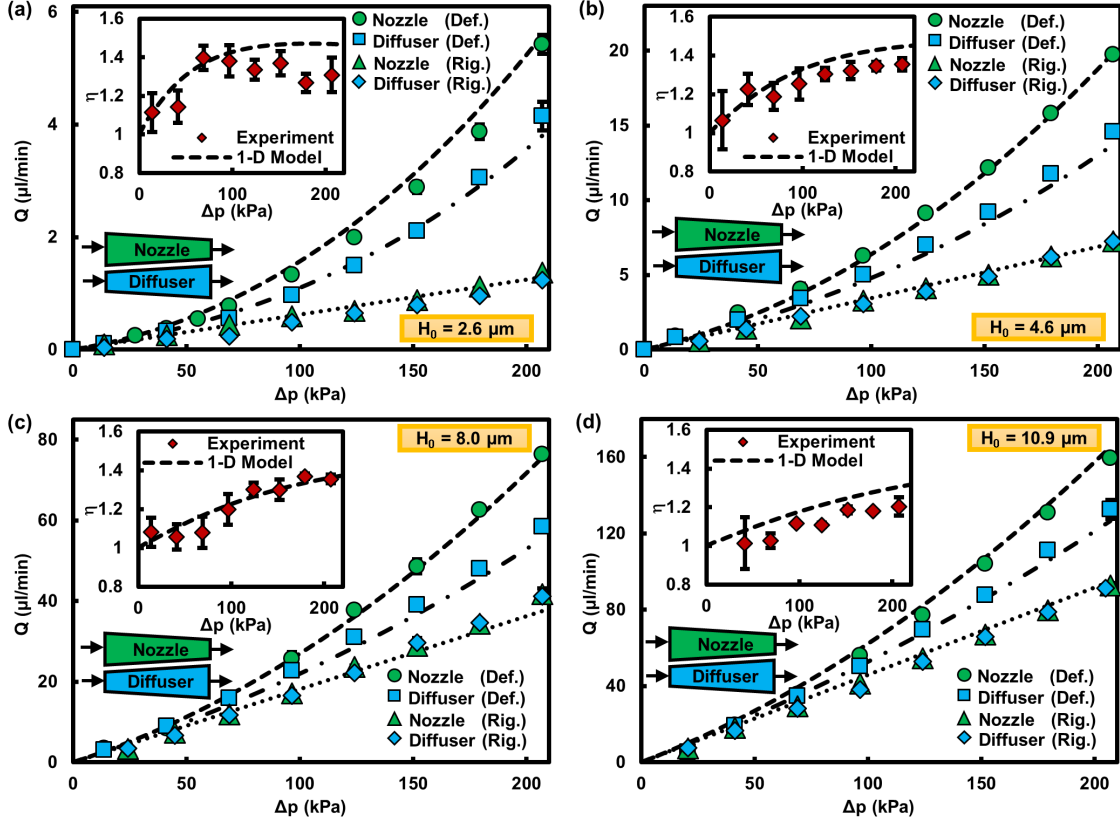


Figure 43: Volumetric flow rates of DI water as a function of pressure difference across the deformable/rigid nozzle/diffuser microchannels for various original heights of  $H_0 =$  (a)  $2.6 \pm 0.1 \mu\text{m}$ , (b)  $4.6 \pm 0.1 \mu\text{m}$ , (c)  $8.0 \pm 0.2 \mu\text{m}$ , and (d)  $10.9 \pm 0.2 \mu\text{m}$ . The dashed, dash-dotted, and dotted lines show the results obtained from the one-dimensional model for deformable nozzle, deformable diffuser, and rigid nozzle/diffuser, respectively. The insets show the rectification ratio, *i.e.*  $\eta = Q_{\text{Nozzle}}/Q_{\text{Diffuser}}$ , as a function of pressure difference across the deformable nozzle/diffuser microchannels. The error bars related to the experimental results (averaged over three runs) are not visible if they are smaller than the markers size.

pressure-dependent. Furthermore, the deformable nozzle delivers a larger volumetric flow rate compared to the deformable diffuser under the same pressure difference resulting in a flow rectification. The rectification ratio is defined as  $\eta = Q_{\text{Nozzle}}/Q_{\text{Diffuser}}$ . The rectification ratio approaches unity as the pressure difference decreases toward zero, since the flexibility parameter's approach to zero diminishes the role of non-linear terms in the governing coupled fluid-solid-mechanics equation shown in Eq. 18. As a result, a deformable microchannel exhibits a characteristic behavior similar to that of its rigid counterpart without flow rectification. A sufficiently large increase in pressure difference activates the non-linear terms of  $\alpha_i \tau^{4i}(\xi) p^{*i}(\xi) : i = 1, 2, \text{ and } 3$  in Eq. 18 allowing the embedded non-linear nature of the governing coupled fluid-solid-mechanics equation to emerge, because of which the flow

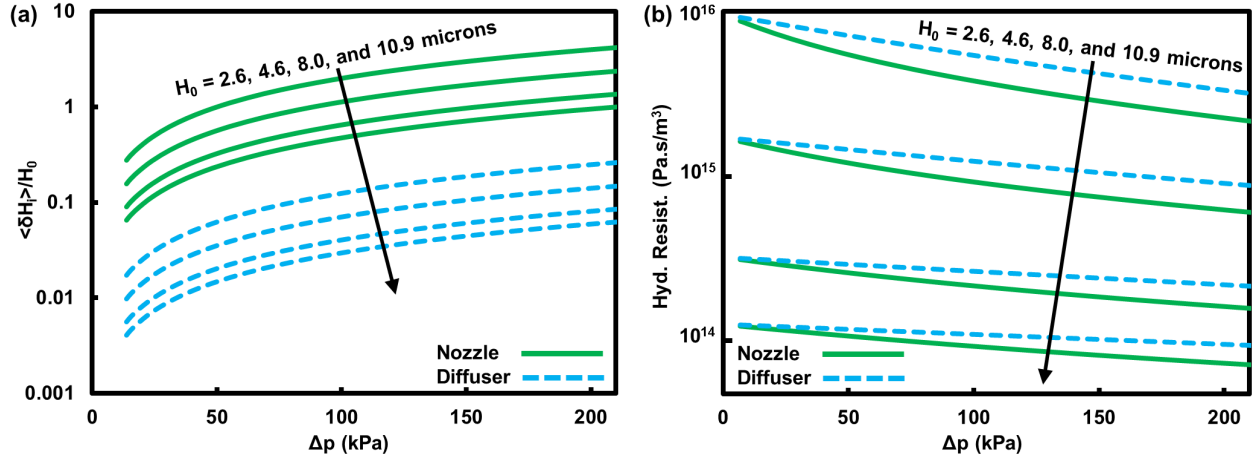


Figure 44: (a) Average of the membrane displacement at inlet over the channel original height and (b) the hydrodynamic resistance, *i.e.*  $R_{\text{hyd.}} = \Delta p / Q$ , as a function of pressure difference across the deformable nozzle/diffuser microchannels with the the half-angle of  $\theta = 1.25^\circ$ , small and large widths of 1 mm and 2 mm, and various original heights, obtained from the 1-D coupled fluid-solid-mechanics model.

rectification is observed.

The averaged membrane displacement at inlet obtained from Eq. 15 is shown in Fig. 44 (a) for the experimentally investigated deformable nozzle/diffuser microchannels. Since the inlet section exhibits the maximum membrane displacement, one can clearly notice that the membrane displacements in the nozzles are about two orders of magnitude larger than those in their counterpart diffusers, leading to the direction-dependent hydrodynamic resistances and fluid flow rectification.

From Fig. 43, increasing the channel original height can attenuate the contrast between the deformable and rigid channels' characteristics, since the membrane deformation becomes less significant compared with the channel original height, and consequently the membrane deformation-induced change in hydrodynamic resistance plays a less noticeable role in the net hydrodynamic resistance; see Fig. 44 (b). As a result, the rectification ratio decreases as the channel original height increases. The contrast between the characteristics of deformable/rigid nozzle/diffuser microchannels becomes even less significant for the channel height of 41  $\mu\text{m}$ , where the maximum rectification ratio is about 1.1, Fig. 45, as opposed to 1.43 for the channel with the original height of 2.6  $\mu\text{m}$ .

It is worth mentioning that the rectification ratio can decrease after reaching its maximum

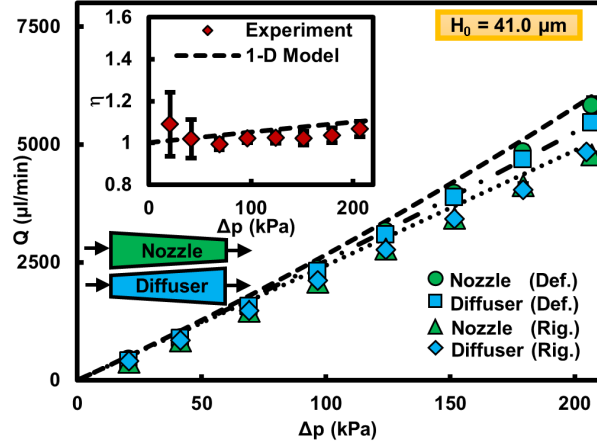


Figure 45: Volumetric flow rate of DI water as a function of pressure difference across the deformable nozzle/diffuser microchannel of  $\sim 41 \mu\text{m}$  in height, small and large widths of  $1 \text{ mm}$  and  $2 \text{ mm}$ , and half-angle of  $\theta = 1.25^\circ$ . The dashed, dash-dotted, and dotted lines show the results obtained from the one-dimensional model for deformable nozzle, deformable diffuser, and rigid nozzle/diffuser, respectively. The inset shows the rectification ratio, *i.e.*  $\eta = Q_{\text{Nozzle}}/Q_{\text{Diffuser}}$ , as a function of pressure difference across the deformable nozzle/diffuser microchannel.

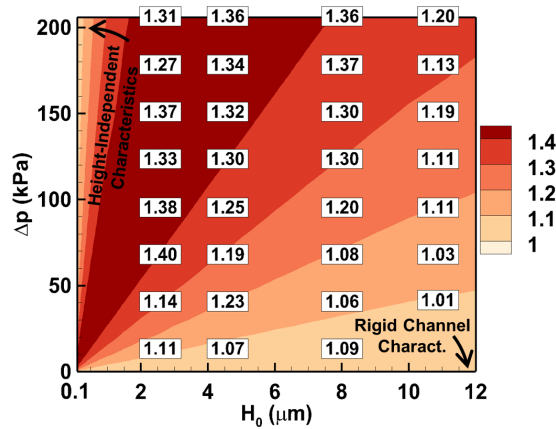


Figure 46: The rectification ratio contour obtained from the 1-D model for the nozzle/diffuser microchannels with the widths of  $1 \text{ mm}$  and  $2 \text{ mm}$  together with the experimental results tabulated at the corresponding  $(H_0, \Delta p)$ .

by further increasing the pressure difference; see Fig. 46. The analytical solution presented in Eqs. 30 and 32, for the case of sufficiently large pressure difference, where the third order of flexibility parameter ( $\chi^3$ ) dictates the behavioral characteristics, shows the rectification ratio approaches unity as the pressure difference increases.

The pressure distribution and the membrane average displacement along the channel are presented in Fig. 47 for the experimentally investigated deformable nozzle/diffuser microchannels. For the fabricated microchannels with established membrane properties and

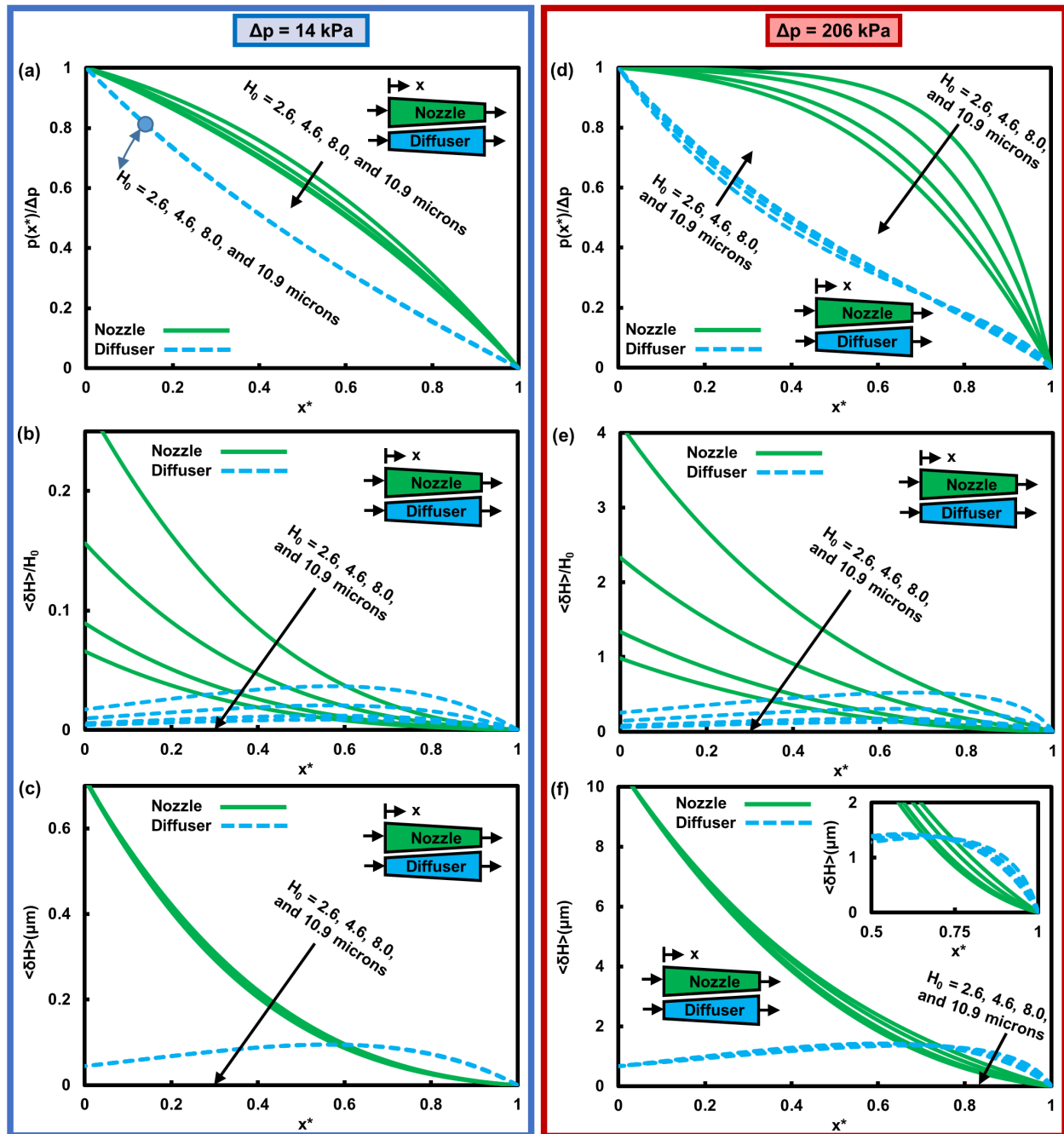


Figure 47: (a and d) Dimensionless pressure, *i.e.*  $p/\Delta p$ , along the channel, together with the (b and e) average of the membrane displacement at any  $x$ -plane over the channel original height, and (c and f) average of the membrane displacement at any  $x$ -plane for deformable nozzle/diffuser microchannels with the the half-angle of  $\theta = 1.25^\circ$ , small and large widths of  $1\text{ mm}$  and  $2\text{ mm}$ , and various original heights under the pressure differences of (a–c)  $\Delta p = 14\text{ kPa}$  and (d–f)  $\Delta p = 206\text{ kPa}$ . Inset in (f) shows the magnified zone between  $x^* = 0.5$  and  $x^* = 1$ .

channel geometry, pressure difference dictates the flow-structure behavior. Under the low pressure difference of  $14\text{ kPa}$ , the membrane deformations are small compared to the original

heights of the microchannels, causing negligible effects on the pressure distributions within the channels. The same microchannels show significantly different characteristics under 206 kPa due to the noticeably larger membrane deformations. Considering Eq. 18 consisting of the terms with different orders of flexibility parameter, depending on the applied pressure difference, various regimes of fluid-solid characteristics can appear spanning from small wall deflections, where the deformable microchannel resembles its rigid counterpart, Eq. 23, to wall deflections much larger than the channel original height, where the height-independent characteristic behavior emerges, Eq. 30.

Considering the terms of  $\alpha_i \tau^{4i}(\xi) p^{*i}(\xi)$  :  $i = 1, 2,$  and  $3$  in Eq. 18, one can conclude that for a straight channel ( $\tau = 1$ ), the pressure distribution is the same within the nozzle and diffuser. By using a width profile function asymmetric with respect to the mid-plane  $x^* = \xi = 1/2$ , the distinct fluid-solid characteristics can appear at opposite fluid flow directions (Fig. 47). For example, under the same pressure difference,  $pW^4 = 0$  at the outlet regardless of the flow direction. Whereas, because of the fourth order of  $W$  in the  $pW^4$  term, a two-time difference in the channel widths causes this term to be one order of magnitude larger at the nozzle inlet compared with the corresponding value at the the diffuser inlet. Such a noticeable difference in the  $pW^4$  term results in a considerable contrast between the membrane deformations (Eqs. 15 and 17) at opposite flow directions, and consequently a flow rectification is obtained.

We define the Reynolds number as

$$\text{Re}(x) = \frac{\rho \bar{u}(x) D_h(x)}{\mu}, \quad (45)$$

where  $\rho$  denotes the fluid density ( $1000 \text{ kg/m}^3$  for water), and  $\bar{u}$  shows the average of the flow-wise component of velocity. In addition,  $D_h$  refers to the hydraulic diameter. For the microchannels studied in this work, where  $H_0 \ll W$ , we consider the hydraulic diameter as

$$D_h(x) \equiv 2 \times \left( H_0 + \langle \delta H \rangle_{(x)} \right). \quad (46)$$

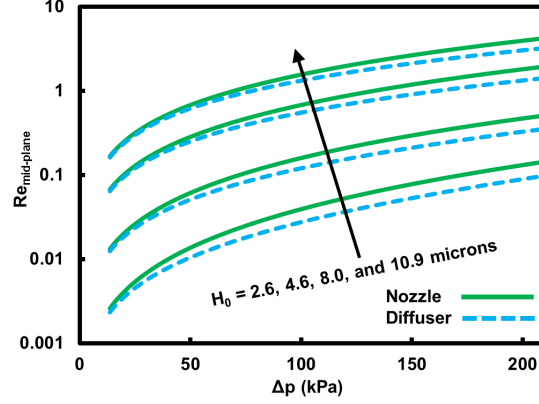


Figure 48: Reynolds number in the mid-plane ( $x^* = 0.5$ ) for water flow through the deformable nozzle/diffuser microchannels with the half-angle of  $\theta = 1.25^\circ$ , small and large widths of  $1 \text{ mm}$  and  $2 \text{ mm}$ , and various original heights, obtained from the 1-D coupled fluid-solid-mechanics model.

We can write

$$\begin{aligned} \bar{u}(x) &= \frac{Q}{W(x)(H_0 + \langle \delta H \rangle_{(x)})} \\ &= \frac{2Q}{W(x)D_h(x)}. \end{aligned} \quad (47)$$

From Eqs. 45 and 47, one can write

$$\text{Re}(x) = \frac{2\rho Q}{\mu W(x)}. \quad (48)$$

The obtained Reynolds number in the mid-plane ( $x^* = 0.5$ ) for water flow through the experimentally investigated deformable nozzle/diffuser microchannels are presented in Fig. 48. According to Fig. 48, most of the experimentally studied cases, *i.e.* the channels with  $2.6 \mu\text{m}$  and  $4.6 \mu\text{m}$  in height under all the investigated pressure differences as well as those with  $8.0 \mu\text{m}$  and  $10.9 \mu\text{m}$  in height under the sufficiently small pressure differences, fall under the Stokes flow regime ( $\text{Re} \ll 1$ ). Particularly, a rectification ratio of about 1.4 has been observed experimentally and theoretically for the channels with  $2.6 \mu\text{m}$  and  $4.6 \mu\text{m}$  in height (Fig. 43) operating under the Stokes flow regime (Fig. 48).

### Other liquids as working fluid: viscosity effects

To investigate the effects of the viscosity, we experimented with different working fluids whose viscosity is substantially different from that of DI water. Methanol ( $\mu = 5.9 \times 10^{-4} \text{ Pa}\cdot\text{s}$ ) and

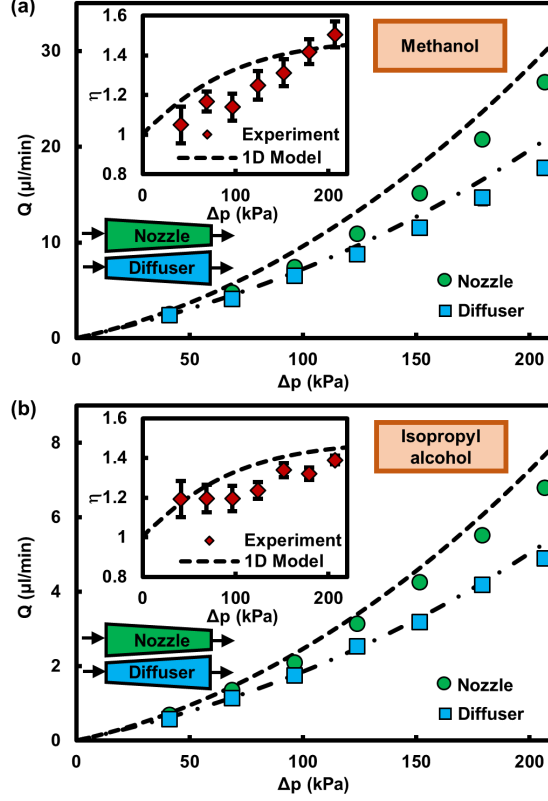


Figure 49: Volumetric flow rate as a function of pressure difference across the deformable nozzle/diffuser microchannel of  $\sim 4.6 \mu\text{m}$  in height for two different working fluids: (a) Methanol ( $\mu = 5.9 \times 10^{-4} \text{ Pa}\cdot\text{s}$ ) and (b) Isopropyl alcohol ( $\mu = 2.3 \times 10^{-3} \text{ Pa}\cdot\text{s}$ ). The dashed and dash-dotted lines show the results obtained from the one-dimensional model for the deformable nozzle and diffuser, respectively. The insets show the rectification ratio, *i.e.*  $\eta = Q_{\text{Nozzle}}/Q_{\text{Diffuser}}$ , as a function of pressure difference across the channel.

Isopropyl Alcohol ( $\mu = 2.3 \times 10^{-3} \text{ Pa}\cdot\text{s}$ ) have been tested in the deformable nozzle/diffuser with  $4.6 \mu\text{m}$  in height. Figure 49 depicts the theoretical and experimental results of the pressure drop vs. volumetric flow rate as well as the flow rectification ratios. Even though the volumetric flow rate decreases as the fluid viscosity increases, the theoretical rectification ratio remains the same for different studied fluids. The dimensionless volumetric flow rate and consequently the rectification ratio depend on the pressure distribution within the nozzle/diffuser microchannels (Eq. 16), which is solely dictated by the membrane properties as well as the channel width and original height; see Eqs. 18 and 19.

## Effects of width profile function

For the purpose of investigating the effects of nonlinear width profile functions, we consider the width profile in diffuser direction as

$$W_D(x^*) = W_{i,D} + (W_{o,D} - W_{i,D})x^{*\beta}, \quad (49)$$

where  $\beta$  is an arbitrary variable for adjusting the width profile. The width profile function for the diffuser direction can then be written as

$$\tau_D(x^*) = \frac{W_D}{W_{i,D}} = 1 + (\tau_{o,D} - 1)x^{*\beta}, \quad (50)$$

where  $\tau_{o,D} = W_{o,D}/W_{i,D}$ . One can show that the same width profile can be written as

$$W_N(x^*) = W_{o,N} + (W_{i,N} - W_{o,N})(1 - x^*)^\beta, \quad (51)$$

for nozzle direction. The width profile function for the nozzle direction can then be written as

$$\tau_N(x^*) = \frac{W_N}{W_{i,N}} = \tau_{o,N} + (1 - \tau_{o,N})(1 - x^*)^\beta, \quad (52)$$

where  $\tau_{o,N} = W_{o,N}/W_{i,N}$ . The schematic representation of the nonlinear microchannel width profiles is shown in Fig. 50 (a). Deformable nozzle/diffuser microchannels are considered to be  $2.6 \mu\text{m}$  in height with the half-angle of  $\theta = 1.25^\circ$ , and small and large widths of  $0.3 \text{ mm}$  and  $2 \text{ mm}$ .

Volumetric flow rates of water together with the rectification ratios obtained from the proposed 1-D coupled fluid-solid-mechanics model are shown in Fig. 50 (b) for three width profile functions related to  $\beta = 0.3, 1.0, \text{ and } 2.0$ . It is perceived that the width profile with  $\beta = 0.3$  exhibits the rectification ratios larger than those of the linear width profile, i.e.  $\beta = 1.0$ , while the width profile with  $\beta = 2.0$  results in the rectification ratios smaller than those of the linear width profile. Although the small and large widths are the same for different investigated profiles, the profile with  $\beta = 0.3$  results in the channel widths larger than those

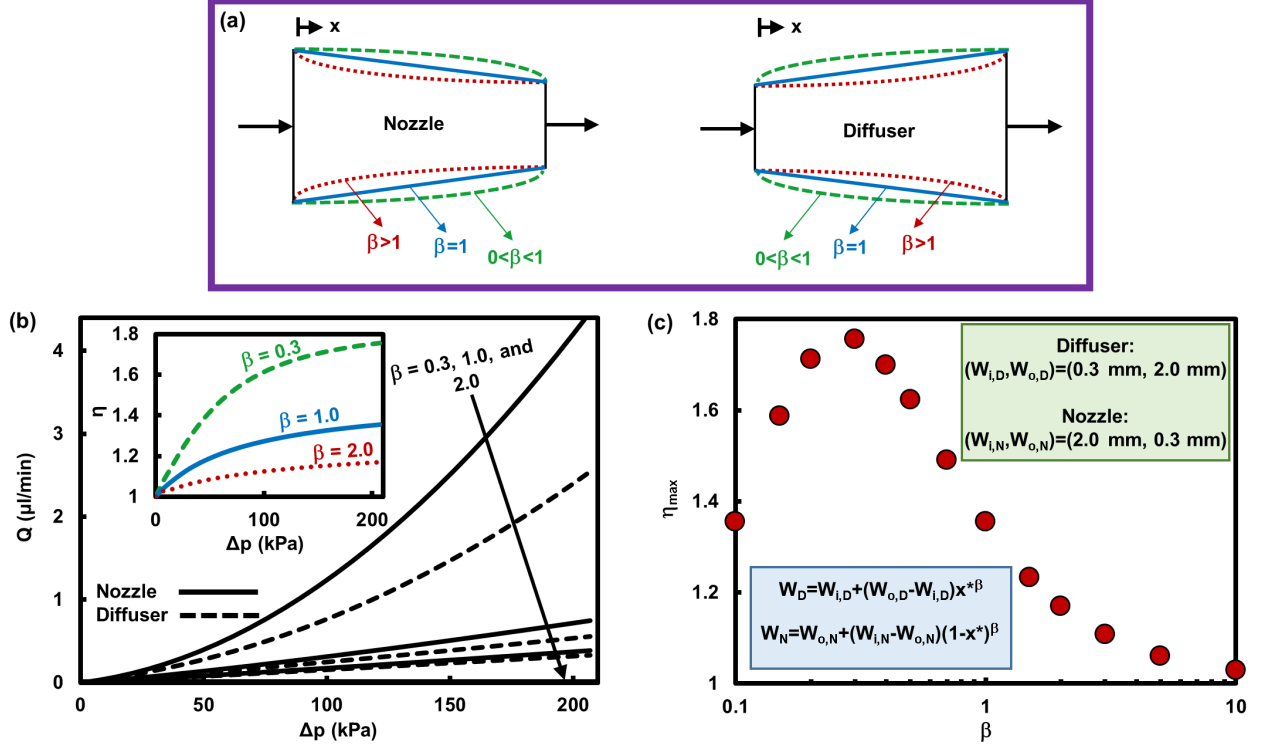


Figure 50: (a) Schematic presentation of the nonlinear microchannel width profiles in the nozzle direction, *i.e.*  $W_N = W_o + (W_i - W_o)(1 - x^*)^\beta$ , as well as the diffuser direction, *i.e.*  $W_D = W_i + (W_o - W_i)x^{*\beta}$ . (b) Volumetric flow rates of water obtained from the 1-D coupled fluid-solid-mechanics model as a function of pressure difference across the deformable nozzle/diffuser microchannels of  $2.6 \mu\text{m}$  in height with the half-angle of  $\theta = 1.25^\circ$ , and small and large widths of  $0.3 \text{ mm}$  and  $2 \text{ mm}$  for different with profiles. The inset shows the rectification ratio, *i.e.*  $\eta = Q_{\text{Nozzle}}/Q_{\text{Diffuser}}$ , as a function of pressure difference across the channel. (c) The maximum rectification ratio for microchannels with different width profiles achievable within the pressure difference range of  $14 \text{ kPa} - 206 \text{ kPa}$ .

of the linear width profile. This increase in width improves the rectification ratio because of extending the “wide” portion and shortening the “narrow” portion of the channel. The wide portion of the channel profile with  $\beta = 0.3$  has a larger contribution in the net hydrodynamic resistance as opposed to the linear width profile. Extending the wide portion of the channel makes the membrane displacement-induced change in the hydrodynamic resistance more comparable with the overall hydrodynamic resistance, leading to the relatively larger rectification ratios. The similar rationale can explain the smaller rectification ratios resulting from the width profile with  $\beta = 2.0$  compared with those of the linear width profile.

The maximum rectification ratio is presented in Fig. 50 (c) for the microchannels with different width profile functions operating within the pressure difference range of  $14 \text{ kPa} -$

206 kPa. As explained earlier, extending the wide portion of the channel, *i.e.* decreasing  $\beta$ , increases the rectification ratio. However, for  $\beta < 0.3$ , the rectification ratio reduces as  $\beta$  decreases, since a very large extension of the wide portion of the channel results in the large membrane deformations for the diffuser direction as well, reducing the contrast between the diffuser and nozzle characteristics. It is observed that the most efficient performance is delivered by the rectifier with the width profile related to  $\beta = 0.3$  and the pertinent maximum rectification ratio is  $\eta \approx 1.76$ . It should be noted that this value is not the maximum rectification ratio achievable using the proposed rectification mechanism based on the asymmetrically-shaped deformable microchannels, since we have fixed the small and large widths and arbitrarily considered a specific shape for the width profile with one design parameter, *i.e.*  $\beta$ , as expressed in Eqs. 49 and 51. One might be able to achieve larger rectification ratios using the more optimized width profile functions.

## Conclusion

We have shown that passive rectification of the Stokes flow regime is possible for Newtonian liquids by introducing the non-linear terms to the otherwise linear equations of motion. The proposed nonlinearity stems from the coupled fluid-solid mechanics of the flow behavior in an asymmetrically-shaped microchannel, *i.e.* nozzle/diffuser, with deformable ceiling. The flow rectification ratio of  $\sim 1.2$ – $1.8$  has been demonstrated for common Newtonian liquids like water and alcohol. The demonstrated rectification ratio of  $\sim 1.2$ – $1.8$  is comparable with many of the rectifiers resorting to non-Newtonian fluids under the Stokes flow regime [176–178]. The proposed platform is also more compatible with biospecies transport as opposed to the rectifiers using the flap structure [180–182], or ball/particle-based check-valves [184, 185], wherein the biospecies can be damaged by or stuck to the flap or particles/balls. Furthermore, due to the large hydrodynamic resistance of such shallow rectifiers, the leakage flow rate under the off mode is significantly small, suggesting the described underlying physics may be exploited to develop precise micropumps with low flow-rates as well as small-leakage microvalves with potential bioapplications such as species transport, drug delivery, etc. We

note that rectifiers with smaller dimensions can be made by using shorter and narrower microchannels sealed by a more compliant membrane, which suggests new opportunities for microfluidic integrated circuits. At the end, it is worth mentioning that the ODE presented in Eq. 18 can be reduced to the Abel's differential equation under the sufficiently low pressure differences across the channel, where the terms with  $\chi^2$  and  $\chi^3$  play minor role in Eq. 18, *i.e.*  $\alpha_2 = \alpha_3 = 0$ . Under these conditions, one might be able to find an analytical solution for the fluid-solid characteristics.

# Chapter 5: Low-Reynolds-number compressible fluid flow through straight deformable microchannels<sup>2</sup>

## Questions

The main questions of this research are enumerated in the following.

- Can an analytical model be derived for low-Reynolds-number compressible fluid flows of Newtonian fluids through a deformable straight microchannel to predict the main structural-fluid characteristics such as the volumetric flow rate, pressure variation through the channel, membrane deformation, etc?
- Can a master curve be found for mass flow rate versus pressure drop?
- How important channel deformability and fluid compressibility are under different regimes?

## Motivations

Compressible fluid flows through microchannels, which are important in Lab-on-a-chip and MEMS technologies, exhibit noticeable deviations from the incompressible Poiseuille flow characteristics. On the other hand, thin layers used in Lab-on-a-chip and MEMS technologies as the sidewalls of microchannels add another layer of complexity to the problem.

---

<sup>2</sup>Reproduced from *Physics of Fluids* 30, 092003 (2018); <https://doi.org/10.1063/1.5043202>, with the permission of AIP Publishing.

To the author’s knowledge, there is no analytical model in the literature taking both fluid compressibility and channel deformability into account, which motivates this research.

## Objectives

The objective of this research are to find an analytical model simultaneously taking both fluid compressibility and channel deformability into account for low-Reynolds-number fluid flows and provide a deeper understanding of the structural-fluid characteristic behavior under various levels of channel deformability and fluid compressibility.

## Introduction

Compressible fluid flows through microchannels have attracted an increasing attention due to its applications in Lab-on-a-chip and MEMS technologies such as micropumps [188, 189], flow rectification [190, 191], gas-liquid segmented microreactors [192–194], development of non-destructive approaches for quality control of small channels [195], etc. In particular, a gas flow through a microchannel is widely investigated theoretically [196–205] and experimentally [206, 207]. As new applications of compressible fluid flows through small channels emerge, new fundamental fluid mechanics problems come to existence, necessitating theoretical and experimental investigations. Gas flows through microchannels with varying cross sections [208–210], transient gas flows in microchannels [211, 212], and gas-liquid flow through microchannels [213, 214] are a few of the pertinent examples.

Compressible fluid flows through a channel exhibit noticeable deviations from the incompressible Poiseuille flow. Specifically, mass flow rate is underestimated under large pressure differences across a channel if the fluid compressibility is neglected. Consideration of fluid compressibility and density variations within a microchannel allows the Navier-Stokes equations to predict the fluid flow characteristics more accurately [204].

All of the aforementioned works focus on rigid channels. However, a microchannel with a sufficiently thin ceiling, which is commonly encountered in MEMS and Lab-on-a-chip

applications, can deform noticeably under sufficiently high pressures, causing the mass flow rate to be underestimated if channel deformability is not taken into account [215]. Channel bulging becomes more influential for shallower microchannels, where ceiling displacement is more comparable with the undeformed channel's height. The microchannel deformability effects have been well studied in the context of incompressible fluid flows [154–160,187]. One-dimensional models with [134] and without [19,163] the need of fitting parameters have been developed to capture main fluid-solid characteristics of an incompressible fluid flow through a deformable channel. However, a theoretical model capturing both channel deformability and fluid compressibility is still missing in the literature.

In this chapter, we utilize the lubrication theory and wide-beam framework to develop a one-dimensional coupled fluid-solid-mechanics model for prediction of characteristic behavior of compressible fluid flows through deformable microchannels. An explicit relationship is extracted for mass flow rate as a function of pressure difference across a microchannel, undeformed channel dimensions, properties of channel's ceiling such as thickness, modulus of elasticity and Poisson's ratio. The resulting fifth-order algebraic equation is also solved numerically to obtain the pressure distribution within the microchannel. As a special case for compressible fluid flows, characteristics of ideal gas flows are extracted from the general model. Rigid and deformable microchannels are fabricated, and mass flow rates of air through the channels are measured under various pressure differences across the channels. The proposed model predicts the mass flow rate with an acceptable accuracy. Our experimental and theoretical results highlight the importance of fluid compressibility and microchannel deformability, demonstrating that neglecting either of them under sufficiently large pressure differences can lead to erroneous results. To the best of the author's knowledge, this is the first theoretical model simultaneously addressing both fluid compressibility and microchannel deformability for an equilibrium pressure-driven compressible fluid flow in microscale.

## Modeling

### General Compressible Fluid Flow

The schematic representation of compressible fluid flow through a microchannel with a deformable ceiling is shown in Fig. 51. The one-dimensional model is based on the lubrication theory, *i.e.*  $H_0 \ll W \ll L$ , where  $H_0$ ,  $W$ , and  $L$  refer to the microchannel original height with no membrane deformation, width, and length, respectively. The thin-plate-bending framework is considered for the elastic deformation, which requires  $\delta H \ll t \ll W$ , where  $\delta H$  is the membrane displacement and  $t$  denotes the membrane thickness. Under these situations, and considering that  $W/L \ll 1$ , an arbitrary membrane's infinitesimal slice across the channel can be considered as a wide beam. The deflection profile of this slice is, therefore, presented as

$$\delta H(x, \zeta) = \frac{p(x)W^4}{384D} f(\zeta), \quad (53)$$

where  $\zeta \equiv 2y/W$ ,  $f(\zeta) = (\zeta + 1)^2(\zeta - 1)^2$ , and  $D = \frac{Et^3}{12(1-\nu^2)}$ .  $E$  and  $\nu$  denote the membrane's modulus of elasticity and Poisson's ratio, respectively [186]. In addition,  $p$  refers to the gauge

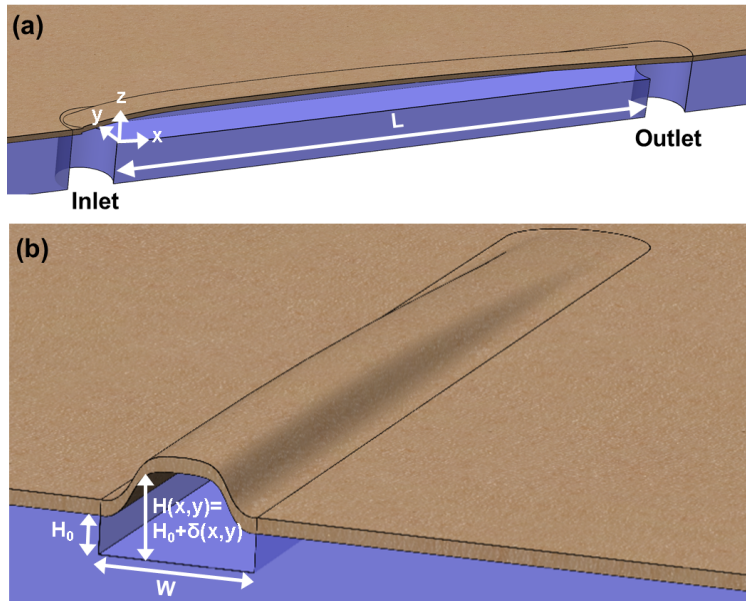


Figure 51: (a) Schematic representation of a compressible fluid flow through a microchannel with a deformable ceiling together with (b) the cross-section view of the channel.

pressure within the channel, which is constant at any x-plane, *i.e.* a plane normal to the x-axis, according to the lubrication theory.

For an isothermal compressible fluid flow, we have:

$$\frac{d\rho}{\rho} = \kappa_T dp, \quad (54)$$

where  $\rho$  refers to the fluid density, and the isothermal compressibility is defined as

$$\kappa_T = -\frac{1}{V} \left( \frac{\partial V}{\partial p} \right)_T, \quad (55)$$

in which  $V$  shows the volume occupied by a fixed number of particles. The fluid density for an isothermal compressible fluid flow with the temperature equal to the ambient temperature, *i.e.*  $T = T_{\text{atm}}$ , can then be written as

$$\rho(p + p_{\text{atm}}, T_{\text{atm}}) = \rho(p_{\text{atm}}, T_{\text{atm}}) + p \left( \frac{d\rho}{dp} \right)_{p_{\text{atm}}, T_{\text{atm}}}, \quad (56)$$

where  $p_{\text{atm}}$  refers to the ambient pressure. Substituting Eq. 54 in Eq. 56 results in

$$\begin{aligned} \rho(p + p_{\text{atm}}, T_{\text{atm}}) = \\ \rho(p_{\text{atm}}, T_{\text{atm}}) \times \left( 1 + p \kappa_T \Big|_{p_{\text{atm}}, T_{\text{atm}}} \right). \end{aligned} \quad (57)$$

By defining  $\rho^* \equiv \rho/\rho_{\text{ref}}$ , where  $\rho_{\text{ref}}$  denotes the fluid density at ambient pressure and ambient temperature, we can write

$$\rho^* = 1 + p \kappa_T \Big|_{p_{\text{atm}}, T_{\text{atm}}}. \quad (58)$$

Since the membrane displacement is significantly smaller than the channel width and length, *i.e.*  $\delta H \ll W \ll L$ , the membrane slope is very small, *i.e.*  $\partial \delta H / \partial x \ll 1$  and  $\partial \delta H / \partial y \ll 1$ . Under these situations, the Poiseuille flow pattern can be assumed to be locally valid. Furthermore, due to the assumption of  $H_0 \ll W$ , a one-dimensional Poiseuille

flow can be locally considered. The local mass flow rate can be written as

$$\dot{m}(x) = -\frac{dp(x)}{dx} \frac{\rho(x)W}{12\mu} \langle H^3 \rangle_{(x)}, \quad (59)$$

where  $\mu$  is the fluid dynamic viscosity, and  $H = H_0 + \delta H$  shows the channel's local height. In addition, the average of an arbitrary variable such as  $\phi$  over a x-plane is obtained through  $\langle \phi \rangle_{(x)} = \frac{1}{2} \int_{\zeta=-1}^{\zeta=+1} \phi(x, \zeta) d\zeta$ .

In a non-dimensional form, where  $\rho_{\text{ref}}, L, \dot{m}_{\text{ref}}, Q_{\text{ref}} = \dot{m}_{\text{ref}}/\rho_{\text{ref}}$ , and  $\Delta p_{\text{ref}} \equiv 12\mu L Q_{\text{ref}}/W H_0^3$  are used as the characteristic scales for length, mass flow rate, volumetric flow rate, and pressure, respectively, the dimensionless mass flow rate through the deformable channel, *i.e.*  $\dot{m}^* \equiv \dot{m}/\dot{m}_{\text{ref}}$ , can be written as

$$\dot{m}^* = -\rho^* \frac{dp^*(x^*)}{dx^*} \frac{\langle H^3 \rangle_{(x^*)}}{H_0^3}, \quad (60)$$

where  $p^* \equiv p/\Delta p_{\text{ref}}$ , and  $x^* \equiv x/L$ . By defining  $\gamma(x) \equiv p(x)W^4/384DH_0$ , Eq. 53 can be rewritten as  $\delta H(x, \zeta)/H_0 = \gamma(x)f(\zeta)$ . Considering that  $\langle H^3 \rangle = H_0^3 + 3H_0^2 \langle \delta H \rangle + 3H_0 \langle (\delta H)^2 \rangle + \langle (\delta H)^3 \rangle$ , one can show that

$$\begin{aligned} \frac{\langle H^3 \rangle}{H_0^3} &= 1 + 3\gamma(x) \langle f(\zeta) \rangle \\ &+ 3\gamma^2(x) \langle f^2(\zeta) \rangle + \gamma^3(x) \langle f^3(\zeta) \rangle. \end{aligned} \quad (61)$$

We know  $\langle f(\zeta) \rangle = 8/15$ ,  $\langle f^2(\zeta) \rangle = 128/315$ , and  $\langle f^3(\zeta) \rangle = 1024/3003$ . Considering that  $p^* = 0$  at  $x^* = 1$  due to the fluid discharge into ambient air. One can define  $\xi \equiv 1 - x^*$  and substitute Eq. 61 in Eq. 60, resulting in an initial-value problem for an arbitrary mass flow rate of  $\dot{m} = \dot{m}_{\text{ref}}$ , *i.e.*  $\dot{m}^* = 1$ , as shown in the following first-order non-linear ordinary

differential equation (ODE):

$$\begin{aligned} & \left( 1 + \alpha_1 p^*(\xi) + \alpha_2 p^{*2}(\xi) + \alpha_3 p^{*3}(\xi) \right) \times \\ & \left( 1 + p^*(\xi) \kappa_T^* \Big|_{p_{\text{atm}}, T_{\text{atm}}} \right) \frac{dp^*(\xi)}{d\xi} = 1, \\ & \text{Initial value: } \quad \xi = 0 : p^* = 0, \end{aligned} \quad (62)$$

where the dimensionless isothermal compressibility is defined as

$$\kappa_T^* \Big|_{p_{\text{atm}}, T_{\text{atm}}} = \kappa_T \Big|_{p_{\text{atm}}, T_{\text{atm}}} \Delta p_{\text{ref}}, \quad (63)$$

and the flexibility parameter, *i.e.*  $\chi$ , and  $\alpha_i$  coefficients are

$$\chi \equiv \frac{W^4 \Delta p_{\text{ref}}}{384 D H_0}, \quad (64a)$$

$$\alpha_1 = \frac{8}{5} \chi, \quad \alpha_2 = \frac{128}{105} \chi^2, \quad \text{and} \quad \alpha_3 = \frac{1024}{3003} \chi^3. \quad (64b)$$

We can write Eq. 62 as

$$\begin{aligned} & \left\{ 1 + \beta_1 p^*(\xi) + \beta_2 p^{*2}(\xi) \right. \\ & \left. + \beta_3 p^{*3}(\xi) + \beta_4 p^{*4}(\xi) \right\} \frac{dp^*(\xi)}{d\xi} = 1, \\ & \text{Initial value: } \quad \xi = 0 : p^* = 0, \end{aligned} \quad (65)$$

where we define

$$\beta_1 = \alpha_1 + \kappa_T^* \Big|_{p_{\text{atm}}, T_{\text{atm}}}, \quad (66a)$$

$$\beta_2 = \alpha_2 + \alpha_1 \kappa_T^* \Big|_{p_{\text{atm}}, T_{\text{atm}}}, \quad (66b)$$

$$\beta_3 = \alpha_3 + \alpha_2 \kappa_T^* \Big|_{p_{\text{atm}}, T_{\text{atm}}}, \quad (66c)$$

$$\text{and } \beta_4 = \alpha_3 \kappa_T^* \Big|_{p_{\text{atm}}, T_{\text{atm}}}. \quad (66d)$$

The analytical solution for the ODE shown in Eq. 65 can be written as

$$p^*(\xi) + \frac{\beta_1}{2}p^{*2}(\xi) + \frac{\beta_2}{3}p^{*3}(\xi) + \frac{\beta_3}{4}p^{*4}(\xi) + \frac{\beta_4}{5}p^{*5}(\xi) = \xi. \quad (67)$$

At inlet section, *i.e.*  $\xi = 1$ , we have

$$p_i^* \left[ 1 + \frac{\beta_1}{2}p_i^* + \frac{\beta_2}{3}p_i^{*2} + \frac{\beta_3}{4}p_i^{*3} + \frac{\beta_4}{5}p_i^{*4} \right] = 1, \quad (68)$$

where  $p_i^* = p_i/\Delta p_{\text{ref}} = \Delta p/\Delta p_{\text{ref}}$ , and  $p_i$  refers to the pressure at inlet. Let us consider an incompressible fluid flow through a rigid microchannel as the reference case. For a given pressure drop, an incompressible flow through a rigid channel represents the least mass flow rate. Any deviation from this reference case due to channel deformability and/or fluid compressibility would increase the mass flow rate. The parameter  $p_i^*$  shows the fraction of pressure difference across a rigid microchannel with an incompressible fluid flow, *i.e.* the reference case, sufficiently large to produce the same mass flow rate in a general case, wherein the channel can be deformable/rigid, and fluid flow can be compressible/incompressible.

Since the ODE presented in Eq. 62 is derived for  $\dot{m}^* = \dot{m}/\dot{m}_{\text{ref}} = 1$ , for a general case, wherein fluid flow can be compressible/incompressible and channel can be deformable/rigid, the mass flow rate of  $\dot{m}_{\text{gen}} = \dot{m}_{\text{ref}}$  is delivered under the pressure difference of  $\Delta p = p_i^* \Delta p_{\text{ref}}$ . Since mass flow rate is a linear function of pressure difference in case of an incompressible flow through a rigid channel, a rigid channel under the pressure difference of  $p_i^* \Delta p_{\text{ref}}$  delivers the mass flow rate of  $\dot{m}_{\text{Incomp., Rigid}} = p_i^* \dot{m}_{\text{ref}}$  with an incompressible working fluid. Therefore, under the same pressure difference of  $p_i^* \Delta p_{\text{ref}}$ , the proportion of the mass flow rate of the general case to that of the reference case, *i.e.* incompressible flow through a rigid channel, equals  $1/p_i^*$ , which can be obtained from Eq. 68:

$$\frac{\dot{m}_{\text{gen}}}{\dot{m}_{\text{Incomp., Rigid}}} \Big|_{\Delta p = \text{const.}} = 1 + \frac{\beta_1}{2}p_i^* + \frac{\beta_2}{3}p_i^{*2} + \frac{\beta_3}{4}p_i^{*3} + \frac{\beta_4}{5}p_i^{*4}. \quad (69)$$

One can show that

$$\Gamma_1 \equiv \frac{\beta_1}{2} p_i^* = \frac{1}{2} \Delta p \kappa_T \Big|_{p_{\text{atm}}, T_{\text{atm}}} + \frac{4}{5} \chi^*, \quad (70a)$$

$$\Gamma_2 \equiv \frac{\beta_2}{3} p_i^{*2} = \frac{8}{15} \chi^* \Delta p \kappa_T \Big|_{p_{\text{atm}}, T_{\text{atm}}} + \frac{128}{315} \chi^{*2}, \quad (70b)$$

$$\Gamma_3 \equiv \frac{\beta_3}{4} p_i^{*3} = \frac{32}{105} \chi^{*2} \Delta p \kappa_T \Big|_{p_{\text{atm}}, T_{\text{atm}}} + \frac{256}{3003} \chi^{*3}, \quad (70c)$$

$$\text{and } \Gamma_4 \equiv \frac{\beta_4}{5} p_i^{*4} = \frac{1024}{15015} \chi^{*3} \Delta p \kappa_T \Big|_{p_{\text{atm}}, T_{\text{atm}}}, \quad (70d)$$

in which the modified flexibility parameter, i.e.  $\chi^*$ , is defined as

$$\chi^* \equiv \frac{W^4 \Delta p}{384 D H_0}. \quad (71)$$

We can then write Eq. 69 as

$$\begin{aligned} \frac{\dot{m}_{\text{gen}}}{\dot{m}_{\text{Incomp., Rigid}} \Big|_{\Delta p = \text{const.}}} = & \\ & 1 + \frac{4}{5} \chi^* + \frac{128}{315} \chi^{*2} + \frac{256}{3003} \chi^{*3} \\ & + \left( \Delta p \kappa_T \Big|_{p_{\text{atm}}, T_{\text{atm}}} \times \right. \\ & \left. \left( \frac{1}{2} + \frac{8}{15} \chi^* + \frac{32}{105} \chi^{*2} + \frac{1024}{15015} \chi^{*3} \right) \right). \end{aligned} \quad (72)$$

Two factors contribute in Eq. 72: 1) microchannel deformability and 2) fluid's compressibility. The terms of  $4\chi^*/5 + 128\chi^{*2}/315 + 256\chi^{*3}/3003$  reflect solely the effects of channel deformability, the term of  $\Delta p \kappa_T|_{p_{\text{atm}}, T_{\text{atm}}}/2$  stems from the compressibility of the fluid, and the terms of  $(8\chi^*/15 + 32\chi^{*2}/105 + 1024\chi^{*3}/15015)\Delta p \kappa_T|_{p_{\text{atm}}, T_{\text{atm}}}$  show the hybrid influence of channel deformability and fluid's compressibility.

For a deformable microchannel under an arbitrary pressure difference, the modified flexibility parameter calculated from Eq. 71 is used to determine the variables  $\Gamma_i : i = 1, 2, 3$

and 4 from Eq. 70, and consequently to obtain the important parameter of  $p_i^*$  as

$$p_i^* = \frac{1}{1 + \Gamma_1 + \Gamma_2 + \Gamma_3 + \Gamma_4}. \quad (73)$$

By combining Eqs. 67, 68, and 70, variation of dimensionless pressure  $\tilde{p} \equiv p/\Delta p$  within the channel can be obtained from the following algebraic equation for  $0 \leq \xi \leq 1$  and  $0 \leq \tilde{p} \leq 1$ :

$$\begin{aligned} \tilde{p}(\xi) + \Gamma_1 \tilde{p}^2(\xi) + \Gamma_2 \tilde{p}^3(\xi) + \Gamma_3 \tilde{p}^4(\xi) + \Gamma_4 \tilde{p}^5(\xi) = \\ (1 + \Gamma_1 + \Gamma_2 + \Gamma_3 + \Gamma_4)\xi. \end{aligned} \quad (74)$$

It is worth mentioning that regardless of existence or non-existence of analytical solutions for roots of this equation, instead of finding  $\tilde{p}$  for a given location ( $\xi$ ), which necessitates dealing with difficulties associated with finding the physically meaningful roots of Eq. 74, we evaluate  $\xi$  for given values of  $\tilde{p}$  to obtain the pressure distribution graphs, *i.e.*  $\tilde{p}$  versus  $\xi$  or equivalently  $\tilde{p}$  versus  $x^*$ . Once the pressure variation within the microchannel is obtained, one can use Eq. 53 to find the membrane deformation profile. In particular, the mean and maximum deflections of the membrane can be written as

$$\begin{aligned} \frac{\langle \delta H \rangle_{(x^*)}}{H_0} &= \frac{8}{15} \tilde{p}(x^*) \chi^*, \\ \frac{\delta H_{\max}(x^*)}{H_0} &= \tilde{p}(x^*) \chi^*. \end{aligned} \quad (75)$$

A few different special cases can be resulted from the general equations presented in Eqs. 72 and 74 as illustrated in the following.

1)  $\chi^* \ll 1$  and  $\Delta p \kappa_T \Big|_{p_{\text{atm}}, T_{\text{atm}}} \ll 1$ : Eqs. 72 and 74 are simplified to

$$\frac{\dot{m}_{\text{gen}}}{\dot{m}_{\text{Incomp., Rigid}}} \approx 1, \quad (76a)$$

$$\text{and } \tilde{p}(\xi) \approx \xi, \quad (76b)$$

respectively. Under these conditions, fluid flow characteristics resemble those of incompressible flow through a rigid channel.

2)  $\chi^* \ll 1$ : Eqs. 72 and 74 are simplified to

$$\frac{\dot{m}_{\text{gen}}}{\dot{m}_{\text{Incomp., Rigid}}} \approx 1 + \frac{1}{2} \Delta p \kappa_T \Big|_{p_{\text{atm}}, T_{\text{atm}}}, \quad (77a)$$

$$\text{and } \tilde{p}(\xi) + \frac{1}{2} \Delta p \kappa_T \Big|_{p_{\text{atm}}, T_{\text{atm}}} \tilde{p}^2(\xi) \approx \left(1 + \frac{1}{2} \Delta p \kappa_T \Big|_{p_{\text{atm}}, T_{\text{atm}}}\right) \xi, \quad (77b)$$

respectively. Under these conditions, fluid flow characteristics resemble those of compressible flow through a rigid channel. From Eq. 77 (b), one can show that pressure distribution within the channel might be written as

$$\tilde{p}(\xi) \approx \sqrt{\left(\frac{1}{\Delta p \kappa_T \Big|_{p_{\text{atm}}, T_{\text{atm}}}}\right)^2 + \left(1 + 2 \frac{1}{\Delta p \kappa_T \Big|_{p_{\text{atm}}, T_{\text{atm}}}}\right) \xi} - \frac{1}{\Delta p \kappa_T \Big|_{p_{\text{atm}}, T_{\text{atm}}}} \quad (78)$$

3)  $\Delta p \kappa_T \Big|_{p_{\text{atm}}, T_{\text{atm}}} \ll 1$ : Eqs. 72 and 74 are simplified to

$$\frac{\dot{m}_{\text{gen}}}{\dot{m}_{\text{Incomp., Rigid}}} \approx 1 + \frac{4}{5} \chi^* + \frac{128}{315} \chi^{*2} + \frac{256}{3003} \chi^{*3}, \quad (79a)$$

and

$$\begin{aligned} \tilde{p}(\xi) + \frac{4}{5} \chi^* \tilde{p}^2(\xi) + \frac{128}{315} \chi^{*2} \tilde{p}^3(\xi) + \frac{256}{3003} \chi^{*3} \tilde{p}^4(\xi) \\ \approx \left(1 + \frac{4}{5} \chi^* + \frac{128}{315} \chi^{*2} + \frac{256}{3003} \chi^{*3}\right) \xi, \end{aligned} \quad (79b)$$

respectively. Under these conditions, fluid flow characteristics resemble those of incompressible fluid flow through a channel with the same modified flexibility parameter, which is investigated in our other work [187]. Depending on the modified flexibility parameter's magnitude, altering the pressure difference across the deformable microchannel can activate/deactivate various orders of the modified flexibility parameter causing various distinct

fluid-structural characteristics to emerge [187].

## Ideal Gas Flow

As a special case of compressible fluid flows, an ideal gas flow can be investigated using the general model derived in previous section. The isothermal compressibility of an ideal gas flow is

$$\kappa_T \Big|_{p_{\text{atm}}, T_{\text{atm}}} = \frac{1}{p_{\text{atm}}}. \quad (80)$$

By substituting the isothermal compressibility of an ideal gas in the pertinent equations derived in previous section, one can find the specialized model for an ideal gas flow, as presented in the following.

**Eq. 58 for an ideal gas flow:**

$$\rho^* = 1 + \frac{p}{p_{\text{atm}}}. \quad (81)$$

**Eq. 70 for an ideal gas flow:**

$$\Gamma_1 = \frac{1}{2} \frac{\Delta p}{p_{\text{atm}}} + \frac{4}{5} \chi^*, \quad (82a)$$

$$\Gamma_2 = \frac{8}{15} \frac{\Delta p}{p_{\text{atm}}} \chi^* + \frac{128}{315} \chi^{*2}, \quad (82b)$$

$$\Gamma_3 = \frac{32}{105} \frac{\Delta p}{p_{\text{atm}}} \chi^{*2} + \frac{256}{3003} \chi^{*3}, \quad (82c)$$

$$\text{and } \Gamma_4 = \frac{1024}{15015} \frac{\Delta p}{p_{\text{atm}}} \chi^{*3}, \quad (82d)$$

**Eq. 72 for an ideal gas flow:**

$$\begin{aligned} \frac{\dot{m}_{\text{gen}}}{\dot{m}_{\text{Incomp., Rigid}}} \Big|_{\Delta p = \text{const.}} = & \\ & 1 + \frac{4}{5} \chi^* + \frac{128}{315} \chi^{*2} + \frac{256}{3003} \chi^{*3} \\ & + \frac{\Delta p}{p_{\text{atm}}} \left( \frac{1}{2} + \frac{8}{15} \chi^* + \frac{32}{105} \chi^{*2} + \frac{1024}{15015} \chi^{*3} \right). \end{aligned} \quad (83)$$

For an ideal gas flow, pressure distribution within the channel can be obtained from Eq. 74 after evaluating the variables  $\Gamma_i$  :  $i = 1, 2, 3$  and 4 from Eq. 82. After finding the pressure distribution, the mean and maximum deflections of the membrane can be obtained from Eq. 75.

It is worth mentioning that the results for the special case of  $\chi^* \ll 1$ , presented in Eqs. 77 and 78, can be written as

$$\frac{\dot{m}_{\text{gen}}}{\dot{m}_{\text{Incomp., Rigid}}} \approx 1 + \frac{1}{2} \frac{\Delta p}{p_{\text{atm}}}, \quad (84a)$$

$$\tilde{p}(\xi) + \frac{1}{2} \frac{\Delta p}{p_{\text{atm}}} \tilde{p}^2(\xi) \approx \left(1 + \frac{1}{2} \frac{\Delta p}{p_{\text{atm}}}\right) \xi, \quad (84b)$$

and

$$\tilde{p}(\xi) \approx \sqrt{\left(\frac{p_{\text{atm}}}{\Delta p}\right)^2 + (1 + 2\frac{p_{\text{atm}}}{\Delta p})\xi} - \frac{p_{\text{atm}}}{\Delta p}, \quad (85)$$

respectively, for an ideal gas flow. Under these conditions, ideal gas flow characteristics resemble those of ideal gas flow through a rigid channel. In addition, when  $\Delta p/p_{\text{atm}} \ll 1$ , ideal gas flow characteristics resemble those of incompressible fluid flow through a channel with the same modified flexibility parameter, where Eqs. 72 and 74 are simplified to Eq. 79.

## Materials and methods

To demonstrate the underlying coupled fluid-solid mechanics of compressible fluid flow through a deformable microchannel, we fabricated deformable microchannels and performed experiments to obtain the mass flow rate over the applied pressure difference range of 14–206 kPa. The detailed fabrication steps were previously reported elsewhere [164]. Briefly, deformable microchannels were created on glass substrates using photolithography and wet etching, and sealed via adhesive bonding with a 2  $\mu\text{m}$ -SU8-coated PET (polyethylene terephthalate) film ( $t = 100 \mu\text{m}$ ,  $E = 3 \text{ GPa}$ , and  $\nu = 0.4$ ). Bonding reinforcement was provided using a glass slide with a sufficiently deep ( $\sim 45 \mu\text{m}$ ) etched pattern of the microchannel allowing the membrane to deform freely under pressure. The reinforcement glass was bonded

to bare side of the membrane using a 16  $\mu\text{m}$  SU8 layer ( $E \sim 2$  GPa) [164, 187]. For the case of rigid microchannels, bonding reinforcement was done using a blank glass slide with no etched pattern to suppress membrane deformations.

Structural effects of adhesive layers were taken into account by using the transformed-section method [165]. The equivalent membrane thickness was calculated from  $\tilde{t} = \sqrt[3]{12I/W}$ , where  $I$  denotes the three-layer membrane's moment of inertia, and was used in parameter  $D$  appearing in Eq. 71 in evaluating the modified flexibility parameter. From the aforementioned values for thickness and modulus of elasticity of different layers,  $\tilde{t} \approx 113 \mu\text{m}$ .

Air was chosen as a model compressible fluid. The in-line pressure of air flow was adjusted using a pressure regulator (PneumaticPlus, PPR2-N02BG-4 Miniature Air Pressure Regulator). A small water plug was placed within the outlet tube and pushed out by the applied air pressure. The movement of water plug was monitored with a camera attached to a stereomicroscope, and linear velocity of liquid meniscus was measured to calculate the volumetric flow rate of air. Depending on the magnitude of volumetric flow rates, different tube diameters were employed to better trace the water meniscus.

## Results and discussion

### Theoretical investigation

Dimensionless pressure variations within microchannel are shown in Fig. 52 for ideal gas flows with various modified flexibility parameters and pressure differences. For a rigid microchannel (solid lines), the pressure variation is linear for an incompressible fluid flow, or an ideal gas flow under sufficiently low pressure differences ( $\Delta p/p_{\text{atm}} \ll 1$ ); see Fig. 52 (a). The pressure variation deviates from a linear distribution as the pressure difference increases. The channel deformability plays a similar role; the contrast between the pressure distribution and the linear variation increases as the modified flexibility parameter increases.

Three general categories that play roles in fluid-solid characteristic behavior are 1) microchannel dimensions:  $W$  and  $H_0$ , 2) membrane thickness and structural properties, which

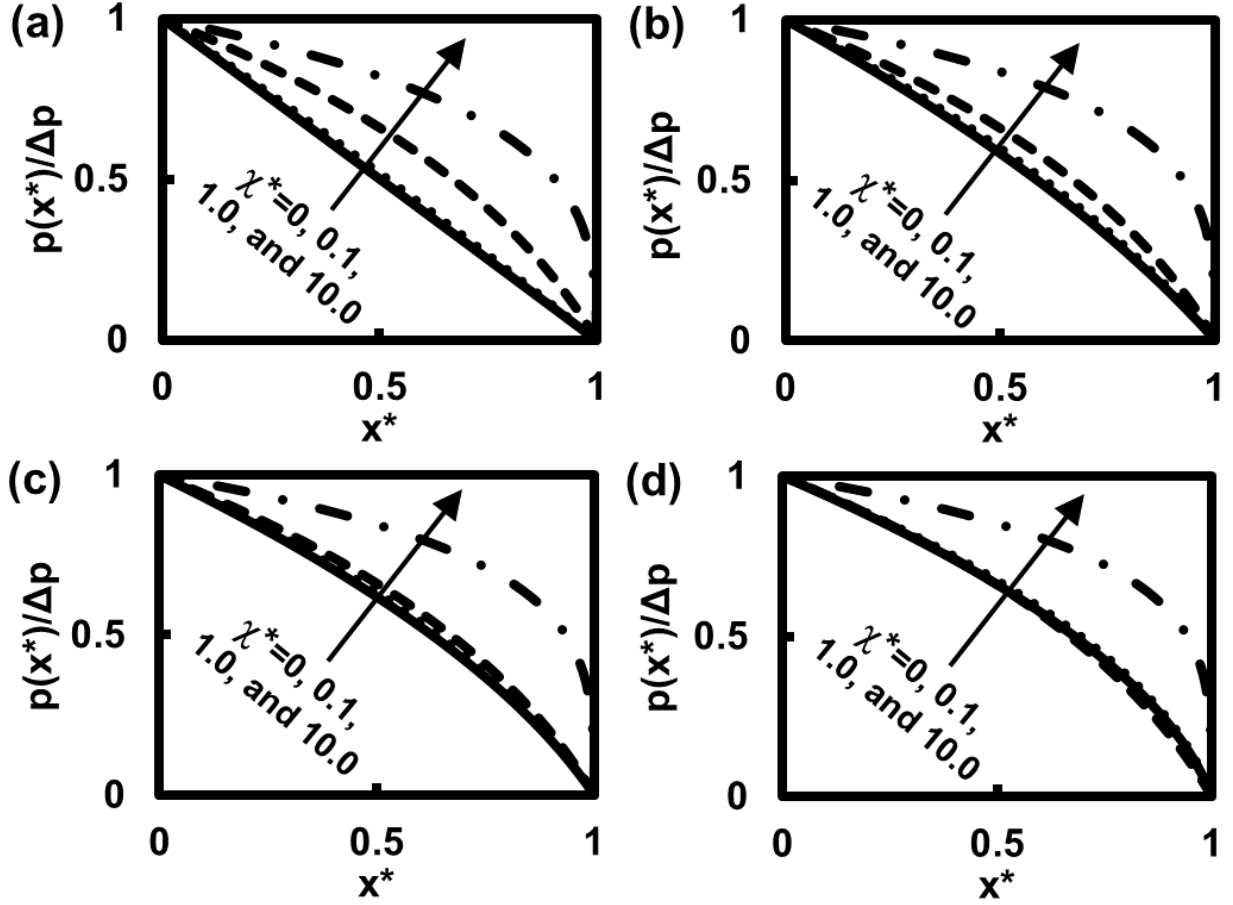


Figure 52: Dimensionless pressure distribution within microchannel for ideal gas flows under (a)  $\Delta p/p_{\text{atm}} \ll 1$ , *i.e.* incompressible fluid flow, (b)  $\Delta p = p_{\text{atm}}$ , (c)  $\Delta p = 2p_{\text{atm}}$ , and (d)  $\Delta p = 5p_{\text{atm}}$  for various modified flexibility parameters. Note: Solid lines, *i.e.*  $\chi^* \rightarrow 0$ , show the rigid microchannel results.

are lumped into the parameter  $D$ , and 3) pressure difference across microchannel,  $\Delta p$ . All of these factors are reflected into the modified flexibility parameter; see Eq. 71. It is worth mentioning that the first and second categories solely influence the channel deformability, while the third factor, *i.e.* pressure difference, affects both channel deformability and fluid compressibility. As a result, for the microchannels with small modified flexibility parameters ( $\chi^* \ll 1$ ), the fluid-solid characteristic behavior is dictated solely by pressure difference regardless of microchannel dimensions or membrane properties. Whereas, the channel deformability effects increase as the modified flexibility parameter grows through any or combination of the following factors: decreasing the channel depth, increasing the channel width, using the thinner and/or more flexible membrane, and increasing the pressure difference.

As the modified flexibility parameter increases, the dominance of pressure difference in fluid-solid characteristic behavior decreases and roles of the aforementioned categories 1 and 2 become more important. For example, one can observe from Fig. 52 that under an arbitrary pressure difference, there are not noticeable differences between pressure distributions when the modified flexibility parameter changes from 0 to 0.1, while a significant contrast appears when the modified flexibility parameter changes from 1 to 10. For a given pressure difference, such contrasts are attributed solely to the first and second aforementioned categories. In addition, one can observe that pressure distribution within channels with the modified flexibility parameters of 0 and 0.1 is noticeably altered by changing the pressure difference over the range of  $0-5p_{\text{atm}}$ , while for microchannels with relatively large modified flexibility parameters of 1 and 10, pressure distribution is not significantly affected by pressure difference.

It is perceived from Fig. 52 that for a sufficiently low pressure difference across a channel with a small deformability, *i.e.*  $\chi^* \ll 1$  and  $\Delta p/p_{\text{atm}} \ll 1$ , the local fluidic resistance is constant (unchanged  $dp/dx$ ). For a sufficiently high pressure difference and/or modified flexibility parameter, however, the local fluidic resistance increases along the channels, *i.e.* the magnitude of  $dp/dx$  increases. Regarding the effects of pressure difference across a channel, a larger pressure drop creates a larger density gradient within the channel due to the compressibility of fluid. The fluid density decreases along the channel as the pressure decreases along the channel. According to the conservation of mass principle, such a decaying density variation causes the fluid speed, shear rate, and local frictional resistance to increase along the channel. Regarding the modified flexibility parameter's effects, a larger modified flexibility parameter represents a larger membrane deformation. According to Fig. 53, membrane deflection at inlet increases as the modified flexibility parameter increases, while there is no membrane deformation at outlet ( $p = 0$ ). As a result, the open area that fluid sees decreases as it flows toward the outlet, causing the local resistance to grow along the channel. In addition, the larger membrane slope under a higher modified flexibility parameter causes a larger growth in local fluidic resistance.

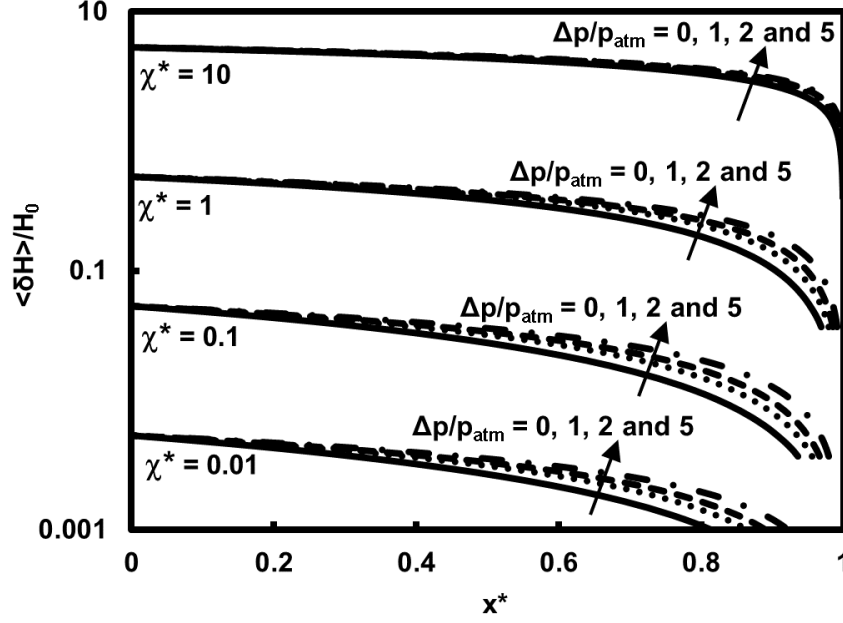


Figure 53: Dimensionless average displacement of membrane along the microchannel for ideal gas flows with various values of  $\chi^*$  and  $\Delta p/p_{\text{atm}}$ . Note: Solid lines, *i.e.*  $\Delta p/p_{\text{atm}} \rightarrow 0$ , show the incompressible fluid flow results.

Variations of the parameters  $p_i^*$  and  $1/p_i^*$  are shown in Fig. 54 for various modified flexibility parameters and pressure differences. As mentioned earlier, the parameter  $p_i^*$  is of importance for compressible fluid flow through a deformable channel, since it captures the effects of fluid compressibility and channel deformability on mass flow rate, *i.e.*  $\dot{m}/\dot{m}_{\text{Incomp., Rigid}} = 1/p_i^*$ . According to Fig. 54, the fluid compressibility effects are dominant under sufficiently small modified flexibility parameters, while channel deformability plays the more important role under sufficiently high modified flexibility parameters. The reason can be deduced by inspecting Eqs. 70 and 73; the terms with higher orders of  $\chi^*$  become more important as the modified flexibility parameter increases, while the compressibility effects appear as the linear term of  $\Delta p/p_{\text{atm}}$ .

### Experimental investigation

Five different microchannels have been experimentally investigated in this work. The microchannels' geometries are summarized in Table 9. The dynamic viscosity of air is considered to be the constant value of  $\mu = 1.8 \times 10^{-5}$  Pa.s. The ambient temperature and pressure

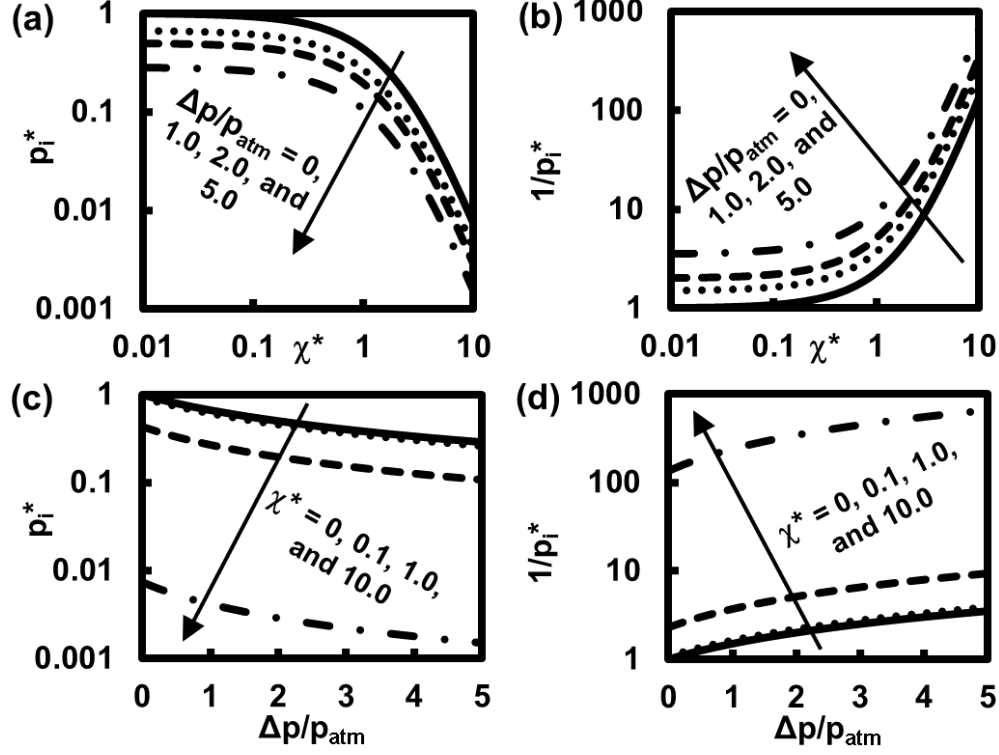


Figure 54: Variations of (a)  $p_i^*$  and (b)  $\dot{m}/\dot{m}_{\text{Incomp., Rigid}}$ , *i.e.*  $1/p_i^*$ , in ideal gas flow as functions of modified flexibility parameter under various pressure differences. Variations of (c)  $p_i^*$  and (d)  $\dot{m}/\dot{m}_{\text{Incomp., Rigid}}$ , *i.e.*  $1/p_i^*$ , in ideal gas flow as functions of pressure difference for various modified flexibility parameters. Note: 1. Solid lines in (a) and (b), *i.e.*  $\Delta p/p_{\text{atm}} \rightarrow 0$ , show the incompressible fluid flow results. 2. Solid lines in (c) and (d), *i.e.*  $\chi^* \rightarrow 0$ , show the rigid microchannel results.

are  $T_{\text{atm}} = 295$  K and  $p_{\text{atm}} = 101$  kPa, respectively. The air specific gas constant equals  $R_{\text{sgc}} = 287.058$  J.kg<sup>-1</sup>.K<sup>-1</sup>.

Mass flow rates through Microchannels A–E are shown in Fig. 55 for various pressure differences across the microchannels. As discussed earlier, an incompressible fluid flow through a rigid channel produces a linear relationship between mass flow rate and pressure drop. The  $\dot{m}$  versus  $\Delta p$  data of air flow through Microchannel A shown in Fig. 55 (a), however, reveals that under sufficiently large pressure differences, mass flow rate is significantly underestimated by the model developed for incompressible fluid flows. Under sufficiently low pressure differences, air flow through the rigid channel exhibits the characteristics of an incompressible fluid flow through a rigid channel, *i.e.* Eq. 76 (a), while an increasing deviation from incompressible flow’s behavior appears at increasing pressure difference, where the compressibility effects become more important; see Eq. 77 (a).

Table 9: The geometry of the microchannels studied experimentally in this chapter.

Microchannel	Length (mm)	Width (mm)	Height ( $\mu\text{m}$ )	Height-to-Width Ratio
<b>Rigid:</b>				
A	$9.0 \pm 0.5$	$1.5 \pm 0.1$	$7.5 \pm 0.4$	$5.00 \times 10^{-3}$
<b>Deformable:</b>				
B	$9.5 \pm 0.5$	$1.25 \pm 0.1$	$2.3 \pm 0.1$	$1.84 \times 10^{-3}$
C	$9.5 \pm 0.5$	$2.0 \pm 0.1$	$2.3 \pm 0.1$	$1.15 \times 10^{-3}$
D	$9.5 \pm 0.5$	$1.15 \pm 0.1$	$7.5 \pm 0.4$	$6.52 \times 10^{-3}$
E	$9.5 \pm 0.5$	$2.2 \pm 0.1$	$8.2 \pm 0.4$	$3.73 \times 10^{-3}$

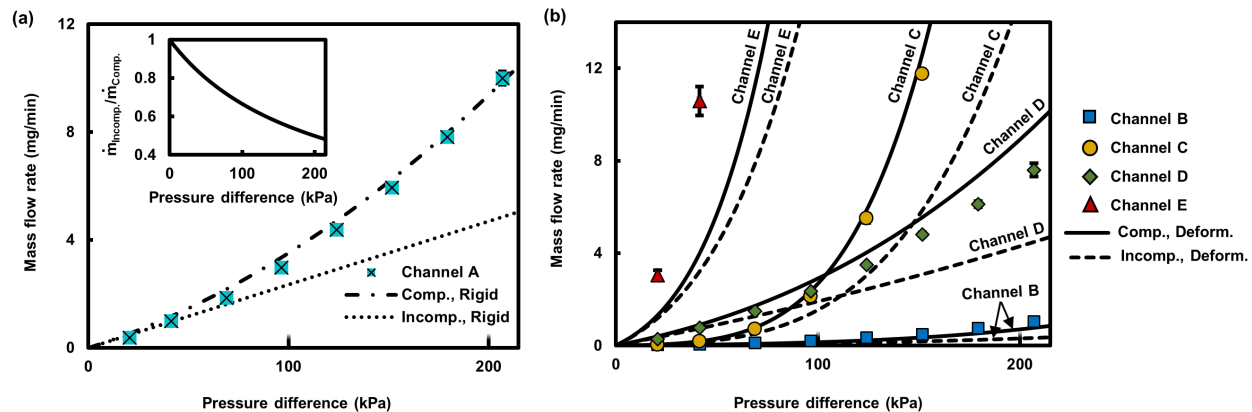


Figure 55: (a) Mass flow rate of air through Microchannel A as a function of pressure difference across the channel together with the modeling results for compressible flow through the rigid channel (Comp., Rigid) and incompressible flow through the rigid channel (Incomp., Rigid). Inset shows the proportion of mass flow rates of air through Microchannel A with and without compressibility taken into account. (b) Mass flow rates of air through Microchannels B–E as functions of pressure difference across the channels together with the modeling results for compressible flows through deformable channels (Comp., Deform.) and incompressible flows through deformable channels (Incomp., Deform.). The error bars related to the experimental results (averaged over three runs) are not visible if they are smaller than the markers’ size.

A non-linear relationship between mass flow rate and pressure drop is observed in Fig. 55 (b) for incompressible flows through deformable channels (dashed lines) due to the deformability of channel ceiling [187]. Similar to the rigid channel case shown in Fig. 55 (a),  $\dot{m}$  versus  $\Delta p$  experimental data shown in Fig. 55 (b) suggests that mass flow rate is significantly underestimated by the one-dimensional fluid-solid mechanics model of incompressible flows (dashed lines). The underestimation of mass flow rates using the incompressible fluid flow model is clearly seen for all four deformable microchannel devices (Microchannels B-E). Much better agreements between the experimental data and theoretical model can be found when the coupled one-dimensional fluid-solid mechanics model captures the compressibility of air flow (solid lines).

Comparing Microchannels B & C and Microchannels D & E, we find that for channels with the same (similar) heights, ones with larger widths produce larger flow rates. Likewise, flow rates of Microchannels B & D and Microchannels C & E can be compared for similar widths and different heights, demonstrating that channels with larger heights produce larger flow rates for similar widths. Therefore, it is obvious that Microchannel E (or B) delivers the largest (or smallest) mass flow rate for a given pressure difference because of having the largest (or smallest) width and height. However, an interesting crossing occurs when comparing Microchannels C and D. Under sufficiently low pressure differences, Microchannel D produces larger mass flow rates than Microchannel C does. However, the difference in flow rates of two channels diminishes with increasing applied pressure, and flow rate of Microchannel C grows at a much faster pace and becomes much larger than that of Microchannel D. This observation demonstrates again the dominance of channel deformability effects under sufficiently large modified flexibility parameters, where higher orders of  $\chi^*$  are activated in Eq. 72, causing Microchannel C to deliver much larger mass flow rates than Microchannel D does.

More insight into the underlying physics can be obtained through examining Eq. 72. A variety of distinct characteristics can emerge depending on the magnitude of modified flexibility parameter. Under sufficiently small modified flexibility parameters, *i.e.*  $\chi^* \ll 1$ , mass flow rate can be approximated as  $\dot{m}_{\text{gen}}/\dot{m}_{\text{Incomp., Rigid}} \approx 1 + \Delta p/2p_{\text{atm}}$ . The terms with higher orders of modified flexibility parameter become more important as  $\chi^*$  increases. For the case of sufficiently large modified flexibility parameter, *i.e.*  $\chi^* \gg 1$ , one can approximate the mass flow rate as  $\dot{m}_{\text{gen}}/\dot{m}_{\text{Incomp., Rigid}} \approx \chi^{*3}(256/3003 + 1024/15015 \times \Delta p/p_{\text{atm}})$ , which results in a height-independent and highly non-linear pressure-dependent characteristic behavior, *i.e.*  $\dot{m}_{\text{gen}} \propto \Delta p^5$ .

Once the microchannel device is fabricated, two categories of channel dimensions and membrane properties become fixed, rendering the pressure difference to be a lone parameter that alters the fluid-solid behavior. In other words, variation of pressure difference across the channel can activate/deactivate different terms in the right side of Eq. 72 through changing

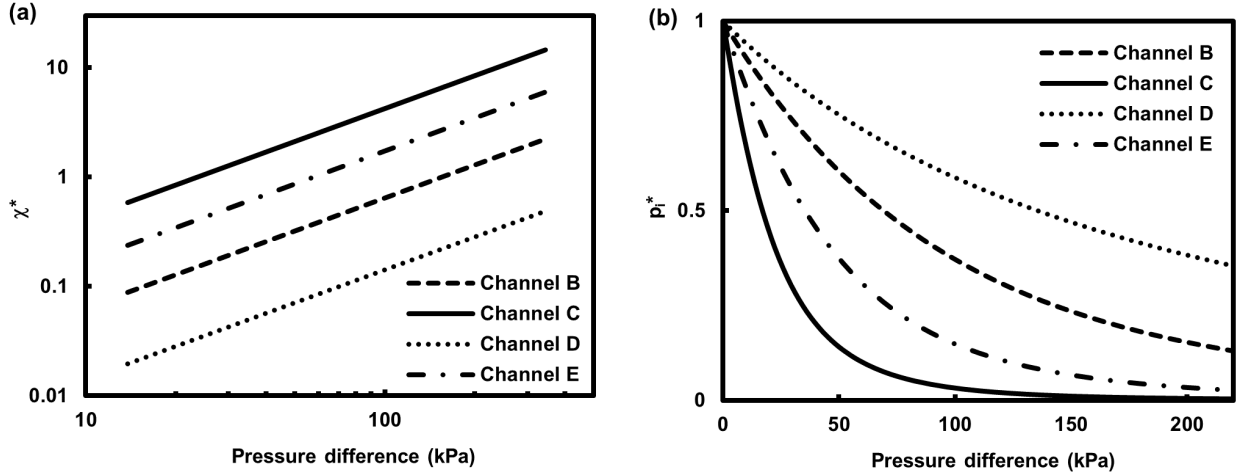


Figure 56: Variations of (a) modified flexibility parameter and (b)  $p_i^*$  as functions of pressure difference across Microchannels B–E.

the order of magnitude of modified flexibility parameter. As a result, a gas flow through a deformable microchannel might exhibit a variety of distinct characteristic behaviors depending on pressure difference applied across the microchannel. Variations of the modified flexibility parameter are presented in Fig. 56 (a) as a function of pressure difference across the investigated deformable microchannels. Among the microchannels studied in this work, because of its relatively large width and small height, Microchannel C shows the largest modified flexibility parameter and consequently the smallest  $p_i^*$ ; see Fig. 56 (b). As a result, the most significant deviations of characteristic behavior of a gas flow through a deformable channel from that of an incompressible flow through a rigid channel are observed in Microchannel C.

In order to further investigate the effects of microchannel deformability and fluid compressibility, the mass flow rate obtained from modeling for different combinations of these two factors are presented in Fig. 57. It is observed from Fig. 57 (b) that for a channel with dimensions equal to those of undeformed Microchannel C, channel deformability plays a significantly more important role in characteristic behavior than fluid compressibility does. The reason is that for such wide and shallow microchannels, the modified flexibility parameter is sufficiently large (Fig. 56 (a)) to activate the terms with higher orders of  $\chi^*$  in Eq. 72, whereas compressibility effects remain linear if present. The situation reverses for relatively narrow and deep channels studied in Fig. 57 (c), where the modified flexibility parameter

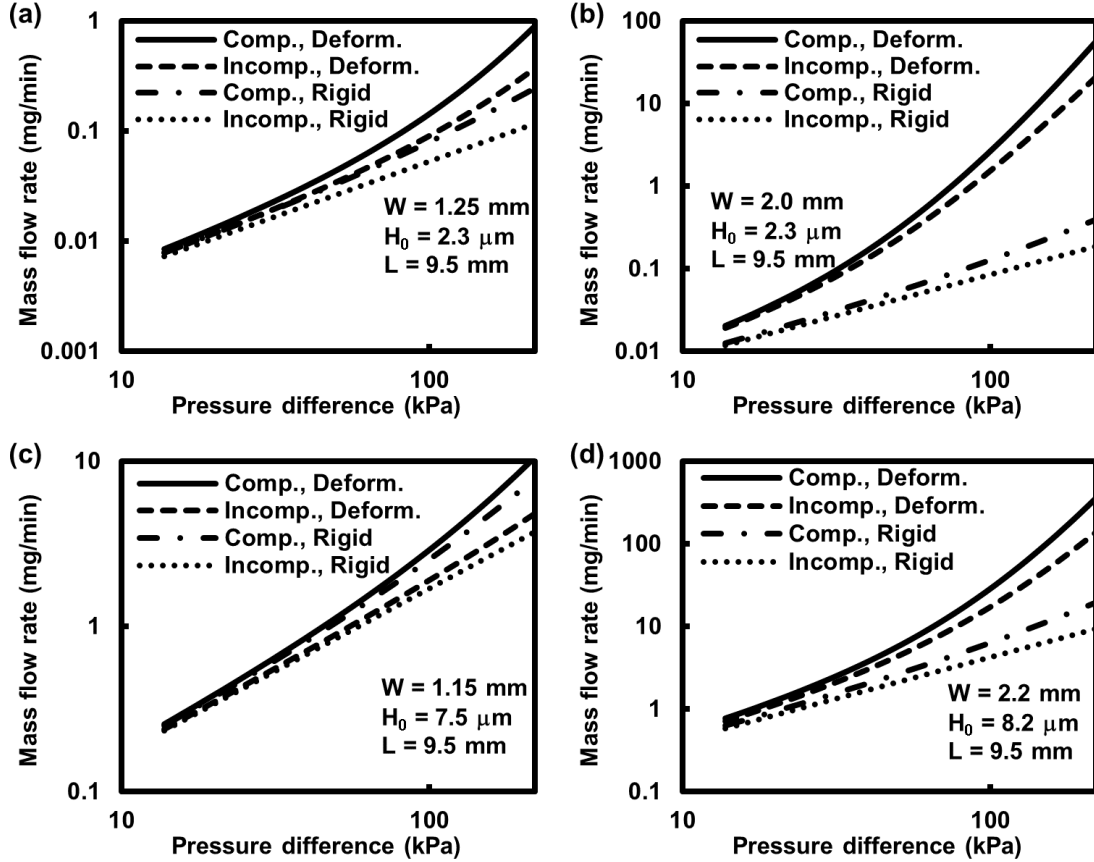


Figure 57: Mass flow rate obtained from the modeling for compressible flows through deformable channels (Comp., Deform.), incompressible flows through deformable channels (Incomp., Deform.), compressible flows through rigid channels (Comp., Rigid), and incompressible flows through rigid channels (Incomp., Rigid). The dimensions of the microchannels are the same as those of undeformed (a) Microchannel B, (b) Microchannel C, (c) Microchannel D, and (d) Microchannel E.

is sufficiently small to deactivate the higher orders of  $\chi^*$  in Eq. 72, because of which the deformable channel acts similar to its rigid counterpart. From Fig. 57 (c), compressibility of fluid under sufficiently high pressure differences causes noticeable effects on mass flow rate versus pressure difference characteristic curves, while there is not remarkable contrast between deformable and rigid microchannels.

The discrepancies between the theoretical and experimental results shown in Fig. 55 can be attributed to several factors as explained in the following:

**1) Clamping effects**— The one-dimensional model does not predict the characteristics accurately close to the inlet/outlet ports due to the inherently three-dimensional nature of fluid-solid mechanics in those areas. In particular, because of correlating membrane defor-

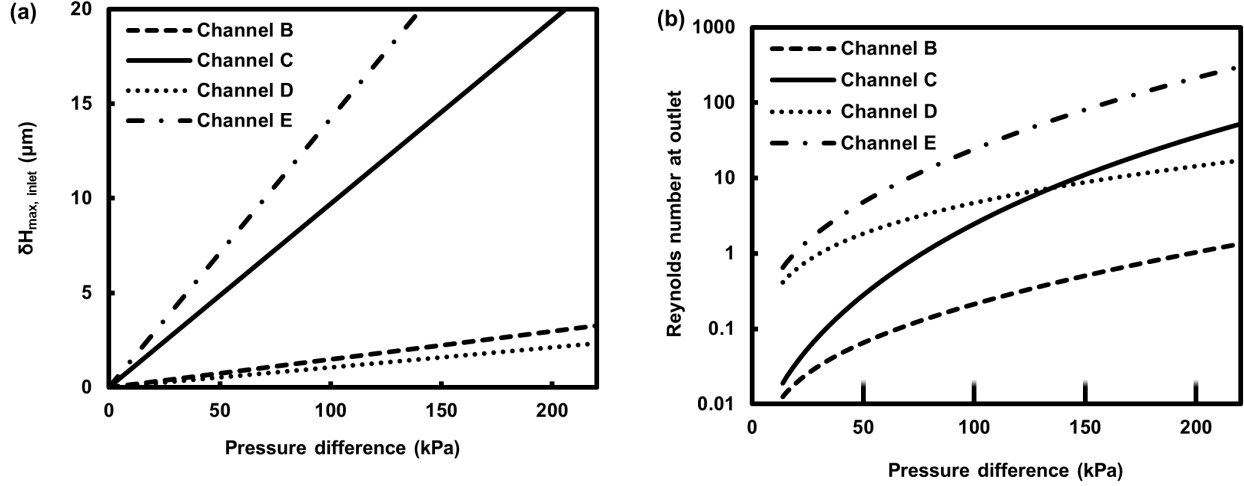


Figure 58: Variations of (a) maximum membrane displacement at inlet and (b) Reynolds number at outlet, as functions of pressure difference across Microchannels B–E.

mation solely with local pressure within the channel, the one-dimensional model predicts the membrane deflection to be maximum at inlet, while in practice a smaller membrane deflection arises close to the inlet because the membrane is clamped. As a result, mass flow rate can be overestimated, similar to what is observed in case of Microchannel D, due to this intrinsic inconsistency of the one-dimensional model.

**2) Relatively large width-to-length ratio**– The lubrication theory and wide-beam framework necessitate the channel length to be much larger than its width, *i.e.*  $W/L \ll 1$ , which is not quite met for the studied microchannels. In particular, the width-to-length ratio is rather large for Microchannel E, *i.e.*  $W/L \approx 0.23$ . If microchannel is not sufficiently long, membrane’s infinitesimally small slices across the channel cannot be accurately approximated as wide beams. Under these situations, local membrane deflection is influenced not only by local pressure but also by upstream pressure within the channel, as a result of which membrane exhibits a larger deformation than predicted by the model, which can cause mass flow rate to be underestimated, similar to what is observed in case of Microchannel E.

**3) Relatively large membrane deformation**– Membrane’s elastic deformation in this work is based on thin-plate-bending framework, which necessitates membrane deformation to be much smaller than its thickness, *i.e.*  $\delta H \ll t$ . As shown in Fig. 58 (a), this requirement is not perfectly met for Microchannels C and E under too large pressure differences.

**4) Relatively large Reynolds number**– The one-dimensional model is developed based on low-Reynolds-number-flow assumption, *i.e.*  $Re \ll 1$ . As shown in Fig. 58 (b), the Reynolds number can be relatively large when pressure difference is large. Under these conditions, inertia effects can cause the Poiseuille flow pattern to be locally disturbed.

**5) Relatively large Knudsen number**– The one-dimensional model developed in this work is based on continuum mechanics with no-slip velocity boundary condition on walls. The limit of continuum models is somewhere between  $Kn = 0.5$  and  $1$  [205], while the transition regime is typically split into a slip regime at lower Knudsen numbers, *i.e.*  $Kn \approx 0.05$  [205], wherein the Navier-Stokes equations are joint with higher-order boundary conditions to predict the gas flow characteristics accurately [205, 216]. The Navier-Stokes equations accompanied by no-slip boundary condition starts to fail for Knudsen numbers larger than about  $0.01$ . The Knudsen number, *i.e.*  $Kn \equiv \lambda/H = \sqrt{\pi/2R_{sgc}T}(\mu/\rho H)$ , where  $\lambda$  denotes mean free path of gas molecules, has been calculated for different microchannels under various pressures. The average Knudsen number  $Kn_{avg} = (Kn_i + Kn_o)/2$ , where  $Kn_i$  and  $Kn_o$  refer to the Knudsen numbers at inlet and outlet, respectively, varies between  $0.004$  and  $0.029$  for the microchannels studied in this work, which partially falls under the slip-flow regime category. Although the Navier-Stokes equations are still applicable to this  $Kn$  range, the velocity slip on walls can cause mass flow rate to be underestimated by our model. The slip boundary condition can be implemented to Eq. 59 in order to derive a more accurate one-dimensional model for the slip-flow regime.

## Conclusion

A theoretical coupled fluid-solid-mechanics model was developed for compressible fluid flow through deformable microchannels to predict fluid-solid characteristics such as the mass flow rate, pressure distribution within microchannel, membrane deformation, etc. The model is based on the lubrication theory and wide-beam framework. The analytical solution allows us to elicit an explicit correlation between pressure difference across the channel and mass flow rate. The effects of fluid compressibility and channel deformability on characteristic behavior

of fluid flow have been studied theoretically and experimentally. The results showed that distinct characteristics can emerge under various pressure differences. Compressible fluid flow through a deformable microchannel resembles incompressible flow through the rigid counterpart under sufficiently small pressure differences, while height-independent and highly non-linear pressure-dependent characteristics, *e.g.*  $\dot{m} \propto \Delta p^5$ , appear under sufficiently large pressure differences. The current model has been developed assuming the no-slip boundary condition on the walls. Implementation of slip velocity boundary condition remains for future works to develop similar models appropriate for larger Knudsen number regimes.

# Chapter 6: Low-Reynolds-number compressible fluid flow through asymmetric deformable microchannels

## Questions

The main questions of this research are enumerated in the following.

- Can an analytical model be derived to simultaneously capture fluid compressibility, channel deformability, and width profile effects for low-Reynolds-number flows of Newtonian fluids?
- How does a width profile affect the fluid-solid mechanics of low-Reynolds-number compressible flows of Newtonian fluids through deformable microchannels?
- Can a membrane deformation-induced change in hydrodynamic resistance provide direction-dependent net hydrodynamic resistance and compressible flow rectification under the Stokes flow regime?

## Motivations

Fluid flows through microchannels with width profiles different from that of a straight microchannel are commonly used in Lab-on-a-chip and MEMS technologies. An analytical model simultaneously taking fluid compressibility, channel deformability, and width profile

effects into account is still missing in the literature, which motivates this research. To the author's knowledge, rectification of low-Reynolds-number gas flows with equilibrium processes has not been demonstrated, which further motivates this research to examine the feasibility of rectifying compressible flows under the Stokes regime.

## Objectives

The objectives of this research are to develop a universal analytical tool for studying Stokes flows of Newtonian liquids and gases through deformable channels with an arbitrary width profile, and to investigate the feasibility of compressible flow rectification.

## Introduction

In Chapter 5, both channel deformability and fluid compressibility were taken into account to study fluid flow through straight microchannels. In this chapter, the model is extended to capture the microchannels' width profile as well. Inspired by our findings from Chapter 4, we are particularly interested in asymmetrically-shaped microchannels in hopes of being able to rectify equilibrium gas flows (Knudsen number smaller than 0.01) under the Stokes flow regime ( $\text{Re} \ll 1$ ). Although a rarefied gas flow rectification ratio of  $\sim 1.1$  has been reported [190, 191] using tapered channels under the slip flow regime ( $O(\text{Kn}) \approx 10^{-2}$ – $10^{-1}$ ), to the author's knowledge, rectification of low-Reynolds-number gas flows with equilibrium processes ( $\text{Kn} < 0.01$ ) has not been demonstrated. Here, we develop a universal analytical tool for studying low-Reynolds-number compressible fluid flows through asymmetrically-shaped deformable microchannels, leading to demonstration of gas rectification ratios of  $\sim 1.2$ – $1.7$ .

## Modeling

### General compressible fluid flow

The schematic presentation of a compressible fluid flow through a nozzle/diffuser microchannel with a deformable ceiling is the same as that shown in Fig. 40. The one-dimensional model developed in this work is based on the lubrication theory necessitating  $H_0 \ll W \ll L$ , where  $H_0$ ,  $W$ , and  $L$  refer to the microchannel original height with no membrane deformation, width, and length, respectively. The thin-plate-bending framework is considered for the elastic deformation, which requires  $\delta H \ll t \ll W$ , where  $\delta H$  is the membrane displacement and  $t$  denotes the membrane thickness. Under these situations, an arbitrary membrane's infinitesimal slice across the channel can be considered as a wide beam. The deflection profile of the slice is then obtained from the Euler-Bernoulli beam theory and can be presented as:

$$\frac{\delta H(x, \zeta)}{H_0} = \gamma(x)f(\zeta), \quad (86)$$

where  $\zeta \equiv 2y/W(x)$ ,  $f(\zeta) = (\zeta + 1)^2(\zeta - 1)^2$ ,  $\gamma(x) = p(x)W^4(x)/384DH_0$ , and  $D = \frac{Et^3}{12(1-\nu^2)}$ , in which  $E$  and  $\nu$  denote the membrane's modulus of elasticity and Poisson's ratio [186]. In addition,  $p$  refers to the gauge pressure within the channel, which is constant at any x-plane (normal to the x-axis) according to the lubrication theory.

Since the membrane displacement is significantly smaller than the channel width and length, *i.e.*  $\delta H \ll W \ll L$ , the membrane slope is very small, *i.e.*  $\partial\delta H/\partial x \ll 1$  and  $\partial\delta H/\partial y \ll 1$ . Under these situations, and considering the sufficiently small nozzle/diffuser half-angle ( $\theta$ ) with an attached flow throughout the channel, a local mass flow rate can be written as  $\dot{m}(x) = -\frac{dp(x)/dx}{12\mu}\rho(x)W(x) \langle H^3 \rangle_{(x)}$ , where  $\rho$  and  $\mu$  refer to the fluid density and dynamic viscosity, respectively, and  $H = H_0 + \delta H$  shows the channel's local height. In addition, the average of an arbitrary variable such as  $\phi$  over a x-plane is obtained through  $\langle \phi \rangle_{(x)} = \frac{1}{2} \int_{\zeta=-1}^{\zeta=+1} \phi(x, \zeta) d\zeta$ . In a non-dimensional form, where the fluid density at ambient pressure and ambient temperature,  $\rho_{\text{ref}}$ , is used for the density unit,  $L$  for the length unit,

$\dot{m}_{\text{ref}}$  for the mass flow rate unit,  $Q_{\text{ref}} = \dot{m}_{\text{ref}}/\rho_{\text{ref}}$  for the volumetric flow rate unit, and  $\Delta p_{\text{ref}} \equiv 12\mu L Q_{\text{ref}}/W_i H_0^3$  as the pressure unit, the dimensionless mass flow rate through the deformable channel, *i.e.*  $\dot{m}^* \equiv \dot{m}/\dot{m}_{\text{ref}}$ , can be written as

$$\dot{m}^* = -\rho^* \frac{dp^*(x^*)}{dx^*} \frac{W^*(x^*)}{W_i^*} \frac{\langle H^3 \rangle_{(x^*)}}{H_0^3}, \quad (87)$$

where  $W_i$  refers to the channel width at inlet,  $\rho^* \equiv \rho/\rho_{\text{ref}}$ ,  $p^* \equiv p/\Delta p_{\text{ref}}$ ,  $x^* \equiv x/L$ ,  $W^* \equiv W/L$ , and  $W_i^* \equiv W_i/L$ . In general, the fluid density can be variable within the channel due to the compressibility effects. For an isothermal fluid flow, we have  $\rho^* = 1 + p\kappa_T$ , where  $\kappa_T$  denotes the isothermal compressibility of the fluid at ambient pressure and ambient temperature. Considering that  $\langle H^3 \rangle = H_0^3 + 3H_0^2 \langle \delta H \rangle + 3H_0 \langle (\delta H)^2 \rangle + \langle (\delta H)^3 \rangle$ , one can show that

$$\begin{aligned} \frac{\langle H^3 \rangle_{(x^*)}}{H_0^3} &= 1 + 3\gamma(x^*) \langle f(\zeta) \rangle_{(x^*)} \\ &+ 3\gamma^2(x^*) \langle f^2(\zeta) \rangle_{(x^*)} + \gamma^3(x^*) \langle f^3(\zeta) \rangle_{(x^*)}. \end{aligned} \quad (88)$$

We know  $\langle f(\zeta) \rangle = 8/15$ ,  $\langle f^2(\zeta) \rangle = 128/315$ , and  $\langle f^3(\zeta) \rangle = 1024/3003$ . Considering that  $p^* = 0$  at  $x^* = 1$  due to the fluid discharge into the ambient air, after defining  $\xi \equiv 1 - x^*$  and substituting Eq. 88 in Eq. 87, one can obtain an initial-value problem for an arbitrary mass flow rate of  $\dot{m} = \dot{m}_{\text{ref}}$ , *i.e.*  $\dot{m}^* = 1$ , as shown in the following first-order non-linear ordinary differential equation (ODE):

$$\begin{aligned} &\left( 1 + \alpha_1 \tau^4(\xi) p^*(\xi) + \alpha_2 \tau^8(\xi) p^{*2}(\xi) + \alpha_3 \tau^{12} p^{*3}(\xi) \right) \times \\ &\quad \left( 1 + p^*(\xi) \kappa_T^* \right) \tau(\xi) \frac{dp^*(\xi)}{d\xi} = 1, \end{aligned} \quad (89)$$

$$\text{Initial value: } \quad \xi = 0 : p^* = 0,$$

where the dimensionless isothermal compressibility of the fluid is defined as  $\kappa_T^* \equiv \kappa_T \Delta p_{\text{ref}}$ ,

and the width profile function, *i.e.*  $\tau(\xi)$ , flexibility parameter, *i.e.*  $\chi$ , and  $\alpha_i$  coefficients are

$$\tau(\xi) \equiv W(\xi)/W_i, \quad (90a)$$

$$\chi \equiv \frac{\Delta p_{\text{ref}} W_i^4}{384 D H_0}, \quad (90b)$$

$$\alpha_1 = \frac{8}{5}\chi, \alpha_2 = \frac{128}{105}\chi^2, \text{ and } \alpha_3 = \frac{1024}{3003}\chi^3. \quad (90c)$$

For a nozzle/diffuser microchannel with a linear variation of the width,  $\tau(\xi) = \tau_o + (1 - \tau_o)\xi$ , where  $\tau_o \equiv W_o/W_i$  and  $W_o$  refers to the channel width at outlet. The governing equation is reduced to that of the fluid flow through a deformable shallow straight microchannel (Chapter 5) [217] for the special case of  $\tau = 1$ . The ODE presented in Eq. 89 is solved numerically to find the pressure distribution within the channel, *i.e.*  $p^*(\xi)$ , and other fluid-solid characteristics.

### Ideal gas flow

As a special case of the compressible fluid flows, an ideal gas flow can be investigated using the general model derived in the previous section (Chapter 5). The isothermal compressibility of an ideal gas flow is

$$\kappa_T \Big|_{p_{\text{atm}}, T_{\text{atm}}} = \frac{1}{p_{\text{atm}}}. \quad (91)$$

By using the isothermal compressibility of the ideal gas, one obtains

$$\kappa_T^* \Big|_{p_{\text{atm}}, T_{\text{atm}}} = \frac{1}{p_{\text{atm}}^*}, \quad (92)$$

where  $p_{\text{atm}}^* \equiv p_{\text{atm}}/\Delta p_{\text{ref}}$ . The governing coupled fluid-solid mechanics equations for the ideal gas flows can then be derived as

$$\left( 1 + \alpha_1 \tau^4(\xi) p^*(\xi) + \alpha_2 \tau^8(\xi) p^{*2}(\xi) + \alpha_3 \tau^{12} p^{*3}(\xi) \right) \times \left( 1 + \frac{p^*(\xi)}{p_{\text{atm}}^*} \right) \tau(\xi) \frac{dp^*(\xi)}{d\xi} = 1, \quad (93)$$

$$\text{Initial value: } \quad \xi = 0 : p^* = 0,$$

where the width profile function, flexibility parameter, and  $\alpha_i$  coefficients are the same as defined in Eq. 90.

## Materials and methods

### Fabrication

The microchannels were created through glass wet etching process, drilling the via-holes, and adhesive bonding using a 2  $\mu m$ -SU8-coated PET (polyethylene terephthalate) film ( $t = 100 \mu m$  and  $\nu = 0.4$ ) followed by bonding reinforcement using a glass slide with the sufficiently deep ( $\sim 45 \mu m$ ) etched pattern of the microchannel allowing the membrane to deform freely under pressure. The reinforcement glass is bonded to the bare side of the membrane using a 16  $\mu m$  SU8 layer [164, 187]. In order to take the structural effects of the adhesive layers into account, by using the transformed-section method [165], the equivalent membrane thickness, calculated from  $\tilde{t} = \sqrt[3]{12I/W}$ , where  $I$  denotes the three-layer membrane's moment of inertia, was used in parameter  $D$  appearing in Eq. 90 (b) to evaluate the flexibility parameter. The modulus of elasticity of SU8 and PET film were considered to be 2.5 GPa and 3.5 GPa, respectively. The reason for considering slightly larger elasticity modulus values for the SU8 and the membrane compared with the corresponding values in Chapter 4 is that we had to carry out our experiments to obtain all the required data-sets of flow rate vs. pressure drop across different devices over several weeks starting with liquids as the working fluid, followed by the investigation of air flow. We noticed that flow rate was slightly decreasing after several weeks, which might be contributed to the membrane becoming slightly stiffer due to aging. Considering the aforementioned values for thickness and modulus of elasticity of different layers,  $\tilde{t} \approx 113.7 \mu m$ .

### Flow rate measurement

Compressed air, whose pressure was adjusted using a pressure regulator (PneumaticPlus, PPR2-N02BG-4 Miniature Air Pressure Regulator) was injected through the microchannel.

The gas discharged from the microchannel was guided through a tube with a known inner diameter, where a small water plug was placed and pushed out by the applied air pressure. The movement of the water plug was monitored with the camera attached to the stereomicroscope, and the linear velocity of the liquid meniscus was measured to calculate the volumetric flow rate in outlet ( $Q$ ) and mass flow rate ( $\dot{m} = \rho_{\text{air}}Q$ ) of the air. Depending on the magnitude of the flow rates, different tube diameters of  $0.794 \text{ mm}$ , and  $3.175 \text{ mm}$  were employed to better trace the water meniscus. The hydrodynamic resistance of the capillary tubes is at least three orders of magnitude smaller than that of the studied devices to avoid the spurious effects on the measured mass flow rates.

## Results and discussion

In Chapter 5, we have already shown the importance of both fluid compressibility and microchannel deformability in studying the coupled fluid-solid mechanics, demonstrating that neglecting either of them under sufficiently large pressure differences can lead to erroneous results. To examine the compressibility effects on the characteristic behavior of the flow, particularly the rectification ratio, we have investigated air flows through the fabricated nozzle/diffuser devices. The devices used in this work are the same as those used in Chapter 4. Regarding the modeling, air is assumed to behave as an ideal gas, and its dynamic viscosity is considered to be a constant value of  $\mu = 1.8 \times 10^{-5} \text{ Pa}\cdot\text{s}$ . The ambient temperature and pressure are  $295 \text{ K}$  and  $101 \text{ kPa}$ , respectively. The air specific gas constant equals  $R_{\text{sgc}} = 287.058 \text{ J}\cdot\text{kg}^{-1}\cdot\text{K}^{-1}$ .

The Reynolds number in the mid-plane ( $x^* = 0.5$ ) varies from  $O(10^{-3})$  to  $O(10^{+1})$  for the investigated flows. The mass flow rates of the air flow through nozzle/diffuser microchannels with different original heights obtained from both modeling and experiments are shown in Figs. 59 and 60 for rigid and deformable microchannels, respectively. In order to obtain the theoretical results for the incompressible fluid flows, the isothermal compressibility is considered to be zero in Eq. 89. Also according to Eq. 90, the flexibility parameter and consequently the  $\alpha_i$  coefficients in Eq. 89 are zero for a fluid flow through a rigid microchannel.

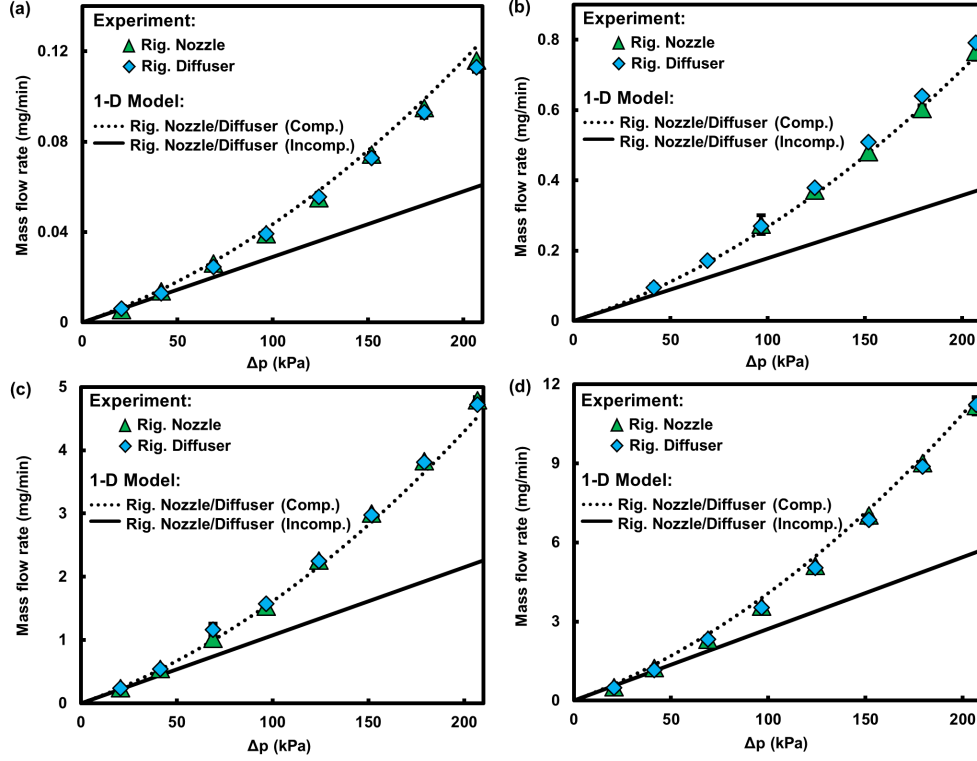


Figure 59: Mass flow rate of air as a function of pressure difference across the rigid (Rig.) nozzle/diffuser microchannels with small and large widths of  $1\text{ mm}$  and  $2\text{ mm}$  and a half-angle of  $1.25^\circ$  for various original heights of  $H_0 =$  (a)  $2.6\ \mu\text{m}$ , (b)  $4.6\ \mu\text{m}$ , (c)  $8.0\ \mu\text{m}$ , and (d)  $10.9\ \mu\text{m}$ . The modeling results with and without compressibility effects taken into account are shown by dotted and solid lines, respectively.

It is perceived from Fig. 59 that unlike an incompressible fluid flow through a rigid microchannel, the mass flow rate of the air flow increases nonlinearly with pressure difference. Yet the rigid nozzle and diffuser exhibit the same characteristic behavior resulting in no flow rectification, *i.e.* the hydrodynamic resistance is not dependent on the fluid flow direction. For the case of deformable microchannels, however, a nozzle delivers a larger mass flow rate under the same pressure difference, resulting in a fluid flow rectification; see Figs. 60 and 61.

The rectification ratio, which is defined in this work as  $\eta = \dot{m}_{\text{Nozzle}}/\dot{m}_{\text{Diffuser}}$ , is presented in Fig. 61 for the investigated deformable microchannels. We found that the rectification ratio of air flow is slightly smaller than that of the liquid flows (Fig. 43). For the flow of a fluid with larger compressibility, the local fluidic resistance increases along the channel because of a larger density gradient within the channel. The fluid density decreases along the channel as the pressure decreases along the channel. According to the conservation of mass principle,

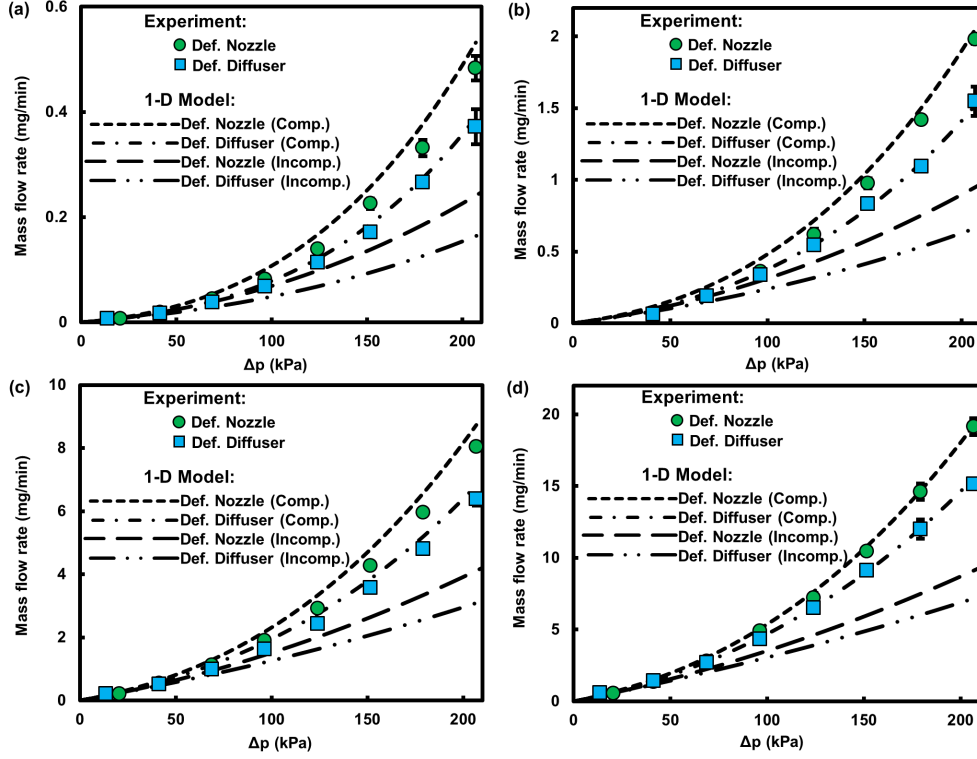


Figure 60: Mass flow rates of air as a function of pressure difference across the deformable (Def.) nozzle/diffuser microchannels with small and large widths of  $1\text{ mm}$  and  $2\text{ mm}$  and a half-angle of  $1.25^\circ$  for various original heights of  $H_0 =$  (a)  $2.6\ \mu\text{m}$ , (b)  $4.6\ \mu\text{m}$ , (c)  $8.0\ \mu\text{m}$ , and (d)  $10.9\ \mu\text{m}$ , together with modeling results for the air flow being considered as a compressible (Comp.) and incompressible (Incomp.) flow.

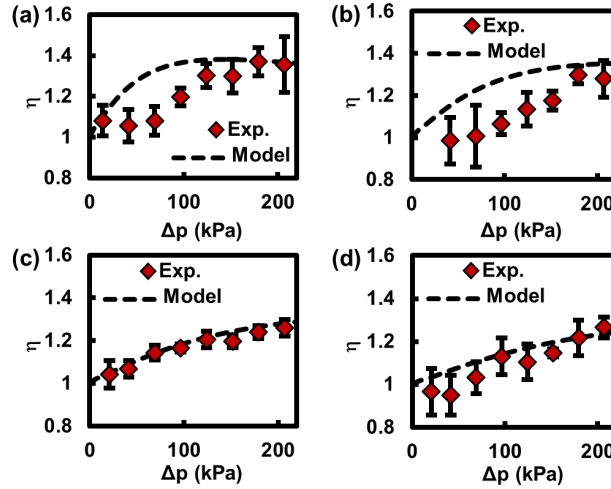


Figure 61: Experimental and theoretical values of the air flow rectification ratio, *i.e.*  $\eta = \dot{m}_{\text{Nozzle}}/\dot{m}_{\text{Diffuser}}$ , as a function of pressure difference across the deformable nozzle/diffuser microchannels with small and large widths of  $1\text{ mm}$  and  $2\text{ mm}$  and a half-angle of  $1.25^\circ$  for various original heights of  $H_0 =$  (a)  $2.6\ \mu\text{m}$ , (b)  $4.6\ \mu\text{m}$ , (c)  $8.0\ \mu\text{m}$ , and (d)  $10.9\ \mu\text{m}$ .

such a decaying density variation causes the fluid speed, shear rate, local frictional resistance, and net fluidic resistance to increase along the channel. As a result, the contribution of the wide portion in the nozzle’s hydrodynamic resistance decreases for a nozzle, while that increases for a diffuser. Consequently, the membrane displacement-induced reduction in the hydrodynamic resistance of a nozzle decreases, while that increases for a diffuser, leading to a rectification ratio smaller than that of the incompressible flows. Regardless of the lower rectification ratios of compressible flows compared with those of incompressible flows, this work still reports the first demonstration of rectifying an equilibrium gas flow (Knudsen number smaller than 0.01) under the Stokes flow regime with rectification ratios of  $\sim 1.4$ .

Similar to incompressible flows studied in Chapter 4, the geometry of rectifiers can be modified for achieving higher rectification ratios. Eqs. 89–90 are the general governing equations applicable to any time-independent compressible Newtonian fluid flows through a long and shallow microchannel with a deformable ceiling and an arbitrary width profile as long as  $dW/dx \ll 1$ , so that the fluid flow characteristics for a straight channel and the straight wide-beam theory are locally valid. As shown in Fig. 62, the linear width profile function can be modified for achieving larger rectification ratios.

An important advantage of the illustrated rectification mechanism and other flow regulation techniques accompanied by a theoretical fluid-solid-mechanics model, such as the elastic snap-through fuse demonstrated by Gomez *et. al* [218], is that the microchannel can be reliably designed using the theoretical model. Whereas, the inertia-based rectifiers inherently functioning in the presence of vortices are governed by the non-linear Navier-Stokes equations, making it difficult to deterministically predict the fluid-solid behavioral characteristics.

The Knudsen number, *i.e.*  $\text{Kn} \equiv \lambda/H = \sqrt{\pi/2R_{\text{sgc}}T_{\text{atm}}(\mu/\rho H)}$ , where  $\lambda$  denotes the mean free path of the gas molecules, has been calculated for different microchannels under various pressures. For the microchannels studied in this work, the average Knudsen number  $\text{Kn}_{\text{avg}} = (\text{Kn}_i + \text{Kn}_o)/2$ , where  $\text{Kn}_i$  and  $\text{Kn}_o$  refer to the Knudsen numbers at inlet and outlet, respectively, varies between  $\sim 0.003$  for highest pressure difference across the deepest channel

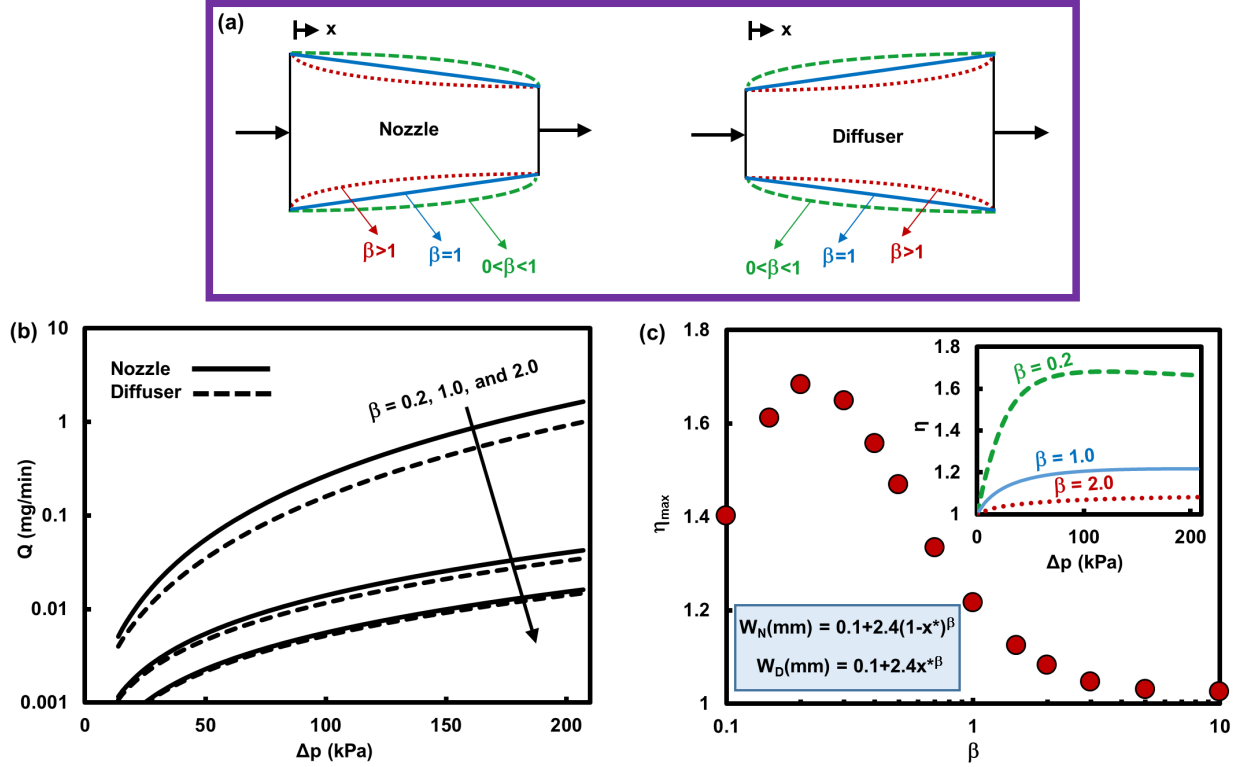


Figure 62: (a) Schematic representation of different channel width profiles in the nozzle direction, *i.e.*  $W_N = W_o + (W_i - W_o)(1 - x^*)^\beta$ , as well as the diffuser direction, *i.e.*  $W_D = W_i + (W_o - W_i)x^{*\beta}$ . (b) Mass flow rates of air obtained from the 1-D coupled fluid-solid-mechanics model as a function of pressure difference across the deformable nozzle/diffuser microchannels of  $2.6 \mu\text{m}$  in height with the half-angle of  $\theta = 1.25^\circ$ , and small and large widths of  $0.1 \text{ mm}$  and  $2.4 \text{ mm}$  for different width profiles. (c) The maximum rectification ratio,  $\eta = \dot{m}_{\text{Nozzle}}/\dot{m}_{\text{Diffuser}}$ , for microchannels with different width profiles achievable within the pressure difference range of 14–206 kPa. The inset shows the rectification ratio as a function of pressure difference across the channel for three width profiles with  $\beta = 0.2, 1.0, \text{ and } 2.0$ .

and  $\sim 0.03$  for lowest pressure difference across the shallowest channel, which partially falls under the slip-flow regime category for few data points related to the low pressure differentials across the shallowest channel. Although the Navier-Stokes equations are still applicable to this Kn range, the velocity slip on the walls can cause the mass flow rate to be underestimated. The slip boundary condition can be implemented to Eq. 87 in order to derive a one-dimensional model suitable for the compressible Stokes flows under the slip-flow regime.

## Conclusion and outlook

The model derived in this work simultaneously takes into account microchannel deformability, fluid compressibility, and microchannel's width profile, which makes it a universal tool for studying low-Reynolds-number flows of Newtonian liquids and gases in microscale. We have mathematically and experimentally demonstrated that the rectification mechanism proposed in Chapter 4 is universally applicable for passive rectification of compressible and incompressible flows of Newtonian fluids (liquids and gases) under the Stokes regime by introducing the non-linear and direction-dependent terms to the otherwise linear equations of motion. The described underlying physics may be exploited to develop gas micropumps, isolation of rare particulate matters within air and accurately determining their size distribution, etc.

# Chapter 7: Passive particle filtration and isolation using deformable microfluidics

## Questions

The main questions this research aiming to address are enumerated in the following.

- Is it feasible to make a passive microfluidic device for particle filtration and isolation purposes without the need to the external actuation?
- What would be a throughput range?
- Are disposable and reusable platforms obtainable for particle filtration?

## Motivations

Size exclusion, yet low-throughput, is among the most precise separation mechanisms. Operating based on this mechanism, rigid microfluidic filters are widely used for separating large particles from their aqueous media. One of the weaknesses of this approach is that once it is fabricated, the microfluidic device has a fixed opening size, which dictates an established specific diameter threshold for the particles being able to pass through the filter. Therefore, filtration of particles with different sizes would require new devices with corresponding

opening sizes. Furthermore, the target large particles are not isolated spontaneously for the potential post-filtration analysis.

Deformable microfluidic filters with a cutoff pore size tunable through squeezing the microchannel using the pneumatic actuation of the membrane with different pressure levels have been, therefore, receiving a growing interest because of a few advantages compared with the traditional rigid microfluidic filters, such as filtration and isolation of particles with different sizes, less problematic channel blockage issues, etc. The difficulties associated with the necessity of employing the pneumatic actuation for particle trapping, and the requirement of the continuous actuation for keeping the trapped particles stationary for the post-trapping analysis and handling purposes motivate this work to seek a new class of pneumatic-actuation-free deformable microfluidics.

## Objectives

The main objective of this research is to design and develop a pneumatic-actuation-free, and passively tunable microfluidic filter for filtration and isolation of particles from aqueous solutions. Both disposable and reusable platforms are of our interest.

## Introduction

In the context of the suspension constituents separation, the filtration techniques [46–48] and the centrifuge-based approaches [219] have probably the longest history of application in various bioanalytical processes. Being time-consuming, expensive, and labor-intensive, however, are the main difficulties associated with the traditional approaches. More importantly, the traditional techniques need a rather large amount of the samples to function properly. This fact limits their applications in the situations that either or both of the specimen volume and the cell count are low. In these situations, the rare species can be lost easily by using a large-scale traditional technique. The idea of the centrifugal force exploitation is successfully miniaturized by emerging the Lab-on-a-CD technology [220, 221].

On the other hand, a variety of different microfluidic devices are developed to miniaturize the filtration process in a much smaller scale [8, 222–230]. Wei *et. al.* [231] fabricated the porous membranes based on the development of the perforated membrane mold to create a single filter containing multiple pore sizes within a monolithic three-dimensional PDMS microfluidic structure. McFaul *et. al.* [232] created a physical cell separation device where cell samples are transported through a matrix of funnel constrictions using an oscillatory flow. Small and deformable cells move through the constrictions in a forward flow, while large and rigid cells are blocked. When the flow direction is reversed to unclog the constrictions, small and deformable cells are unable to pass back through due to the higher resistance in this direction. Wang *et. al.* [233] developed a porous silicon nanowire-on-micropillar structure for trapping exosome-like lipid vesicles, while simultaneously filtering out the proteins and cell debris. Interestingly, the trapped lipid vesicles are recovered intact after dissolving the porous nanowires in the PBS buffer.

The particles even smaller than the filter pore size can be trapped among the larger particles. The accumulation of all these large and small particles can result in the filter clogging rather quickly. In order to alleviate the difficulties associated with channel clogging, Yoon *et. al.* [53] imposed a low frequency mechanical oscillation to the fluid flow by using a piezoelectric actuator, to release the smaller species trapped among the larger ones so that the smaller species can pass through the filter. The fouling phenomenon caused by the particle deposition is also a significant limitation in the filtration applications. The effects of the ionic strength, pH, and solution concentration need to be studied to reveal the underlying mechanism of fouling and mitigate the difficulties associated with fouling [234–236]. The other drawback of the filtration process, in general, is its relatively low throughput, compared to many of the other available techniques particularly based on the inertia-based separation approaches [43, 44, 237]. The inertia-based techniques as well as those based on the hydrodynamic fractionation [238, 239], fractionation using the external electric field [64, 240], magnetic field [241, 242], acoustic field [243, 244], etc., are generally capable of sorting the particles into several separate size bands, while the filtration strategy

is suitable for filtering particles larger than a specific cutoff pore size.

In spite of these restrictions, filtration is still widely used because it is among the most reliable techniques with regards to the separation efficiency. The pore size of the filters can be wisely designed so that almost none of the target cells can pass through the filter, while the purity level of the collected solution is generally lower using the other techniques [245]. This unique advantage keeps the filtration strategy as one of the most widely used techniques in order to filter/concentrate cells, in general, and rare cancer tumor cells, in particular.

Externally adjusting the geometry of the flexible microfluidic devices have already been reported for tuning the functionality of the microfluidic separators [14, 78–81]. There have been also numerous efforts to develop the tunable microfluidic filters with an adjustable cutoff pore size by using the external pneumatic actuators [15–17, 152, 153, 246–248]. The main strategy of these techniques is to utilize a sufficiently deep and deformable microchannel, which can be squeezed under a pressure applied on the membrane using the external pneumatic actuation in a separate control chamber. The decrease in the microchannel height can be tuned by adjusting the pressure of the control chamber. Huang *et. al.* [15, 153] have used this gating control mechanism to adjust the cutoff pore size by applying various pressures to the movable membrane sealing the microfluidic filter. They have demonstrated the microbeads and cells with different diameters can be trapped under various pressures. A similar strategy was employed by Beattie *et. al.* [17] to trap different sizes of beads/cells by adjusting the control layer pressure. They have used the resettable structures with the ability to alternate between capturing the target beads and cells from the mixture and releasing them back into the flow channel. Liu *et. al.* [16] have also used the adjustable pneumatic structures for trapping and releasing the target cells. Besides the requirement of the pneumatic actuation for trapping the target particles, the necessity of the continuous pneumatic actuation of the membrane for the trapped particles to remain stationary can pose difficulties with regard to the convenience of working with these devices, whenever the pertinent post-analysis, microscopy, and handling of the device are important.

Here, we introduce a new class of deformable microfluidics for particle filtration and

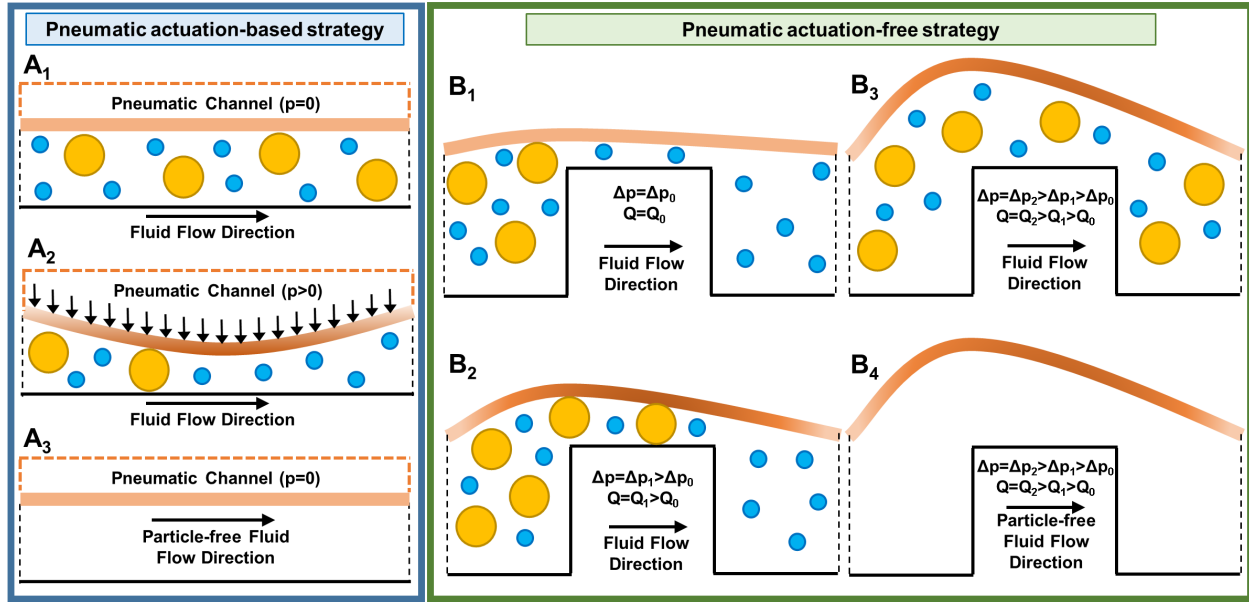


Figure 63: The schematic representation of (A<sub>1</sub> – A<sub>3</sub>) the pneumatic actuation-based strategy for particle trapping in comparison with (B<sub>1</sub> – B<sub>4</sub>) the new idea presented in this work without the the need to the pneumatic actuation. In the pneumatic actuation-based approach, the channel is sufficiently deep so that all the particles can pass through the channel (A<sub>1</sub>), while a sufficiently large pressure in the pneumatic channel can cause the membrane deformation and trapping the sufficiently large particles (A<sub>2</sub>). The trapped particles can be retrieved by lifting the pressure within the pneumatic channel and applying a particle-free fluid flow (A<sub>3</sub>). In the new strategy presented in this work, the duct on the weir is sufficiently shallow not to allow the large particles to enter the shallow passage under the sufficiently low pressure difference across the channel, *i.e.* filtration (B<sub>1</sub>), while the membrane deforms more with increasing the pressure difference enabling the target particles to be trapped on the weir under an appropriate pressure difference range, *i.e.* isolation (B<sub>2</sub>). Under a sufficiently large pressure difference, the particles can pass through the device without membrane obstructions (B<sub>3</sub>). The trapped particles can be retrieved using a particle-free fluid flow with a sufficiently large volumetric-flow rate (B<sub>4</sub>).

isolation without the need of a separate actuation scheme for adjusting a control layer. The schematic representation of the conventional pneumatic actuation-based tunable microfluidic filters and that of the pneumatic actuation-free strategy proposed in this work are presented in Fig. 63. The technique proposed in this work utilizes a micro-weir with a deformable ceiling providing a shallow duct (several microns in height in the absence of membrane deformations) with a tunable height on top of the weir. The microchannel width on the micro-weir is sufficiently large (several millimeters) to allow a sufficiently large membrane deflection ( $O(1-10 \mu m)$ ). Under the sufficiently small pressure differences across the microchannel, the large particles are filtered behind the micro-weir, *i.e.* filtration (Fig. 63 (B<sub>1</sub>)). The bulging due to the membrane deformation under an appropriate range of the pressure difference

across the channel allows the large particles to enter the shallow region of the microchannel, and to be trapped there, *i.e.* isolation, while the sufficiently small particles can be filtered out (Fig. 63 (B<sub>2</sub>)). The microchannel returns to its undeformed geometry when the pressure difference is lifted, causing the trapped particles on top of the micro-weir to be sandwiched and remain stationary. By increasing the pressure difference sufficiently, the large particles find a sufficiently large opening to pass through the channel (Fig. 63 (B<sub>3</sub>)), which enables the retrieval of the trapped particles (Fig. 63 (B<sub>4</sub>)).

After providing some design guidelines and illustrating the fabrication technique, we divide the rest of this chapter into two parts: Part I: disposable platforms, in which retrieving the trapped particles is not needed, and Part II: reusable platforms, in which an efficient particle retrieval is required. It should be noted that in Part I, trapped particles are still removed whenever possible to be able to carry out multiple experiments using the fabricated devices.

## Design

In order to provide some design guidelines, single-height straight microchannels are considered in this section. Effects of different parameters such as the microchannel dimensions and pressure difference across the channel on the membrane deflection and particle sieving are investigated via numerical simulations based on the model described in Chapter 2. The PET film thickness is 200  $\mu m$  throughout this work.

### Pressure effects

The different height levels of the deformed PET film by pressurized fluid flows have been shown in Figs. 64 and 65 for two microchannels with different dimensions. The PET film deflection profile for various pressure differences across the two studied channels are also shown in Fig. 66 for the inlet and outlet sections. It is perceived that the deformable microchannel can be hypothetically exploited as a tunable sieve with various opening levels at the outlet. Such mechanism does not need an external actuation. Instead, it relies on the

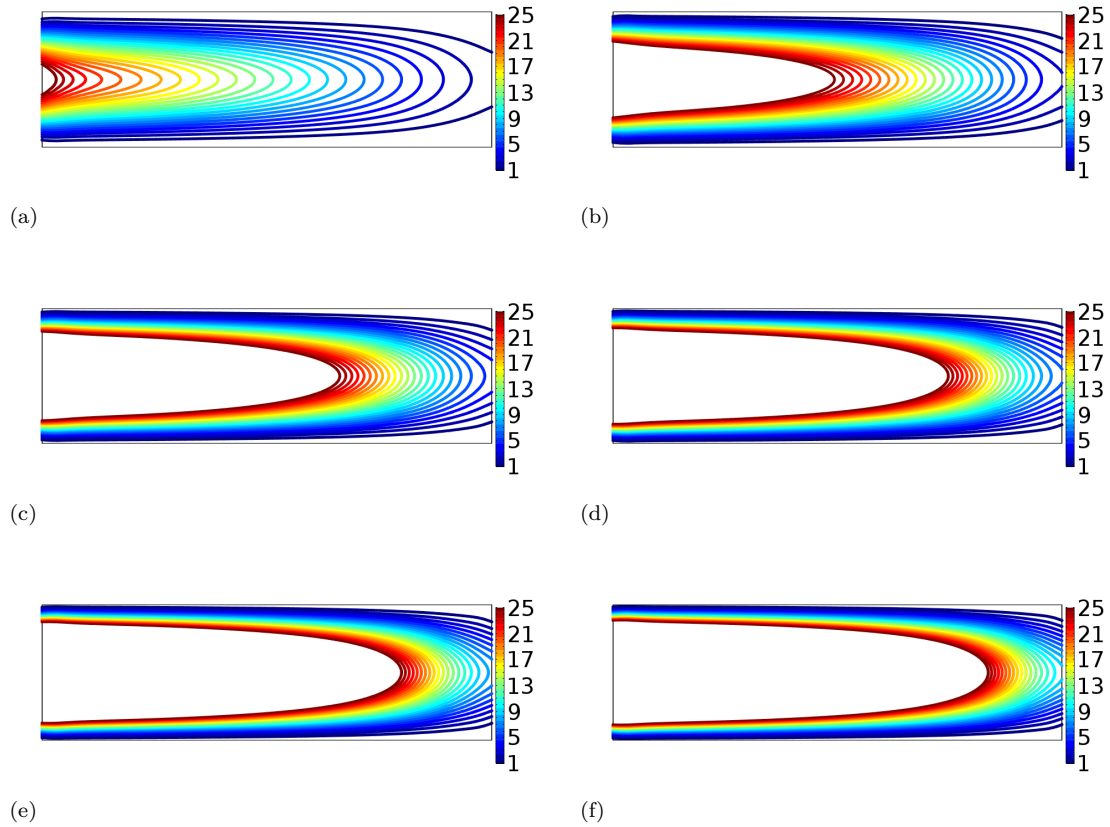


Figure 64: The different height levels ( $\mu m$ ) of the 200-micron-thick PET film at various pressure differences of (a) 15 kPa, (b) 30 kPa, (c) 45 kPa, (d) 60 kPa, (e) 75 kPa, and (f) 90 kPa across the microchannel 6 mm and 2 cm in width and length, respectively.

different membrane deflections under various pressure differences across the microchannel. For example, the configuration shown in Fig. 64 (a) can be used to allow the particles with diameters smaller than  $H_0 + 1.5 \mu m$  to pass through the channel, where  $H_0$  refers to the original height of the microchannel in absence of the pressure difference across the channel, while the particles larger than  $H_0 + 1.5 \mu m$  will be trapped inside the channel. On the other hand, according to Fig. 64 (f) the same device can still be used to allow particles with diameters between  $H_0$  and  $H_0 + 9.5 \mu m$  to pass through the filter under the pressure difference of 90 kPa across the channel, while the particles larger than  $H_0 + 9.5 \mu m$  will be trapped inside the channel. It is worth mentioning that the magnitude of  $H_0$  determines the minimum particle size that can be sieved. The shallow microchannel is, therefore, of utmost importance for such passively tunable filters to be applicable to the target cells several mi-

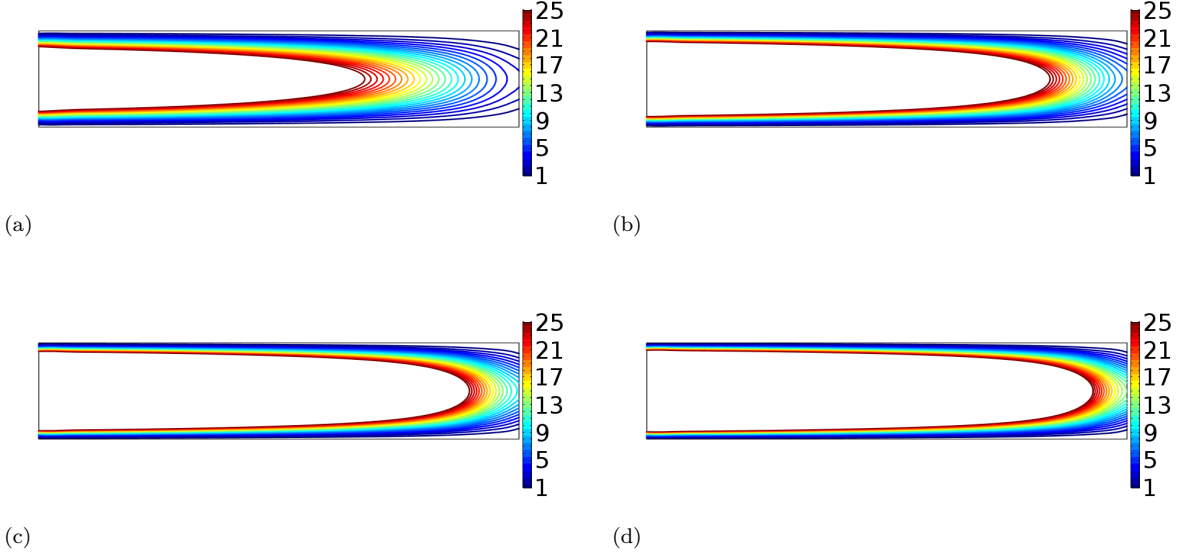


Figure 65: The different height levels ( $\mu\text{m}$ ) of the PET film at various pressure differences of (a) 15 kPa, (b) 30 kPa, (c) 45 kPa, and (d) 60 kPa across the microchannel 8 mm and 4 cm in width and length, respectively.

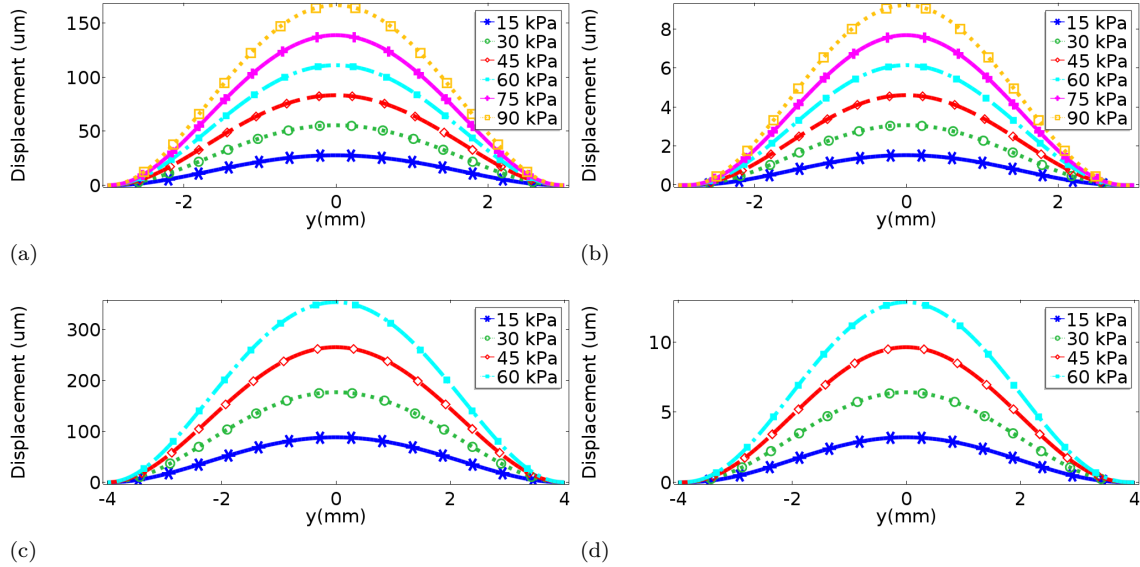


Figure 66: The PET film deflection profile under various pressure differences at the (a, c) inlet and (b, d) outlet sections for two microchannels of (a, b) 6 mm and 2 cm in width and length, respectively, and (c, d) 8 mm and 4 cm in width and length, respectively.

crons in diameter. It should be noted here that at this step, the discussion is purely based on the membrane deflection contours. Later in this chapter, we will discuss that the particles momentum cannot be boundlessly high, since it can cause:

Table 10: The pressure effects investigation for a microchannel 6 mm and 2 cm in width and length, respectively.

Pressure (kPa)	30	45	60	75	90
Mean deflection ( $\mu m$ )	13.4	20.2	26.9	33.6	40.3
Maximum deflection at outlet ( $\mu m$ )	3.1	4.7	6.2	7.8	9.4
<b>Initial height (<math>H_0</math>) = 2.2 <math>\mu m</math>:</b>					
Volume flow rate ( $ml/min$ )	1.4	6	17.4	40.5	81.1
Average velocity $\bar{u}$ ( $m/s$ )	0.1215	0.371	0.83	1.58	2.66
Reynolds number ( $\frac{\rho \bar{u} d_h}{\mu}$ )	7.55	33	96	222	444
Particle Reynolds number for a 10-micron bead ( $Re \times (d_p/d_h)^2$ )	0.8	1.7	2.9	4.4	6.2
Stokes number for a 10-micron bead ( $\frac{\rho_p d_p^2 / 18 \mu}{d_h / \bar{u}}$ )	0.024	0.051	0.088	0.135	0.192

- the particles larger than expected to pass through the channel too because of the PET film compliance, which allows the PET film to deform more in contact with the high-momentum particles, and
- the particles to be stuck in the wedges, which makes it significantly hard to remove the trapped particles at the end.

Similarly, the microchannel 8 mm and 4 cm in width and length, respectively, can be used to separate particles with diameters smaller than  $H_0 + 3.5 \mu m$  and smaller than  $H_0 + 9.5 \mu m$  under the pressure differences of 15 kPa and 45 kPa across the channel, respectively, as shown in Fig. 65 (a) and (c) and Fig. 66.

In the next step, in order to predict the fluid flow and the particles motion behavior, the important parameters representing the fluid flow characteristics are estimated. The model proposed for the ultra-low-aspect-ratio microchannels in Chapter 2 will be used. Briefly, the deformable microchannel is replaced by a non-deformable channel with a height equal to the average height of the deformable microchannel under pressure. The mean PET film deflection is shown in Table 10 in presence of the various pressure differences across a microchannel 6 mm and 2 cm in width and length, respectively. Furthermore, by considering a microchannel with the original height equal to 2.2  $\mu m$ , more details about the fluid flow and the motion of particles 10  $\mu m$  in diameter with a density of 1100  $kg/m^3$  are presented.

The high volumetric flow rate might be attractive in operation, since it would generate high-throughput microfluidic filters with tunable opening size. However, as previously

Table 11: The effects of the pressure difference across the channel as well as the microchannel original height on the PET film deformation and the characteristics of the flow through a microchannel 8 mm and 4 cm in width and length, respectively.

Pressure (kPa)	15	30	45	60
Mean deflection ( $\mu m$ )	21.0	42.1	63.1	84.2
Maximum deflection at outlet ( $\mu m$ )	3.2	6.5	9.7	13
<b>Initial height (<math>H_0</math>) = 2.2 <math>\mu m</math>:</b>				
Volume flow rate ( $ml/min$ )	0.188	2.6	12.5	38.4
Average velocity $\bar{u}$ ( $m/s$ )	0.0169	0.1222	0.4	0.93
Reynolds number ( $\frac{\rho \bar{u} d_h}{\mu}$ )	0.7812	10.76	52	158
Particle Reynolds number for a 10-micron bead ( $Re \times (d_p/d_h)^2$ )	0.036	0.139	0.310	0.541
Stokes number for a 10-micron bead ( $\frac{\rho_p d_p^2 / 18 \mu}{d_h / \bar{u}}$ )	0.002	0.008	0.019	0.033
<b>Initial height (<math>H_0</math>) = 7 <math>\mu m</math>:</b>				
Volume flow rate ( $ml/min$ )	0.33	3.5	15.4	45.1
Average velocity $\bar{u}$ ( $m/s$ )	0.0245	0.15	0.46	1.03
Reynolds number ( $\frac{\rho \bar{u} d_h}{\mu}$ )	1.37	14.63	64	186
Particle Reynolds number for a 10-micron bead ( $Re \times (d_p/d_h)^2$ )	0.044	0.154	0.331	0.572
Stokes number for a 10-micron bead ( $\frac{\rho_p d_p^2 / 18 \mu}{d_h / \bar{u}}$ )	0.003	0.009	0.020	0.035

pointed briefly, the particles cannot have a very large momentum. For the design purposes, in order to quantitatively take the particles momentum into account the particles Reynolds number is evaluated. In order to achieve a deterministic behavior of the particles, the Stokes number as well as the particle Reynolds number are preferred to be as small as possible so that the particles trajectory can be more accurately predicted by considering the fluid flow velocity field and the deflection contour of the membrane.

### Height effects

The original height of the microchannel in absence of the pressure difference across the channel,  $H_0$ , plays an important role in determining the height of channel after applying the pressure:  $H = H_0 + \delta$ , where  $\delta$  is the average PET film deflection. Therefore, it can affect the fluid flow behavior as well as the particles' motion through the channel. The important characteristics of the flow are presented in Table 11 for two microchannels 8 mm and 4 cm in width and length, respectively, with different original heights of 2.2  $\mu m$  and 7  $\mu m$ . It can be seen that the effects of the microchannel original height are noticeable on the volumetric flow rate due to the flow rate dependency on  $H^3$ . The non-dimensional parameters, however, do not change significantly, since the PET film deformation is much

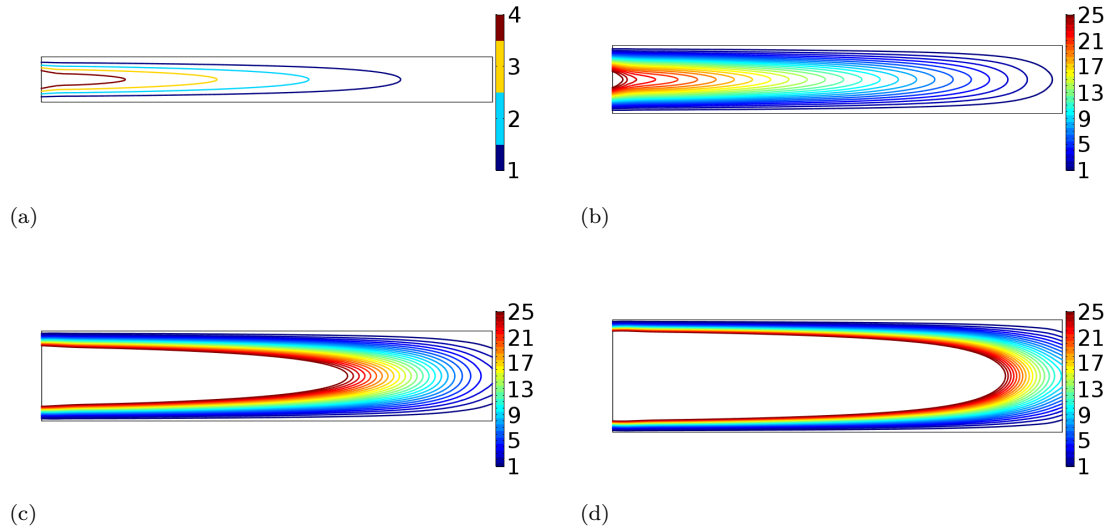


Figure 67: The different height levels of the PET film at the pressure difference of 15 kPa across the 4 *cm*-long microchannels of (a) 4 *mm*, (b) 6 *mm*, (c) 8 *mm*, and (d) 10 *mm* in width.

larger than the original height of the channel, and consequently the deformed channels heights are almost the same for the two studied microchannels. Hence, for the case that the membrane deflection is much larger than the channel original height, the microchannel original height can be flexibly modified for the design purposes without the significant change in the fluid flow characteristics.

### Width effects

As the fluid flow through the deformable microchannels was examined analytically in chapter , the microchannel width plays a crucially important role in the membrane deflection, fluid-solid interactions, and consequently the fluid flow behavior. The different height levels of the PET film at the pressure difference of 15 kPa across the 4 *cm*-long microchannels with various widths are shown in Fig. 67. The important characteristics of the fluid flow are also presented in Table 12 for the studied microchannels assuming the original height of the channels to be equal to 2.2  $\mu\text{m}$ . It is noticed that the characteristic parameters like (particle) Reynolds number and Stokes number can vary orders of magnitude with slightly changing the microchannel width. Among the considered cases, only the microchannels with

Table 12: The microchannel width effects for the microchannels 4 cm long and a pressure difference of 15 kPa.

Width (mm)	10	8	6	4
Mean deflection ( $\mu m$ )	51.3	21.0	6.7	1.3
Maximum deflection at outlet ( $\mu m$ )	9.9	3.2	0.8	0.1
<b>Initial height (<math>H_0</math>) = 2.2 <math>\mu m</math>:</b>				
Volume flow rate ( $ml/min$ )	2.9	0.188	0.008	3e-4
Average velocity $\bar{u}$ ( $m/s$ )	0.0893	0.0169	0.0025	3.9e-4
Reynolds number ( $\frac{\rho \bar{u} d_h}{\mu}$ )	9.51	0.78	0.0437	0.003
Particle Reynolds number for a 10-micron bead ( $Re \times (d_p/d_h)^2$ )	0.084	0.036	0.014	0.006
Stokes number for a 10-micron bead ( $\frac{\rho_p d_p^2 / 18 \mu}{d_h / \bar{u}}$ )	0.0051	0.0022	0.0009	0.0003

Table 13: The effects of microchannel width on the structural-fluid characteristics of the fluid flow through the microchannels 4 cm long with nearly identical opening size at the outlet section.

Width (mm)	6	8	10
Pressure difference (kPa)	90	20	7
Mean deflection ( $\mu m$ )	40.1	28.1	24.0
Maximum deflection at outlet ( $\mu m$ )	4.6	4.3	4.6
<b>Initial height (<math>H_0</math>) = 2.2 <math>\mu m</math>:</b>			
Volume flow rate ( $ml/min$ )	5.1	0.55	0.16
Average velocity $\bar{u}$ ( $m/s$ )	0.334	0.038	0.01
Reynolds number ( $\frac{\rho \bar{u} d_h}{\mu}$ )	28.1	2.3	0.52
Particle Reynolds number for a 10-micron bead ( $Re \times (d_p/d_h)^2$ )	0.40	0.06	0.02
Stokes number for a 10-micron bead ( $\frac{\rho_p d_p^2 / 18 \mu}{d_h / \bar{u}}$ )	0.0242	0.0039	0.0012

8 and 10 mm widths are able to provide a reasonable opening size at the outlet section for the studied pressure difference of 15 kPa.

In order to be able to compare the structural-fluid characteristics of various microchannels, they need to be considered under the different appropriate pressures so that all the deformable channels, *i.e.* tunable microfluidic filters/sieves, provide the same opening size at the outlet. In this way, all the tunable sieves allow the same size of particles to pass through the channel or to be trapped inside the channel. Then, one can compare the solid-fluid characteristics of the microchannels with various geometries and choose the one with more suitable characteristics in terms of volumetric flow rate, (particle) Reynolds number, Stokes number, etc. For example, the different height levels of the PET film are shown in Fig. 68 for the microchannels with various widths under the appropriate pressure differences so that the opening size at the outlet section is about 4.5  $\mu m$ . The effects of microchannel width on the structural-fluid characteristics of the fluid flow through these microchannels are also reported in Table 13. Immediately, the very important fact is noticed:

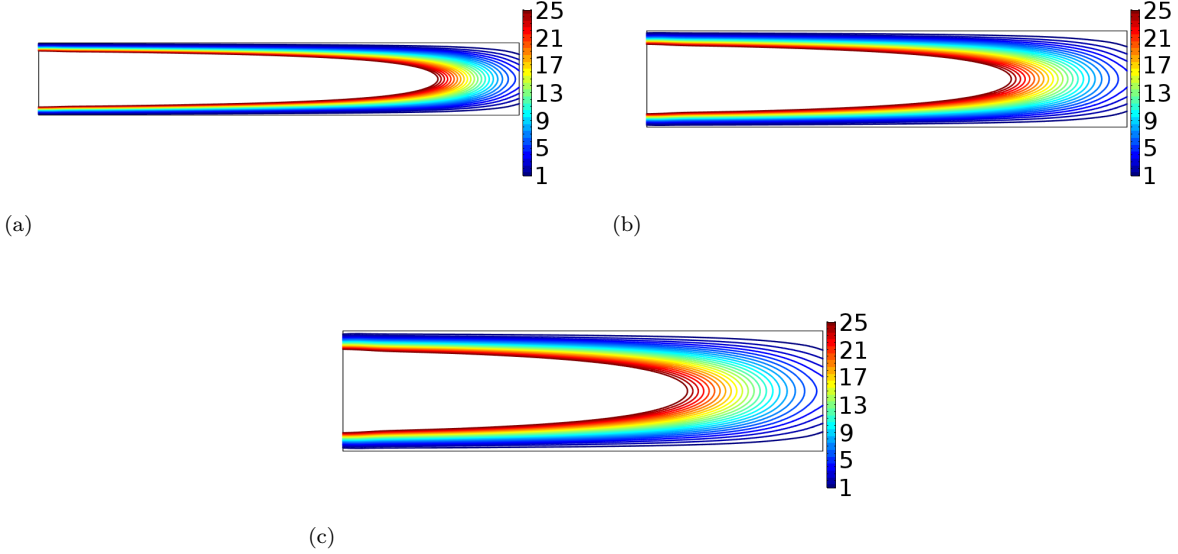


Figure 68: The different height levels of the PET film for 4 *cm*-long microchannels with (a) 6 *mm* width and 90 kPa pressure difference, (b) 8 *mm* width and 20 kPa pressure difference, and (c) 10 *mm* width and 7 kPa pressure difference. The maximum membrane deflection at the outlet is about 4.5  $\mu\text{m}$  for all the cases.

For the same opening size at the outlet, the slightly narrower microchannel might necessitate the orders of magnitude larger (particle) Reynolds number and Stokes number. Under these conditions, the particles possess high momentum causing adverse effects such as clogging, passing through the filter even with diameters larger than the opening size, and so on. The shallow microchannels with ultra-low aspect-ratios are, therefore, of utmost importance for the idea of the *tunable microfilters without the need to the pneumatic actuation* to be made reality.

After discussing the importance of having an ultra-low-aspect-ratio microchannel, it is worth mentioning that the microchannel width should not be too large because:

- the required pressure to cause a specific membrane deflection can decrease below the resolution of the commonly available and economic pressure regulators, and
- for a specific opening size at the outlet section, the volumetric flow rate decreases

noticeably as the microchannel width increases, see Table 13.

## Fabrication

The single-height microchannels and rigid double-height microchannels are fabricated based on the developed two-step sealing—and—reinforcement approach illustrated in Chapter 2. The schematic presentation of the fabrication process flow for double-height deformable microchannels is also shown in Fig. 69. The procedure is similar to what we described in [164] with the difference that the flexible membrane is allowed to deform even after the reinforcement step. Briefly, the patterns of the microchannel sidewalls are created through the glass wet etching procedure. The via-holes are drilled in the glass slide (Fig. 69 (A)). The 190  $\mu\text{m}$ -thick PET (Polyethylene terephthalate) film coated with a thin SU8 film ( $\sim 2 \mu\text{m}$ ) then seals the channel sidewalls on the hotplate at  $69 \pm 1^\circ\text{C}$ . The bubbles are removed using the tweezers (Fig. 69 (S<sub>1</sub>)). The SU8 adhesive layer is cured using the UV exposure and baking on the hotplate (Fig. 69 (S<sub>2</sub>)). The SU8 layer of about 15  $\mu\text{m}$  in thickness is spun on the bare side of the PET film. The pattern of the microchannel sidewalls is created in a separate glass slide, which is used for the bonding reinforcement. The patterns in the reinforcement glass slide are sufficiently deep ( $\sim 50 \mu\text{m}$ ) to enable the membrane to deflect freely. The reinforcement glass slide's pattern is aligned with that of the main microchannel under the mask aligner. The reinforcement glass slide is brought in contact with the SU8 layer spun on the bare side of the PET film. An initial bonding is made by applying a slight pressure on the reinforcement glass slide against the PET film (Fig. 69 (R<sub>1</sub>)). The stack is then clamped using several clips. The stack is baked in the oven at about  $69^\circ\text{C}$ . After the UV exposure and baking on the hotplate, the bonding procedure is completed (Fig. 69 (S<sub>2</sub>)). A PDMS interconnect with holes are bonded to the glass slide for injection and collection of sample.

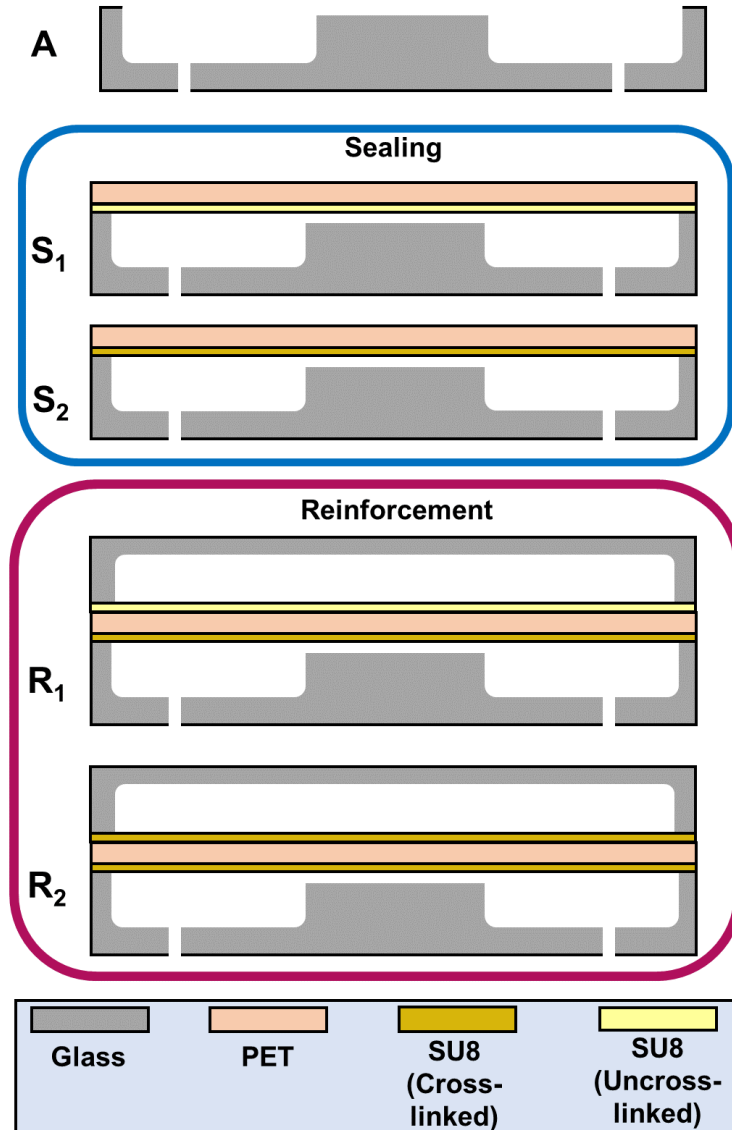


Figure 69: Schematic presentation of the fabrication process flow: (A) the microchannel sidewalls are created using the double-step glass wet etching. (S<sub>1</sub>) A PET film coated with a thin layer of SU8 seals the microchannel sidewalls. (S<sub>2</sub>) The chip is undergone with UV illumination and post-exposure baking to cure the adhesive layer. (R<sub>1</sub>) A glass substrate with the same pattern as that of the main channel is aligned and brought in contact with the SU8 layer coated on the bare side of the PET film. (R<sub>2</sub>) The sample is undergone with UV illumination and post-exposure baking to cure the adhesive layer at the bonding interface of the reinforcement glass and the PET film.

## Part I: Disposable platforms

For the purpose of making single-use devices, particle trapping is the only task to accomplish and particle removal is not needed. A microfluidic sieve based on the traditional rigid strategy will be studied in the following. A single-height deformable channel will then be used to

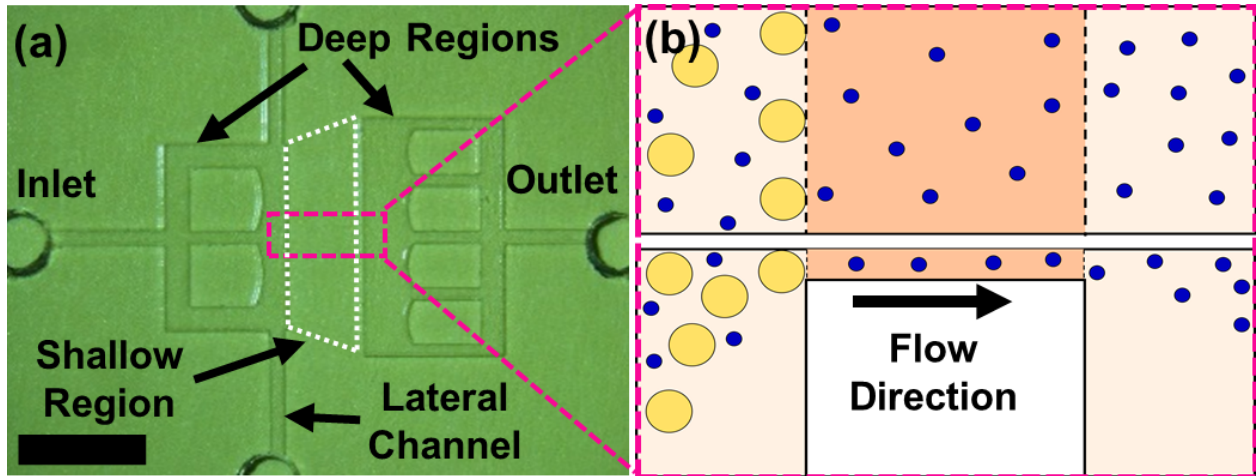


Figure 70: (a) The microscope image of the double-height deep–shallow microfluidic sieve, together with (b) a schematic presentation of the (top) top-down-view and (bottom) side-view of the deep–shallow–deep interfaces, showing the small enough particles passing through the channel, while the large enough ones are trapped. The channel height is  $32.0\ \mu\text{m}$  and  $5.7\ \mu\text{m}$  in the deep and shallow regions, respectively. Scale bar =  $5\ \text{mm}$  in (a).

investigate the feasibility of adjusting the pore size. The design will be modified afterwards for achieving a more efficient particle trapping.

### Rigid microfluidic filter

In this section, the results for a rigid microfluidic sieve, consisting of the double-height deep–shallow microchannel, are presented. The microscope image of the microchannel together with a schematic presentation of the size exclusion mechanism are shown in Figs. 70 (a) and (b), respectively. The microchannel is reinforced using a blank glass slide to avoid the PET film deflection. Hence, the opening size of the filter remains fixed under pressure. The solution containing the particles is injected from the inlet, and the small enough particles passing through the channel are collected from the outlet. The valves connected to the lateral channels are closed during the sample injection step. For removing the trapped particles, the DI water is injected from the outlet and the lateral ports. In order to filter the 10-micron microspheres from a solution containing 3- and 10-micron particles (from Polysciences, Inc.), the microchannel is fabricated in such a manner that the deep and shallow regions are  $32.0\ \mu\text{m}$  and  $5.7\ \mu\text{m}$  in height, respectively.

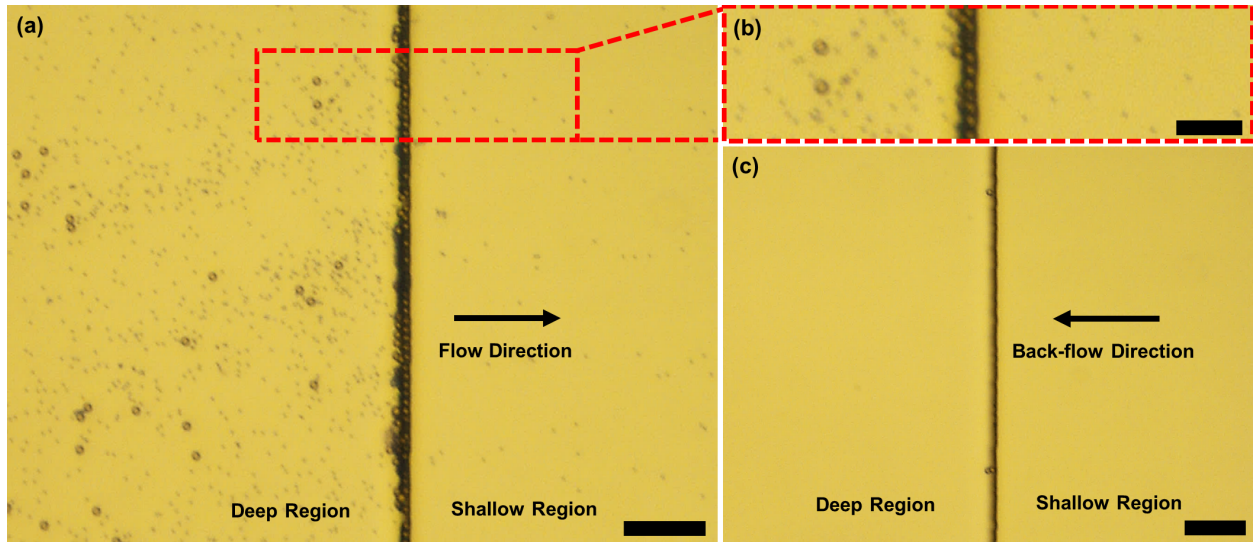


Figure 71: (a) The microscope image of the deep–shallow interface of the microfluidic filter, while the experiment of sieving 3-micron and 10-micron particles is running under the volumetric flow rate of  $10 \mu\text{l}/\text{min}$ , showing the 3-micron particles can pass through the channel, whereas the 10-micron particles are trapped, together with a higher magnification image in (b). (c) The microscope image of the deep–shallow interface after applying the back- and lateral-flows to remove the trapped particles. Scale bar =  $100 \mu\text{m}$  in (a) and (c), and  $50 \mu\text{m}$  in (b).

The particles are mixed with the DI water and 0.05% Triton X-100, so that the number concentration of 10-micron and 3-micron particles is  $2 \times 10^5 \text{ ml}^{-1}$  and  $3 \times 10^6 \text{ ml}^{-1}$ , respectively. Before running the experiments, the microchannel is filled with the phosphate buffer solution (from Sigma-Aldrich) mixed with 1% Triton X-100. After one hour, the buffer solution and the excess of the surfactant molecules are removed by gently flushing the DI water through the channel. The device is then ready for the filtration experiment.

The microscope images of the deep–shallow interface, while the sieving experiment is running under the volumetric flow rate of  $10 \mu\text{l}/\text{min}$ , are shown in Figs. 71 (a) and (b). It can be seen that the 10-micron particles are trapped behind the deep–shallow interface, while the 3-micron beads are passing through the channel. The microscope image of the deep–shallow interface is also shown in in Fig. 71 (c) after the trapped particles are removed by applying the back- and lateral- flows. As shown, most of the trapped particles are removed from the channel, and the sieve is ready for the next injection step. Making the process of injection and collection of the particles automated, and finding the optimized

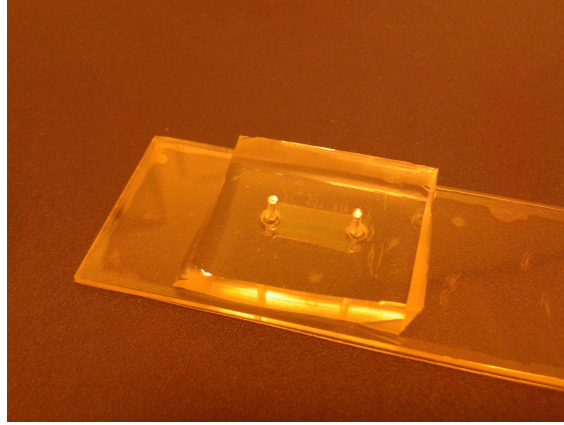


Figure 72: A camera image showing the microchannel 5 mm, 1 cm, and 7.1  $\mu\text{m}$  in width, length, and height, respectively, together with the PDMS interconnect for insertion of tubing used for the injection and collection of sample.

injection/collection flow rates and duration times, etc., can be done to make such simple filters efficiently applicable.

### **Particle filtration using a tunable microfluidic sieve with the simple design**

As a simple examination, in order to investigate the possibility of altering the opening level of the sieve, and consequently filtering the particles with various diameters, a microchannel is fabricated, which is 5 mm, 1 cm, and 7.1  $\mu\text{m}$  in width, length, and height, respectively. The ceiling of the microchannel is the deformable PET film without reinforcement. A camera image showing the microchannel together with a PDMS interconnect is presented in Fig. 72.

The utilized sample in this work is the hollow glass microspheres (from Sigma-Aldrich) with the density of  $\rho = 1100 \text{ kg/m}^3$  mixed with DI water in a number concentration of  $10^6 \text{ ml}^{-1}$ . The nominal size range of the microspheres is 9–13  $\mu\text{m}$ , but examination of sample under the microscope revealed that there are indeed particles with the diameter even as small as few microns and as large as several tens of microns. The size distribution of the sample is shown in Fig. 73 (a). In order to avoid the potential agglomeration of particles, a 0.2%(W/V)Triton X-100 is also added to the mixture. First, the solution is injected through the channel under the pressure of 2 psi, *i.e.* about 13.8 kPa. The filtrate is collected in a

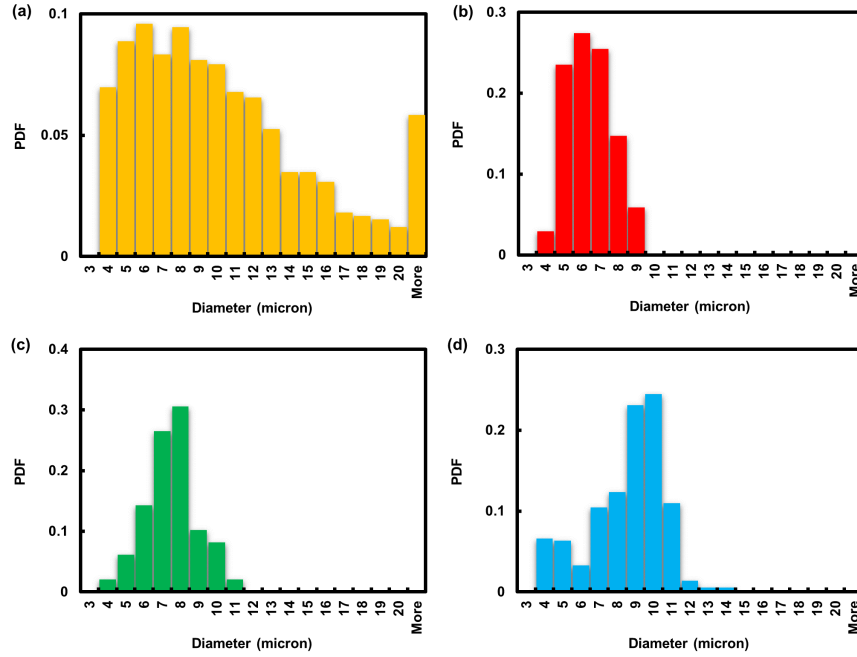


Figure 73: The particles size distribution related to the (a) injected sample, as well as that of the collected particles from the outlet under the pressure differences of (b) 2 psi (13.8 kPa), (c) 6 psi (41.4 kPa), and (d) 10 psi (69.0 kPa) across the microchannel sequentially after the microchannel is blocked at lower pressure difference. The microchannel is 5 mm, 1 cm, and 7.1  $\mu\text{m}$  in width, length, and height, respectively. The number concentration of the glass particles in the main sample is  $10^6 \text{ ml}^{-1}$ .

vial, which is put on an analytical balance so that the flow rate is also monitored over time. After the microchannel is virtually blocked, several droplets of the filtrate are sandwiched between the cover slips. The size distribution of the particles in the filtrate is obtained by analyzing the images taken under the microscope by using the ImageJ software. The same process is followed for the pressures of 6 psi, *i.e.* about 41.4 kPa, and 10 psi, *i.e.* about 69.0 kPa.

The size distribution related to the particles in the injected sample together with that of the particles within the filtrate under various pressure differences across the channel are compared in Fig. 73. It can be seen that the maximum size of the particles passing through the channel is about 9  $\mu\text{m}$ , 11  $\mu\text{m}$ , and 15  $\mu\text{m}$  under the pressure differences of 2 psi, 6 psi, and 10 psi, respectively.

The PET film deformation contours obtained from the modeling are shown in Fig. 74 for the pressure differences of 2 psi, 6 psi, and 10 psi across the microchannel. In addition,

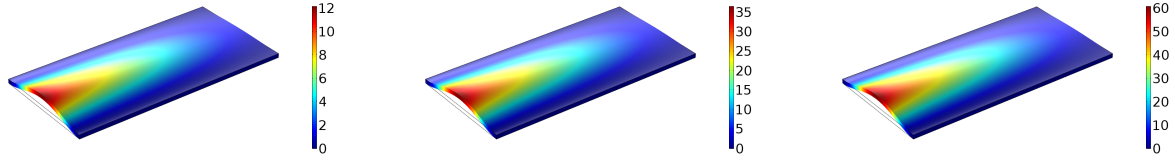


Figure 74: The PET film deflection ( $\mu m$ ) contour for the microchannel 1 *cm* and 5 *mm* in length and width, respectively, under the pressure differences of (left) 2 psi (13.8 kPa), (middle) 6 psi (41.4 kPa), and (right) 10 psi (69.0 kPa).

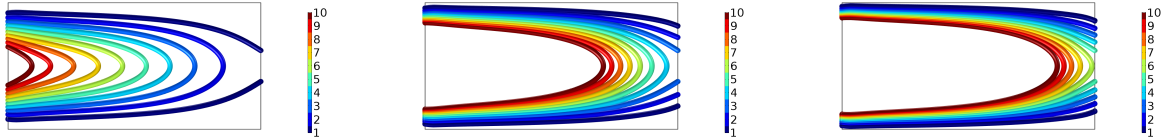


Figure 75: The different height levels ( $\mu m$ ) of the PET film under the pressure differences of (left) 2 psi (13.8 kPa), (middle) 6 psi (41.4 kPa), and (right) 10 psi (69.0 kPa) across the microchannel 1 *cm* and 5 *mm* in length and width, respectively.

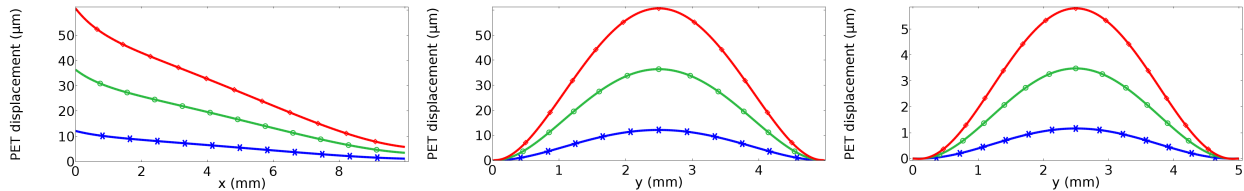


Figure 76: The PET film deflection profile (left) along the centerline of the microchannel 1 *cm* and 5 *mm* in length and width, respectively, (middle) across the inlet section of the channel, and (right) across the outlet section of the channel, under the pressure differences of 2 psi, *i.e.* 13.8 kPa, (cross), 6 psi, *i.e.* 41.4 kPa, (circle), and 10 psi, *i.e.* 69.0 kPa (diamond).

the top-down view of the different height levels of the PET film is shown in Fig. 75. The PET film deflection profile along the channel at the center-line as well as that across the channel at the inlet and outlet sections are also shown in Fig. 76. According to the PET film deformation profile at the outlet, the maximum displacement of the microchannel ceiling is about 1.1  $\mu m$ , 3.5  $\mu m$ , and 5.8  $\mu m$  under the pressure differences of 2 psi, 6 psi, and 10 psi, across the channel, respectively. Since the microchannel original height in absence of the pressure is 7.1  $\mu m$ , the sieve opening is predicted to be about 8.2  $\mu m$ , 10.6  $\mu m$ , and 12.9  $\mu m$  under the pressure differences of 2 psi, 6 psi, and 10 psi, respectively. These results are in agreement with the size distributions found for the collected particles under the different pressures (Fig. 73).

Even though the filtration of particles with different diameters under various pressure

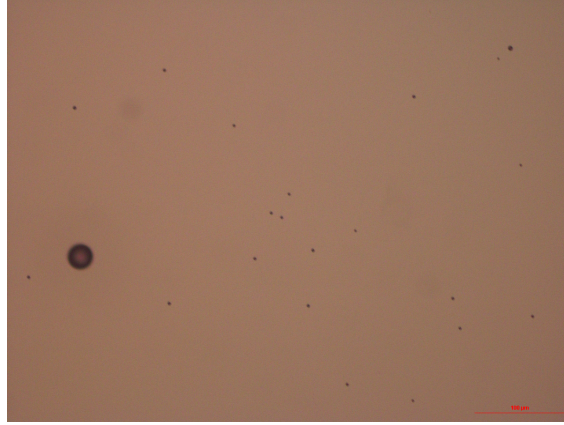


Figure 77: A particle larger than the predicted filter opening size found in the filtrate. The particle is about  $26 \mu\text{m}$  in diameter. The scale bar is 100 microns.

differences is demonstrated in overall, some particles larger than the predicted sieve opening size are also found sporadically in the filtrate as shown in Fig. 77, which is not reflected clearly in the size distribution of the filtrate shown in Fig. 73, since these large particles form a small fraction of the population examined statistically. Presence of particles with the diameter larger than the opening size of the sieve means that the particles momentum is not sufficiently low, as a result of which the PET film is forced to deflect more than that predicted from the modeling. It is worth mentioning that the all the modeling approaches considered in this work are based on the **membrane deflection under the static load**. It has already been demonstrated that this approach can acceptably predict the steady state fluid flow characteristics. In the case of the particulate suspensions, however, the particles momentum is exchanged with the membrane whenever they collide with the wall resulting in a force exerted on both particles and membrane in opposite directions. If the particles momentum is too large, *i.e.* both or one of the large mass and high speed, it can cause a force/pressure on the membrane locally larger than that that resulted in just by the much smaller fluid atoms. As a result, even if the fluid flow is considered to be in the steady state, the presence of particles causes the unsteady forces on the membrane typically larger than that predicted by the models only based upon the static pressure of the fluid flows.

In this work, we still keep using the developed models for the membrane deflection under the static pressure of the fluid flow, but the inertia effects of the fluid and particles are

Table 14: The effects of pressure difference on the structural-fluid characteristics of the fluid flow through the simple tunable sieve consisting of a deformable microchannel 1 *cm* long and 5 *mm* wide.

Pressure difference (psi)	2	6	10
Pressure difference (kPa)	13.8	41.4	69.0
Mean deflection ( $\mu m$ )	3.0	8.9	14.9
Maximum deflection at outlet ( $\mu m$ )	1.1	3.5	5.8
<b>Initial height (<math>H_0</math>) = 7.1 <math>\mu m</math>:</b>			
Volume flow rate ( <i>ml/min</i> )	0.035	0.423	1.831
Average velocity $\bar{u}$ ( <i>m/s</i> )	0.0117	0.0881	0.2774
Reynolds number ( $\frac{\rho \bar{u} d_h}{\mu}$ )	0.2361	2.8101	12.1517
Particle Reynolds number for a 10-micron bead ( $Re \times (d_p/d_h)^2$ )	0.0581	0.2762	0.6332
Stokes number for a 10-micron bead ( $\frac{\rho_p d_p^2 / 18 \mu}{d_h / \bar{u}}$ )	0.0035	0.0169	0.0387
Particle Reynolds number for a 30-micron bead ( $Re \times (d_p/d_h)^2$ )	0.5228	2.4857	5.6988
Stokes number for a 30-micron bead ( $\frac{\rho_p d_p^2 / 18 \mu}{d_h / \bar{u}}$ )	0.0319	0.1519	0.3483

also examined through the characteristic parameters of (particle) Reynolds number and the Stokes number. The structural-fluid characteristics of the particulate fluid flow through the studied tunable sieve are presented in Table 14. The observation of particles larger than the opening size of the sieve implies that the Stokes and particle Reynolds numbers are not sufficiently small for these beads to all be trapped within the deformable filter. The particle momentum and consequently the Stokes and particle Reynolds numbers significantly increase with diameter ( $\propto d_p^2$ ). For example the Stokes and particle Reynolds numbers for the 30-micron beads are 9 times as large as those of the 10-micron beads. In order to ensure the most precise filtering process the Stokes and particle Reynolds numbers need to be as small as possible for the largest beads within the sample. As previously shown theoretically, the aforementioned characteristic numbers can be significantly reduced by increasing the microchannel width. Later in this chapter, the modified design with the larger microchannel width will be studied as well.

The volumetric flow rate of DI water through the fabricated tunable sieve obtained through the experiments compared with the modeling results is shown in Fig. 78 (left). The models are able to acceptably predict the flow rate through the channel under various pressure differences. In addition, the accumulated mass over time in the series of sequential experiments of injecting the samples containing about  $10^6$  glass micro-particles per milli-litre with various pressure differences across the channel is presented in Fig. 78 (right). It can be

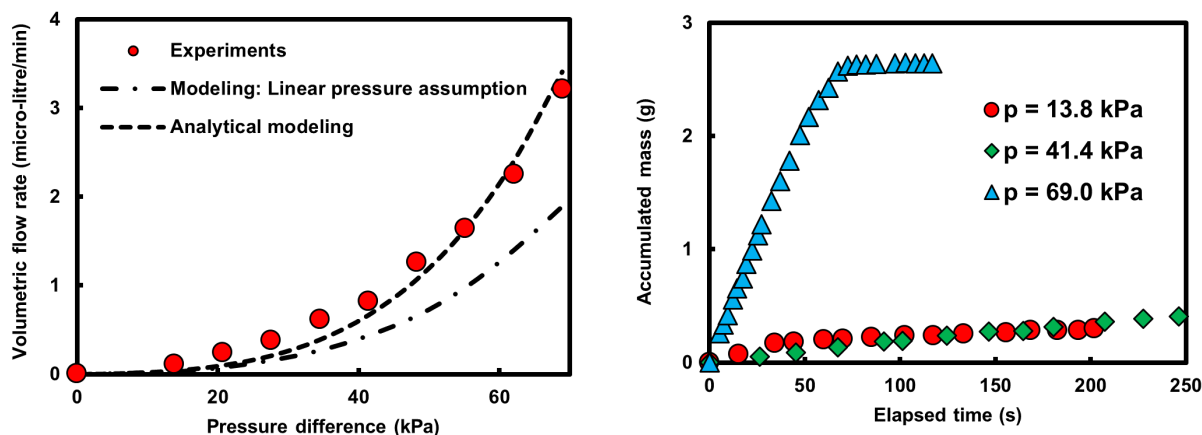


Figure 78: (left) The volumetric flow rate of DI water through the microchannel 5 mm, 1 cm, and 7.1  $\mu\text{m}$  in width, length, and height, respectively, obtained through the experiments compared with a primitive numerical model used in this work. (right) The accumulated mass over time in a series of sequential experiments of injecting the sample containing about  $10^6$  glass micro-particles per milli-litre with the pressure differences of 2 psi (13.8 kPa), 6 psi (41.4 kPa), and 10 psi (69.0 kPa) across the channel.

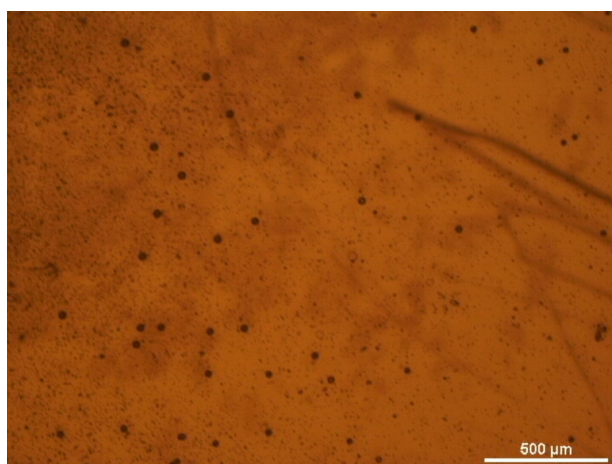


Figure 79: A microscopy image showing the trapped particles in the microchannel after the channel is blocked under the pressure difference of 10 psi (69.0 kPa).

perceived that the channel gets clogged after about one minute under the pressure of 2 psi (13.8 kPa). In this time window, about 200  $\mu\text{l}$  filtrate is collected. For the highest pressure studied in this work, 10 psi (69.0 kPa), the channel clogging happens after similar time period, but a larger amount of filtrate, about 2.5 ml, is collected during this time period.

A microscopy image showing the trapped particles within the microchannel after the microchannel is blocked under the pressure difference of 10 psi (69.0 kPa) can be seen in Fig. 79. Based on our observations, the sufficiently small particles can be removed under

a very low back pressure, while the sufficiently large trapped particles remain stationary, since they do not have the needed momentum to cause sufficient membrane deflection to move backward through the channel. Such a simple mechanism for preparing **anchored monolayers of cells/particles** might be useful for highly sensitive bio-analysis.

### **Particle filtration using a tunable microfluidic sieve with the modified design**

In this section, a tunable microfluidic sieve with the modified design is investigated with the aim to resolve the difficulties observed previously associated with particles larger than the pore size passing through the filter because of possessing high linear momentums. As observed earlier, wider microchannels are useful to mitigate the aforementioned issue. For such wide microchannels (several millimeters in width), a double-height channel is needed to guide particles through a deep channel until they reach the main part of the device, which is the wide and shallow duct.

The design of the device is the same as that shown in Fig. 70. However, the membrane is free to deform, since the channel is reinforced using a glass slide with the same pattern of the main channel. The patterns in the reinforced glass slide are  $50\ \mu\text{m}$  deep, which dictates the maximum deflection of the PET film. The deep and shallow regions of the channel are about 50 and 6 microns, respectively. The channels connecting the active zone of the device, *i.e.* shallow region, to the inlet/outlet ports required to be deep enough for the particles to easily move through the rest of the channel. In general, the larger depth of the deep regions is more preferred, since it decreases the hydrodynamic resistance of the channel. However, if the difference between the depths of the deep and shallow regions is large enough the shallow region dominates the total hydrodynamic resistance of the channel. In that situation, increasing the depth of the deep regions is no longer recommended because:

- it makes the glass etching process longer, and
- the dead volume of the device increases, which is not desirable for the bioapplications relying on the minute amount of the sample.

The number concentration of 10-micron and 3-micron particles is  $2 \times 10^5 \text{ ml}^{-1}$  and  $3 \times 10^6 \text{ ml}^{-1}$ , respectively. The same procedure described earlier is repeated here regarding the channel and sample preparation. The solution containing the particles is **injected along the nozzle direction** using the syringe pump. The small enough particles passing through the filter are collected from the other port in the opposite side. The valves connected to the lateral channels are closed during the sample injection step.

The experiments show that under the rather low volume flow rates ( $< 20 \text{ } \mu\text{l}/\text{min}$ ), the 10-micron beads are trapped at the deep–shallow interface, while the 3-micron beads pass through the channel. One of the problems associated with the filters is the channel clogging, which causes that even the particles smaller than the filter opening size to be trapped among the larger trapped particles, which adversely affects the performance of the filter. It has already been demonstrated that this problem can be mitigated using the cyclic back-flows. The idea of creating a back-and-forth oscillation in the particles motion by using the piezoelectric has also been successfully reported for rare cancer cells isolation. We have observed that displacing the syringe pump, while it is stopped running, by almost 10–20 cm vertically to the lower heights can produce the large enough pressure gradient to push the particles away from the filter opening. Displacing the syringe pump to the opposite direction, *i.e.* to the higher heights, causes the particles to move forward again through the microchannel, which helps the small beads to released. This simple idea can be automatized to be repeated periodically with an appropriate frequency for several continuous back-and-forth displacements and a suitable delay time period between two consecutive sets of oscillations. The microscope images showing the effects of the pressure oscillation on releasing 3-micron beads trapped among the 10-micron beads next to the deep–shallow interface, enabling the 3-micron beads to pass through the filter are presented in Fig. 80. The displacement has been done manually. The time duration of the shown cycle is about 5 seconds.

Under the high volume flow rates ( $> 100 \text{ } \mu\text{l}/\text{min}$ ), both of the 3- and 10-micron beads can pass through the filter. For the intermediate flow rates, the 10-micron beads can cross the first deep–shallow interface, but they are trapped within the filter zone before the second

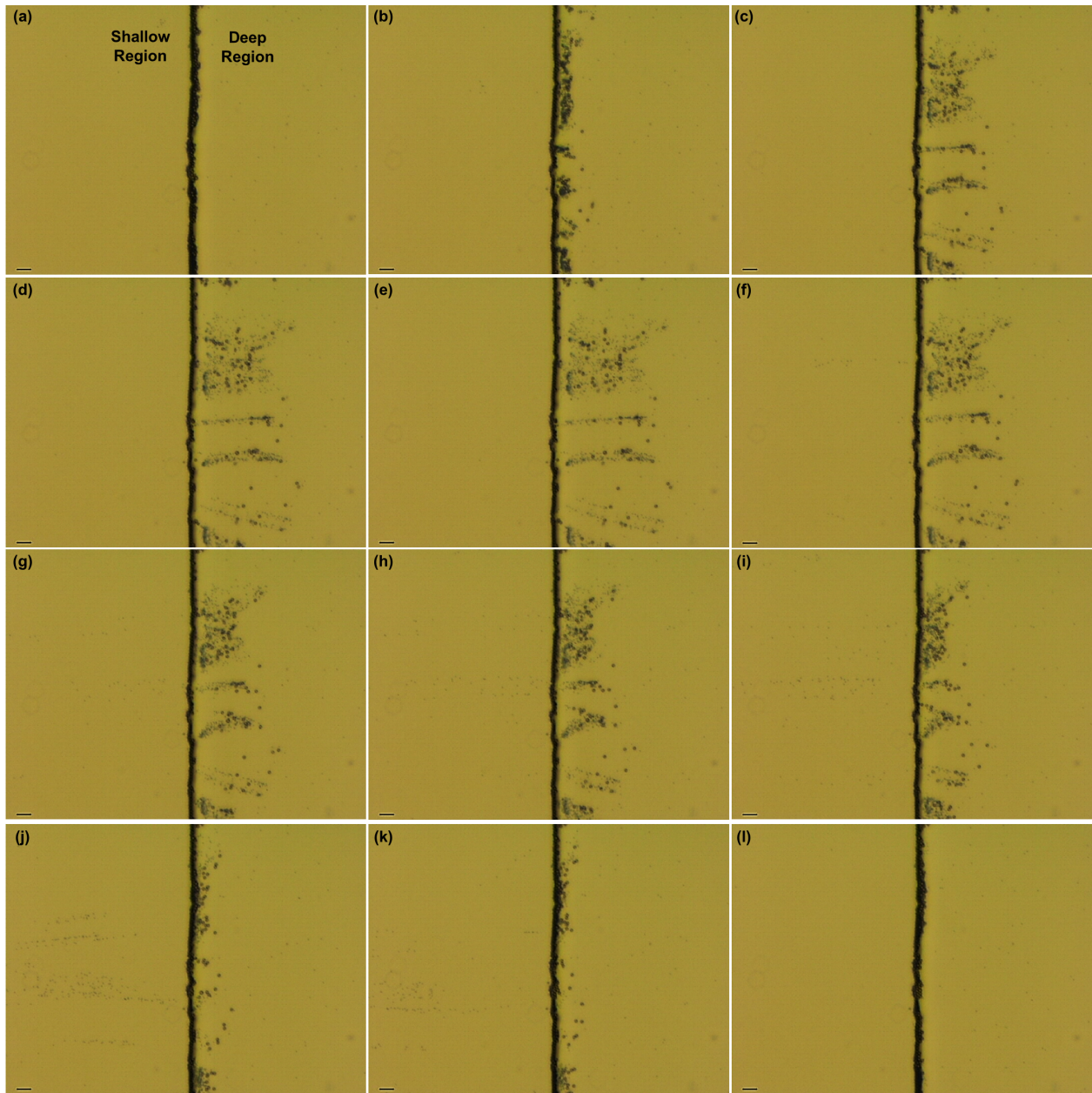


Figure 80: The microscope images showing the effects of the pressure oscillation on releasing 3-micron beads trapped among the 10-micron beads next to the deep–shallow interface, enabling the 3-micron beads to pass through the filter. The pressure gradient forces particles to move toward the deep region for the images (a)–(e), while it reverses toward the shallow region for the images (f)–(l). The time duration of the shown cycle is about 5 seconds. The scale bars in the microscope images are  $50 \mu m$ .

deep–shallow interface. The trapped particles form the profile close to that predicted by the modeling. The profile of the trapped 10-micron particles are shown in Fig. 81 under the fluid flow rate of  $90 \mu l/min$  together with the modeling results showing the PET film deflection

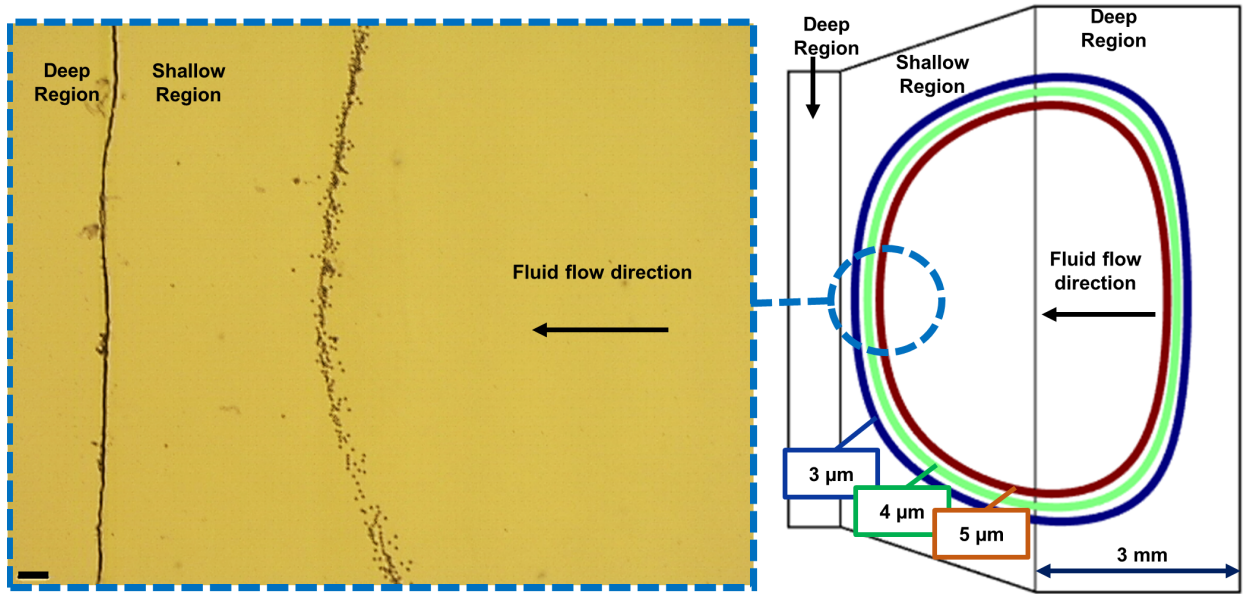


Figure 81: A microscope image showing the trapped 10-micron beads under the flow rate of  $90 \mu\text{l}/\text{min}$  together with the modeling results showing the PET film deflection contour for three levels of 3, 4, and 5 microns. The deep and shallow regions are about 50 and 6 microns, respectively. The scale bar in the microscope image is  $100 \mu\text{m}$ .

contour for three levels of 3, 4, and 5 microns. Since the shallow region is about 6 microns in depth, the membrane deflection contour related to the  $4 \mu\text{m}$  level predicts the front profile of the trapped 10-micron particles, which is in acceptable agreement with the experimental results. The pressure difference is also obtained from the modeling, which is about 9 kPa.

In comparison with the simple device studied earlier, the modified design has the following advantages:

- the filtration precision is more reliable, and
- the higher flow rates are achievable.

More importantly, in comparison with the rigid microfluidic filters, the developed tunable microfluidic sieves offer the following advantages:

- the various particle/cell sizes can be isolated by adjusting the pressure difference applied across the channel, or equivalently the volumetric flow rate injected through the channel,
- the higher flow rates are obtainable,

- the trapped particles in the active zone of the device, *i.e.* shallow region, can be directly analyzed using the (fluorescent) microscopy or other applicable techniques for the relevant bioapplications, and
- the membrane's slope is very small on the filter zone: deflection/shallow region length  $\approx O(\mu m)/O(mm)$ . Such a gentle slope is very useful for the cells isolation applications in terms of the cell viability.

## Part II: Reusable platforms

### Particle trapping

In order to make a reusable device, an efficient particle retrieval is required after each experiment to make the device ready for the consequent runs. A photograph of the modified deformable microfluidic device is presented in Fig. 82 (A). In order to achieve a more efficient particle trapping process, the side-channels  $C_1$  and  $C_2$  have been embedded to create reverse sheath flows for avoiding the particles from approaching the lateral sidewalls of the microchannel, where the particles can get stuck because of the small membrane deformation due to the clamping effects. As depicted in Fig. 82 (B), the particles are repelled from the lateral sidewalls in presence of the sheath flows, becoming relatively concentrated in the central portion of the device, while they uniformly approach the first deep-shallow interface in absence of the sheath flows (Fig. 82 (C)). Because of the smaller membrane deformations in narrower portions of the channel, the tapered shape of the shallow region results in a funnel-shaped ceiling once the membrane deforms, enabling the particles with proper sizes to be trapped on the weir.

A solution containing the 3-, 6-, and 10-micron particles with the number concentration of  $2.7 \times 10^5 \text{ ml}^{-1}$ ,  $1.9 \times 10^5 \text{ ml}^{-1}$ , and  $4.2 \times 10^4 \text{ ml}^{-1}$ , respectively, is injected from the port A. The sufficiently small particles passing through the channel are collected from the port B. DI water solution mixed with 0.1% Triton 100-X is injected from the ports  $C_1$  and  $C_2$ . The streams injected from the ports  $C_1$  and  $C_2$  serve as the reverse sheath flows.

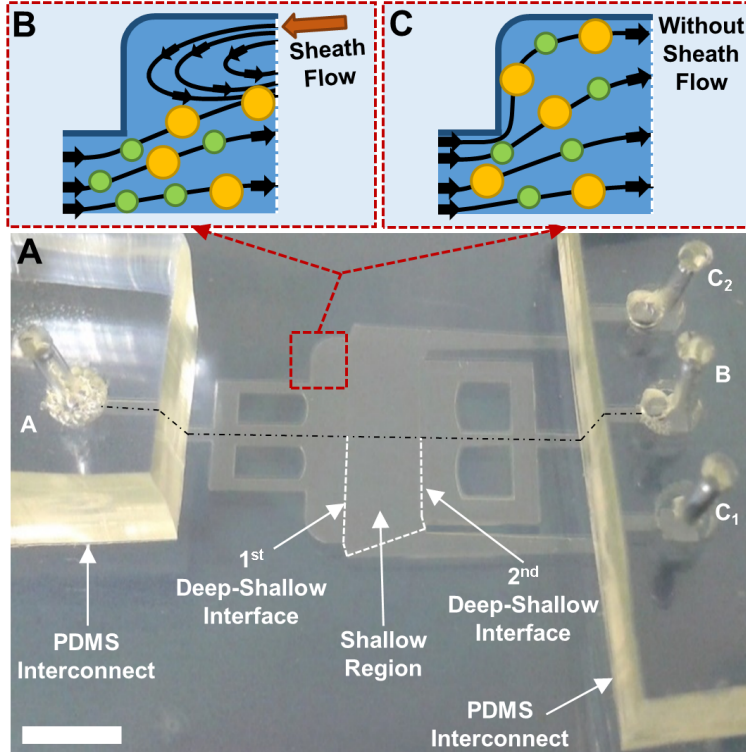


Figure 82: (A) A photograph of the microfluidic device consisting of a microchannel symmetric with respect to the dash-dotted line, together with the schematic presentations of the streamlines before the first deep-shallow interface and close to the lateral sidewall in (B) presence and (C) absence of the sheath flow injected from the port  $C_2$ . The  $\sim 36$ -micron deep regions are separated from the  $\sim 5$ -micron shallow region in lower half of the photograph in (A) using the dashed lines. Scale bar is 4 mm in (A).

Experiments show that in absence of the sheath flows, the sufficiently small particles approaching the central portion of the first deep-shallow interface are trapped on the weir, while those flowing towards the lateral portions of this interface are trapped behind the weir; see Fig. 83. The membrane displacement contours, obtained from the model and shown in Fig. 83 (A), acceptably predict the trapping cites for different particle sizes. Retrieving the particles trapped close to the lateral sidewalls becomes less efficient, since the small membrane displacements in those areas do not allow the trapped particles to be removed under the reasonably small volumetric flow rates. This difficulty is alleviated by using the  $C_1$  and  $C_2$  reverse sheath flows to guide particles towards the central portion of the device, preventing their trapping close to the lateral sidewalls.

In order to avoid adding another driving pressure source/syringe pump in presence of the sheath flows, the total volumetric flow rate of the  $C_1$  and  $C_2$  streams is considered to be equal

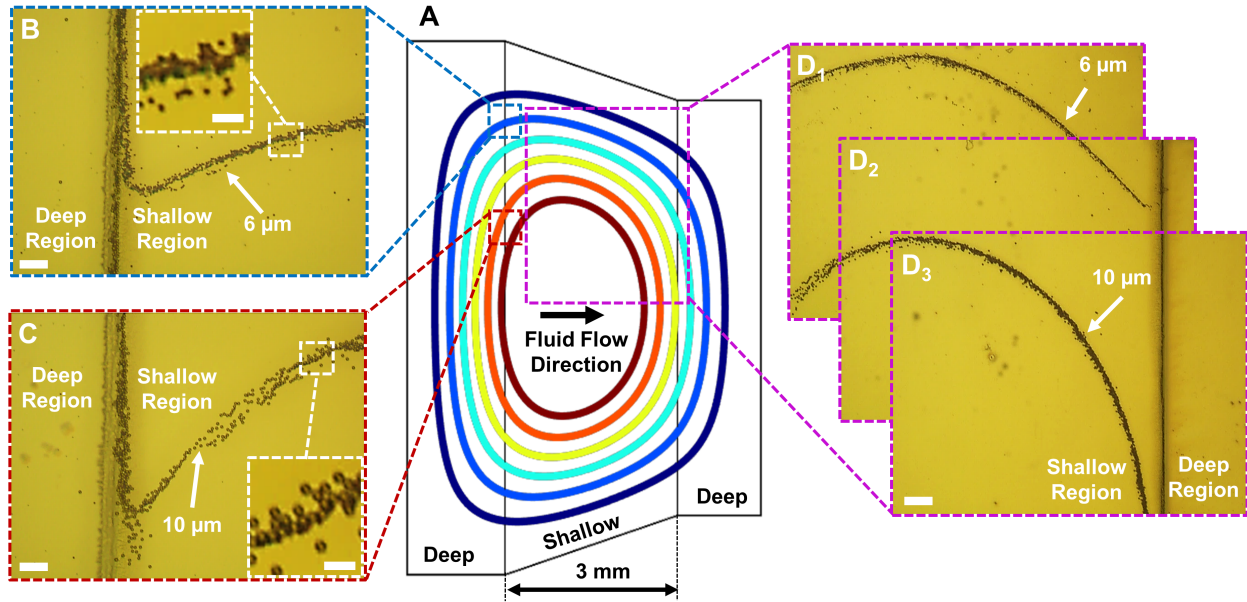


Figure 83: (A) Membrane displacement contours ranging from  $1 \mu\text{m}$  (outermost) to  $6 \mu\text{m}$  (innermost) with an increment of  $1 \mu\text{m}$ , obtained from the model, together with (B, C, D<sub>1</sub>, D<sub>2</sub>, and D<sub>3</sub>) the microscope images showing the trapped 6- and 10-micron beads under the volumetric flow rate of  $40 \mu\text{l}/\text{min}$  in absence of the reverse sheath flows. Microchannel is about  $5 \mu\text{m}$  and  $36 \mu\text{m}$  in depth within the shallow and deep regions, respectively. Scale bars are  $100 \mu\text{m}$  in (B) and (C),  $30 \mu\text{m}$  in insets of (B) and (C), and  $200 \mu\text{m}$  in (D<sub>1</sub>), (D<sub>2</sub>), and (D<sub>3</sub>).

to that of the particles sample injected from the port A, *i.e.*  $Q_A = 2Q_{C_1} = 2Q_{C_2} = 0.5Q_{\text{net}}$ . Experimental results presented in Fig. 84 demonstrate that the 10-micron beads are trapped behind the weir under the sufficiently small volumetric flow rates, *e.g.*  $Q_{\text{net}} = 5 \mu\text{l}/\text{min}$ . A sufficient increase in the volumetric flow rate, *e.g.*  $Q_{\text{net}} = 40 \mu\text{l}/\text{min}$ , causes the 10-micron particles to be isolated on the weir before the second deep-shallow interface, while they are filtered out under a sufficiently large flow rate, *e.g.*  $Q_{\text{net}} = 140 \mu\text{l}/\text{min}$ . These observations are acceptably in agreement with the membrane displacement contours obtained from the model. The filtrate size distributions also confirm the other experimental-theoretical results. More than %99 of the injected 10-micron beads are trapped behind the weir, isolated on the weir, or filtered out depending on the applied volumetric flow rate.

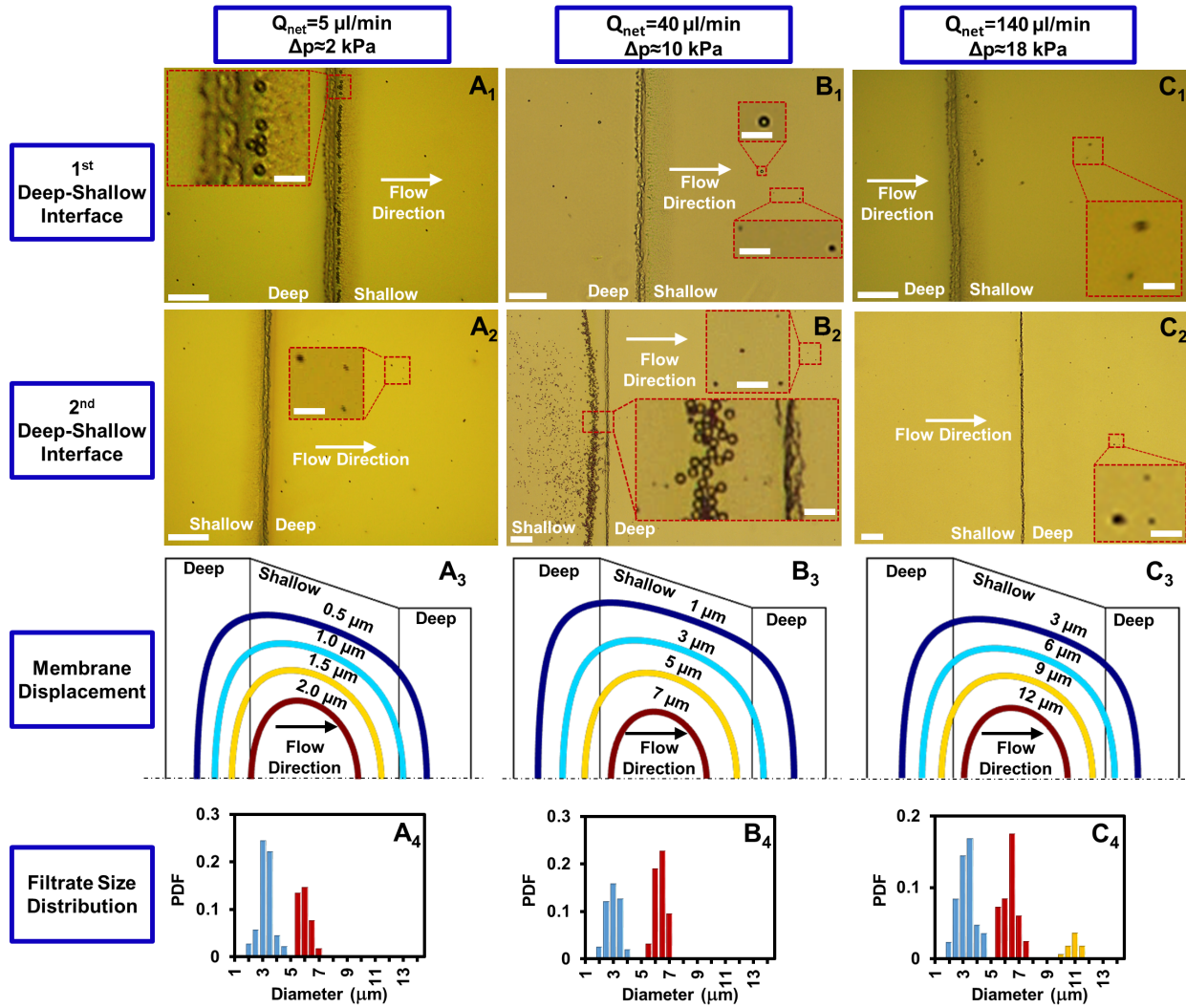


Figure 84: Microscope images of ( $A_1$ – $C_1$ ) the 1<sup>st</sup> and ( $A_2$ – $C_2$ ) 2<sup>nd</sup> deep-shallow interfaces, together with ( $A_3$ – $C_3$ ) the membrane displacement contours obtained from the model, and ( $A_4$ – $C_4$ ) the size distribution of the filtrate for three net volumetric flow rates of  $Q_{\text{net}} = (A_1$ – $A_4)$   $5 \mu\text{l}/\text{min}$ , ( $B_1$ – $B_4$ )  $40 \mu\text{l}/\text{min}$ , and ( $C_1$ – $C_4$ )  $140 \mu\text{l}/\text{min}$ . The volumetric flow rate of the injected particles sample through the port A shown in Fig. 82 is the same as that of the total sheath flows through the ports  $C_1$  and  $C_2$ . The driving pressure difference obtained from the model is  $\Delta p \approx (A_1$ – $A_4)$  2 KPa, ( $B_1$ – $B_4$ ) 10 KPa, and ( $C_1$ – $C_4$ ) 18 KPa. Scale bars are  $150 \mu\text{m}$  for the main images and  $30 \mu\text{m}$  for their insets in ( $A_1$ – $C_1$ ) and ( $A_2$ – $C_2$ ).

## Particle retrieval

A particle-free fluid flow with a sufficiently large volumetric flow rate ( $\sim 800 \mu\text{l}/\text{min}$ ) is used for removing the trapped particles. As shown in Fig. 85, more than %99 of the trapped particles have been successfully retrieved.

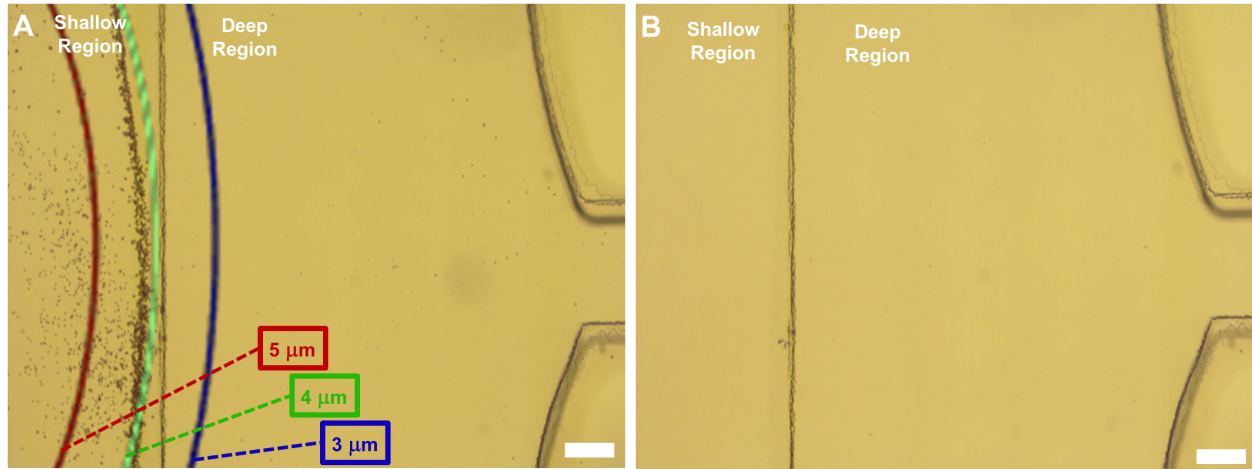


Figure 85: (A) Microscope image of the particles close to the 2<sup>nd</sup> deep-shallow interface under the net volumetric flow rate of  $Q_{\text{net}} = 40 \mu\text{l}/\text{min}$  together with the membrane displacement contours obtained from the ODF-3DS model, and (b) the microscope image of the 2<sup>nd</sup> deep-shallow interface after the trapped particles are retrieved. Scale bars are  $200 \mu\text{m}$ .

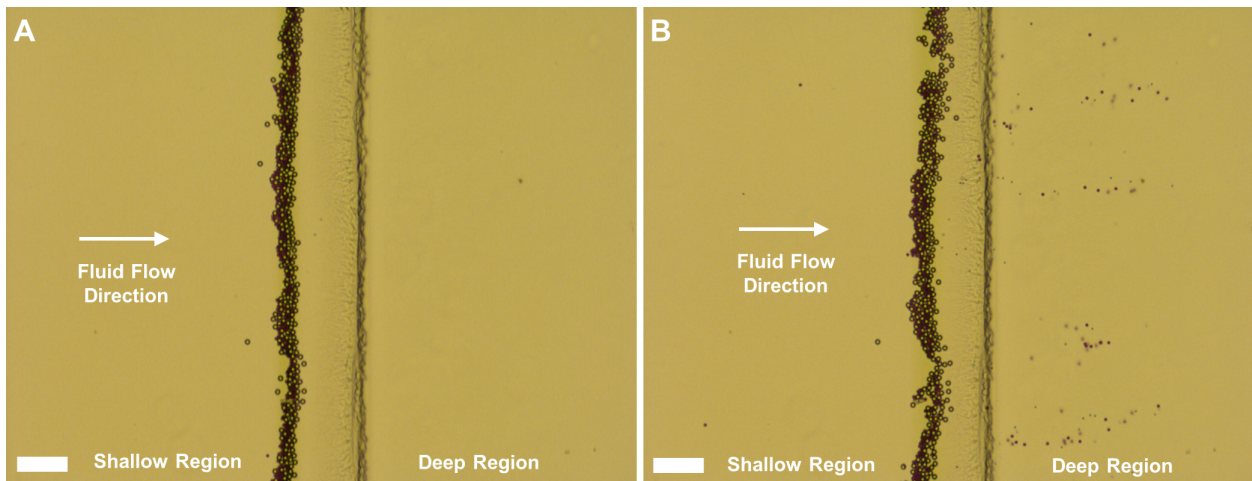


Figure 86: Microscope images showing (a) the isolated particles next to the 2<sup>nd</sup> deep-shallow interface under the net volumetric flow rate of  $Q_{\text{net}} = 40 \mu\text{l}/\text{min}$  and (b) their partial release over time due to the buildup pressure as a result of the particle trapping and open area decrease about one minute later. Scale bars are  $100 \mu\text{m}$ .

### Pressure buildup effects

The open cross sectional area decreases as the particles are filtered within the microchannel. As a result, the hydrodynamic resistance of the microchannel increases over time, causing the pressure difference across the microchannel to gradually increase for delivering the target volumetric flow rate being injected using the syringe pump. As shown in Fig. 86, after

a sufficiently long time, the trapped particles are forced by the buildup pressure to move forward through the microchannel and finally be filtered out. In future works, programmable injection and collection with appropriate pertinent duration times can be employed to resolve this issue for developing efficient continuous particle separation techniques.

## Summary and future works

In this work, a new class of deformable microfluidics was proposed for tunable particle trapping without the need to the pneumatic actuation. In this technique, the pore size is altered through the deformable microchannel expansion under various volumetric flow rates of the injected samples, *i.e.* under different pressure differences across the microchannel. Unlike the currently available deformable microfluidic filters, the proposed platform consisting of a micro-weir structure does not need the pneumatic actuation to trap the particles. Furthermore, the particles trapped on the weir remain stationary after the sample injection ceases, since the membrane returns to its undeformed situation under no pressure difference across the channel (isolation), which makes this platform portable and suitable for post-trapping analysis and handling. The devices can be readily fabricated for single-use purposes, while the proposed modified platform with the sheath flows can be used as a reusable device. The model accompanying the proposed pneumatic-actuation-free tunable particle-trapping strategy can be used as a starting point to design the pertinent microfluidic devices. The funnel-shaped membrane's slope in this technique is very small on the micro-weir, *i.e.* membrane displacement divided by shallow region length/width  $\approx O(\mu m)/O(mm) \approx O(10^{-3})$ . Such gentle slopes can be useful for the cell isolation applications when the cell viability is important. Programming the injections of the sample and sheath flows for achieving a more efficient and continuous operation of similar devices remains for the future works.

# Chapter 8: Conclusion and future work

## Conclusion

In this work, we provided a new analytical model for studying low-Reynolds-number flows of Newtonian fluids by simultaneously capturing the microchannel deformability, fluid compressibility, and microchannel's width profile. We demonstrated theoretically and experimentally that coupled fluid-solid interactions underlying the fluid flow through shallow deformable microchannels lead to some interesting physics. Our investigations revealed that various distinct fluid-structural characteristics emerge under different flexibility parameter scales. A shallow deformable microchannel behaves similar to its rigid counterpart under the sufficiently small flexibility parameter. In this regime, the flow rate is proportional to  $WH_0^3$ , where  $W$  and  $H_0$  respectively refer to the microchannel width and original height. On the other hand, applying a sufficiently large pressure difference across the microchannel can result in the transition to the higher-flexibility regimes. Under the sufficiently large pressure differences across the shallow deformable microchannel with ultralow height-to-width aspect ratios, the original height of microchannel is negligible compared with the membrane deflection, and consequently does not influence the fluid-solid characteristics. In these situations, the volumetric flow rate becomes proportional to  $W^{13}$  and independent of  $H_0$ . We also found a threshold for the fluid and solid mechanics aspects of this problem to be considered decoupled. We showed theoretically that the linear pressure assumption through a deformable

microchannel is acceptable (less than 1% error in flow rates) for the flexibility parameter smaller than 0.241, while this assumption is noticeably erroneous for the regimes with a large flexibility parameter. For the cases that the flexibility parameter is smaller than 0.241, the fluid and solid mechanics can be considered decoupled, while the fluid-solid intersections should be considered coupled for the larger flexibility parameter.

Master curves were also obtained for compressible fluid flows through any arbitrary shallow and long deformable microchannel presenting the dimensionless flow rate as functions of flexibility parameter and dimensionless fluid compressibility. Investigation of the fluid's compressibility demonstrates that compressible fluid flow through a deformable microchannel resembles incompressible flow through the rigid counterpart under sufficiently small pressure differences, while height-independent and highly non-linear pressure-dependent characteristics, *e.g.*  $\dot{m} \propto \Delta p^5$ , appear under sufficiently large pressure differences.

When investigating the effects of microchannel's width profile on fluid-structural characteristics, we discovered that an asymmetrically-shaped microchannel with a deformable ceiling provides a direction-dependent membrane deformation and hydrodynamic resistance, enabling the passive rectification of both compressible and incompressible Newtonian fluid flows under the Stokes regime ( $Re \ll 1$ ). The flow rectification ratio of  $\sim 1.2$ – $1.8$  has been demonstrated for common Newtonian fluids such as water, alcohol, and air.

A new deformable microfluidic platform was developed for particle trapping and separation without the need of a separate actuation/control mechanism. The pore size was altered through the deformable microchannel expansion under various pressure differences across the device. Trapped particles remained stationary once the fluid flow ceases, since the membrane returns to its undeformed situation under no pressure difference across the channel. The developed 0DF-3DS model accompanying the proposed strategy was used for designing such microfluidic devices. The provided model predicted the profile of trapped particles acceptably. The funnel-shaped membrane's slope is very small, *i.e.* membrane displacement divided by shallow region length/width  $\approx O(\mu m)/O(mm) \approx O(10^{-3})$ , which is favorable for cell isolation applications when the cell viability is important.

## Future work

Some of the research topics envisioned as a continuation of this thesis are discussed in the following:

- **Slip regime of gas flows through deformable microchannels**– The one-dimensional model developed in this work was based on continuum mechanics with no-slip velocity boundary condition on walls. The limit of continuum models is somewhere between  $\text{Kn} = 0.5$  and 1 [205], while the transition regime is typically split into a slip regime at lower Knudsen numbers, *i.e.*  $\text{Kn} \approx 0.05$  [205], wherein the Navier-Stokes equations are joint with higher-order boundary conditions to predict the gas flow characteristics accurately [205, 216]. The Navier-Stokes equations accompanied by the no-slip boundary condition starts to fail for Knudsen numbers larger than about 0.01. Instead, the slip boundary condition can be implemented to Eq. 59 in order to derive a one-dimensional model suitable for studying the gas dynamics within a deformable channel under the slip-flow regime. For experimental investigation of this topic, the height of deformable microchannel should be at least one order smaller than that of the current study (this thesis), *i.e.*,  $O(0.1\mu m)$ , considering the mean free path of gas molecules is about 50 to 100 *nm* under the standard pressure and temperature conditions (atmospheric pressure and room temperature). Therefore, a different fabrication scheme would be needed to fabricate a deformable channel with submicron- or nanometer-scale height, which can be challenging. One or combination of the following two approaches can result in the larger Knudsen number and the slip flow regime: 1) fabrication of shallower microchannels, *e.g.*  $H_0 \approx O(0.1 \mu m)$ , and 2) decreasing the absolute pressure levels of inlet, outlet, and ambient air to decrease the gas density, where a vacuum needs to be provided around the outermost side of the membrane and the outlet of microchannel for the latter approach.
- **Analytical solution for behavior of rectifier**– The ODE presented in Eq. 18 can be reduced to the Abel’s differential equation under the sufficiently low pressure differences

across the channel, where the terms with  $\chi^2$  and  $\chi^3$  play minor role in Eq. 18, *i.e.*  $\alpha_2 = \alpha_3 = 0$ . An analytical solution might be found under these conditions for the fluid-solid characteristics.

- **Flows of non-Newtonian fluids through asymmetrically-shaped deformable microchannels**— It was demonstrated in this work that an asymmetrically-shaped deformable microchannel gives rise to a direction-dependent membrane deflection and hydrodynamic resistance, enabling the rectification of Newtonian fluid flows under the Stokes regime ( $\text{Re} \ll 1$ ) by introducing the direction-dependent terms into the otherwise linear Stokes equations. On the other hand, the non-linear rheology of non-Newtonian fluids has already been resorted to for rectifying the fluid flow under the Stokes regime [176–178]. An exciting question is “can the non-Newtonian fluids amplify the rectification mechanism provided by asymmetrically-shaped deformable microchannels and lead to higher rectification ratios?”
- **Size distribution of rare particulate matters**— Atmospheric aerosol particles, also known as particulate matter (PM), or particulates refer to a mixture of solid particles and liquid droplets found in the air. Some particles less than 10 micrometers in diameter ( $\text{PM}_{10}$ ) can get deep into one’s lungs and some may even get into bloodstream. Of these, particles less than 2.5 micrometers in diameter, also known as fine particles or  $\text{PM}_{2.5}$ , pose the greatest risk to health. Particle number size spectra can be measured using the optical particle spectrometer [249]. Other techniques such as microscopy, mobility analysis, centrifugal measurement of particle mass, etc, can also be found in the literature [250]. Particularly, regarding the microscopy-based techniques, image analysis offers a broad range of information such as rotation radius, size distribution of aggregates, fractal dimension, number of primary particles per aggregate, and size distribution of primary particles [250]. The deformable microfluidic filter developed in this work might find applications in determining the size distribution of rare particulates. In this technique, one would inject the sample through the disposable device.

The particulates would be isolated after the injection ceased. The image analysis could be done afterwards to elicit the desired statistical information.

- **Rare cancer cell isolation**– Rare cancer cell isolation is one of the appealing applications envisaged for the deformable microfluidic sieve developed in this work. In this approach, the trapped cells would remain stationary after lifting the pressure difference across the channel, since the membrane would return to its original position sandwiching the trapped cells. This platform may, therefore, provide a convenient post-isolating analysis, since the chip can be transferred without the risk of trapped cells to escape.

# APPENDIX

## Fabrication: detailed protocol

A detailed and step-by-step description of the process flow related to the fabrication of the microchannel sidewalls as well as the two-step bonding paradigm is presented in the following.

### Fabrication of sidewalls

In this work, two well-known approaches are utilized to create the microchannel sidewalls: wet etching of glass, and SU8 photo-lithography. These approaches are schematically presented in Fig. 87, and explained in the following:

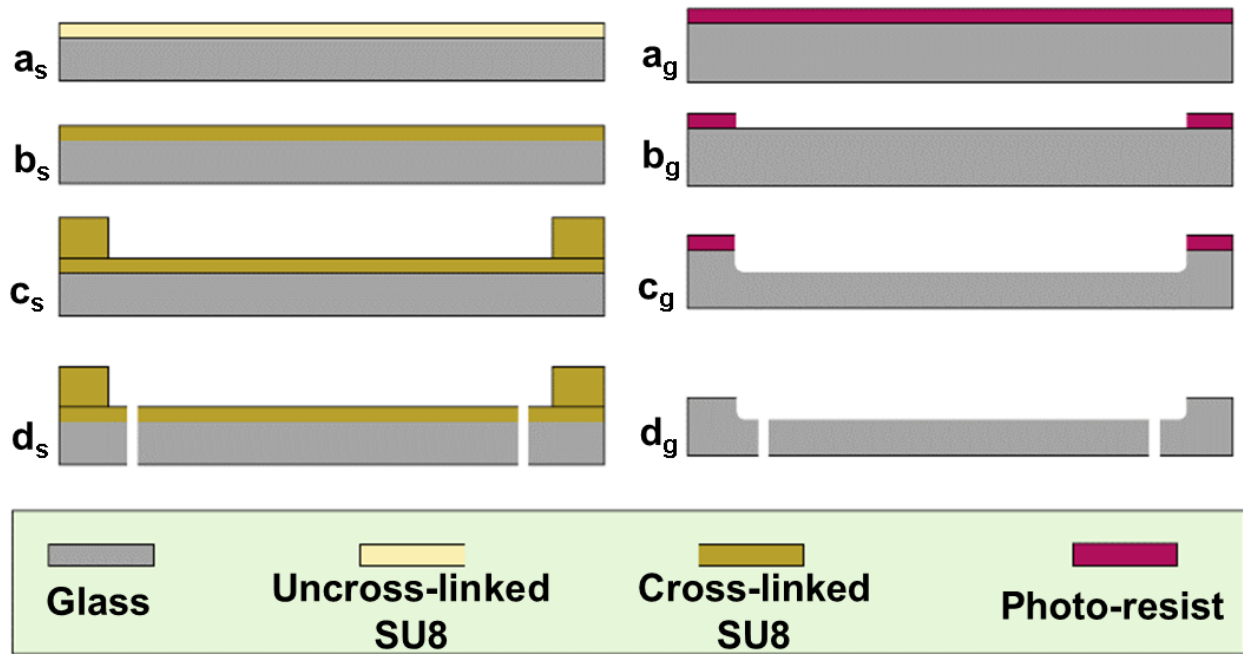


Figure 87: The procedure to fabricate the sidewalls of microchannel based on:

**SU8 photo-lithography**— (a<sub>s</sub>) Spin coating a thin layer of SU8 on the glass substrate, (b<sub>s</sub>) soft-baking and UV exposure followed by a post-exposure baking, (c<sub>s</sub>) patterning the side-walls of the microchannel following the standard photo-lithography process followed by a sufficiently long hard baking, and (d<sub>s</sub>) drilling the via-holes.

**Wet etching of the glass**— (a<sub>g</sub>) spin coating a thick enough layer of photo-resists AZ4620, AZ4330, or S1813 based on the required duration time of etching, (b<sub>g</sub>) patterning the mask following the standard photo-lithography process followed by a sufficiently long hard baking, (c<sub>g</sub>) wet etching of the glass substrate in a bath of etchant, and (d<sub>g</sub>) drilling the via-holes.

### Sidewalls made of SU8

After a standard cleaning process using Acetone, IPA, rinsing with DI water, and dehydration, the soda-lime glass chips are soaked in the piranha bath (sulfuric acid (98%) : hydrogen peroxide (30%) with volume ratio 3:1) for 20 minutes at the solution temperature of 100–110 °C to render the chips a highly hydrophilic surface, which significantly enhances the SU8-glass adhesion. In order to create a microchannel with the entire innermost surfaces made of SU8, a thin ( $\sim 1 \mu\text{m}$ ) layer of SU8 is first spun on the glass substrate (Fig. 87 (a<sub>s</sub>)).

In order to obtain such a thin layer, the SU8-2100 is diluted with a SU8 thinner so that the weight percentage of SU8-2100 in the final solution is about 23.8% (*i.e.*  $\frac{1}{1+3.2}$ ). Unless otherwise mentioned, the following spin coating procedure is used in this work: the spinner speed is ramped at a rate of 83 *rpm/s* up to 500 *rpm* and kept there for 15–20 seconds. The speed is then ramped up to the maximum speed, which is 1500 *rpm* unless otherwise mentioned, at a rate of 83 *rpm/s*, remaining constant for 45 seconds, and then ramped down to zero at a rate of about 250 *rpm/s*. The maximum speed for spinning the first layer is 3000 *rpm* to obtain a  $\sim 1$   $\mu\text{m}$ -thick SU8 layer. The SU8 is baked on the hotplate for 5 minutes at 95°C. The SU8 layer is then exposed to 200  $\text{mJ}/\text{cm}^2$  UV followed by a 5-minute post-exposure baking on the hotplate at 95°C (Fig. 87 (b<sub>s</sub>)). A 30-minute-long hard baking at 170°C is also done in the oven to improve the glass-SU8 adhesion. The metal electrodes can also be fabricated (if needed) following the lift-off or wet etching processes.

In the next step, the microchannel sidewalls are created by photo-lithography (Fig. 87 (c<sub>s</sub>)). Based on our experiments, a short (1–5 minutes) oxygen plasma at 120 *W* and 100 *mT* ( $\sim 40$  *sccm* *O*<sub>2</sub>) before SU8 spinning on the underlying SU8 layer significantly improves the uniformity of the spun layer. A much more gentle plasma treatment can be done for the cases that metal electrodes are prone to be etched. As a recommended step, after creating the pattern of sidewalls, a 30-minute-long hard baking at 140°C is performed on the hotplate to render the SU8 better mechanical properties. It is worth mentioning that the photo-lithography mask can be designed in such a manner that the areas close to the edge of the chip block the UV, and consequently the areas with the most height non-uniformity, *i.e.*, the edge bead will be removed during the SU8 development.

In the next step, the through-holes are drilled using a 2-mm diamond coated drill bit (Fig. 87 (d<sub>s</sub>)). Drilling the via-holes after all the other required features are created on the glass substrate avoids the enormous height non-uniformity that could arise around the via-holes during the spin-coating of the SU8 layers. Such a large non-uniformity could result in poor contact between the adhesive sealing layer and the sidewalls of the microchannel, and consequently a much lower bonding strength [99]. According to our experiments, soaking the glass chips in the piranha bath at the very beginning of the process flow significantly improves the glass/SU8 adhesion which is of utmost importance to avoid any SU8 delamination when the via holes are drilled, during the later cleaning steps in an ultrasonic bath, or in real applications of the microfluidic device when a high pressure driven flow through the channel is needed. We have observed that skipping the piranha treatment step from the process flow results in the delamination of the SU8 layer during the via-hole drilling step for thick SU8 layers ( $> 10$   $\mu\text{m}$ ).

In order to keep the created structures intact while drilling the holes, one or few layers of photo-resist Shipley S1813 are spun on the created patterns and cured. Similarly, the photo-resist S1813 is spun and cured on the back side of the glass substrate as well. In addition, in order to avoid the shattering of the glass throughout the drilling process, the glass chip is fixed on a dummy glass substrate using a thin layer of wax (Aquabond-55 from Aquabond Technologies a division of Universal Photonics), in such a manner that the photo-resist protecting the patterns is in contact with the wax. Following this approach, the yield of the drilling process is close to 100%. After the holes are drilled, the glass chip is debonded from the dummy substrate at about 65°C and cleaned through performing a series of short sonication in an ultrasonic bath of acetone, IPA and DI water to make sure all the photo-resist S1813, wax and potential residues from the drilling step are removed. After a

short ( $\sim 10$  minutes) dehydration on the hotplate at  $100^\circ\text{C}$ , the microchannels on the glass chip are ready to be sealed by the SU8-covered PET film.

### Sidewalls made of glass

In order to create the microchannel sidewalls through the glass wet etching, a buffered oxide etchant (BOE) solution mixed with hydrochloric acid ( $\text{HF}(48\%):\text{NH}_4\text{F}(40%):\text{HCl}(37\%) = 1:6:1.4$  (v/v)) is used as an etchant, while the photo-resists S1813 (or AZ4330) and AZ4620 are used as the mask for the fabrication of shallow and deep microchannels, respectively. The glass is mounted horizontally and facing downward on a holder. In addition, the magnetic stirring is used to enhance the etch rate [131]. Based on our experiments, the speed of stirring not only significantly affects the etch rate, but also plays a key role in the uniformity of the etched surfaces. We observed that very uniform etched surfaces (variations in the depth less than 1% of the maximum etching depth) can be obtained when the magnetic stirring speed is equal to or greater than 600 rpm.

First, the potential contamination on the glass slide is removed through a series of sonication in the ultrasonic baths of acetone, IPA, DI water, following by dehydration. To improve the adhesion of photo-resist, the glass slides are then soaked in the piranha solution ( $\text{H}_2\text{SO}_4$  (98%): $\text{H}_2\text{O}_2$ (30%) = 3:1 (v/v)) at the solution temperature of  $100\text{--}110^\circ\text{C}$  for 20 minutes, followed by a 20-minute dehydration on a hotplate at  $200^\circ\text{C}$ .

The photo-resist is then spun on the glass substrate (Fig. 87 (a<sub>g</sub>)). Next, the photo-resist is baked on the hotplate, and patterned by UV using a suitable mask of the sidewalls' pattern. After the development, a one-hour hard-baking is done in an oven at  $140^\circ\text{C}$  (Fig. 87 (b<sub>g</sub>)). Next, the glass slides are etched in the etchant bath (Fig. 87 (c<sub>g</sub>)). The via-holes are then created (Fig. 87 (d<sub>g</sub>)).

### SU8 bonding—step 1: Sealing

After creating the microchannel sidewalls, they need to be sealed properly. The process flow for the sealing step is schematically presented in Fig. 88. First, a piece of the PET film ( $\sim 190\ \mu\text{m}$  in thickness) is prepared in such a manner that its size is preferably equal to or slightly smaller than that of the glass chip in order to (1) avoid dealing with the areas close to the edge of the glass chip, where the height non-uniformity of the SU8 layer might be too large to be compensated by the thin layer of SU8 available on the PET film, and (2) make the future handling of the device much safer, since there will not be any unwanted torque applied to the edge of the PET film that would might cause debonding between the PET film and the rest of the SU8-glass stack.

The PET films is then cleaned through a standard cleaning procedure. As well as evaporating all the droplets on the PET, a dehydration at a temperature above the glass transition temperature of the PET (*e.g.*  $95^\circ\text{C}$  in this work) helps it to become flat and the following spin coating process much more convenient. A thin layer of SU8 is then spun on the PET film (Fig. 88 (a)). The  $2\ \mu\text{m}$  and  $7\ \mu\text{m}$  thick layers of SU8 are used in the sealing step based on the severity of the height non-uniformity. The suitable SU8 solutions for spinning these layers can be obtained through dilution of SU8-2100 with a SU8 thinner so that the weight percentage of SU8-2100 in the final solution is about 28.6% (*i.e.*  $\frac{1}{1+2.5}$ ) and 50% (*i.e.*  $\frac{1}{1+1}$ ), respectively. The SU8-covered PET film is then baked according to Table 4. The PET film is then removed from the hotplate, and it is ready to be bonded to the other substrate with the microchannel pattern.

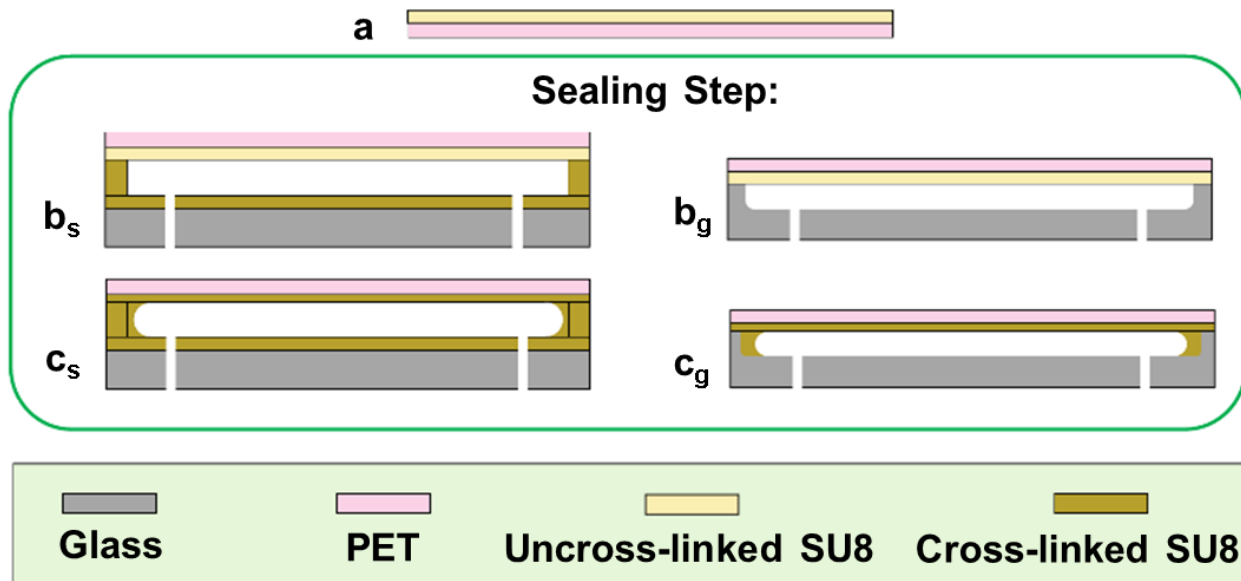


Figure 88: The sealing step of the two-step SU8 bonding paradigm: (a) spin coating a thin SU8 layer on the PET film, ( $b_s$  and  $b_g$ ) bringing the uncross-linked SU8 on the PET in contact with the sidewalls of microchannel, and ( $c_s$  and  $c_g$ ) sufficiently long UV exposure through the PET film, followed by a post-exposure baking, for two different approaches that sidewalls are made based on SU8 photo-lithography ( $b_s$  and  $c_s$ ) or wet etching of the glass ( $b_g$  and  $c_g$ ). The slight SU8 reflow might result in a cross-section with round corners.

The prepared glass substrate with the sidewalls pattern is then put on a  $69^\circ\text{C}$  hotplate. The temperature measurements all over the hotplate surface showed  $\pm 1^\circ\text{C}$  deviations from the set temperature. After about three minutes that the glass substrate and the patterns on it have reached their steady state temperature, the PET film is also put on the same hotplate. After one minute, the PET film is flipped over, and its SU8 cover is brought in contact with the patterned SU8 on the glass substrate for the case the sidewalls are made through the SU8 photo-lithography (Fig. 88 ( $b_s$ )), or with the glass surface for the case the sidewalls are made through the glass wet etching (Fig. 88 ( $b_g$ )). Our observations show a very poor adhesion between the SU8 adhesive layer and the glass top surface in the case of making the sidewalls through wet etching. Based on our experiments, either one of the following two approaches can resolve this problem:

- a 20-minute surface treatment of the glass chips (with the etched channels) in the piranha bath ( $\text{H}_2\text{SO}_4$  (98%): $\text{H}_2\text{O}_2$ (30%) = 3:1 (v/v)) at the solution temperature of  $100\text{--}110^\circ\text{C}$ , followed by a 20-minute dehydration on a hotplate at  $200^\circ\text{C}$  prior to bonding.
- deposition of a thin (50–150 nm) silicon dioxide everywhere on the glass chip using a PECVD instrument, followed by a short and gentle oxygen plasma treatment before the bonding.

After the SU8 covered PET film is brought in contact with the sidewalls of the microchannel, the trapped air is then removed using tweezers and/or finger pressure starting from one corner of the PET film sweeping towards its opposite corner on the other side in a line-by-line fashion. Based on the size and complexity of the microchannel geometry, the bubble removal might take between one and several minutes. After the bubble removal step is accomplished, the chip remains on the hotplate at  $69^\circ\text{C}$  for overall  $\sim 30$  minutes and then

is cooled down to room temperature over about 20 minutes. The chip is then undergone with the UV illumination of  $1.4 \text{ J/cm}^2$  through the PET film. The sample is then put on a hotplate, initially at  $65^\circ\text{C}$  in such a manner that the PET film is in contact with the hotplate and the glass piece is on top. The temperature is then ramped up to  $95^\circ\text{C}$  over about 4 minutes, remaining constant at  $95^\circ\text{C}$  for 20 minutes, and then decreases to room temperature over 30 minutes to complete the sealing step (Fig. 88 ( $c_s$ ) and ( $c_g$ )). Finally, the SU8 reflow during the sealing step has been explored in the main text.

### SU8 bonding—step 2: Bonding reinforcement

The process flow for bonding reinforcement is schematically presented in Fig. 89. First, a

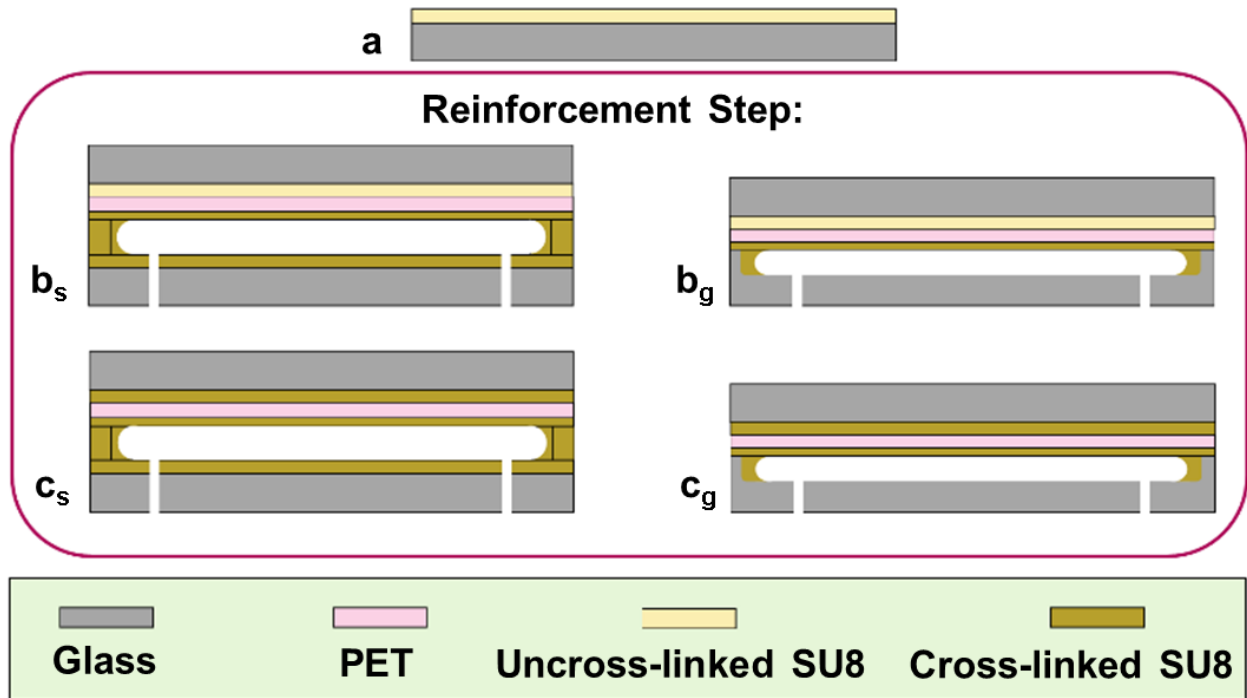


Figure 89: The bonding reinforcement step of the two-step SU8 bonding paradigm: (a) spin coating a thick enough layer of SU8 on the glass substrate and soft-baking, ( $b_s$  and  $b_g$ ) bringing the uncross-linked SU8 on the reinforcement glass in contact with the bare side of the PET film, and ( $c_s$  and  $c_g$ ) sufficiently long UV exposure through the reinforcement glass substrate, followed by a post-exposure baking, for two different approaches that sidewalls are made based on SU8 photo-lithography ( $b_s$  and  $c_s$ ) or wet etching of the glass ( $b_g$  and  $c_g$ ).

SU8 layer is spun on a glass substrate, which is already cleaned through a standard cleaning process using Acetone, IPA, rinsing with DI water, and dehydration (Fig. 89 (a)). The SU8 layer used in this step needs to be thick enough to cover all the height non-uniformity on the PET surface because of the defects on the PET film itself as well as that of the SU8 layers forming the microchannel sidewalls. Based on the severity of the height non-uniformity, SU8 layers with different thicknesses of  $7 \mu\text{m}$ ,  $15 \mu\text{m}$ , and  $22 \mu\text{m}$  are used for the purpose of reinforcement. The suitable SU8 solution for spinning these layers can be obtained through dilution of SU8-2100 with a SU8 thinner so that the weight percentage of SU8-2100 in the final solution is about 50% (*i.e.*  $\frac{1}{1+1}$ ), 75% (*i.e.*  $\frac{3}{3+1}$ ), and 83% (*i.e.*  $\frac{5}{5+1}$ ), respectively. The

SU8-covered reinforcement glass is then baked according to Table 5. The reinforcement glass is then ready to be bonded to the PET film.

In the next step, the fabricated chip is put on a hotplate initially at  $65^{\circ}\text{C}$ . The temperature is then ramped up to the bonding temperature shown in Table 5 at a rate of about  $7^{\circ}\text{C}/\text{min}$ . The SU8-covered reinforcement glass is then put on the same hotplate. After one minute, the reinforcement glass is grabbed using a pair of tweezers, flipped over, and brought in contact with the PET film (Fig. 89 (b<sub>s</sub>) and (b<sub>g</sub>)). The bubble removal is then done using a pair of tweezers, finger pressures (in the case of low temperature bonding), and/or putting heavy enough objects on top of the glass substrate. It is worth mentioning here that the microchannel clogging is not a matter of concern in this step, since the SU8 layers forming the sidewalls of the microchannel have already been cured without any possibility to reflow. Hence, as much uniform pressure as desired can be applied as long as it does not damage the glass pieces. A desirable feature of thicker SU8 layers in this step is that lower temperatures and pressures can be applied for bubble removal and obtaining a conformal contact [97].

After bubble removal is done, the chip remains on the hotplate for 10 minutes and then cools down to room temperature at a rate of about  $3^{\circ}\text{C}/\text{min}$ . The chip is then undergone with the UV illumination of  $2.1\text{ J}/\text{cm}^2$  through the reinforcement glass, following by baking on a hotplate, initially at  $65^{\circ}\text{C}$ . The temperature is then ramped up to  $95^{\circ}\text{C}$  over about 4 minutes, remaining constant at  $95^{\circ}\text{C}$  for 10 minutes, and then decreases to room temperature at a rate of about  $3^{\circ}\text{C}/\text{min}$  to finish the bonding reinforcement step (Fig. 89 (c<sub>s</sub>) and (c<sub>g</sub>)).

### **Fabrication of the multi-height deep–shallow microchannels**

In this section, the fabrication of multi-height deep–shallow microchannels is described. The pattern of the sidewalls is established through a two-step wet etching procedure. First, the deep regions are etched in the glass by using the steps of a<sub>g</sub>–c<sub>g</sub> in the wet etching procedure. After removing the etching mask (photo-resist AZ4620), a new layer of the photo-resist AZ4620 or AZ4330 is spun coated on the glass by using the following spin coating procedure: the spinner speed is ramped at a rate of 83 rpm/s up to 500 rpm and kept there for 15 seconds. The speed is then ramped up to 1800 rpm at a rate of 83 rpm/s, remaining constant for 45 seconds, and then ramped down to zero at a rate of about 250 rpm/s. After soft-baking and the alignment between the patterned glass and the second photo-lithography mask, the photo-resist is patterned in such a manner that the windows open up to the already deeply-patterned areas of the glass as well as to the areas that need to be shallowly etched. In the next step, the photo-resist is hard-baked in an oven at  $110^{\circ}\text{C}$  for 30 minutes. The glass is then etched shallowly. At the end of the two-step wet etching procedure, the depth of the deep regions of the channel is the summation of the etching depths related to the first and the second etching processes, while the shallow regions' depth is dictated purely by the second wet etching step. After the inlet/outlet via-holes are drilled through the glass, the patterned glass is sealed and reinforced (if needed).

### **PDMS interconnect**

In order to connect the tubing to the microfluidic chips, a PDMS interconnect is bonded on the top of the glass slide after a short and gentle oxygen plasma treatment of both PDMS and glass surfaces (Fig. 90).

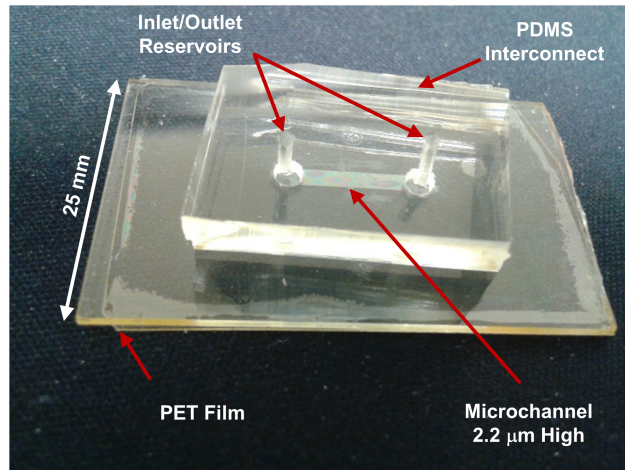


Figure 90: A microfluidic channel about  $2.2 \mu\text{m}$  in height sealed by a PET film coated with a  $2 \mu\text{m}$ -thick SU8 layer. The PDMS interconnect with holes corresponding to the via-holes of the glass substrate has been bonded to the glass surface after a short and gentle oxygen plasma treatment.

## Fabrication: supportive results

### Air bubbles trapped during the bonding reinforcement step

It is much more challenging to achieve a perfect void-free SU8 bonding between two rigid substrates. This fact is clearly reflected in the outcome of the reinforcement step, where a rigid glass substrate is to be bonded to the sealed microchannel. As it can be seen in Fig. 91 (a), in which the focal plane is on the interface between the PET film and the reinforcement glass substrate, some small bubbles are trapped between the PET film and the reinforcement glass during the bonding reinforcement step. The image of the chip at the same location with focal plane on the microchannels, shown in Fig. 91 (b), however, shows a perfect and bubble-free conformal sealing, that demonstrates again the advantage of using the PET film for achieving a void-free and conformal bonding during the sealing step.

### Large microchannels

An optical microscopy image showing the cross-section of a large microchannel about  $30 \mu\text{m}$  and  $100 \mu\text{m}$  in height and width, respectively, sealed by an almost  $7 \mu\text{m}$ -SU8-covered PET film is shown in Fig. 92. As shown, there is no noticeable SU8 reflows, since the channel dimensions are much larger than the SU8 adhesive layer.

### Oxygen Plasma effects

The optical microscopy images related to the cross-section of two microchannels with and without oxygen plasma treatment of the sidewalls prior to the bonding process are shown in Fig. 93. As shown in Fig. 93 (a), the channel dimensions remain the same as dictated by the photo-lithography ( $100 \mu\text{m} \times 30 \mu\text{m}$ ) in the case the sidewalls are treated with oxygen plasma (*i.e.* hydrophilic lateral sidewalls), since there is no reflow of the hydrophobic SU8 towards the hydrophilic sidewalls, while the SU8 reflow in absence of the oxygen plasma treatment of the sidewalls (*i.e.* hydrophobic lateral sidewalls) causes an almost  $4 \mu\text{m}$  reduction in the thickness of the adhesive layer in the middle of channel, as a result of which the height

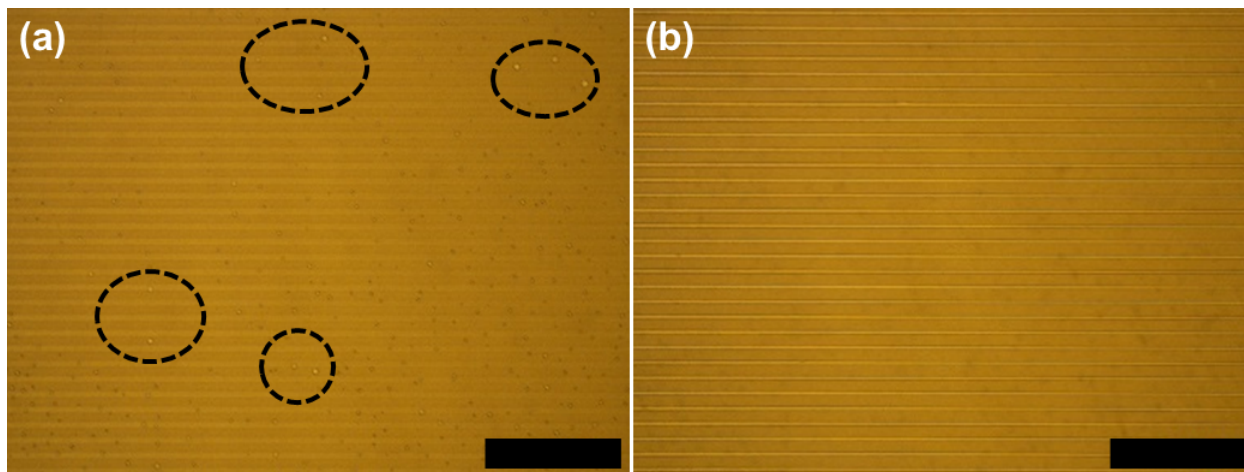


Figure 91: The optical microscopy images showing the center of a serpentine microchannel  $\sim 4 \mu\text{m}$  and  $\sim 15 \mu\text{m}$  in height and width, respectively, sealed by a  $2 \mu\text{m}$ -SU8-covered PET and reinforced by a  $7 \mu\text{m}$ -SU8-covered microscope slide. The focal plane is on the interface between the PET film and the reinforcement microscope slide in (a), and on the microchannels in (b). Some small trapped air bubbles that formed during the bonding reinforcement step are circled in (a). These bubbles do not adversely affect the microchannels, since the channels have already been cured and sealed perfectly without defects/voids, as shown in (b), before the commencement of the bonding reinforcement step. Scale bars =  $500 \mu\text{m}$ .

of channel in its middle is about  $4 \mu\text{m}$  larger than defined through the photo-lithography process. In addition, it should be noted that according to Fig. 93, the cover glass, because of having some slight level of flexibility, has been successfully used together with a  $7 \mu\text{m}$ -thick SU8 layer to seal rather large microchannels with an acceptably uniform height across the chip. However, the cover glass is usually provided in some limited small dimensions, which does not allow its usage for sealing a long microchannel. Furthermore, it is still challenging to seal small microfluidic networks using a  $7 \mu\text{m}$ -thick SU8-coated cover glass because of the channel blockage difficulties. On the other hand, this is also difficult to achieve a conformal contact using a cover glass coated with only  $2 \mu\text{m}$ -thick SU8 layer to seal small microchannels, where the flexible PET film coated with a  $2 \mu\text{m}$ -thick SU8 layer was demonstrated to be a good candidate.

### Long microchannels

A microchannel about  $6 \text{ cm}$ ,  $7 \mu\text{m}$  and  $250 \mu\text{m}$  in length, height and width, respectively, sealed by a  $2 \mu\text{m}$ -thick-SU8-coated PET film is shown in Fig. 94. As shown, the flexibility of the PET film enables fabricating the long and small channels using a thin ( $2 \mu\text{m}$  thick) SU8 adhesive layer.

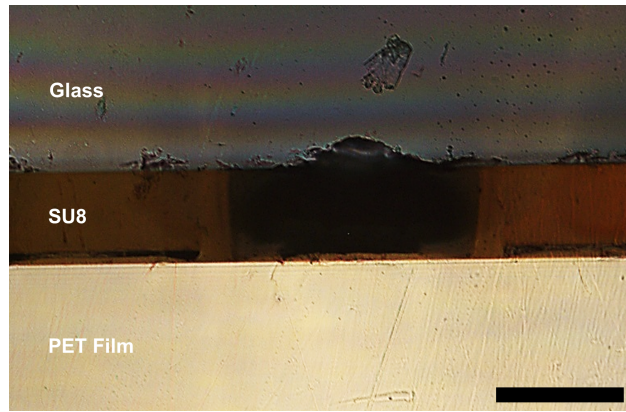


Figure 92: An optical microscopy image showing the cross-section of a microchannel about  $30\ \mu\text{m}$  and  $100\ \mu\text{m}$  in height and width, respectively, sealed by an almost  $7\ \mu\text{m}$ -SU8-covered PET film. Scale bar =  $50\ \mu\text{m}$ .

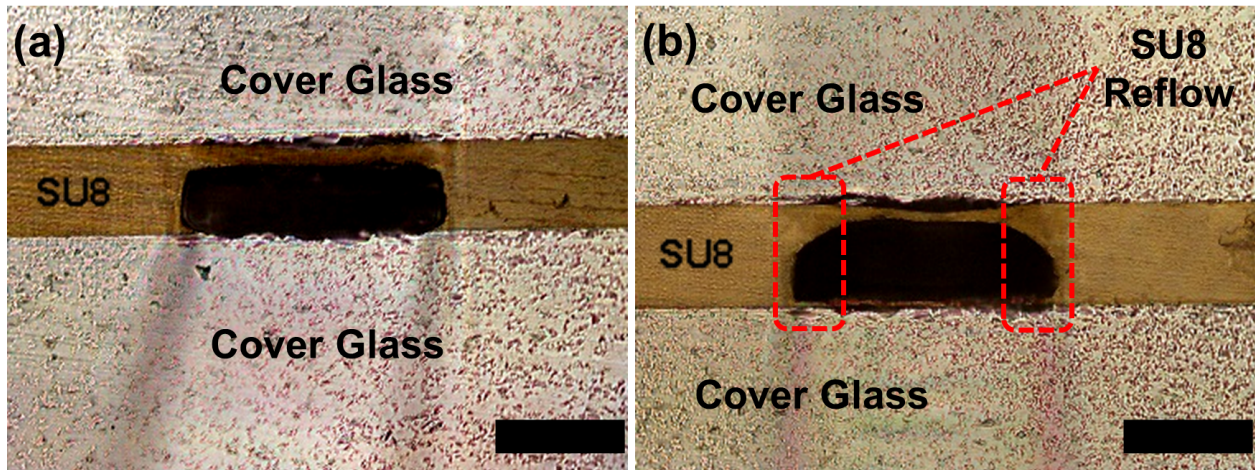


Figure 93: The optical microscopy images showing the cross-section of a microchannel about  $30\ \mu\text{m}$  and  $100\ \mu\text{m}$  in height and width, respectively, sealed by an almost  $7\ \mu\text{m}$ -SU8-covered cover glass (a) with, and (b) without oxygen plasma treatment of the sidewalls before the bonding. Scale bars =  $50\ \mu\text{m}$ .

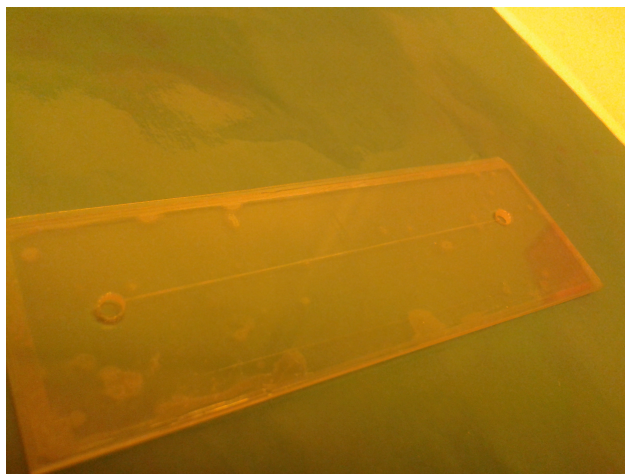


Figure 94: The camera image showing a microchannel about  $7\ \mu\text{m}$ ,  $250\ \mu\text{m}$ , and  $6\ \text{cm}$  in height, width, and length, respectively after the sealing step using a PET film coated with a  $2\ \mu\text{m}$ -thick SU8 layer. The microscope slide dimensions are  $25\ \text{mm} \times 75\ \text{mm}$ .

# BIBLIOGRAPHY

## BIBLIOGRAPHY

- [1] L. Y. Yeo, H.-C. Chang, P. P. Chan and J. R. Friend, *Microfluidic devices for bioapplications*, *small* **7** (2011) (1), pp. 12–48,  
URL: <http://onlinelibrary.wiley.com/doi/10.1002/smll.201000946/full>
- [2] D. Di Carlo, D. Irimia, R. G. Tompkins and M. Toner, *Continuous inertial focusing, ordering, and separation of particles in microchannels*, *Proceedings of the National Academy of Sciences* **104** (2007) (48), pp. 18892–18897,  
URL: <http://www.pnas.org/content/104/48/18892.short>
- [3] J. Zhang, W. Li, M. Li, G. Alici and N.-T. Nguyen, *Particle inertial focusing and its mechanism in a serpentine microchannel*, *Microfluidics and Nanofluidics* **17** (2014) (2), pp. 305–316,  
URL: <http://link.springer.com/10.1007/s10404-013-1306-6>
- [4] D. H. Yoon, J. B. Ha, Y. K. Bahk, T. Arakawa, S. Shoji and J. S. Go, *Size-selective separation of micro beads by utilizing secondary flow in a curved rectangular microchannel*, *Lab Chip* **9** (2009) (1), pp. 87–90,  
URL: <http://xlink.rsc.org/?DOI=B809123D>
- [5] M. Yamada, M. Nakashima and M. Seki, *Pinched Flow Fractionation: Continuous Size Separation of Particles Utilizing a Laminar Flow Profile in a Pinched Microchannel*, *Analytical Chemistry* **76** (2004) (18), pp. 5465–5471,  
URL: <http://pubs.acs.org/doi/abs/10.1021/ac049863r>
- [6] M. Yamada and M. Seki, *Hydrodynamic filtration for on-chip particle concentration and classification utilizing microfluidics*, *Lab on a Chip* **5** (2005) (11), p. 1233,  
URL: <http://xlink.rsc.org/?DOI=b509386d>
- [7] S. Kuiper, C. J. M. v. Rijn, W. Nijdam and M. C. Elwenspoek, *Development and applications of very high flux microfiltration membranes*, *Journal of Membrane Science* **150** (1998) (1), pp. 1 – 8,  
URL: <http://www.sciencedirect.com/science/article/pii/S0376738898001975>
- [8] S. Wickramasinghe, B. KalbfuSS, A. Zimmermann, V. Thom and U. Reichl, *Tangential flow microfiltration and ultrafiltration for human influenza A virus concentration and purification*, *Biotechnology and Bioengineering* **92** (2005) (2), pp. 199–208,  
URL: <http://doi.wiley.com/10.1002/bit.20599>
- [9] S. Zheng, H. K. Lin, B. Lu, A. Williams, R. Datar, R. J. Cote and Y.-C. Tai, *3D microfilter device for viable circulating tumor cell (CTC) enrichment from blood*, *Biomedical Microdevices* **13** (2011) (1), pp. 203–213,  
URL: <http://link.springer.com/10.1007/s10544-010-9485-3>
- [10] I. Doh, H.-i. Yoo, Y.-H. Cho, J. Lee, H. Kwan Kim and J. Kim, *Viable capture and release of cancer cells in human whole blood*, *Applied Physics Letters* **101** (2012) (4), p. 043701,  
URL: <http://aip.scitation.org/doi/10.1063/1.4737936>

- [11] V. VanDelinder and A. Groisman, *Separation of Plasma from Whole Human Blood in a Continuous Cross-Flow in a Molded Microfluidic Device*, *Analytical Chemistry* **78** (2006) (11), pp. 3765–3771,  
URL: <http://pubs.acs.org/doi/abs/10.1021/ac060042r>
- [12] X. Chen, D. Cui, C. Liu and H. Li, *Microfluidic chip for blood cell separation and collection based on crossflow filtration*, *Sensors and Actuators B: Chemical* **130** (2008) (1), pp. 216–221,  
URL: <http://linkinghub.elsevier.com/retrieve/pii/S0925400507006077>
- [13] T. Wang, M. Zhang, D. D. Dreher and Y. Zeng, *Ultrasensitive microfluidic solid-phase ELISA using an actuatable microwell-patterned PDMS chip*, *Lab on a Chip* **13** (2013) (21), p. 4190,  
URL: <http://xlink.rsc.org/?DOI=c31c50783a>
- [14] J. P. Beech and J. O. Tegenfeldt, *Tuneable separation in elastomeric microfluidics devices*, *Lab on a Chip* **8** (2008) (5), p. 657,  
URL: <http://xlink.rsc.org/?DOI=b719449h>
- [15] S.-B. Huang, M.-H. Wu and G.-B. Lee, *A tunable micro filter modulated by pneumatic pressure for cell separation*, *Sensors and Actuators B: Chemical* **142** (2009) (1), pp. 389–399,  
URL: <http://linkinghub.elsevier.com/retrieve/pii/S092540050900611X>
- [16] W. Liu, L. Li, J.-c. Wang, Q. Tu, L. Ren, Y. Wang and J. Wang, *Dynamic trapping and high-throughput patterning of cells using pneumatic microstructures in an integrated microfluidic device*, *Lab on a Chip* **12** (2012) (9), p. 1702,  
URL: <http://xlink.rsc.org/?DOI=c21c00034b>
- [17] W. Beattie, X. Qin, L. Wang and H. Ma, *Clog-free cell filtration using resettable cell traps*, *Lab on a Chip* **14** (2014) (15), p. 2657,  
URL: <http://xlink.rsc.org/?DOI=c41c00306c>
- [18] H. Bruus, *Theoretical microfluidics*, no. 18 in Oxford master series in physics (Oxford University Press, Oxford ; New York, 2008)
- [19] I. C. Christov, V. Cognet, T. C. Shidhore and H. A. Stone, *Flow ratepressure drop relation for deformable shallow microfluidic channels*, *Journal of Fluid Mechanics* **841** (2018), pp. 267–286,  
URL: <https://www.cambridge.org/core/journals/journal-of-fluid-mechanics/article/flow-ratepressure-drop-relation-for-deformable-s-798E21E2643E415BFA721DDD6298D4A6>
- [20] M. Javanmard, A. H. Talasaz, M. Nemat-Gorgani, F. Pease, M. Ronaghi and R. W. Davis, *Targeted cell detection based on microchannel gating*, *Biomicrofluidics* **1** (2007) (4), p. 044103,  
URL: <http://aip.scitation.org/doi/10.1063/1.2815760>
- [21] K. Jang, Y. Tanaka, J. Wakabayashi, R. Ishii, K. Sato, K. Mawatari, M. Nilsson and T. Kitamori, *Selective cell capture and analysis using shallow antibody-coated microchannels*, *Biomicrofluidics* **6** (2012) (4), p. 044117,  
URL: <http://aip.scitation.org/doi/10.1063/1.4771968>

- [22] S. Nagrath, L. V. Sequist, S. Maheswaran, D. W. Bell, D. Irimia, L. Ulkus, M. R. Smith, E. L. Kwak, S. Digumarthy, A. Muzikansky, P. Ryan, U. J. Balis, R. G. Tompkins, D. A. Haber and M. Toner, *Isolation of rare circulating tumour cells in cancer patients by microchip technology*, *Nature* **450** (2007) (7173), pp. 1235–1239, URL: <http://www.nature.com/doi/10.1038/nature06385>
- [23] A. A. Adams, P. I. Okagbare, J. Feng, M. L. Hupert, D. Patterson, J. Göttert, R. L. McCarley, D. Nikitopoulos, M. C. Murphy and S. A. Soper, *Highly Efficient Circulating Tumor Cell Isolation from Whole Blood and Label-Free Enumeration Using Polymer-Based Microfluidics with an Integrated Conductivity Sensor*, *Journal of the American Chemical Society* **130** (2008) (27), pp. 8633–8641, URL: <http://pubs.acs.org/doi/abs/10.1021/ja8015022>
- [24] S. L. Stott, C.-H. Hsu, D. I. Tsukrov, M. Yu, D. T. Miyamoto, B. A. Waltman, S. M. Rothenberg, A. M. Shah, M. E. Smas and G. K. Korir, *Isolation of circulating tumor cells using a microvortex-generating herringbone-chip*, *Proceedings of the National Academy of Sciences* **107** (2010) (43), pp. 18392–18397
- [25] J. Jiang, H. Zhao, W. Shu, J. Tian, Y. Huang, Y. Song, R. Wang, E. Li, D. Slamon, D. Hou, X. Du, L. Zhang, Y. Chen and Q. Wang, *An integrated microfluidic device for rapid and high-sensitivity analysis of circulating tumor cells*, *Scientific Reports* **7** (2017), p. 42612, URL: <http://www.nature.com/articles/srep42612>
- [26] X. Cheng, D. Irimia, M. Dixon, K. Sekine, U. Demirci, L. Zamir, R. G. Tompkins, W. Rodriguez and M. Toner, *A microfluidic device for practical label-free CD4+ T cell counting of HIV-infected subjects*, *Lab Chip* **7** (2007) (2), pp. 170–178, URL: <http://xlink.rsc.org/?DOI=B612966H>
- [27] P. Gascoyne, C. Mahidol, M. Ruchirawat, J. Satayavivad, P. Watcharasit and F. F. Becker, *Microsample preparation by dielectrophoresis: isolation of malaria*, *Lab on a Chip* **2** (2002) (2), p. 70, URL: <http://xlink.rsc.org/?DOI=b110990c>
- [28] H. W. Hou, A. A. S. Bhagat, A. G. Lin Chong, P. Mao, K. S. Wei Tan, J. Han and C. T. Lim, *Deformability based cell margination: A simple microfluidic design for malaria-infected erythrocyte separation*, *Lab on a Chip* **10** (2010) (19), p. 2605, URL: <http://xlink.rsc.org/?DOI=c003873c>
- [29] W.-T. Wu, A. B. Martin, A. Gandini, N. Aubry, M. Massoudi and J. F. Antaki, *Design of microfluidic channels for magnetic separation of malaria-infected red blood cells*, *Microfluidics and Nanofluidics* **20** (2016) (2), URL: <http://link.springer.com/10.1007/s10404-016-1707-4>
- [30] J. A. Korecka, J. Verhaagen and E. M. Hol, *Cell-replacement and gene-therapy strategies for Parkinsons and Alzheimers disease*, *Regenerative Medicine* **2** (2007) (4), pp. 425–446, URL: <http://www.futuremedicine.com/doi/10.2217/17460751.2.4.425>
- [31] *Selection of Embryonic Stem Cell-Derived Enhanced Green Fluorescent Protein-Positive Dopamine Neurons Using the Tyrosine Hydroxylase Promoter Is Confounded*

*by Reporter Gene Expression in Immature Cell Populations - Hedlund - 2007 - STEM CELLS - Wiley Online Library,*

URL: <http://onlinelibrary.wiley.com/doi/10.1634/stemcells.2006-0540/pdf>

- [32] Y. Chen, P. Li, P.-H. Huang, Y. Xie, J. D. Mai, L. Wang, N.-T. Nguyen and T. J. Huang, *Rare cell isolation and analysis in microfluidics*, *Lab on a Chip* **14** (2014) (4), p. 626,  
URL: <http://xlink.rsc.org/?DOI=c31c90136j>
- [33] C. Wyatt Shields IV, C. D. Reyes and G. P. López, *Microfluidic cell sorting: a review of the advances in the separation of cells from debulking to rare cell isolation*, *Lab Chip* **15** (2015) (5), pp. 1230–1249,  
URL: <http://xlink.rsc.org/?DOI=C4LC01246A>
- [34] G. Segré and A. Silberberg, *Radial Particle Displacements in Poiseuille Flow of Suspensions*, *Nature* **189** (1961), pp. 209–210,  
URL: <http://adsabs.harvard.edu/abs/1961Natur.189..209S>
- [35] B. P. Ho and L. G. Leal, *Inertial migration of rigid spheres in two-dimensional unidirectional flows*, *Journal of Fluid Mechanics* **65** (1974) (02), p. 365,  
URL: [http://www.journals.cambridge.org/abstract\\_S0022112074001431](http://www.journals.cambridge.org/abstract_S0022112074001431)
- [36] B. Chun and A. J. C. Ladd, *Inertial migration of neutrally buoyant particles in a square duct: An investigation of multiple equilibrium positions*, *Physics of Fluids* **18** (2006) (3), p. 031704,  
URL: <http://aip.scitation.org/doi/10.1063/1.2176587>
- [37] D. Di Carlo, J. F. Edd, D. Irimia, R. G. Tompkins and M. Toner, *Equilibrium Separation and Filtration of Particles Using Differential Inertial Focusing*, *Analytical Chemistry* **80** (2008) (6), pp. 2204–2211,  
URL: <http://pubs.acs.org/doi/abs/10.1021/ac702283m>
- [38] J. Zhang, S. Yan, R. Sluyter, W. Li, G. Alici and N.-T. Nguyen, *Inertial particle separation by differential equilibrium positions in a symmetrical serpentine micro-channel*, *Scientific Reports* **4** (2014),  
URL: <http://www.nature.com/articles/srep04527>
- [39] S. C. Hur, A. J. Mach and D. Di Carlo, *High-throughput size-based rare cell enrichment using microscale vortices*, *Biomicrofluidics* **5** (2011) (2), p. 022206,  
URL: <http://aip.scitation.org/doi/10.1063/1.3576780>
- [40] N. Nivedita, P. Ligrani and I. Papautsky, *Dean Flow Dynamics in Low-Aspect Ratio Spiral Microchannels*, *Scientific Reports* **7** (2017), p. 44072,  
URL: <http://www.nature.com/articles/srep44072>
- [41] A. Zebay, M. Karimzadehkhoei, S. Akg?n?, D. Gozuacik and A. Ko?ar, *Inertial Focusing of Microparticles in Curvilinear Microchannels*, *Scientific Reports* **6** (2016) (1),  
URL: <http://www.nature.com/articles/srep38809>

- [42] X. Wang, C. Liedert, R. Liedert and I. Papautsky, *A disposable, roll-to-roll hot-embossed inertial microfluidic device for size-based sorting of microbeads and cells*, *Lab Chip* **16** (2016) (10), pp. 1821–1830,  
URL: <http://xlink.rsc.org/?DOI=C6LC00215C>
- [43] M. Rafeie, J. Zhang, M. Asadnia, W. Li and M. E. Warkiani, *Multiplexing slanted spiral microchannels for ultra-fast blood plasma separation*, *Lab Chip* **16** (2016) (15), pp. 2791–2802,  
URL: <http://xlink.rsc.org/?DOI=C6LC00713A>
- [44] J. Kim, J. Lee, C. Wu, S. Nam, D. Di Carlo and W. Lee, *Inertial focusing in non-rectangular cross-section microchannels and manipulation of accessible focusing positions*, *Lab Chip* **16** (2016) (6), pp. 992–1001,  
URL: <http://xlink.rsc.org/?DOI=C5LC01100K>
- [45] M. Yamada and M. Seki, *Microfluidic Particle Sorter Employing Flow Splitting and Recombining*, *Analytical Chemistry* **78** (2006) (4), pp. 1357–1362,  
URL: <http://pubs.acs.org/doi/abs/10.1021/ac0520083>
- [46] C. Grobstein, *Trans-filter induction of tubules in mouse metanephrogenic mesenchyme*, *Experimental cell research* **10** (1956) (2), pp. 424–440,  
URL: <http://www.sciencedirect.com/science/article/pii/0014482756900167>
- [47] R. L. Fleischer, P. B. Price and E. M. Symes, *Novel Filter for Biological Materials*, *Science* **143** (1964), pp. 249–250
- [48] S. Seal, *A SIEVE FOR THE ISOLATION OF CANCER CELLS AND OTHER LARGE CELLS FROM THE BLOOD*, *Cancer* **17** (1964), pp. 637–642,  
URL: <http://onlinelibrary.wiley.com/doi/10.1002/1097-0142%28196405%2917:5%3C637::AID-CNCR2820170512%3E3.0.CO;2-I/full>
- [49] P. Gravesen, J. Branbjerg and O. S. Jensen, *Microfluidics-a review*, *Journal of Micromechanics and Microengineering* **3** (1993) (4), p. 168,  
URL: <http://stacks.iop.org/0960-1317/3/i=4/a=002>
- [50] P. Wilding, J. Pfahler, H. H. Bau, J. N. Zemel and L. J. Kricka, *Manipulation and flow of biological fluids in straight channels micromachined in silicon.*, *Clinical Chemistry* **40** (1994) (1), pp. 43–47,  
URL: <http://clinchem.aaccjnl.org/content/40/1/43.short>
- [51] J. de Jong, R. G. H. Lammertink and M. Wessling, *Membranes and microfluidics: a review*, *Lab on a Chip* **6** (2006) (9), p. 1125,  
URL: <http://xlink.rsc.org/?DOI=b603275c>
- [52] L. S. Lim, M. Hu, M. C. Huang, W. C. Cheong, A. T. L. Gan, X. L. Looi, S. M. Leong, E. S.-C. Koay and M.-H. Li, *Microsieve lab-chip device for rapid enumeration and fluorescence in situ hybridization of circulating tumor cells*, *Lab on a Chip* **12** (2012) (21), p. 4388,  
URL: <http://xlink.rsc.org/?DOI=c21c20750h>

- [53] Y. Yoon, S. Kim, J. Lee, J. Choi, R.-K. Kim, S.-J. Lee, O. Sul and S.-B. Lee, *Clogging-free microfluidics for continuous size-based separation of microparticles*, *Scientific Reports* **6** (2016) (1),  
URL: <http://www.nature.com/articles/srep26531>
- [54] R. J. Wakeman and C. J. Williams, *Additional techniques to improve microfiltration*, *Separation and Purification Technology* **26** (2002) (1), pp. 3–18,  
URL: <http://www.sciencedirect.com/science/article/pii/S1383586601001125>
- [55] H. M. Ji, V. Samper, Y. Chen, C. K. Heng, T. M. Lim and L. Yobas, *Silicon-based microfilters for whole blood cell separation*, *Biomedical Microdevices* **10** (2008) (2), pp. 251–257,  
URL: <http://link.springer.com/10.1007/s10544-007-9131-x>
- [56] T. A. Crowley and V. Pizziconi, *Isolation of plasma from whole blood using planar microfilters for lab-on-a-chip applications*, *Lab on a Chip* **5** (2005) (9), p. 922,  
URL: <http://xlink.rsc.org/?DOI=b502930a>
- [57] M. Javanmard, S. Emaminejad, C. Gupta, J. Provine, R. Davis and R. Howe, *Depletion of cells and abundant proteins from biological samples by enhanced dielectrophoresis*, *Sensors and Actuators B: Chemical* **193** (2014), pp. 918–924,  
URL: <http://linkinghub.elsevier.com/retrieve/pii/S0925400513014500>
- [58] M. J. Kim, D. J. Lee, J. R. Youn and Y. S. Song, *Two step label free particle separation in a microfluidic system using elasto-inertial focusing and magnetophoresis*, *RSC Adv.* **6** (2016) (38), pp. 32090–32097,  
URL: <http://xlink.rsc.org/?DOI=C6RA03146C>
- [59] P. Hoffmann, H. Ji, R. L. Moritz, L. M. Connolly, D. F. Frecklington, M. J. Layton, J. S. Eddes and R. J. Simpson, *Continuous freeflow electrophoresis separation of cytosolic proteins from the human colon carcinoma cell line LIM 1215: A non twodimensional gel electrophoresisbased proteome analysis strategy*, *PROTEOMICS* **1** (2001) (7), pp. 807–818,  
URL: [http://onlinelibrary.wiley.com/doi/10.1002/1615-9861\(200107\)1:7<807::AID-PROT807>3.0.CO;2-6/abstract](http://onlinelibrary.wiley.com/doi/10.1002/1615-9861(200107)1:7<807::AID-PROT807>3.0.CO;2-6/abstract)
- [60] M. Hajduch, R. Rakwal, G. K. Agrawal, M. Yonekura and A. Pretova, *High-resolution two-dimensional electrophoresis separation of proteins from metal-stressed rice (*Oryza sativa* L.) leaves: Drastic reductions/ fragmentation of ribulose-1,5-bisphosphate carboxylase/oxygenase and induction of stress-related proteins*, *ELECTROPHORESIS* **22** (2001) (13), pp. 2824–2831,  
URL: [http://onlinelibrary.wiley.com/doi/10.1002/1522-2683\(200108\)22:13<2824::AID-ELPS2824>3.0.CO;2-C/abstract](http://onlinelibrary.wiley.com/doi/10.1002/1522-2683(200108)22:13<2824::AID-ELPS2824>3.0.CO;2-C/abstract)
- [61] P. R. C. Gascoyne and J. Vykoukal, *Particle separation by dielectrophoresis*, *Electrophoresis* **23** (2002) (13), pp. 1973–1983,  
URL: <https://www.ncbi.nlm.nih.gov/pmc/articles/PMC2726256/>

- [62] B. ?etin and D. Li, *Dielectrophoresis in microfluidics technology*, ELECTROPHORESIS **32** (2011) (18), pp. 2410–2427,  
URL: <http://doi.wiley.com/10.1002/elps.201100167>
- [63] M. P. Hughes, *Fifty years of dielectrophoretic cell separation technology*, Biomicrofluidics **10** (2016) (3),  
URL: <https://www.ncbi.nlm.nih.gov/pmc/articles/PMC4930443/>
- [64] H. Jeon, Y. Kim and G. Lim, *Continuous particle separation using pressure-driven flow-induced miniaturizing free-flow electrophoresis (PDF-induced -FFE)*, Scientific Reports **6** (2016) (1),  
URL: <http://www.nature.com/articles/srep19911>
- [65] I. Doh, Y. Kim and Y.-H. Cho, *A particle trapping chip using the wide and uniform slit formed by a deformable membrane with air bubble plugs*, Current Applied Physics **13** (2013) (5), pp. 902–906,  
URL: <http://www.sciencedirect.com/science/article/pii/S1567173913000552>
- [66] H. Kim and J. Kim, *A microfluidic-based dynamic microarray system with single-layer pneumatic valves for immobilization and selective retrieval of single microbeads*, Microfluidics and Nanofluidics **16** (2014) (4), pp. 623–633,  
URL: <http://link.springer.com/10.1007/s10404-013-1267-9>
- [67] B. Kim, S. Yoo, Y.-J. Kim, J. Park, B. Kang, S. Haam, S.-W. Kang, K. Kang and U. Jeong, *A Strain-Regulated, Refillable Elastic Patch for Controlled Release*, Advanced Materials Interfaces **3** (2016) (9), pp. n/a–n/a,  
URL: <http://onlinelibrary.wiley.com/doi/10.1002/admi.201500803/abstract>
- [68] W. Song, A. E. Vasdekis and D. Psaltis, *Elastomer based tunable optofluidic devices*, Lab on a Chip **12** (2012) (19), p. 3590,  
URL: <http://xlink.rsc.org/?DOI=c2lc40481h>
- [69] D. M. Vogt, Y. L. Park and R. J. Wood, *Design and Characterization of a Soft Multi-Axis Force Sensor Using Embedded Microfluidic Channels*, IEEE Sensors Journal **13** (2013) (10), pp. 4056–4064
- [70] A. Raj, R. Halder, P. Sajeesh and A. K. Sen, *Droplet generation in a microchannel with a controllable deformable wall*, Microfluidics and Nanofluidics **20** (2016) (7),  
URL: <http://link.springer.com/10.1007/s10404-016-1768-4>
- [71] R. Anoop and A. K. Sen, *Capillary flow enhancement in rectangular polymer microchannels with a deformable wall*, Physical Review E **92** (2015) (1),  
URL: <https://link.aps.org/doi/10.1103/PhysRevE.92.013024>
- [72] C.-H. Hsu and A. Folch, *Microfluidic devices with tunable microtopographies*, Applied Physics Letters **86** (2005) (2), p. 023508,  
URL: <http://aip.scitation.org/doi/10.1063/1.1850593>

- [73] N. Li, C.-H. Hsu and A. Folch, *Parallel mixing of photolithographically defined nanoliter volumes using elastomeric microvalve arrays*, *ELECTROPHORESIS* **26** (2005) (19), pp. 3758–3764,  
URL: <http://doi.wiley.com/10.1002/elps.200500171>
- [74] R. Madhumitha, S. Arunkumar, K. K. Karthikeyan, S. Krishnah, V. Ravichandran and M. Venkatesan, *Computational Modeling and Analysis of Fluid Structure Interaction in Micromixers with Deformable Baffle*, *International Journal of Chemical Reactor Engineering* **15** (2017) (3),  
URL: <http://www.degruyter.com/view/j/ijcre.2017.15.issue-3/ijcre-2016-0121/ijcre-2016-0121.xml>
- [75] D. C. Leslie, C. J. Easley, E. Seker, J. M. Karlinsey, M. Utz, M. R. Begley and J. P. Landers, *Frequency-specific flow control in microfluidic circuits with passive elastomeric features*, *Nature Physics* **5** (2009) (3), pp. 231–235,  
URL: <http://www.nature.com/doi/10.1038/nphys1196>
- [76] E. W. Lam, G. A. Cooksey, B. A. Finlayson and A. Folch, *Microfluidic circuits with tunable flow resistances*, *Applied Physics Letters* **89** (2006) (16), p. 164105,  
URL: <http://aip.scitation.org/doi/10.1063/1.2363931>
- [77] R. R. Collino, N. Reilly-Shapiro, B. Foresman, K. Xu, M. Utz, J. P. Landers and M. R. Begley, *Flow switching in microfluidic networks using passive features and frequency tuning*, *Lab on a Chip* **13** (2013) (18), p. 3668,  
URL: <http://xlink.rsc.org/?DOI=c31c50481f>
- [78] J. Zhu, J. Shang, T. Olsen, K. Liu, D. Brenner and Q. Lin, *A mechanically tunable microfluidic cell-trapping device*, *Sensors and Actuators A: Physical* **215** (2014), pp. 197–203,  
URL: <http://linkinghub.elsevier.com/retrieve/pii/S0924424713005219>
- [79] J. Alvankarian and B. Yeop Majlis, *A technique of optimization of microfiltration using a tunable platform*, *Journal of Micromechanics and Microengineering* **25** (2015) (8), p. 084011,  
URL: <http://stacks.iop.org/0960-1317/25/i=8/a=084011?key=crossref.dd4d1bd6599ac4aa812c2c51e5eeed7>
- [80] J. Alvankarian, N. S. Jaddi, M. Vakilian, F. Barantalab, R. Jamal and B. Y. Majlis, *Consideration of Nonuniformity in Elongation of Microstructures in a Mechanically Tunable Microfluidic Device for Size-Based Isolation of Microparticles*, *Journal of Microelectromechanical Systems* **24** (2015) (2), pp. 309–318,  
URL: <http://ieeexplore.ieee.org/document/6995983/>
- [81] J. Alvankarian and B. Majlis, *Tunable Microfluidic Devices for Hydrodynamic Fractionation of Cells and Beads: A Review*, *Sensors* **15** (2015) (12), pp. 29685–29701,  
URL: <http://www.mdpi.com/1424-8220/15/11/29685>
- [82] P. N. Nge, C. I. Rogers and A. T. Woolley, *Advances in Microfluidic Materials, Functions, Integration, and Applications*, *Chemical Reviews* **113** (2013) (4), pp. 2550–2583,  
URL: <http://pubs.acs.org/doi/abs/10.1021/cr300337x>

- [83] P. Abgrall and A.-M. Gué, *Lab-on-chip technologies: making a microfluidic network and coupling it into a complete microsystema review*, Journal of Micromechanics and Microengineering **17** (2007) (5), pp. R15–R49,  
URL: <http://stacks.iop.org/0960-1317/17/i=5/a=R01?key=crossref.c24504191bbdbbc35f746483f719698a>
- [84] Y. Temiz, R. D. Lovchik, G. V. Kaigala and E. Delamarche, *Lab-on-a-chip devices: How to close and plug the lab?*, Microelectronic Engineering **132** (2015), pp. 156–175,  
URL: <http://linkinghub.elsevier.com/retrieve/pii/S0167931714004456>
- [85] D. Bartolo, G. Degré, P. Nghe and V. Studer, *Microfluidic stickers*, Lab Chip **8** (2008) (2), pp. 274–279,  
URL: <http://xlink.rsc.org/?DOI=B712368J>
- [86] R. Arayanarakool, S. Le Gac and A. van den Berg, *Low-temperature, simple and fast integration technique of microfluidic chips by using a UV-curable adhesive*, Lab on a Chip **10** (2010) (16), p. 2115,  
URL: <http://xlink.rsc.org/?DOI=c004436a>
- [87] E. P. Dupont, R. Luisier and M. A. Gijs, *NOA 63 as a UV-curable material for fabrication of microfluidic channels with native hydrophilicity*, Microelectronic Engineering **87** (2010) (5-8), pp. 1253–1255,  
URL: <http://linkinghub.elsevier.com/retrieve/pii/S0167931709007394>
- [88] A. T. Ciftlik and M. A. M. Gijs, *A low-temperature parylene-to-silicon dioxide bonding technique for high-pressure microfluidics*, Journal of Micromechanics and Microengineering **21** (2011) (3), p. 035011,  
URL: <http://stacks.iop.org/0960-1317/21/i=3/a=035011?key=crossref.0ee20486dd9104dee4f7d26f3ef02393>
- [89] A. T. Ciftlik and M. A. M. Gijs, *Parylene to silicon nitride bonding for post-integration of high pressure microfluidics to CMOS devices*, Lab Chip **12** (2012) (2), pp. 396–400,  
URL: <http://xlink.rsc.org/?DOI=C1LC20727J>
- [90] J. Kim, R. Surapaneni and B. K. Gale, *Rapid prototyping of microfluidic systems using a PDMS/polymer tape composite*, Lab on a Chip **9** (2009) (9), p. 1290,  
URL: <http://xlink.rsc.org/?DOI=b818389a>
- [91] A. W. Martinez, S. T. Phillips and G. M. Whitesides, *Three-dimensional microfluidic devices fabricated in layered paper and tape*, Proceedings of the National Academy of Sciences **105** (2008) (50), pp. 19606–19611,  
URL: <http://www.pnas.org/content/105/50/19606.short>
- [92] S. Zhao, H. Cong and T. Pan, *Direct projection on dry-film photoresist (DP2): do-it-yourself three-dimensional polymer microfluidics*, Lab on a Chip **9** (2009) (8), p. 1128,  
URL: <http://xlink.rsc.org/?DOI=b817925e>
- [93] P. Vulto, N. Glade, L. Altomare, J. Bablet, L. D. Tin, G. Medoro, I. Chartier, N. Manaresi, M. Tartagni and R. Guerrieri, *Microfluidic channel fabrication in dry film resist for production and prototyping of hybrid chips*, Lab on a Chip **5** (2005) (2), p. 158,  
URL: <http://xlink.rsc.org/?DOI=b411885e>

- [94] P. Abgrall, V. Conedera, H. Camon, A.-M. Gue and N.-T. Nguyen, *SU-8 as a structural material for labs-on-chips and microelectromechanical systems*, *ELECTROPHORESIS* **28** (2007) (24), pp. 4539–4551,  
URL: <http://doi.wiley.com/10.1002/elps.200700333>
- [95] L. Chang, D. Gallego-Perez, C.-L. Chiang, P. Bertani, T. Kuang, Y. Sheng, F. Chen, Z. Chen, J. Shi, H. Yang, X. Huang, V. Malkoc, W. Lu and L. J. Lee, *Controllable Large-Scale Transfection of Primary Mammalian Cardiomyocytes on a Nanochannel Array Platform*, *Small* **12** (2016) (43), pp. 5971–5980,  
URL: <http://doi.wiley.com/10.1002/smll.201601465>
- [96] A. M. Skelley, O. Kirak, H. Suh, R. Jaenisch and J. Voldman, *Microfluidic control of cell pairing and fusion*, *Nature Methods* **6** (2009) (2), pp. 147–152,  
URL: <http://www.nature.com/doifinder/10.1038/nmeth.1290>
- [97] R. J. Jackman, T. M. Floyd, R. Ghodssi, M. A. Schmidt and K. F. Jensen, *Microfluidic systems with on-line UV detection fabricated in photodefinable epoxy*, *Journal of Micromechanics and Microengineering* **11** (2001) (3), p. 263,  
URL: <http://stacks.iop.org/0960-1317/11/i=3/a=316>
- [98] S. Li, C. B. Freidhoff, R. M. Young and R. Ghodssi, *Fabrication of micronozzles using low-temperature wafer-level bonding with SU-8*, *Journal of Micromechanics and Microengineering* **13** (2003) (5), p. 732,  
URL: <http://iopscience.iop.org/article/10.1088/0960-1317/13/5/328/meta>
- [99] F. J. Blanco, M. Agirregabiria, J. Garcia, J. Berganzo, M. Tijero, M. T. Arroyo, J. M. Ruano, I. Aramburu and K. Mayora, *Novel three-dimensional embedded SU-8 microchannels fabricated using a low temperature full wafer adhesive bonding*, *Journal of Micromechanics and Microengineering* **14** (2004) (7), pp. 1047–1056,  
URL: <http://stacks.iop.org/0960-1317/14/i=7/a=027?key=crossref.88de949a705a1789c2551619d3e5fbc9>
- [100] S. Tuomikoski and S. Franssila, *Free-standing SU-8 microfluidic chips by adhesive bonding and release etching*, *Sensors and Actuators A: Physical* **120** (2005) (2), pp. 408–415,  
URL: <http://linkinghub.elsevier.com/retrieve/pii/S0924424705000348>
- [101] M. Agirregabiria, F. J. Blanco, J. Berganzo, M. T. Arroyo, A. Fullaondo, K. Mayora and J. M. Ruano-López, *Fabrication of SU-8 multilayer microstructures based on successive CMOS compatible adhesive bonding and releasing steps*, *Lab on a Chip* **5** (2005) (5), p. 545,  
URL: <http://xlink.rsc.org/?DOI=b500519a>
- [102] P. Abgrall, C. Lattes, V. Conédéra, X. Dollat, S. Colin and A. M. Gué, *A novel fabrication method of flexible and monolithic 3D microfluidic structures using lamination of SU-8 films*, *Journal of Micromechanics and Microengineering* **16** (2006) (1), p. 113,  
URL: <http://stacks.iop.org/0960-1317/16/i=1/a=016>
- [103] P. Abgrall, S. Charlot, R. Fulcrand, L. Paul, A. Boukabache and A.-M. Gué, *Low-stress fabrication of 3D polymer free standing structures using lamination of photosensitive films*, *Microsystem Technologies* **14** (2008) (8), pp. 1205–1214,  
URL: <http://link.springer.com/10.1007/s00542-008-0625-0>

- [104] C. Pang, Z. Zhao, L. Du and Z. Fang, *Adhesive bonding with SU-8 in a vacuum for capacitive pressure sensors*, *Sensors and Actuators A: Physical* **147** (2008) (2), pp. 672 – 676,  
URL: <http://www.sciencedirect.com/science/article/pii/S0924424708003087>
- [105] X. Wang, L. Ge, J. Lu, X. Li, K. Qiu, Y. Tian, S. Fu and Z. Cui, *Fabrication of enclosed nanofluidic channels by UV cured imprinting and optimized thermal bonding of SU-8 photoresist*, *Microelectronic Engineering* **86** (2009) (4-6), pp. 1347–1349,  
URL: <http://linkinghub.elsevier.com/retrieve/pii/S0167931709001087>
- [106] C. Aracil, F. Perdigones, J. M. Moreno and J. M. Quero, *BETTS: bonding, exposing and transferring technique in SU-8 for microsystems fabrication*, *Journal of Micromechanics and Microengineering* **20** (2010) (3), p. 035008,  
URL: <http://stacks.iop.org/0960-1317/20/i=3/a=035008?key=crossref.fd15d3b81c371c6373067e8b5cb6e67a>
- [107] R. C. Meier, V. Badilita, J. Brunne, U. Wallrabe and J. G. Korvink, *Complex three-dimensional high aspect ratio microfluidic network manufactured in combined PerMX dry-resist and SU-8 technology*, *Biomicrofluidics* **5** (2011) (3), p. 034111,  
URL: <http://aip.scitation.org/doi/10.1063/1.3613668>
- [108] E. Mitri, G. Birarda, L. Vaccari, S. Kenig, M. Tormen and G. Grenzi, *SU-8 bonding protocol for the fabrication of microfluidic devices dedicated to FTIR microspectroscopy of live cells*, *Lab Chip* **14** (2014) (1), pp. 210–218,  
URL: <http://xlink.rsc.org/?DOI=C3LC50878A>
- [109] R. S. Lima, P. A. G. C. Leão, M. H. O. Piazzetta, A. M. Monteiro, L. Y. Shiroma, A. L. Gobbi and E. Carrilho, *Sacrificial adhesive bonding: a powerful method for fabrication of glass microchips*, *Scientific Reports* **5** (2015), p. 13276,  
URL: <http://dx.doi.org/10.1038/srep13276>
- [110] B. Helbo, A. Kristensen and A. Menon, *A micro-cavity fluidic dye laser*, *Journal of Micromechanics and Microengineering* **13** (2003) (2), p. 307,  
URL: <http://iopscience.iop.org/article/10.1088/0960-1317/13/2/320/meta>
- [111] P. Svasek, E. Svasek, B. Lendl and M. Vellekoop, *Fabrication of miniaturized fluidic devices using SU-8 based lithography and low temperature wafer bonding*, *Sensors and Actuators A: Physical* **115** (2004) (23), pp. 591 – 599,  
URL: <http://www.sciencedirect.com/science/article/pii/S0924424704002389>

ANNOTATION: The 17th European Conference on Solid-State Transducers

- [112] J. El-Ali, I. Perch-Nielsen, C. Poulsen, D. Bang, P. Telleman and A. Wolff, *Simulation and experimental validation of a SU-8 based PCR thermocycler chip with integrated heaters and temperature sensor*, *Sensors and Actuators A: Physical* **110** (2004) (1-3), pp. 3–10,  
URL: <http://linkinghub.elsevier.com/retrieve/pii/S0924424703004710>
- [113] Y. Song, C. S. S. R. Kumar and J. Hormes, *Fabrication of an SU-8 based microfluidic reactor on a PEEK substrate sealed by a flexible semi-solid transfer (FST) process*,

- Journal of Micromechanics and Microengineering **14** (2004) (7), pp. 932–940,  
 URL: <http://stacks.iop.org/0960-1317/14/i=7/a=013?key=crossref.9e08f7c639cc98af097fcdcefa4a511d>
- [114] T. Sikanen, S. Tuomikoski, R. A. Ketola, R. Kostiainen, S. Franssila and T. Kotiaho, *Characterization of SU-8 for electrokinetic microfluidic applications*, Lab on a Chip **5** (2005) (8), p. 888,  
 URL: <http://xlink.rsc.org/?DOI=b503016a>
- [115] N.-C. Tsai and C.-Y. Sue, *SU-8 based continuous-flow RT-PCR bio-chips under high-precision temperature control*, Biosensors and Bioelectronics **22** (2006) (2), pp. 313–317,  
 URL: <http://linkinghub.elsevier.com/retrieve/pii/S0956566305004203>
- [116] M. Gersborg-Hansen and A. Kristensen, *Optofluidic third order distributed feedback dye laser*, Applied Physics Letters **89** (2006) (10), p. 103518,  
 URL: <http://aip.scitation.org/doi/10.1063/1.2345602>
- [117] J. Ruano-López, M. Aguirregabiria, M. Tijero, M. Arroyo, J. Elizalde, J. Berganzo, I. Aranburu, F. Blanco and K. Mayora, *A new SU-8 process to integrate buried waveguides and sealed microchannels for a Lab-on-a-Chip*, Sensors and Actuators B: Chemical **114** (2006) (1), pp. 542–551,  
 URL: <http://linkinghub.elsevier.com/retrieve/pii/S0925400505005125>
- [118] T. Sikanen, L. Heikkilä, S. Tuomikoski, R. A. Ketola, R. Kostiainen, S. Franssila and T. Kotiaho, *Performance of SU-8 Microchips as Separation Devices and Comparison with Glass Microchips*, Analytical Chemistry **79** (2007) (16), pp. 6255–6263,  
 URL: <http://pubs.acs.org/doi/abs/10.1021/ac0703956>
- [119] S. Arscott, *SU-8 as a material for lab-on-a-chip-based mass spectrometry*, Lab on a Chip **14** (2014) (19), p. 3668,  
 URL: <http://xlink.rsc.org/?DOI=C4LC00617H>
- [120] R. S. Lima, P. A. G. Carneiro Leão, A. M. Monteiro, M. H. de Oliveira Piazzetta, A. L. Gobbi, L. H. Mazo and E. Carrilho, *Glass/SU-8 microchip for electrokinetic applications: Microfluidics and Miniaturization*, ELECTROPHORESIS (2013), pp. n/a–n/a,  
 URL: <http://doi.wiley.com/10.1002/elps.201300167>
- [121] Z. Yin, E. Cheng and H. Zou, *A novel hybrid patterning technique for micro and nanochannel fabrication by integrating hot embossing and inverse UV photolithography*, Lab Chip **14** (2014) (9), pp. 1614–1621,  
 URL: <http://xlink.rsc.org/?DOI=C3LC51369F>
- [122] F. E. Tay, J. A. Van Kan, F. Watt and W. O. Choong, *A novel micro-machining method for the fabrication of thick-film SU-8 embedded micro-channels*, Journal of Micromechanics and Microengineering **11** (2001) (1), p. 27,  
 URL: <http://iopscience.iop.org/article/10.1088/0960-1317/11/1/305/meta>
- [123] Y.-J. Chuang, F.-G. Tseng, J.-H. Cheng and W.-K. Lin, *A novel fabrication method of embedded micro-channels by using SU-8 thick-film photoresists*, Sensors and Actuators A: Physical **103** (2003) (1), pp. 64–69,

- URL: <http://www.sciencedirect.com/science/article/pii/S0924424702003254>
- [124] C. Fu, C. Hung and H. Huang, *A novel and simple fabrication method of embedded SU-8 micro channels by direct UV lithography*, Journal of Physics: Conference Series **34** (2006), pp. 330–335,  
URL: <http://stacks.iop.org/1742-6596/34/i=1/a=054?key=crossref.ce9eccf766ac146ff2ea8cab98e9529>
- [125] D. M. Koller, N. Galler, H. Ditlbacher, A. Hohenau, A. Leitner, F. R. Aussenegg and J. R. Kren, *Direct fabrication of micro/nano fluidic channels by electron beam lithography*, Microelectronic Engineering **86** (2009) (4-6), pp. 1314–1316,  
URL: <http://linkinghub.elsevier.com/retrieve/pii/S0167931708005352>
- [126] Y.-T. Huang and W. Hsu, *Fabricating embedded SU-8 microstructures with asymmetric inside cross section by double-side multiple partial exposure method*, Microelectronic Engineering **121** (2014), pp. 64–67,  
URL: <http://linkinghub.elsevier.com/retrieve/pii/S0167931714000951>
- [127] C. Chung and M. Allen, *Uncrosslinked SU-8 as a sacrificial material*, Journal of Micromechanics and Microengineering **15** (2005) (1), pp. N1–N5,  
URL: <http://stacks.iop.org/0960-1317/15/i=1/a=N01?key=crossref.8e48761bac53edd5ee24c1c6f8738ecd>
- [128] I. G. Foulds, R. W. Johnstone and M. Parameswaran, *Polydimethylglutarimide (PMGI) as a sacrificial material for SU-8 surface-micromachining*, Journal of Micromechanics and Microengineering **18** (2008) (7), p. 075011,  
URL: <http://stacks.iop.org/0960-1317/18/i=7/a=075011?key=crossref.ee0ccedf4ac5cbd21f5ced09eb887955>
- [129] V. Martinez, P. Behr, U. Drechsler, J. Polesel-Maris, E. Potthoff, J. Vörös and T. Zambelli, *SU-8 hollow cantilevers for AFM cell adhesion studies*, Journal of Micromechanics and Microengineering **26** (2016) (5), p. 055006,  
URL: <http://stacks.iop.org/0960-1317/26/i=5/a=055006?key=crossref.7d0713d8c96d7f452ee5c9a79e5d13ff>
- [130] N. Wangler, L. Gutzweiler, K. Kalkandjiev, C. Müller, F. Mayenfels, H. Reinecke, R. Zengerle and N. Paust, *High-resolution permanent photoresist laminate TMMF for sealed microfluidic structures in biological applications*, Journal of Micromechanics and Microengineering **21** (2011) (9), p. 095009,  
URL: <http://stacks.iop.org/0960-1317/21/i=9/a=095009?key=crossref.d43d4b3612c97ce6c928dba9da1d3e28>
- [131] Q. Chen, G. Li, Q. H. Jin, J. L. Zhao, Q. S. Ren and Y. S. Xu, *A Rapid and Low-Cost Procedure for Fabrication of Glass Microfluidic Devices*, Journal of Microelectromechanical Systems **16** (2007) (5), pp. 1193–1200
- [132] J. R. Anderson, D. T. Chiu, H. Wu, O. J. Schueller and G. M. Whitesides, *Fabrication of microfluidic systems in poly (dimethylsiloxane)*, Electrophoresis **21** (2000) (1), pp. 27–40,

- URL: [https://www.researchgate.net/profile/Hongkai\\_Wu/publication/227935955\\_Fabrication\\_of\\_microfluidic\\_systems\\_in\\_polydimethylsiloxane/links/55800ca808aec87640df1c7f.pdf](https://www.researchgate.net/profile/Hongkai_Wu/publication/227935955_Fabrication_of_microfluidic_systems_in_polydimethylsiloxane/links/55800ca808aec87640df1c7f.pdf)
- [133] S. K. Sia and G. M. Whitesides, *Microfluidic devices fabricated in Poly(dimethylsiloxane) for biological studies*, *ELECTROPHORESIS* **24** (2003) (21), pp. 3563–3576,  
URL: <http://doi.wiley.com/10.1002/elps.200305584>
- [134] T. Gervais, J. El-Ali, A. Günther and K. F. Jensen, *Flow-induced deformation of shallow microfluidic channels*, *Lab on a Chip* **6** (2006) (4), p. 500,  
URL: <http://xlink.rsc.org/?DOI=b513524a>
- [135] D. Qin, Y. Xia and G. M. Whitesides, *Soft lithography for micro- and nanoscale patterning*, *Nature Protocols* **5** (2010) (3), pp. 491–502,  
URL: <http://www.nature.com/doifinder/10.1038/nprot.2009.234>
- [136] J. Friend and L. Yeo, *Fabrication of microfluidic devices using polydimethylsiloxane*, *Biomicrofluidics* **4** (2010) (2), p. 026502,  
URL: <http://aip.scitation.org/doi/10.1063/1.3259624>
- [137] C. De Marco, S. Girardo, E. Mele, R. Cingolani and D. Pisignano, *Ultraviolet-based bonding for perfluoropolyether low aspect-ratio microchannels and hybrid devices*, *Lab on a Chip* **8** (2008) (8), p. 1394,  
URL: <http://xlink.rsc.org/?DOI=b803243b>
- [138] J. R. Smith, I. G. Arcibal, A. Polini, M. R. Dokmeci and A. Khademhosseini, *Research highlights*, *Lab Chip* **14** (2014) (1), pp. 157–160,  
URL: <http://xlink.rsc.org/?DOI=C3LC90120C>
- [139] E. Sollier, C. Murray, P. Maoddi and D. Di Carlo, *Rapid prototyping polymers for microfluidic devices and high pressure injections*, *Lab on a Chip* **11** (2011) (22), p. 3752,  
URL: <http://xlink.rsc.org/?DOI=c11c20514e>
- [140] F. Walther, P. Davydovskaya, S. Zürcher, M. Kaiser, H. Herberg, A. M. Gigler and R. W. Stark, *Stability of the hydrophilic behavior of oxygen plasma activated SU-8*, *Journal of Micromechanics and Microengineering* **17** (2007) (3), pp. 524–531,  
URL: <http://stacks.iop.org/0960-1317/17/i=3/a=015?key=crossref.69e6bd867608071b001b2268de5b2f49>
- [141] M. Nordström, R. Marie, M. Calleja and A. Boisen, *Rendering SU-8 hydrophilic to facilitate use in micro channel fabrication*, *Journal of Micromechanics and Microengineering* **14** (2004) (12), pp. 1614–1617,  
URL: <http://stacks.iop.org/0960-1317/14/i=12/a=003?key=crossref.f6a72554406cddc5044f16aa4a56f136>
- [142] A. Sobiesierski, R. Thomas, P. Buckle, D. Barrow and P. M. Smowton, *A two-stage surface treatment for the long-term stability of hydrophilic SU-8: Two-stage treatment for long-term stability of hydrophilic SU-8*, *Surface and Interface Analysis* **47** (2015) (13), pp. 1174–1179,  
URL: <http://doi.wiley.com/10.1002/sia.5870>

- [143] F. Walther, T. Drobek, A. M. Gigler, M. Hennemeyer, M. Kaiser, H. Herberg, T. Shimitsu, G. E. Morfill and R. W. Stark, *Surface hydrophilization of SU-8 by plasma and wet chemical processes*, *Surface and Interface Analysis* **42** (2010) (12-13), pp. 1735–1744, URL: <http://doi.wiley.com/10.1002/sia.3515>
- [144] M. A. Unger, H.-P. Chou, T. Thorsen, A. Scherer and S. R. Quake, *Monolithic micro-fabricated valves and pumps by multilayer soft lithography*, *Science* **288** (2000) (5463), pp. 113–116, URL: <http://science.sciencemag.org/content/288/5463/113.short>
- [145] D. Huh, K. L. Mills, X. Zhu, M. A. Burns, M. D. Thouless and S. Takayama, *Tuneable elastomeric nanochannels for nanofluidic manipulation*, *Nature Materials* **6** (2007) (6), pp. 424–428, URL: <http://www.nature.com/doifinder/10.1038/nmat1907>
- [146] K. R. Rajagopal, *On the nonlinear elastic response of bodies in the small strain range*, *Acta Mechanica* **225** (2014) (6), pp. 1545–1553, URL: <http://link.springer.com/10.1007/s00707-013-1015-y>
- [147] S. Gupta, M. Dixit, K. Sharma and N. Saxena, *Mechanical study of metallized polyethylene terephthalate (PET) films*, *Surface and Coatings Technology* **204** (2009) (5), pp. 661–666, URL: <http://linkinghub.elsevier.com/retrieve/pii/S0257897209006859>
- [148] J. Carlier, S. Arscott, V. Thomy, J. C. Fourrier, F. Caron, J. C. Camart, C. Druon and P. Tabourier, *Integrated microfluidics based on multi-layered SU-8 for mass spectrometry analysis*, *Journal of micromechanics and Microengineering* **14** (2004) (4), p. 619, URL: <http://iopscience.iop.org/article/10.1088/0960-1317/14/4/024/meta>
- [149] F. Malloggi, N. Pannacci, R. Attia, F. Monti, P. Mary, H. Willaime, P. Tabeling, B. Cabane and P. Poncet, *Monodisperse Colloids Synthesized with Nanofluidic Technology*, *Langmuir* **26** (2010) (4), pp. 2369–2373, URL: <http://pubs.acs.org/doi/abs/10.1021/la9028047>
- [150] L. Shui, A. van den Berg and J. C. T. Eijkel, *Scalable attoliter monodisperse droplet formation using multiphase nano-microfluidics*, *Microfluidics and Nanofluidics* **11** (2011) (1), pp. 87–92, URL: <http://link.springer.com/10.1007/s10404-011-0776-7>
- [151] A. R. Abate, M. B. Romanowsky, J. J. Agresti and D. A. Weitz, *Valve-based flow focusing for drop formation*, *Applied Physics Letters* **94** (2009) (2), p. 023503, URL: <http://aip.scitation.org/doi/10.1063/1.3067862>
- [152] T. Gerhardt, S. Woo and H. Ma, *Chromatographic behaviour of single cells in a microchannel with dynamic geometry*, *Lab on a Chip* **11** (2011) (16), p. 2731, URL: <http://xlink.rsc.org/?DOI=c11c20092e>
- [153] S.-B. Huang, Y. Zhao, D. Chen, H.-C. Lee, Y. Luo, T.-K. Chiu, J. Wang, J. Chen and M.-H. Wu, *A clogging-free microfluidic platform with an incorporated pneumatically*

- driven membrane-based active valve enabling specific membrane capacitance and cytoplasm conductivity characterization of single cells*, Sensors and Actuators B: Chemical **190** (2014), pp. 928–936,  
URL: <http://linkinghub.elsevier.com/retrieve/pii/S0925400513011118>
- [154] P. Cheung, K. Toda-Peters and A. Q. Shen, *In situ pressure measurement within deformable rectangular polydimethylsiloxane microfluidic devices*, Biomicrofluidics **6** (2012) (2), p. 026501,  
URL: <http://aip.scitation.org/doi/10.1063/1.4720394>
- [155] O. Ozsun, V. Yakhot and K. L. Ekinici, *Non-invasive measurement of the pressure distribution in a deformable micro-channel*, Journal of Fluid Mechanics **734** (2013),  
URL: [http://www.journals.cambridge.org/abstract\\_S0022112013004746](http://www.journals.cambridge.org/abstract_S0022112013004746)
- [156] E. Seker, D. C. Leslie, H. Haj-Hariri, J. P. Landers, M. Utz and M. R. Begley, *Nonlinear pressure-flow relationships for passive microfluidic valves*, Lab on a Chip **9** (2009) (18), p. 2691,  
URL: <http://xlink.rsc.org/?DOI=b903960k>
- [157] B. S. Hardy, K. Uechi, J. Zhen and H. Pirouz Kavehpour, *The deformation of flexible PDMS microchannels under a pressure driven flow*, Lab Chip **9** (2009) (7), pp. 935–938,  
URL: <http://xlink.rsc.org/?DOI=B813061B>
- [158] C. Kang, C. Roh and R. A. Overfelt, *Pressure-driven deformation with soft polydimethylsiloxane (PDMS) by a regular syringe pump: challenge to the classical fluid dynamics by comparison of experimental and theoretical results*, RSC Advances **4** (2014) (7), pp. 3102–3112
- [159] R. Neelamegam and V. Shankar, *Experimental study of the instability of laminar flow in a tube with deformable walls*, Physics of Fluids **27** (2015) (2), p. 024102,  
URL: <http://aip.scitation.org/doi/10.1063/1.4907246>
- [160] M. K. Raj, S. DasGupta and S. Chakraborty, *Hydrodynamics in deformable microchannels*, Microfluidics and Nanofluidics **21** (2017) (4),  
URL: <http://link.springer.com/10.1007/s10404-017-1908-5>
- [161] D. Chakraborty, J. R. Prakash, J. Friend and L. Yeo, *Fluid-structure interaction in deformable microchannels*, Physics of Fluids **24** (2012) (10), p. 102002,  
URL: <http://aip.scitation.org/doi/10.1063/1.4759493>
- [162] T. C. Shidhore and I. C. Christov, *Static response of deformable microchannels: a comparative modelling study*, Journal of Physics: Condensed Matter **30** (2018) (5), p. 054002,  
URL: <http://stacks.iop.org/0953-8984/30/i=5/a=054002>
- [163] A. Raj and A. K. Sen, *Flow-induced deformation of compliant microchannels and its effect on pressureflow characteristics*, Microfluidics and Nanofluidics **20** (2016) (2),  
URL: <http://link.springer.com/10.1007/s10404-016-1702-9>
- [164] A. Mehboudi and J. Yeom, *A two-step sealing-and-reinforcement SU8 bonding paradigm for the fabrication of shallow microchannels*, Journal of Micromechanics and Microengineering **28** (2018) (3), p. 035002,  
URL: <http://stacks.iop.org/0960-1317/28/i=3/a=035002>

- [165] J. M. Gere, *Mechanics of materials*, 6th ed ed. (Brooks/Cole-Thomas Learning, Belmont, CA, 2004)
- [166] C. Luo, T. W. Schneider, R. C. White, J. Currie and M. Paranjape, *A simple deflection-testing method to determine Poisson's ratio for MEMS applications*, Journal of Micromechanics and Microengineering **13** (2003) (1), pp. 129–133,  
URL: <http://stacks.iop.org/0960-1317/13/i=1/a=318?key=crossref.81166d0e06484fabd83d63f992861edc>
- [167] B. Mosadegh, C.-H. Kuo, Y.-C. Tung, Y.-s. Torisawa, T. Bersano-Begey, H. Tavana and S. Takayama, *Integrated elastomeric components for autonomous regulation of sequential and oscillatory flow switching in microfluidic devices*, Nature Physics **6** (2010) (6), pp. 433–437,  
URL: <https://www.nature.com/articles/nphys1637>
- [168] J. A. Weaver, J. Melin, D. Stark, S. R. Quake and M. A. Horowitz, *Static control logic for microfluidic devices using pressure-gain valves*, Nature Physics **6** (2010) (3), pp. 218–223,  
URL: <http://www.nature.com/articles/nphys1513>
- [169] B. Mosadegh, T. Bersano-Begey, J. Y. Park, M. A. Burns and S. Takayama, *Next-generation integrated microfluidic circuits*, Lab on a Chip **11** (2011) (17), p. 2813,  
URL: <http://xlink.rsc.org/?DOI=c11c20387h>
- [170] E. Stemme and G. Stemme, *A valveless diffuser/nozzle-based fluid pump*, Sensors and Actuators A **39** (1993), pp. 159–167
- [171] A. Olsson, P. Enoksson, G. Stemme and E. Stemme, *Micromachined flat-walled valveless diffuser pumps*, Journal of microelectromechanical systems **6** (1997) (2), pp. 161–166
- [172] F. Amirouche, Y. Zhou and T. Johnson, *Current micropump technologies and their biomedical applications*, Microsystem Technologies **15** (2009) (5), pp. 647–666,  
URL: <http://link.springer.com/10.1007/s00542-009-0804-7>
- [173] A. Nisar, N. Afzulpurkar, B. Mahaisavariya and A. Tuantranont, *MEMS-based micropumps in drug delivery and biomedical applications*, Sensors and Actuators B: Chemical **130** (2008) (2), pp. 917–942,  
URL: <http://linkinghub.elsevier.com/retrieve/pii/S0925400507009148>
- [174] D. Eddington, *Flow control with hydrogels*, Advanced Drug Delivery Reviews **56** (2004) (2), pp. 199–210,  
URL: <http://linkinghub.elsevier.com/retrieve/pii/S0169409X03001947>
- [175] V. Tandon, W. S. Kang, T. A. Robbins, A. J. Spencer, E. S. Kim, M. J. McKenna, S. G. Kujawa, J. Fiering, E. E. L. Pararas, M. J. Mescher, W. F. Sewell and J. T. Borenstein, *Microfabricated reciprocating micropump for intracochlear drug delivery with integrated drug/fluid storage and electronically controlled dosing*, Lab on a Chip **16** (2016) (5), pp. 829–846,  
URL: <http://xlink.rsc.org/?DOI=C5LC01396H>

- [176] A. Groisman, M. Enzelberger and S. R. Quake, *Microfluidic Memory and Control Devices*, *Science* **300** (2003) (5621), pp. 955–958,  
URL: <http://science.sciencemag.org/content/300/5621/955>
- [177] A. Groisman and S. R. Quake, *A Microfluidic Rectifier: Anisotropic Flow Resistance at Low Reynolds Numbers*, *Physical Review Letters* **92** (2004) (9), p. 094501,  
URL: <https://link.aps.org/doi/10.1103/PhysRevLett.92.094501>
- [178] N.-T. Nguyen, Y.-C. Lam, S.-S. Ho and C. L.-N. Low, *Improvement of rectification effects in diffuser/nozzle structures with viscoelastic fluids*, *Biomicrofluidics* **2** (2008) (3), p. 034101,  
URL: <http://aip.scitation.org/doi/10.1063/1.2959099>
- [179] P. Sousa, F. Pinho, M. Oliveira and M. Alves, *Efficient microfluidic rectifiers for viscoelastic fluid flow*, *Journal of Non-Newtonian Fluid Mechanics* **165** (2010) (11-12), pp. 652–671,  
URL: <http://linkinghub.elsevier.com/retrieve/pii/S0377025710000911>
- [180] M. L. Adams, M. L. Johnston, A. Scherer and S. R. Quake, *Polydimethylsiloxane based microfluidic diode*, *Journal of Micromechanics and Microengineering* **15** (2005) (8), pp. 1517–1521,  
URL: <http://stacks.iop.org/0960-1317/15/i=8/a=020?key=crossref.821ea1ad1c6aa5b8952d6e99ea6a5880>
- [181] J. J. Loverich, I. Kanno and H. Kotera, *Concepts for a new class of all-polymer micropumps*, *Lab on a Chip* **6** (2006) (9), p. 1147,  
URL: <http://xlink.rsc.org/?DOI=b605525g>
- [182] J. Loverich, I. Kanno and H. Kotera, *Single-step replicable microfluidic check valve for rectifying and sensing low Reynolds number flow*, *Microfluidics and Nanofluidics* **3** (2007) (4), pp. 427–435,  
URL: <http://link.springer.com/10.1007/s10404-006-0127-2>
- [183] T. Pan, S. J. McDonald, E. M. Kai and B. Ziaie, *A magnetically driven PDMS micropump with ball check-valves*, *Journal of Micromechanics and Microengineering* **15** (2005) (5), pp. 1021–1026,  
URL: <http://stacks.iop.org/0960-1317/15/i=5/a=018?key=crossref.8de0785abff67a47908c70de53a80100>
- [184] K. Ou, J. Jackson, H. Burt and M. Chiao, *Microspheres as resistive elements in a check valve for low pressure and low flow rate conditions*, *Lab on a Chip* **12** (2012) (21), pp. 4372–4380
- [185] R. D. Sochol, A. Lu, J. Lei, K. Iwai, L. P. Lee and L. Lin, *Microfluidic bead-based diodes with targeted circular microchannels for low Reynolds number applications*, *Lab Chip* **14** (2014) (9), pp. 1585–1594,  
URL: <http://xlink.rsc.org/?DOI=C3LC51069G>
- [186] R. J. Roark, W. C. Young and R. G. Budynas, *Roark's formulas for stress and strain*, 7th ed ed. (McGraw-Hill, New York, 2002)

ANNOTATION: Originally published under title: Formulas for stress and strain

- [187] A. Mehboudi and J. Yeom, *Experimental and theoretical investigation of a low-Reynolds-number flow through deformable shallow microchannels with ultra-low height-to-width aspect ratios*, arXiv:1809.04868 [physics.flu-dyn] (2018),  
URL: <https://arxiv.org/abs/1809.04868>
- [188] J. Liu, N. K. Gupta, K. D. Wise, Y. B. Gianchandani and X. Fan, *Demonstration of motionless Knudsen pump based micro-gas chromatography featuring micro-fabricated columns and on-column detectors*, Lab on a Chip **11** (2011) (20), p. 3487,  
URL: <http://xlink.rsc.org/?DOI=c11c20511k>
- [189] Y. Qin and Y. B. Gianchandani, *iGC2 : an architecture for micro gas chromatographs utilizing integrated bi-directional pumps and multi-stage preconcentrators*, Journal of Micromechanics and Microengineering **24** (2014) (6), p. 065011,  
URL: <http://stacks.iop.org/0960-1317/24/i=6/a=065011?key=crossref.18fd2b034e57ec2d40b90a53eb4552e4>
- [190] L. Szalmás, T. Veltzke and J. Thöming, *Analysis of the diodic effect of flows of rarefied gases in tapered rectangular channels*, Vacuum **120** (2015), pp. 147–154,  
URL: <http://linkinghub.elsevier.com/retrieve/pii/S0042207X15300038>
- [191] I. Graur, T. Veltzke, J. G. Méolans, M. T. Ho and J. Thöming, *The gas flow diode effect: theoretical and experimental analysis of moderately rarefied gas flows through a microchannel with varying cross section*, Microfluidics and Nanofluidics **18** (2015) (3), pp. 391–402,  
URL: <http://link.springer.com/10.1007/s10404-014-1445-4>
- [192] A. Günther, S. A. Khan, M. Thalmann, F. Trachsel and K. F. Jensen, *Transport and reaction in microscale segmented gasliquid flow*, Lab Chip **4** (2004) (4), pp. 278–286,  
URL: <http://xlink.rsc.org/?DOI=B403982C>
- [193] V. Sebastian Cabeza, S. Kuhn, A. A. Kulkarni and K. F. Jensen, *Size-Controlled Flow Synthesis of Gold Nanoparticles Using a Segmented Flow Microfluidic Platform*, Langmuir **28** (2012) (17), pp. 7007–7013,  
URL: <http://pubs.acs.org/doi/10.1021/la205131e>
- [194] A. Larrea, V. Sebastian, A. Ibarra, M. Arruebo and J. Santamaria, *Gas Slug Microfluidics: A Unique Tool for Ultrafast, Highly Controlled Growth of Iron Oxide Nanostructures*, Chemistry of Materials **27** (2015) (12), pp. 4254–4260,  
URL: <http://pubs.acs.org/doi/10.1021/acs.chemmater.5b00284>
- [195] A. Grattoni, E. De Rosa, S. Ferrati, Z. Wang, A. Giancesini, X. Liu, F. Hussain, R. Goodall and M. Ferrari, *Analysis of a nanochanneled membrane structure through convective gas flow*, Journal of Micromechanics and Microengineering **19** (2009) (11), p. 115018,  
URL: <http://stacks.iop.org/0960-1317/19/i=11/a=115018?key=crossref.310247d632ebf83b8fa8d8d4f003fd81>
- [196] Y. Zohar, S. Y. K. Lee, W. Y. Lee, L. Jiang and P. Tong, *Subsonic gas flow in a straight and uniform microchannel*, Journal of Fluid Mechanics **472** (2002),  
URL: [http://www.journals.cambridge.org/abstract\\_S0022112002002203](http://www.journals.cambridge.org/abstract_S0022112002002203)

- [197] Y. Asako, T. Pi, S. E. Turner and M. Faghri, *Effect of compressibility on gaseous flows in micro-channels*, International Journal of Heat and Mass Transfer **46** (2003) (16), pp. 3041–3050,  
URL: <http://linkinghub.elsevier.com/retrieve/pii/S0017931003000747>
- [198] S. Roy, R. Raju, H. F. Chuang, B. A. Cruden and M. Meyyappan, *Modeling gas flow through microchannels and nanopores*, Journal of Applied Physics **93** (2003) (8), pp. 4870–4879,  
URL: <http://aip.scitation.org/doi/10.1063/1.1559936>
- [199] G. Hetsroni, A. Mosyak, E. Pogrebnyak and L. Yarin, *Fluid flow in micro-channels*, International Journal of Heat and Mass Transfer **48** (2005) (10), pp. 1982–1998,  
URL: <http://linkinghub.elsevier.com/retrieve/pii/S0017931005000244>
- [200] D. C. Venerus, *Laminar capillary flow of compressible viscous fluids*, Journal of Fluid Mechanics **555** (2006), p. 59,  
URL: [http://www.journals.cambridge.org/abstract\\_S0022112006008755](http://www.journals.cambridge.org/abstract_S0022112006008755)
- [201] F.-H. Qin, D.-J. Sun and X.-Y. Yin, *Perturbation analysis on gas flow in a straight microchannel*, Physics of Fluids **19** (2007) (2), p. 027103,  
URL: <http://aip.scitation.org/doi/10.1063/1.2564671>
- [202] E. G. Taliadorou, M. Neophytou and G. C. Georgiou, *Perturbation solutions of Poiseuille flows of weakly compressible Newtonian liquids*, Journal of Non-Newtonian Fluid Mechanics **163** (2009) (1-3), pp. 25–34,  
URL: <http://linkinghub.elsevier.com/retrieve/pii/S0377025709001360>
- [203] N. Dongari, A. Sharma and F. Durst, *Pressure-driven diffusive gas flows in micro-channels: from the Knudsen to the continuum regimes*, Microfluidics and Nanofluidics **6** (2009) (5), pp. 679–692,  
URL: <http://link.springer.com/10.1007/s10404-008-0344-y>
- [204] D. C. Venerus and D. J. Bugajsky, *Compressible laminar flow in a channel*, Physics of Fluids **22** (2010) (4), p. 046101,  
URL: <http://aip.scitation.org/doi/10.1063/1.3371719>
- [205] M. Torrilhon, *Modeling Nonequilibrium Gas Flow Based on Moment Equations*, Annual Review of Fluid Mechanics **48** (2016) (1), pp. 429–458,  
URL: <http://www.annualreviews.org/doi/10.1146/annurev-fluid-122414-034259>
- [206] S. E. Turner, L. C. Lam, M. Faghri and O. J. Gregory, *Experimental Investigation of Gas Flow in Microchannels*, Journal of Heat Transfer **126** (2004) (5), p. 753,  
URL: <http://HeatTransfer.asmedigitalcollection.asme.org/article.aspx?articleid=1447435>
- [207] M. Kohl, S. Abdel-Khalik, S. Jeter and D. Sadowski, *An experimental investigation of microchannel flow with internal pressure measurements*, International Journal of Heat and Mass Transfer **48** (2005) (8), pp. 1518–1533,  
URL: <http://linkinghub.elsevier.com/retrieve/pii/S0017931004005253>

- [208] N. D. Stevanovic, *A new analytical solution of microchannel gas flow*, Journal of Micromechanics and Microengineering **17** (2007) (8), pp. 1695–1702,  
URL: <http://stacks.iop.org/0960-1317/17/i=8/a=036?key=crossref.509b58e92ef46d2ca90db4f07b817a00>
- [209] I. Graur, J. G. Méolans, P. Perrier, J. Thöming and T. Veltzke, *A physical explanation of the gas flow diode effect*, Microfluidics and Nanofluidics **20** (2016) (10),  
URL: <http://link.springer.com/10.1007/s10404-016-1809-z>
- [210] V. Hemadri, V. V. Varade, A. Agrawal and U. V. Bhandarkar, *Investigation of rarefied gas flow in microchannels of non-uniform cross section*, Physics of Fluids **28** (2016) (2), p. 022007,  
URL: <http://aip.scitation.org/doi/10.1063/1.4942183>
- [211] S. Colin, *Rarefaction and compressibility effects on steady and transient gas flows in microchannels*, Microfluidics and Nanofluidics **1** (2005) (3), pp. 268–279,  
URL: <http://link.springer.com/10.1007/s10404-004-0002-y>
- [212] K. P. Chen and D. Shen, *Drainage flow of a viscous compressible fluid from a small capillary with a sealed end*, Journal of Fluid Mechanics **839** (2018), pp. 621–643,  
URL: [https://www.cambridge.org/core/product/identifier/S0022112018000563/type/journal\\_article](https://www.cambridge.org/core/product/identifier/S0022112018000563/type/journal_article)
- [213] Y. Zhao, G. Chen, C. Ye and Q. Yuan, *Gas-liquid two-phase flow in microchannel at elevated pressure*, Chemical Engineering Science **87** (2013), pp. 122–132,  
URL: <http://linkinghub.elsevier.com/retrieve/pii/S0009250912006069>
- [214] C. Yao, Z. Dong, Y. Zhao and G. Chen, *Gas-liquid flow and mass transfer in a microchannel under elevated pressures*, Chemical Engineering Science **123** (2015), pp. 137–145,  
URL: <http://linkinghub.elsevier.com/retrieve/pii/S0009250914006290>
- [215] S. Wu, J. Mai, Y. Zohar, Y. Tai and C. Ho, *A suspended microchannel with integrated temperature sensors for high-pressure flow studies* (IEEE, 1998), pp. 87–92,  
URL: <http://ieeexplore.ieee.org/document/659734/>
- [216] G. E. Karniadakis and A. Beskok, *Micro Flows: Fundamentals and Simulation* (New York: Springer, 2001)
- [217] A. Mehboudi and J. Yeom, *A one-dimensional model for compressible fluid flows through deformable microchannels*, Physics of Fluids **30** (2018) (9), p. 092003,  
URL: <https://doi.org/10.1063/1.5043202>
- [218] M. Gomez, D. E. Moulton and D. Vella, *Passive Control of Viscous Flow via Elastic Snap-Through*, Physical Review Letters **119** (2017) (14), p. 144502,  
URL: <https://link.aps.org/doi/10.1103/PhysRevLett.119.144502>
- [219] V. Glisin, R. Crkvenjakov and C. Byus, *Ribonucleic acid isolated by cesium chloride centrifugation*, Biochemistry **13** (1974) (12), pp. 2633–2637
- [220] M. Madou, J. Zoval, G. Jia, H. Kido, J. Kim and N. Kim, *Lab on a Cd*, Annual Review of Biomedical Engineering **8** (2006) (1), pp. 601–628,  
URL: <https://doi.org/10.1146/annurev.bioeng.8.061505.095758>

- [221] J. C. Yeo, Z. Wang and C. T. Lim, *Microfluidic size separation of cells and particles using a swinging bucket centrifuge*, *Biomicrofluidics* **9** (2015) (5), p. 054114, URL: <http://aip.scitation.org/doi/10.1063/1.4931953>
- [222] H. C. Kim, J. Park, Y. Cho, H. Park, A. Han and X. Cheng, *Lateral-flow particle filtration and separation with multilayer microfluidic channels*, *Journal of Vacuum Science & Technology B: Microelectronics and Nanometer Structures* **27** (2009) (6), p. 3115, URL: <http://scitation.aip.org/content/avs/journal/jvstb/27/6/10.1116/1.3258155>
- [223] W. Chen, N.-T. Huang, B. Oh, R. H. W. Lam, R. Fan, T. T. Cornell, T. P. Shanley, K. Kurabayashi and J. Fu, *Surface-Micromachined Microfiltration Membranes for Efficient Isolation and Functional Immunophenotyping of Subpopulations of Immune Cells*, *Advanced Healthcare Materials* **2** (2013) (7), pp. 965–975, URL: <http://doi.wiley.com/10.1002/adhm.201200378>
- [224] S. C. Gifford, A. M. Spillane, S. M. Vignes and S. S. Shevkoplyas, *Controlled incremental filtration: a simplified approach to design and fabrication of high-throughput microfluidic devices for selective enrichment of particles*, *Lab Chip* **14** (2014) (23), pp. 4496–4505, URL: <http://xlink.rsc.org/?DOI=C4LC00785A>
- [225] C.-L. Chang, W. Huang, S. I. Jalal, B.-D. Chan, A. Mahmood, S. Shahda, B. H. O’Neil, D. E. Matei and C. A. Savran, *Circulating tumor cell detection using a parallel flow micro-aperture chip system*, *Lab Chip* **15** (2015) (7), pp. 1677–1688, URL: <http://xlink.rsc.org/?DOI=C5LC00100E>
- [226] T. Leïchl e and D. Bourrier, *Integration of lateral porous silicon membranes into planar microfluidics*, *Lab Chip* **15** (2015) (3), pp. 833–838, URL: <http://xlink.rsc.org/?DOI=C4LC01094A>
- [227] J.-N. Kuo and Y.-H. Zhan, *Microfluidic chip for rapid and automatic extraction of plasma from whole human blood*, *Microsystem Technologies* **21** (2015) (1), pp. 255–261, URL: <http://link.springer.com/10.1007/s00542-013-2048-9>
- [228] X. Fan, C. Jia, J. Yang, G. Li, H. Mao, Q. Jin and J. Zhao, *A microfluidic chip integrated with a high-density PDMS-based microfiltration membrane for rapid isolation and detection of circulating tumor cells*, *Biosensors and Bioelectronics* **71** (2015), pp. 380–386, URL: <http://linkinghub.elsevier.com/retrieve/pii/S0956566315300816>
- [229] S. Torino, M. Iodice, I. Rendina, G. Coppola and E. Schonbrun, *Hydrodynamic self-focusing in a parallel microfluidic device through cross-filtration*, *Biomicrofluidics* **9** (2015) (6), p. 064107, URL: <http://aip.scitation.org/doi/10.1063/1.4936260>
- [230] M. Bassu, P. Holik, S. Schmitz, S. Steltenkamp and T. P. Burg, *Continuous high throughput nanofluidic separation through tangential-flow vertical nanoslit arrays*, *Lab Chip* **16** (2016) (23), pp. 4546–4553, URL: <http://xlink.rsc.org/?DOI=C6LC01089J>

- [231] H. Wei, B.-h. Chueh, H. Wu, E. W. Hall, C.-w. Li, R. Schirhagl, J.-M. Lin and R. N. Zare, *Particle sorting using a porous membrane in a microfluidic device*, *Lab Chip* **11** (2011) (2), pp. 238–245,  
URL: <http://xlink.rsc.org/?DOI=C0LC00121J>
- [232] S. M. McFaul, B. K. Lin and H. Ma, *Cell separation based on size and deformability using microfluidic funnel ratchets*, *Lab on a Chip* **12** (2012) (13), p. 2369,  
URL: <http://xlink.rsc.org/?DOI=c21c21045b>
- [233] Z. Wang, H.-j. Wu, D. Fine, J. Schmulen, Y. Hu, B. Godin, J. X. J. Zhang and X. Liu, *Ciliated micropillars for the microfluidic-based isolation of nanoscale lipid vesicles*, *Lab on a Chip* **13** (2013) (15), p. 2879,  
URL: <http://xlink.rsc.org/?DOI=c31c41343h>
- [234] I. S. Ngene, R. G. Lammertink, M. Wessling and W. van der Meer, *A microfluidic membrane chip for in situ fouling characterization*, *Journal of Membrane Science* **346** (2010) (1), pp. 202–207,  
URL: <http://linkinghub.elsevier.com/retrieve/pii/S0376738809006929>
- [235] M. E. Warkiani, F. Wicaksana, A. G. Fane and H.-Q. Gong, *Investigation of membrane fouling at the microscale using isopore filters*, *Microfluidics and Nanofluidics* **19** (2015) (2), pp. 307–315,  
URL: <http://link.springer.com/10.1007/s10404-014-1538-0>
- [236] H. Di, G. J. Martin and D. E. Dunstan, *A microfluidic system for studying particle deposition during ultrafiltration*, *Journal of Membrane Science* **532** (2017), pp. 68–75,  
URL: <http://linkinghub.elsevier.com/retrieve/pii/S0376738816320762>
- [237] K. Loutharback, J. D’Silva, L. Liu, A. Wu, R. H. Austin and J. C. Sturm, *Deterministic separation of cancer cells from blood at 10 mL/min*, *AIP Advances* **2** (2012) (4), p. 042107,  
URL: <http://aip.scitation.org/doi/10.1063/1.4758131>
- [238] N. Watkins, B. M. Venkatesan, M. Toner, W. Rodriguez and R. Bashir, *A robust electrical microcytometer with 3-dimensional hydrofocusing*, *Lab on a Chip* **9** (2009) (22), p. 3177,  
URL: <http://xlink.rsc.org/?DOI=b912214a>
- [239] Y.-Y. Chiu, C.-K. Huang and Y.-W. Lu, *Enhancement of microfluidic particle separation using cross-flow filters with hydrodynamic focusing*, *Biomicrofluidics* **10** (2016) (1), p. 011906,  
URL: <http://aip.scitation.org/doi/abs/10.1063/1.4939944>
- [240] S.-C. Lin, Y.-L. Sung, C.-C. Peng, Y.-C. Tung and C.-T. Lin, *An in-situ filtering pump for particle-sample filtration based on low-voltage electrokinetic mechanism*, *Sensors and Actuators B: Chemical* **238** (2017), pp. 809–816,  
URL: <http://linkinghub.elsevier.com/retrieve/pii/S0925400516311959>
- [241] S. Kim, S. Han and J. Lee, *Asymmetric bead aggregation for microfluidic immunodetection*, *Lab Chip* **17** (2017) (12), pp. 2095–2103,  
URL: <http://xlink.rsc.org/?DOI=C7LC00138J>

- [242] Y. Zhou, L. Song, L. Yu and X. Xuan, *Inertially focused diamagnetic particle separation in ferrofluids*, *Microfluidics and Nanofluidics* **21** (2017) (1),  
URL: <http://link.springer.com/10.1007/s10404-016-1839-6>
- [243] X. Ding, P. Li, S.-C. S. Lin, Z. S. Stratton, N. Nama, F. Guo, D. Slotcavage, X. Mao, J. Shi, F. Costanzo and T. J. Huang, *Surface acoustic wave microfluidics*, *Lab on a Chip* **13** (2013) (18), p. 3626,  
URL: <http://xlink.rsc.org/?DOI=c31c50361e>
- [244] Z. Ma, D. J. Collins and Y. Ai, *Single-actuator Bandpass Microparticle Filtration via Traveling Surface Acoustic Waves*, *Colloid and Interface Science Communications* **16** (2017), pp. 6–9,  
URL: <http://linkinghub.elsevier.com/retrieve/pii/S221503821630067X>
- [245] K. J. Storslett and S. J. Muller, *Evaluation and comparison of two microfluidic size separation strategies for vesicle suspensions*, *Biomicrofluidics* **11** (2017) (3), p. 034112,  
URL: <http://aip.scitation.org/doi/10.1063/1.4984302>
- [246] N. Sundararajan Authors contributed equ, D. Kim Current address: Department of B and A. A. Berlin, *Microfluidic operations using deformable polymer membranes fabricated by single layer soft lithography*, *Lab on a Chip* **5** (2005) (3), p. 350,  
URL: <http://xlink.rsc.org/?DOI=b500792p>
- [247] S. Choi and J.-K. Park, *Tunable hydrophoretic separation using elastic deformation of poly(dimethylsiloxane)*, *Lab on a Chip* **9** (2009) (13), p. 1962,  
URL: <http://xlink.rsc.org/?DOI=b820364d>
- [248] Y.-H. Chang, C.-J. Huang and G.-B. Lee, *A tunable microfluidic-based filter modulated by pneumatic pressure for separation of blood cells*, *Microfluidics and Nanofluidics* **12** (2012) (1-4), pp. 85–94,  
URL: <http://link.springer.com/10.1007/s10404-011-0851-0>
- [249] A. M. Taiwo, D. C. Beddows, Z. Shi and R. M. Harrison, *Mass and number size distributions of particulate matter components: Comparison of an industrial site and an urban background site*, *Science of The Total Environment* **475** (2014), pp. 29–38,  
URL: <https://linkinghub.elsevier.com/retrieve/pii/S004896971301557X>
- [250] S. Amaral, J. de Carvalho, M. Costa and C. Pinheiro, *An Overview of Particulate Matter Measurement Instruments*, *Atmosphere* **6** (2015) (9), pp. 1327–1345,  
URL: <http://www.mdpi.com/2073-4433/6/9/1327>